# Sol-gel synthesis of TiO2 anatase in a fluorinated medium and its applications as negative electrode for Li+ and Na+ batteries

Wei Li

Université Pierre et Marie Curie

Ecole doctorale : 388

*Physicochimie des électrolytes et nanosystèmes interfaciaux (PHENIX)*

*/L'équipe Electrochimie et Liquides Ioniques (ELI)*

# Sol-gel synthesis of $TiO_2$ anatase in a fluorinated medium and its applications as negative electrode for $Li^+$ and $Na^+$ batteries

Par Wei LI

Thèse de doctorat de Chimie et physicochimie des matériaux

Dirigée par Henri Groult et Damien Dambournet

Présentée et soutenue publiquement le 25 Septembre 2015

Devant un jury composé de :

| | | |
|---|---|---|
| M. DEMOURGUES Alain | Directeur de Recherche | Rapporteur |
| M. LEGEIN Christophe | Professeur | Rapporteur |
| Mme. RAYMUNDO Encarnacion | Chargé de Recherche | Examinatrice |
| M. SAUVAGE Frédéric | Chargé de Recherche | Examinateur |
| Mme. LABERTY Christel | Professeur | Examinatrice |
| M. GROULT Henri | Directeur de Recherche | Examinateur |
| M. DAMBOURNET Damien | Maître de Conférence | Directeur de thèse |

*Dédicace*

# Remerciements

*Les travaux de thèse, présentés dans ce mémoire ont été réalisés au sein du laboratoire PHysicochimie des Electrolytes et Nanosystèmes InterfaciauX (PHENIX) dirigé par le Dr. Pierre Levitz. Je le remercie de m'avoir accueillie au sein de son laboratoire.*

*Je remercie vivement Damien Dambournet, Maître de Conférences, Henri Groult, Directeur de Recherche au CNRS et Didier Devilliers, Professeur, pour m'avoir accueillie au sein de leur équipe durant cette thèse, et pour l'intérêt porté à ce travail.*

*Mes remerciements vont particulièrement à mon directeur de thèse, Damien Dambournet, pour m'avoir encadré, soutenue et formé au long de cette thèse, pour avoir suivi ce travail avec beaucoup d'enthousiasme, dynamisme et efficacité. Merci pour vos conseils, votre disponibilité et votre esprit critique. Bien au-delà de mes remerciements, je vous adresse toute mon estime et ma sincère reconnaissance.*

*Que Madame Sandrine Leclerc et Ana Gabriela Porras Gutiérrez reçoive ici l'expression de ma sincère gratitude pour leur aide lors des tests électrochimiques.*

*Je suis reconnaissant à Alain Demourgues et Madhu Chennabasappa (ICMCB) pour m'avoir accueilli dans leur équipe pour une période de recherche.*

*Un grand merci à Christophe Legein et Monique Body (Université du Maine) pour les mesures de RMN, Christine Labrugère (ICMCB) pour l'XPS, Sandra Casale pour la microscopie, Dario Corradini et Mathieu Salanne (PHENIX) pour la simulation DFT, Olaf Borkiewicz et Karena Chapman (ANL, USA) pour l'analyse de PDF.*

*Un grand merci à Dongya, David, Antonin, Jiwei, Augusta, Xudong, mes collègues au laboratoire, pour leur aide non seulement dans la recherche mais aussi dans la vie quotidienne en France.*

*Merci aussi à Encarnacion Raymundo, Frédéric Sauvage et Christel Laberty pour avoir accepté d'être le jury de cette thèse.*

*Ces remerciements seraient incomplets si j'omettais de remercier tous les membres du groupe PHENIX. Je tiens à les remercier pour leur accueil, leur sympathie ainsi que leurs précieux conseils.*

*Merci à tous ceux que je n'ai pas cité mais à qui je pense très fort.*

*Et enfin, je voudrais adresser ma plus profonde gratitude à ma famille pour leur soutien, leurs encouragements et leur confiance.*

# Table of contents

# General Introduction

The energy is the foundation of all the human beings activity. With the growth of the global population and the development of the economies, the energy consumption increases rapidly, especially in the recent years. The energy demand increased six times from 1950 to 2010. Some studies predict that this demand will be doubled at the year of 2050. Currently, 87 % of the total energy consumption comes from the combustion of fossil fuels, generating a great amount of greenhouse gas and air pollutants. This emission not only causes a severe environmental effect but also lead to global warming. More than 90 % of greenhouse gas emission originates from the combustion of fossil fuels. An international treaty, the Kyoto protocol, was signed in 1997 at addressing this global environmental problem by reducing the emission of greenhouse gas. In addition, the use of fossil fuels has caused the civil unrest, such as the Middle East oil crisis. Therefore, exploitation of renewable energy is necessary to account for the abovementioned problems.

Another problem is how to store energy. After capturing energy, a system of energy storage is needed prior to its use by devices. Energy storage in the form of electric is of great interest due to the high energy conversion efficiency. For instance, electrical efficiency is about three times higher than fuel efficiency.

Among the systems of storing electric energy, lithium-ion batteries (LIBs) have received extensive interest due to their high volume and gravimetric energy density. LIBs have been widely used as energy source in portable electrical devices and electric vehicles. However, cost, safety and power density are issues that still hinder the development of LIBs. The non-abundant Li source leads to a high cost of LIBs, thus alternative battery systems, such as sodium-ion batteries (SIBs), should be developed for grid energy storage. The safety issues of the LIBs are caused by the use of electrode having low operating potentials for which liquid electrolyte is not stable. Moreover, the development of electric vehicles demands for materials with high energy density. Our research aims at addressing these problems by means of synthesizing new electrode materials for LIBs and SIBs. In this thesis, we start from an earth abundant nontoxic compound $TiO_2$, which is a promising and versatile material in the

energy storage and conversion. Strategies such as nanotechnology, doping/substitution and morphology control have been used to tune its electrochemical properties.

This manuscript can be divided into four parts:

The first chapter provides a bibliographic support of our research. The properties of $TiO_2$, especially its electrochemical property vs. $Li^+$ are presented. The lithium insertion mechanism as well as the effect of particle size and morphology is emphasized. The solution-based synthesis of $TiO_2$ is reviewed subsequently. The influence of fluorine on the properties of $TiO_2$ particles is particularly presented.

The second chapter focuses on tuning the structure of $TiO_2$ anatase by $F^-/OH^-$ substitution. The atomic structure and chemical composition of the newly formed polyanionic phase was characterized by advanced techniques. Then, efforts are conducted on atomistic study of the formation mechanism of this phase. The intermediate phase and evolution of the anatase phase with reaction time are investigated.

The third chapter provides a systematical study on the effect of reaction parameters on the structure, morphology and chemical composition of the resulting phase. Various parameters including the nature of precursor and solvent, reactant concentrations and reaction temperature are studied.

The fourth chapter consists of studying the electrochemical properties of $TiO_2$ and the newly formed phase. The electrochemical performance vs. $Li^+$ and the $Na^+$ insertion mechanism are highlighted.

# Chapter I. Generalities on the Properties, Applications and Syntheses of $TiO_2$ anatase

Among the 9th elements the most abundant on earth, titanium, is one of the most studied elements in material science. Titanium dioxide ($TiO_2$), commercially produced in the early twentieth century, has been used as white pigment in paint due to its relatively high refractive index which results in high brightness. Since Fujishima and Honda discovered the photocatalytic activity of $TiO_2$ for water splitting in 1972,[1] applications of $TiO_2$ have been expanded to numerous domains, e.g. photoelectrochemical cell,[1-3] photocatalysis,[4,5] photovoltaic cell,[6,7] sensor,[8] lithium-ion batteries,[9-12] supercapacitors[13]. Moreover, $TiO_2$ has other apparent merits such as low cost, non-toxicity, thermal and chemical stability. All these advantages make it one of the most investigated materials.

$TiO_2$ has eleven allotropic forms. Among them, anatase, rutile and brookite polymorphs have gained the most attention, because the other forms do not exist naturally and their syntheses require very harsh conditions, i.e. high temperature or pressure.

The stability of $TiO_2$ allotropic forms depends on the particle size. Rutile is thermodynamically the most stable form for bulk titania and anatase was proved to be the most stable titania at nanoscale (<14 nm).[14] Brookite is a metastable polymorph and difficult to synthesize in pure form. This thesis would focus on the stabilization and crystal engineering of anatase $TiO_2$ nanoparticles.

This chapter is an overview about $TiO_2$ anatase. It focused mainly on the key points of this thesis and provides fundamental information in this domain.

Two parts are included in this chapter:

1. The first part presents the structural properties and applications of $TiO_2$ anatase, in particular its uses in energy storage, i.e. electrode for lithium/sodium-ion batteries.

2. The second part consists of an overview of solution-phase synthesis of $TiO_2$ prepared in a fluorinated medium.

# 1. Structural properties and applications of $TiO_2$ anatase

## 1.1. Structural considerations

### 1.1.1. Crystal structure

For the allotropic forms of titania, their structural difference generally lies in the way of the connectivity of $TiO_6$ octahedra subunits where each titanium is octahedrally surrounded by six oxygen atoms. Depending on the crystal structure, $TiO_6$ octahedra are connected by a various number of corner, edge and/or face-sharing.

The crystal parameters of $TiO_2$ anatase are gathered in **Table 1.1**. $TiO_2$ anatase crystallizes in a tetragonal cell with a space group of $I4_1/amd$. The unit cell contains 4 formula units, i.e. 12 atoms (**Figure 1.1a**). $TiO_2$ anatase involves one cation site for Ti and one anion site for O with multiplicities of 4 and 8, respectively. $TiO_2$ anatase consists of distorted $TiO_6$ octahedra sharing four edges. Two different Ti-O distances can be distinguished. Larger distance (1.964 Å) originates from two Ti-O bonds along c-axis, while shorter distance (1.937 Å) comes from four Ti-O bonds at (ab) plan. Each oxygen atom is coordinated with three titanium atoms. The 3D anatase network is formed by the stacking of zigzag chains along the c-axis (**Figure 1.1b**). The stacking mode for anatase results in a density of ca. 3.9 $g/cm^3$, which is lower than rutile and brookite. It means that, anatase shows larger area for same weight of material, indicating a higher degree of structural openness. Moreover, the stacking of zigzag chains creates vacant sites which are able to accommodate heteroatoms, i.e. intercalation properties.

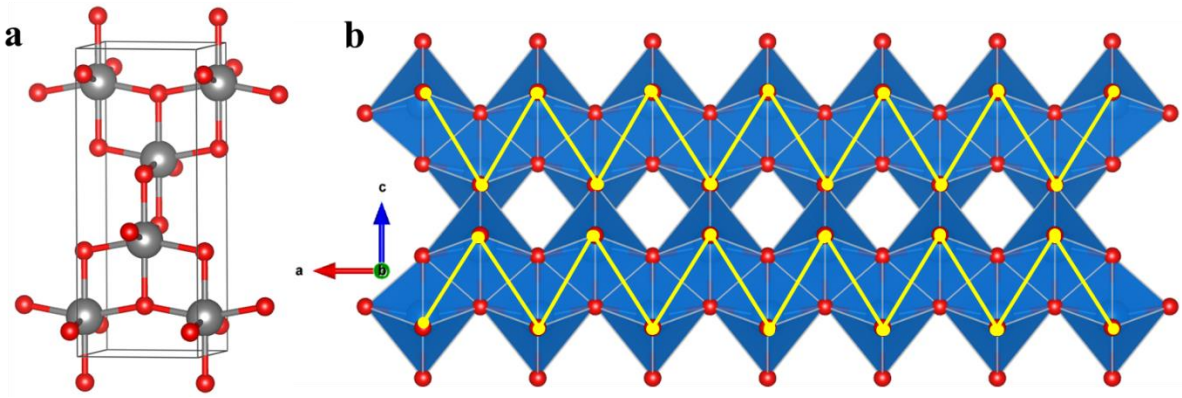


**Figure 1.1:** Structural representation of $TiO_2$ anatase: (a) ball-stick configuration of a unit cell, (b) extended unit cell showing the connectivity of $TiO_6$ octahedra (Grey: Ti, red: O).

**Table 1.1: Crystal structure information of $TiO_2$ anatase (Reference: ICSD #44882).**

| Crystal system | Space group | Lattice constant (Å) | Volume (Å$^3$) | $d_{Ti-O}$ (Å) | Density (g/cm$^3$) | Atomic Positions | | | | |
|---|---|---|---|---|---|---|---|---|---|---|
| | | | | | | Atoms | Site | x | y | z |
| Tetragonal | $I4_1/amd$ | a = b = 3.785<br>c = 9.514 | 136.3 | 2*1.964<br>4*1.937 | 3.88 | Ti | 4a | 0 | 0 | 0 |
| | | | | | | O | 8e | 0 | 0 | 0.2064 |

## 1.1.2. Electronic structure

Titanium dioxide is a semiconductor. **Figure 1.2** presents the molecular-orbital bonding diagram of $TiO_2$ anatase.[15] It shows that the upper valence band (VB) are dominantly composed of 2p orbital of oxygen atom. 3d orbital of titanium atom are mainly located at the bottom of conduction band (CB). For pure $TiO_2$ anatase, the energy gap $E_g$ between the top of VB and the bottom of CB is 3.2 eV. This value of band gap induces adsorption of photon below wavelength of ca. 380 nm. Consequently, $TiO_2$ is a white powder. It can absorb the light in the ultraviolet region, making it a good candidate as UV absorber and providing applications in cosmetics.

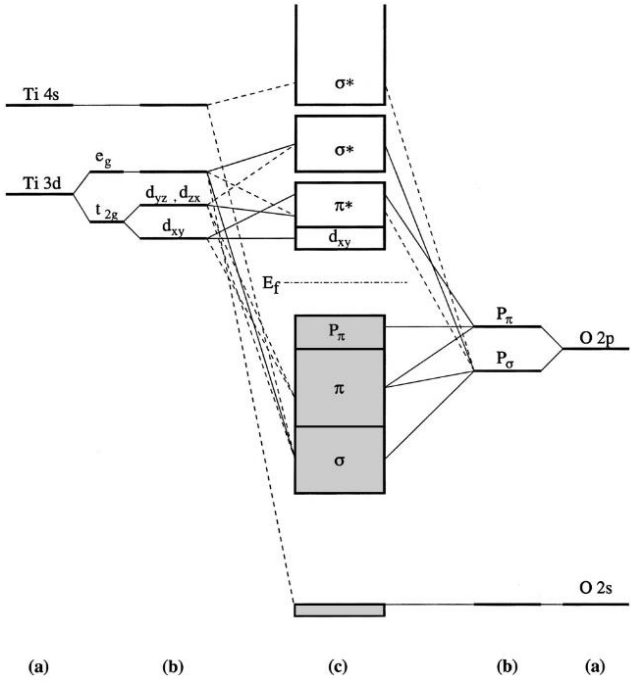


**Figure 1.2:** Molecular-orbital bonding structure for anatase $TiO_2$: (a) atomic levels; (b) crystal-field split levels; (c) final interaction states. Dashed lines represent weak contributions and solid lines represent strong contributions.[15] Reprinted with permission from Asahi, R. et al. J. Phys. Rev. B 2000, 61, 7459. Copyright 2000 American Physical Society.

### 1.1.3. Surface structure

According to the Wulff construction, $TiO_2$ anatase shows the equilibrium shape of a slightly truncated octahedron dominated by eight {101} facets on the sides (more than 94 %) and two {001} facets on the top and bottom (less than 6 %) (The left panel in **Figure 1.3a**).[16] The possible shapes of $TiO_2$ anatase derived from the truncated octahedron are shown in the right panel of **Figure 1.3a**. Different facets have different surface energy. For low-indexed facets, the order of surface energies is {110} (1.09 J $m^{-2}$) > {001} (0.90 J $m^{-2}$) > {010} (0.53 J $m^{-2}$) > {101} (0.44 J $m^{-2}$).[16,17] {110} facet is the most reactive surface whereas {101} facet is thermodynamically the most stable surface. The surface energy of $TiO_2$ anatase is likely related to the density of undercoordinated surface Ti atoms.[18] For example, {110} facets contain 4-fold coordinated Ti ($Ti_{4c}$) atoms. {001} facets are composed of 5-fold coordinated Ti ($Ti_{5c}$) atoms (**Figure 1.3b**) and {101} facets have 50 % 5-fold coordinated Ti ($Ti_{5c}$) and 50 % saturated $Ti_{6c}$ atoms (**Figure 1.3c**). It shows that the surface energy increases with the number of unsaturated titanium. Driven by the minimization of surface energy, high reactive surface is usually unstable and vanishes rapidly during crystal growth. Therefore, it is difficult to stabilize high energy surfaces.

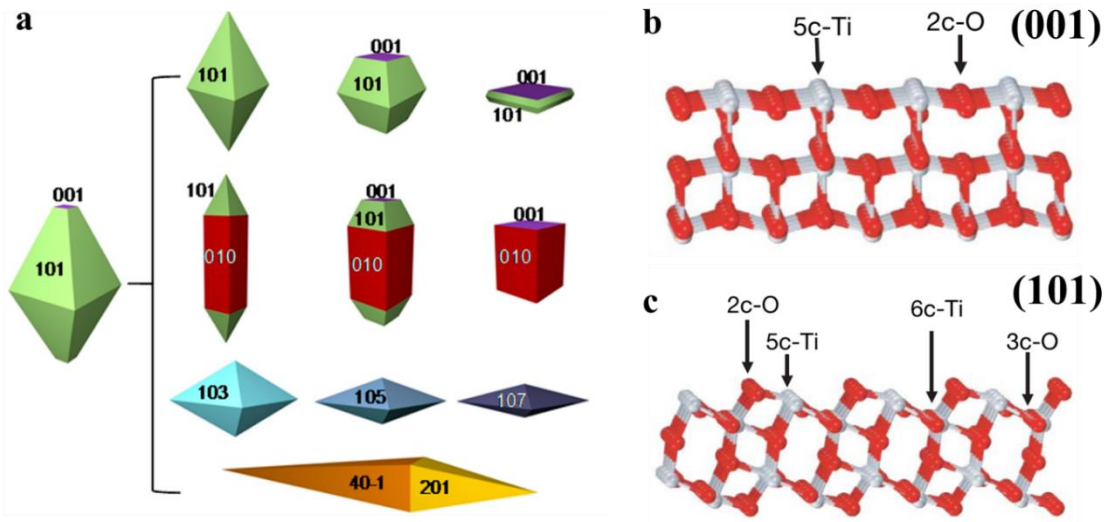


**Figure 1.3:** (a) Equilibrium crystal shape of anatase $TiO_2$ through the Wulff construction[16] and the evolved other shapes.[19] Reprinted with permission from Liu, G. et al. Chem. Rev. 2014, 114, 9559. Copyright 2014 American Chemical Society. Clean (001) and (101) surfaces of anatase $TiO_2$ are shown in (b) and (c), respectively.[20] Reprinted with permission from Yang, H. G. et al. Nature 2008, 453, 638. Copyright 2008 Nature Publishing Group.

## 1.2. Photocatalytical applications

When $TiO_2$ anatase is under the irradiation of the light in which photons have the energy equal or higher than 3.2 eV, electrons in VB will be excited into the unoccupied conduction band. As a result, a positive hole ($h^+$) is created in the VB (**Figure 1.3**). The photogenerated electron-hole pairs can recombine in a very limited time scale, or be trapped and react with electron donors/acceptors through redox reactions. This process in $TiO_2$ was first discovered by Fujishima and Honda in 1972,[1] the pioneering work has broadened the application of $TiO_2$ to the domain of photocatalysis. One representative application of $TiO_2$ in energy conversion is photoeletrochemical water splitting (**Figure 1.3**). This process consists of a dissociation of water into its constituent parts, hydrogen ($H_2$) and oxygen ($O_2$). Water will be oxidized by positive hole to form oxygen gas (**Eq. 1.1**) and hydrogen will be concomitantly formed through electron-induced reduction reaction (**Eq. 1.2**).

$$H_2O + 2h^+ \rightarrow \frac{1}{2} O_2 + 2H^+ \qquad \textbf{(Eq. 1.1)}$$

$$2H^+ + 2e^- \rightarrow H_2 \qquad \textbf{(Eq. 1.2)}$$

$TiO_2$ can also serve to prevent the recombination of electron-hole pairs, affording photovoltaic applications. An example is the dye-sensitized solar cell (DSC or Grätzel cell).[7] In that case, $TiO_2$ does not adsorb light, but collects the electrons photogenerated by dyes. The electrons are then conducted through the CB of $TiO_2$ to the outer circuit to make electric power.

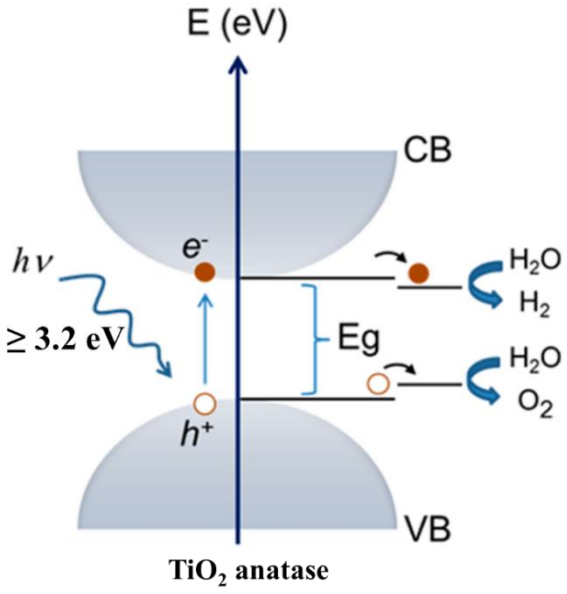


**Figure 1.3:** Schematic presentation of the typical light-induced decomposition of water molecules wherein (i) hydrogen is produced via a reduction process at the conduction band assisted by a photoelectron and (ii) oxygen is produced via an oxidation process assisted by a photoinduced hole in the valence band of the photocatalyst.[21] Reprinted with permission from Kapilashrami, M. et al. Chem. Rev. 2014, 114, 9662. Copyright 2014 American Chemical Society.

## 1.3. Electrochemical applications

### 1.3.1. General introduction to energy storage and conversion

Capacitors, supercapacitors, batteries and fuel cells are systems capable of storing energy. **Figure 1.4a** illustates the Ragone chart of the power density *vs.* energy density of each system. Capacitors, which typically store the energy electrostatically between two electrical conductors separated by isolators, have a very high power density but the lowest energy density. Supercapacitors have better energy density than capacitors because the energy is stored electrochemically within electrochemical double-layer at the electrolyte-electrode interface. For batteries and fuel cells, the energy is stored in chemical form. The chemical energy can be converted into electric energy by means of redox reactions. As fuel cells

usually require high energy sources, i.e. $H_2$, consequently they exhibit the highest specific energy among the presented energy storage devices.

Batteries are largely used in portable electronic devices and electric vehicles. The enormous application market of batteries is due to its reliability and intermediate power and energy characteristics. A battery is constituted by three components: an anode (negative electrode), a cathode (positive electrode), an electrolyte and a separator which separates the two electrodes to prevent internal short-circuit. When an external device is used to connect these two electrodes, the difference of potential between two electrodes will spontaneously drive the electron to flow from negative to positive side. The charge balance will be maintained through simultaneous ions transportation by the electrolyte. The amount of electrical energy that a battery can deliver depends on two factors: overall voltage of a cell and capacity of electrodes. These two factors are the chemistry characters of materials. Batteries can be divided into two categories: primary cells and secondary cells. The formers are designed for once use and then be discarded after discharge. Secondary cells are rechargeable and can be charged/discharged for hundred to a thousand time. Among the different existing battery systems (**Figure 1.4b**), Lead-acid and nickel cadmium batteries have been first developed. These systems have low energy density and contain toxic metals. To address the development of portable electronic devices and electric vehicles, alternative battery systems, which show high specific energy density and environmentally friendly properties, e.g. lithium batteries, have been largely investigated.[22]

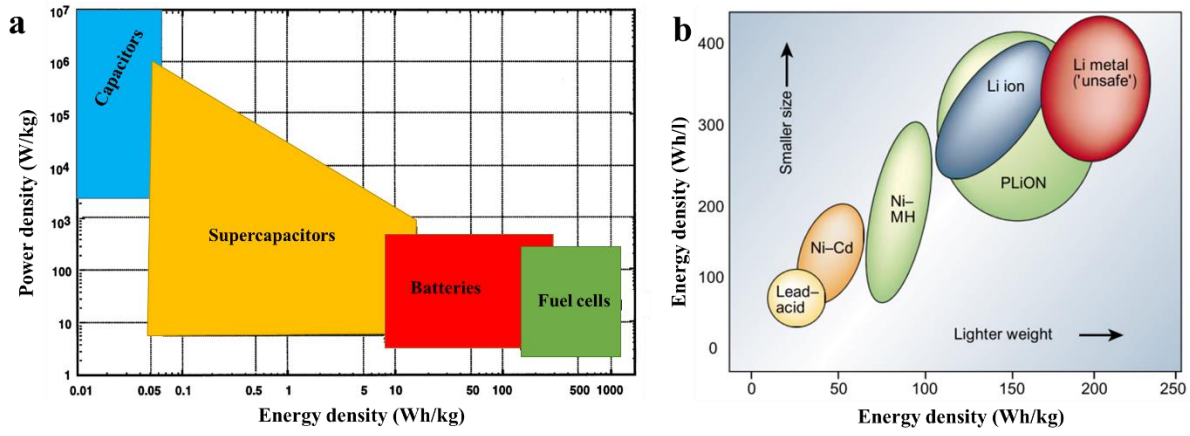


**Figure 1.4:** (a) Ragone chart for different energy storage devices.[23] Reprinted with permission from Kötz, R.; Carlen, M. Electrochimica Acta 2010, 45, 2483. Copyright 2000 Elsevier. (b) Comparison of the different battery technologies in terms of volumetric and gravimetric energy density.[22] Reprinted

with permission from Tarascon, J.-M.; Armand, M. Nature 2001, 414, 359. Copyright 2001 Nature Publishing Group.

## 1.3.2. Electrochemical properties of $TiO_2$ anatase vs. $Li^+$

### 1.3.2.1.State of the art of lithium batteries

Lithium batteries, first commercialized in 1991 by Sony, have attracted enormous attention from industry to scientific community, due to their reliability, longer shelf life, good cyclability and high coulombic efficiency, especially the excellent gravimetric and volumetric storage capacities. Today, they have been widely used as power source for portable electronic devices, electric vehicles, etc. **Figure 1.5** schematically illustrates the operation principle of lithium-ion rechargeable batteries (LIBs).[24] In this example, the system used graphite as the anode and layered Li-intercalated compound $LiCoO_2$ as the cathode. During the process of charge, lithium is extracted from the cathode, inducing the oxidation of transition metal $Co^{3+}$ which releases electrons to the external circuit through the current collector. The lithium will then migrate to the negative electrode where it is reduced to its metallic state. Upon discharge, opposite processes take place, consequently leading to the lithium back to the cathode, giving rise to the rechargeability of LIBs.

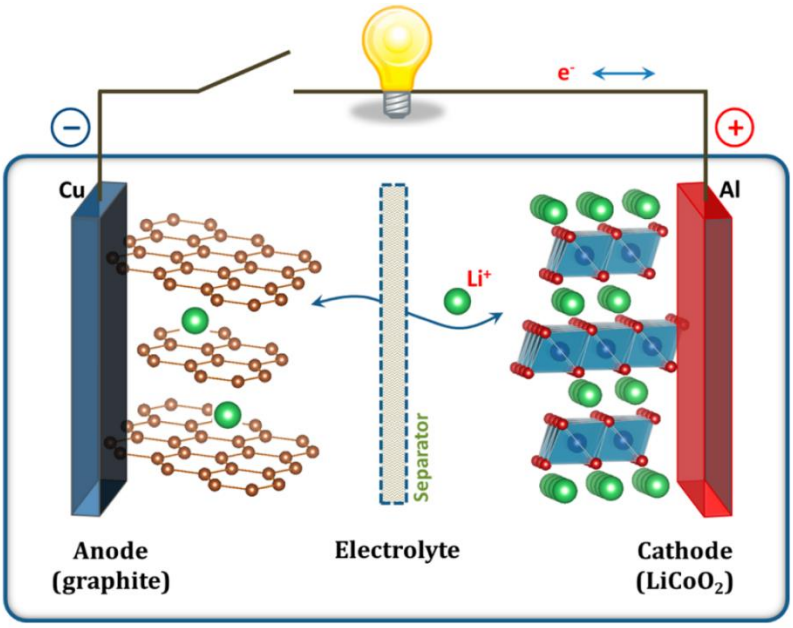


**Figure 1.5:** Schema illustrating the operation principle of lithium-ion batteries. The negative electrode is graphite, whereas the positive electrode is a Li-intercalation compound $LiCoO_2$.[24] Reprinted with permission from Goodenough, J.B.; Park, K.-S. J. Am. Chem. Soc. 2013, 135, 1167. Copyright 2013 American Chemical Society.

**Lithium metal batteries.** Lithium batteries can be categorized, based on the materials of negative electrode, as lithium metal batteries and lithium-ion batteries (LIBs). A lithium metal battery uses metallic lithium and lies on the $Li^+/Li$ redox couple. Metal lithium not only acts as negative electrode, but supplies lithium ions. The lowest operating potential (-3.04 V vs. the standard hydrogen electrode) and the highest specific capacity (3861 mAh/g) of metallic Li result in the highest energy density of lithium metal batteries. However, some drawbacks have limited their uses over decades. Firstly, metal lithium has a high electropositivity and is very reactive. The exothermal reaction with oxygen and/or water poses safety issues. Secondly, the low operating potential of $Li^+/Li$ causes the decomposition of organic electrolyte, leading to the formation of solid electrolyte interface (SEI) layer composed of LiF, Li alkoxide and Li carbonate on the surface of anode.[25] SEI layer has low mechanic stability, continuously breaks under deformation and repairs during cycling. These processes consume the electrolyte and lower the coulombic efficiency of batteries. Moreover, the SEI layer is thermally instable, causing serious consequences. Another problem is that the deposition of metallic lithium on the electrode surface upon charge is not uniform. Long term discharge/charge cycles would lead to the formation of dendrites of lithium, which can grow across the electrolyte and break the separators, consequently short-circuit the cell of batteries.[26,27]

**Lithium-ion batteries.** In a lithium-ion battery, metal lithium is replaced by materials that can accommodate the charge-carrying ions, i.e. $Li^+$. That avoids the direct use of metallic lithium, thus becoming the most used rechargeable battery system. Nevertheless, the most common used anode material for LIBs is carbonaceous-based compounds. These materials have a lithium-ion intercalation potential of ca. 0.1 V *vs.* $Li^+/Li$. As a result, LIBs have suffered similar safety issues than that of lithium metal batteries, i.e. electrolyte decomposition and lithium plating.[28] The safety problems has haunted carbonaceous-based materials as anode for LIBs. Numerous approaches have been conducted to address the abovementioned problems, such as the use of solid electrolyte, building thin protecting films on electrode.[22,28,29] Among them, use of a material of which the operating potential locates within the electrolyte stability region (1.0 – 4.3 V vs. $Li^+/Li$) is an effective method to improve the safety of the Li-cell. Many transition metal oxides, phosphides and nitrides have the operating potential at this region.[30]

#### 1.3.2.2.Lithium intercalation into $TiO_2$ anatase

Titanium dioxide, displaying an operating potential of ca. 1.7 V vs. $Li^+/Li$, can efficiently prohibit the decomposition of most types of electrolytes. Therefore, it is a good candidate as an anode materials for LIBs. $TiO_2$ can theoretically accommodate one lithium atom per formula unit, resulting in a capacity of 335 mAh/g. The electrochemical reaction of lithium intercalation into $TiO_2$ can be written as following:

$$TiO_2 + nLi^+ + ne^- = Li_nTiO_2 \qquad \textbf{(Eq. 1.3)}$$

Where n is the number of inserted $Li^+$ per formula unit of $TiO_2$. Furthermore, $TiO_2$ can sustain high discharge/charge rate and is promising in high power applications such as electric vehicles.[31-33]

$TiO_2$ anatase shows favorable properties for $Li^+$ insertion due to the three dimensional open structure. The stacking of zigzag chains provides possible interstitial sites and diffusion path for $Li^+$ (**Figure 1.1**). It is well-known that spontaneous phase separation occurred when lithium is inserted into $TiO_2$ anatase.[9,11,34,35] Upon lithiation, lithium was found to insert in the interstitial voids of $TiO_2$ anatase,[9] leading to an orthorhombic distortion of the tetragonal structure (space group: $I4_1/amd$) of $TiO_2$ anatase. As a result, $Li_{0.5}TiO_2$ (Li-titanate) phase indexed by the space group Imma is formed (**Figure 1.6a** and **Table 1.2**). Lithium was considered to be randomly distributed in the interstitial sites, the phase separation was proposed due to Jahn-Teller distortion.[36] Recently, according to density functional calculations, Morgan predicted that this phase transformation originates from the pairing effect of $LiO_6$ octahedra.[37] For n(Li) < 0.5, the system energy was minimized when the phase was separated into anatase and Li-titanate. For n(Li) = 0.5, the lowest energy was found for $Li_{0.5}TiO_2$ orthorhombic structure in which pairs of $LiO_6$ octahedra are edge-shared in the xz plane (**Figure 1.6b**). Hence, lithium is not randomly intercalated into interstitial sites but shows local ordering.

**Table 1.2: Variation of lattice parameters and space group of $TiO_2$ upon lithiation.[34]**

| | *Space group* | *a (Å)* | *b (Å)* | *c (Å)* |
|---|---|---|---|---|
| **$TiO_2$ Anatase** | $I4_1/amd$ | 3.787 | 3.787 | 9.515 |
| **$Li_{0.5}TiO_2$** | Imma | 3.819 | 4.084 | 9.066 |

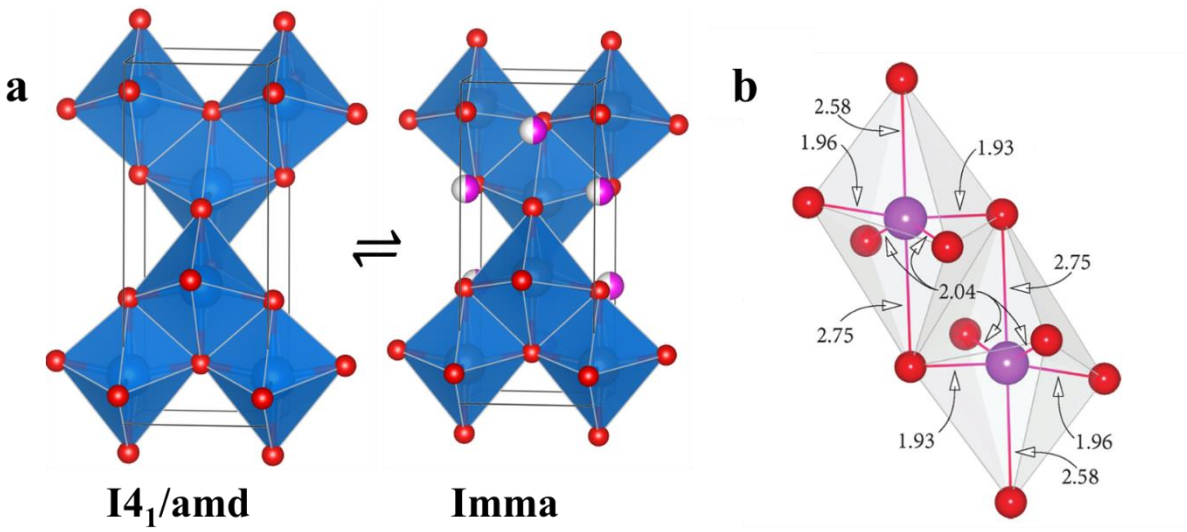


**Figure 1.6:** (a) Structural representation of phase transition from anatase ($I4_1/amd$) to $Li_{0.5}TiO_2$ (Imma) upon lithiation. Lithium has an occupancy of 0.5 and is considered to be randomly distributed. Grey: Ti, red: O, violet: Li. (b) Coordination geometry for the paired Li-occupied octahedra.[37] Reprinted with permission from Morgan, B.J.; Watson, G.W. J. Phys. Chem. Lett. 2011, 2, 1657. Copyright 2011 American Chemical Society.

**Size effect.** It has been found that the property of lithium insertion into $TiO_2$ anatase is strongly affected by particle size.[11,34,35] At room temperature, the theoretical capacity (335 mAh/g) for bulk $TiO_2$ anatase cannot be reached due to poor ionic conductivity of the $Li_1TiO_2$ phase.[34] The formation of $Li_1TiO_2$ was observed only at elevated temperatures, indicating that this process is kinetically hindered.[38] The number of intercalated lithium into bulk $TiO_2$ anatase is generally reported to be inferior of 0.6.[39] However, downsizing material particles to nanoscale has been shown to be a very promising strategy to overcome physico-chemical restrict of bulk material, and provide favorable electrochemical properties.[40,41] Nanosized anatase can accommodate more lithium greater than 0.6 Li per $TiO_2$. It is reported that only the first 3 – 4 nm shell of $TiO_2$ anatase nanoparticles can be converted into $Li_1TiO_2$.[34] The fully occupied sites by lithium prevent further lithium diffusion into deeper region. Therefore, upon lithiation, fully utilized $Ti^{4+}/Ti^{3+}$ redox couple can be obtained only for anatase with the size below 7 nm.[34]

**Figure 1.7a** shows a typical galvanostatic voltage profile of $TiO_2$ anatase nanoparticles.[11] Three voltage regions can be identified and marked as i, ii, iii. A rapid decrease of potential from 3 to ~1.75 V at region (i) is attributed to the homogeneous insertion of $Li^+$ into anatase *via* solid solution mechanism. A plateau at region (ii) is associated to the 2-phase reaction where tetragonal anatase is transformed into orthorhombic Li-titanate. Below

the plateau can be observed a slope voltage curve at region (iii) which is related to monophasic lithium insertion into Li-titanate as well as surface/interfacial lithium storage. These three different domains are highly dependent on particle size. Downsizing anatase particles can increase the Li solubility in anatase and Li-titanate, thus enlarging the region i and iii and reducing the length of plateau at region ii.[34,35] The disappearance of the plateau can be observed for very small anatase particles (4.5 nm)[42] and amorphous phase[11].

The anatase-titanate phase separation displayed as a plateau region in the voltage profile is a non-equilibrium process and size-dependent.[34,35] Upon lithiation, larger particles (130 nm) involve co-existence of anatase and Li-titanate phases within one particle, Li-titanate grow through phase boundary migration. For smaller particles (15 nm), due to short lithium diffusion path and instantaneous initial boundary movement, the phase transforms particle by particle (**Figure 1.7b**). The modified phase transition mechanism for smaller particles gives rise to the better electrochemical performance of nanosized $TiO_2$ anatase than microsized materials.

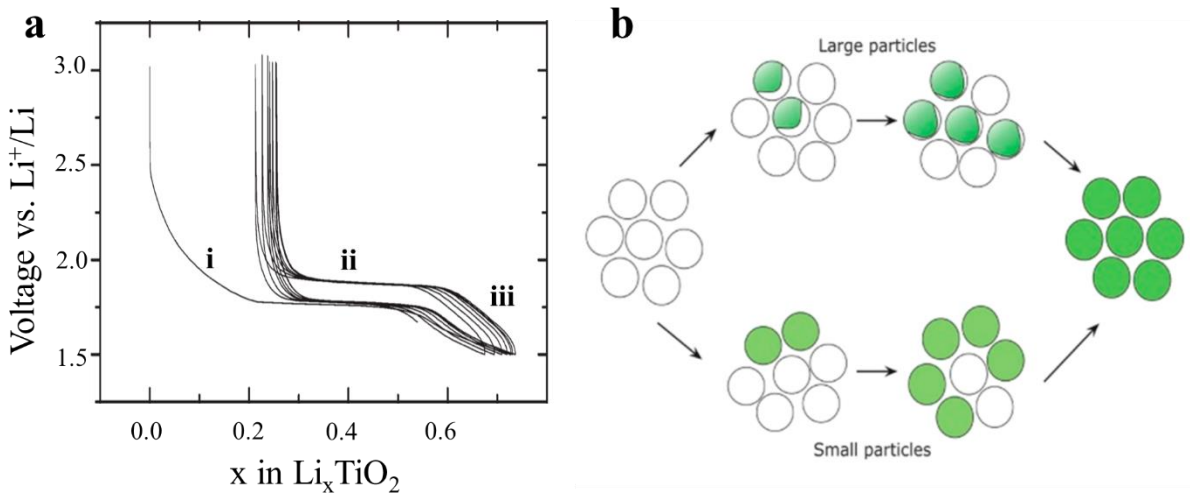


**Figure 1.7:** (a) Galvanometric voltage profiles of $TiO_2$ anatase cycled between 1 – 3 V.[11] Reprinted with permission from Sudant, G. et al. J. Mater. Chem. 2005, 15, 1263. Copyright 2005 Royal Society of Chemistry. (b) Schematic view of the sequential nucleation mechanism in $TiO_2$ electrodes during discharge for different particle sizes. White indicates the lithiated anatase and the green the Li titanate phase.[35] Reprinted with permission from Shen, K. et al. Chem. Mater. 2014, 26, 1608. Copyright 2014 American Chemical Society.

**Surface effect.** Surfaces orientation also affects the lithium storage performance, as the reactivity of different surfaces is not the same.[19,33] The energy barrier of $Li^+$ diffusion into bulk $TiO_2$ anatase (0.35 – 0.65 eV) is smaller than that into surfaces (2.73 eV for the most

stable (101) surface), indicating that surface insertion is rate-limiting step.[33] Computational study of $Li_4Ti_5O_{12}$ showed that high energy (100) surfaces are energetically more favorable for lithium insertion, whereas insertion by (111) surfaces provides higher capacity.[43] Moreover, surface property can extend nanometers into the particles, leading to enhanced Li storage performance for faceted nanoparticles. Therefore, surface engineering of nanoparticles is crucial to improve the electrochemical performance *vs.* $Li^+$. (001) surfaces of anatase have lower energy barrier (1.33 eV) than (101) surfaces. Faster interfacial charge transfer and more open structure in the direction of c-axis of (001) surfaces provide enhanced $Li^+$ insertion/extraction kinetics.[44] Moreover, {001} facets show enhanced electron migration rate at $TiO_2$ and current collector interface.[45] The synergistic effect of both electron and lithium migration rate gives rise to a superior lithium storage capability of $TiO_2$ anatase dominated with {001} facets. Electrochemical experiments performed by Sun et al. showed that at a current density 165 mA/g, $TiO_2$ anatase dominated by (101) and (001) surfaces didn't show significant difference in terms of capacity.[33] When the loading rate rose tenfold, however, anatase with dominant (001) facets showed pronounced rate behavior, highlighting surface effect on battery performance.

In addition to size and surface effect, lithium intercalation behavior can also be modified by bulk structure, i.e. defects.[46] It has been reported that the electrochemical performance of γ-$MnO_2$[47] and γ-$Fe_2O_3$[48] nanoparticles was enhanced by introducing cation vacancies in the bulk structure. Vacancies not only favor $Li^+$ diffusion kinetics, but also act as vacant sites for lithium accommodation.[48] Electrochemical study of cation-defected $TiO_2$ has not been reported so far. We successfully incorporated high concentration of cation vacancies within $TiO_2$ anatase structure (Chapter II.1) and their impact on electrochemical properties is presented in Chapter III.2.

### 1.3.3. Electrochemical properties of $TiO_2$ anatase vs. $Na^+$

Located just below lithium in the periodic table, sodium is the second lightest and smallest alkali metal. It is one of the most abundant elements in the Earth's crust particularly in sea water and salt deposits. Physical properties of $Li^+$ and $Na^+$ as charge carriers are compared in **Table 1.3**. The redox couple of sodium $Na^+/Na$ has the standard electrochemical potential of -2.71 V *vs.* SHE, a little higher than that for lithium (-3.04 V). Sodium-ion batteries (NIBs) are pre-seen as an alternative to lithium-ion batteries. However, intensive

efforts have been conducted for LIBs in the last three decades, whereas research of NIBs almost disappeared. Recently, the limited world's lithium resources and the demand for large-scale energy storage have motivated the search for alternative charge carriers besides lithium. Therefore, NIBs have regained researcher's attention and the relative publications increased dramatically since 2010.[49]

**Table 1.3: Physical properties for $Li^+$ and $Na^+$.[49]**

| | *Atomic mass* | *Shannon's ionic radii (Å)* | *Standard potential (V)* | *Melting point (°C)* | *Theoretical capacity for metal electrode (mAh/g)* |
|---|---|---|---|---|---|
| **$Li^+$** | 6.94 | 0.76 | -3.04 | 180.5 | 3861 |
| **$Na^+$** | 23.00 | 1.02 | -2.71 | 97.7 | 1166 |

$TiO_2$ anatase, a promising anode for LIBs as shown in Chapter I.1.3.2, was initially found to be not suitable to reversibly (de-)insert $Na^+$ into the anatase lattice.[50] A very recent research first claimed that nanocrystalline $TiO_2$ anatase can successfully sustain reversible sodium uptake and release.[51] The operating potential of $TiO_2$ in a Na-cell is ca. 0.8 V, lower than that in Li-cell. The theoretical capacity of $TiO_2$ anatase in Na-cell is the same with that in Li-cell, i.e. 335 mAh/g, indicating that nanosized $TiO_2$ anatase might be a promising anode for NIBs.

It is well-known that lithium insertion into anatase bases on a biphasic reaction characterized by a significant plateau in voltage profile. For the sodiation, however, the plateau region cannot be clearly distinguished, indicating that there might be a difference between electrochemical reactions with sodium and lithium. In addition, the difference in operating voltage of $TiO_2$ in Li- and Na-cell might due to modified ion insertion mechanism. Many studies have been conducted in revealing the sodiation reaction mechanism in $TiO_2$.[52-55] Nevertheless, contradictory conclusions were reported, indicating that sodium insertion into $TiO_2$ anatase should be very complicated, e.g. presence of amorphous phase, local disorder. Therefore, it is of great interest to study the electrochemical sodiation of $TiO_2$ anatase. A powerful analytical tool, the PDF analysis, has been applied to investigate such mechanism. The results are shown in Chapter III.3.

# 2. Elaboration of $TiO_2$ in solution

Numerous synthetic methods have been reported to prepare $TiO_2$ nanomaterials, such as sol-gel, chemical vapor deposition, microwave method, electrodeposition.[4,56] Among them, sol-gel method is a versatile tool and widely used to prepare $TiO_2$ due to its flexibility in dopant introduction and effective control of particle size, morphology and chemical composition of $TiO_2$. This part would focus on the elaboration of $TiO_2$ in solution. General reactions and steps for the synthesis of an oxide via sol-gel process are presented. The role of anions, particularly the fluorine during the preparation of $TiO_2$, are reviewed.

## 2.1. Generality on sol-gel chemistry

Sol-gel method has been used to stabilize a great number of metal oxide compositions that cannot be obtained through traditional ceramic powder methods.[57-59] Oxide network is obtained from the polymerization of molecular precursors occurring in solutions. The sol-gel processes provide many advantages such as high purity and homogeneity[60,61] and lower temperature required as compared to the ceramic method.[62] Sols and gels can be used to fabricate films, fibers and powders through different techniques such as dip-coating and spinning.[63,64] Materials can be tailored by controlling the sol-gel process by varying synthetic parameters.[65] All these features have stimulated an enormous growth of interest of sol-gel process during the past decades.

### 2.1.1. The sol-gel process

Sol is a colloid solution containing very small particles whose size ranges from 1 nm to hundred nm. A gel is a solid, interconnected three dimensional network with submicrometer pores and cross-linked chains having average length larger than a micrometer. The sol-gel method involves firstly the formation of sols through hydrolysis and condensation of inorganic or metal-organic precursors. Secondly, liquid sols undergo a series of chemical reactions and transform towards solid skeleton within liquid phase. The biphasic system containing liquid phases trapped into solid is a gel. Metal oxides can be obtained when the liquid phase is further removed. Three approaches have been conducted to fabricate oxides through sol-gel process[66]: (i) gelation of colloidal particles; (ii) hypercritical drying of gels formed through hydrolysis and condensation of alkoxide precursors; (iii) aging and drying of

gels formed through hydrolysis and condensation of alkoxide precursors. In this thesis, titanium dioxide frameworks are prepared by the approach 'iii' of which the mechanism of the process is emphasized in the follows.

The formation of an oxide from molecular precursor via sol-gel process generally involves four main steps[66]: (1) Mixing alkoxide precursors with water to initiate hydrolysis and condensation reactions. The polymeric framework of sols can be obtained by linking metal ions through M-O-M bonds. This step is controllable by varying synthetic parameters, such as hydrolysis ratio and pH. (2) Linking the sols together through prolonging reaction time (gelation). Three dimensional gels can thus be formed. (3) Coarsening the solid by spontaneous polycondensation and dissolution/recrystallization processes (aging). Neighboring hydroxyl groups can condense spontaneously, increasing the strength of the gel. Meanwhile, driven by minimization of surface energy, small particles would dissolve and reprecipitate on large ones, leading to the increase of the thickness of the gel. (4) Removing the liquid (drying). When liquid in the gel is evaporates, precipitation of metal oxide occurs. This process can take place under heating in aqueous (hydrothermal) and non-aqueous conditions (solvothermal). Metal oxide obtained from sol-gel reactions has a low crystallinity. A thermal treatment is generally needed.

The abovementioned four steps consist of the main processes of the transformation from molecular alkoxide precursors to solid oxides networks *via* sol-gel method. They provide control over the physical characteristics of a material from the early stage of processing. The purity and homogeneity of oxides have been greatly enhanced through sol-gel process. The next part will mainly focus on the reaction mechanism occurring during sol-gel process: hydrolysis and condensation reactions.

### 2.1.2. Reaction mechanisms of the sol-gel method

Precursors used in sol-gel reactions generally involve metal alkoxides $M(OR)_n$, where R represents an alkyl group. The reactivity of precursors arises from the electronegativity of alkoxo groups which results in high reactivity of metal ions towards nucleophilic attack.[67] Therefore, metal alkoxides can react with water to form metal oxides. The mechanism of precursor to oxide network transformation consists of two processes:

- Hydrolysis which corresponds to the activation reaction.

- Condensation which induces the growth of metal oxide.

**Hydrolysis.** Hydrolysis is a reaction which breaks the chemical bond in a molecule by water. When water is added into precursor solution, a reactive M-OH hydroxo group is formed through the following reaction:

Hydrolysis: $M(OR)_n + xH_2O \rightarrow M(OR)_{n-x}(OH)_x + xROH$ (**Eq. 1.4**)

This reaction can be divided into three steps:[65] (i) nucleophilic addition of water molecule onto the titanium center; (ii) proton transfer from the water molecule to alkoxy groups via a transition state; (iii) departure of alcohol molecule.

Hydrolysis of metal alkoxides can be regarded as nucleophilic substitution. The thermodynamics of this reaction is governed by the several factors. (1) The nucleophilic property of entering group: when the entering group is more nucleophilic, it can react with the metal atom easier. (2) The electrophilic character of the central metal atom: hydrolysis is favored when the eletrophilicity of the central metal atom increased. (3) Coordination unsaturation of metal atom, given by the discrepancy between oxidation state (z) and coordination number (N) of the metal atom: Larger N-z induces lower activation energy for nucleophilic addition.

**Condensation.** Condensation process occurs spontaneously to connect precursor molecules as soon as alkoxide precursors are hydrolyzed. Three different reactions are involved:

Olation: $-M-OH + H_2O - M- \rightarrow -M-OH-M- + H_2O$ (**Eq. 1.5**)

Oxolation: $-M-OH + HO - M- \rightarrow -M-O-M- + H_2O$ (**Eq. 1.6**)

Alcoxolation : $-M-OR + HO - M- \rightarrow -M-O-M- + ROH$ (**Eq. 1.7**)

The olation reaction involves elimination reaction of aquo ligand and formation of bridging $\mu_2$-OH from terminated $\mu_1$-OH (**Eq. 1.5**). Such a reaction is usually very fast due to the lability of the coordinated water. The oxolation and alcoxolation reactions induce the formation of metal oxo bridges M-O-M which are the precursors of the final oxide frameworks. These two reactions show similar mechanism, as hydrolysis, involving

nucleophilic addition, proton transfer and departure of protonated ligand. The thermodynamics of these two reactions are therefore governed by the same factors as for hydrolysis.

Metal alkoxide precursors undergoing the aforementioned four reactions (hydrolysis, olation, oxolation and alcoxolation) can transform into oxide frameworks. Hydrolysis and condensation reactions are usually competitive and show different rates at different pH values. The contribution of each reaction strongly affects the structure and morphology of final oxide phases.[65] At neutral solution, condensation is much faster than hydrolysis by 4 orders of magnitude. Precursor would be immediately condensed when they are hydrolyzed. At high pH, however, hydrolysis rate is very fast due to high concentration of nucleophilic $OH^-$. Therefore, acids and bases are commonly used to catalyze these two processes. Furthermore, the kinetics of these reactions can be controlled by adjusting experimental reaction conditions, such as nature of precursor, solvent, temperature, reactant ratio and concentration.

## 2.1.3. Parameters affecting the sol-gel process

### 2.1.3.1.Nature of alkoxide precursor

Titanium alkoxides $Ti(OR)_4$ ($R = C_nH_{2n+1}$) are the most used precursors in the preparation of $TiO_2$ *via* the non-aqueous sol-gel method. It has been reported that the nature of hydrolysis rate strongly depends upon the organic groups of the precursor.[65] Hydrolysis of titanium alkoxides is slowed down when the length of alkyl group increases. The alkyl group also exerts steric hindrance, affecting the rate of hydrolysis as well. For example, when R = Et or $^i$Pr, titanium dioxide can be precipitated,[68] whereas linear polymers is formed when R = $Bu^n$.[69] $TiO_2$ powder obtained after calcinating a gel contains both rutile and anatase phases. The ratio rutile/anatase can be tuned while changing the length of alkyl group.[70]

### 2.1.3.2.Nature of solvent

Non-aqueous sol-gel chemistry is based on the reaction of alkoxides precursor dissolved in non-aqueous solvent. It is reported that nature of solvent influences the physic-chemical properties of resulting materials as it can react with alkoxide precursors by alcohol interchange.[71-73] The reaction can be expressed as following:

Alcohol interchange: $M(OR)_n + xR'OH \rightarrow M(OR)_{n-x}(OR')_x + xROH$ (**Eq. 1.8**)

When titanium alkoxides are dissolved into alcohol solvent, exchange of alkoxy groups takes place by substitution reaction, modifying the chemical composition and therefore the reactivity of titanium alkoxides. For instance, when $Ti(OPr^i)_4$ is dissolved in tert-amyl alcohol, $Ti(OPr^i)_{4-x}(OAm^t)_x$ (x = 0–4) species are formed instantaneously upon alcoholysis reactions.[72] Their concentration can be tuned by the concentration of tert-amyl alcohol. Different species show different reaction phenomena. Hydrolyses of $Ti(OPr^i)_4$, $Ti(OAm^t)_4$ and $Ti(OPr^i)_{4-x}(OAm^t)_x$ (x = 2, 3) lead to precipitation[74], stable colloidal solution[71] and white gels[72], respectively, highlighting strong effect of solvent on the reactivity of alkoxide precursors.

#### 2.1.3.3.Role of the anions

For alkoxide precursors, metal ions are surrounded by alkoxo groups. Adding an inorganic salt in the solution generally leads to the presence of counter anion bonded to metal atoms. Some anions can be strongly coordinated on alkoxide precursor through nucleophilic substitution, modifying the chemical composition of alkoxide precursor. The new molecular precursor shows different reactivity towards hydrolysis and condensation. Therefore, these anions play a decisive role during the precipitation process of metal oxides.[65] The size, morphology and chemical composition of the metal oxides prepared through sol-gel method can thus be drastically influenced by complexing anions.[65,66]

Modified precursor can be expressed as $M(OR)_xL_y$, where L represents counter anion. The stability of the anion complex depends on the electronegativity of the anion.[65] If L is more electronegative than $RO^-$, electrons are attracted by L. The negative charge of anion increases. The M-L bond are more ionic. Therefore, L tends to detach from metal atom and the complex is not stable. In contrast, if L is less electronegative than $RO^-$, electron is transferred to the precursor. The bond between M and L becomes more covalent and L shows strong ability to coordinate with the metal cation.

Capping anions can decrease the functionality of titanium precursors and lead to reduced reactivity for sol-gel processing.[71,75,76] For example, when acetic acid is added in the solution of $Ti(OBu^n)_4$, acetate groups can bond with Ti as a bidentate ligand. The reaction time increases from several seconds to months.[76] The more $AcO^-$ is added, the longer the

gelation time. In addition to that, anions are commonly used to influence metal oxides in the following two aspects:

**Phase selectivity.** Complexing anion can modify the geometry of precursors in solution. As the geometry influences the assembly type of titanium octahedral, it can thus influence the formation of a particular phase. An example showed that $Ti(OH)_2Cl_2(H_2O)_2$ molecule is likely formed in high concentration solution of HCl, resulting in the formation of brookite phase.[77] While another ligand ammonia is added in the solution followed by solvothermal treatment, pure cubic-like anatase phase can be stabilized.[78]

**Guidance of particle growth.** Complexing anion can also guide the growth of metal oxide particles, affecting the size and shape of the final phase. Liu et al. provided a comprehensive study regarding this effect by adding different anions in a common precursor $Ti(OH)_4$.[79] They showed that reaction of $Ti(OH)_4$ in a water/2-propanol mixture results in anatase particles with 20 nm in size. While ammonium oxalate and lactate salts are added in the solution, rutile (100 – 200 nm) and brookite (60 – 80 nm) particles can be obtained, respectively. Presence of $F^-$ and $SO_4^{2-}$ anions can lead to the formation of anatase particles presenting the shape of truncated bipyramids and rods, respectively. The use of same precursor might imply that anions can coordinate to a particular surface and direct the growth of $TiO_2$ anatase particles.

## 2.2. Synthesis of $TiO_2$ in fluorinated medium

Fluorine is a strong complexing anion and has been found to be effective in tuning particle size, shape, nature and composition of $TiO_2$ particles synthesized *via* sol-gel method.[19,20,56,80-84] These modifications have led to enhanced catalytical[21,80,83] and electrochemical properties.[19,85] So far, fluorine substances such as HF, $NH_4F$, NaF, $NH_4HF_2$ and $TiF_4$, which can release fluorine ions in solution, are used as fluorine sources. This thesis is devoted to stabilize $TiO_2$ particles in fluorine medium. Therefore, it is worth reviewing the effect of fluorine on the preparation of $TiO_2$ in solution-phase.

### 2.2.1. Phase selectivity

Fluorine is a structure-directing agent. It has been reported that fluorination of titanium precursors promotes the crystallization of anatase phase by affecting the reaction dynamics and precursors linking modes.[83,84] Yu et al. demonstrated that the addition of $NH_4F$-water mixture in the solution of titanium isopropoxide suppressed the formation of brookite phase and favored the crystallization of $TiO_2$ anatase, highlighting the effect of fluorine on the selective formation of anatase phase.[83] Dong et al. reported a rutile to anatase phase transition by increasing fluorine concentration in $TiCl_4$ solution.[86] The formation mechanism can be viewed as the result of arrangement of $TiO_6$ octahedra which are the building blocks for $TiO_2$ crystals. As for rutile, $TiO_6$ octahedra share two edges and show linear chains, while octahedra in anatase share four edges and form spiral zigzag chains (**Figure 1.1**). There isn't a convincing mechanism explaining how fluorine influences the assemblage of $TiO_6$ octahedra, thus resulting in the selective phase formation of anatase structure. However, the formation mechanism of anatase in the presence of $SO_4^{2-}$ was proposed by Yan et al. (**Figure 1.8**).[87] That can be used as analogy for fluorine. (1) $TiO_6$ octahedral hydroxyls firstly interacts with $SO_4^{2-}$. (2) Another octahedron would condense along the converse direction to decrease the repulsion. (3) The third octahedron would finally condense spirally, resulting in the formation of anatase nucleus. As for the case of fluorine, $Ti(OH)_xF_y$ octahedral can be formed by both fluorolysis[88] (**Eq. 1.9**) and substitution of hydroxyl by fluorine. Fluorine inhibits linear growth of octahedra, eventually leading to the condensation of zigzag chains.

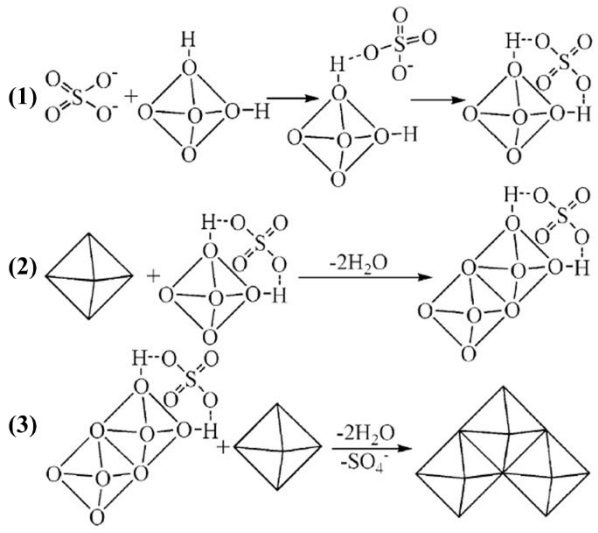


**Figure 1.8:** Proposed formation mechanism of anatase in the presence of $SO_4^{2-}$: (1) Interaction between $SO_4^{2-}$ and $TiO_6$ octahedral hydroxyls. (2) Two $TiO_6$ octahedra share edge in the presence of $SO_4^{2-}$. (3) Spiral zigzag chain growth.[87] Reprinted with permission from Yan, M. et al. J. Phys. Chem. B 2005, 109, 8673. Copyright 2005 American Chemical Society.

$TiO_2$ anatase can be mediated by fluorine. Increasing fluorine concentration in solution enhanced the crystallization of anatase, promoted growth of crystalline size and modified the morphology of the anatase phase.[83,89] Yu et al. showed that, by increasing the fluorine to titanium ratio ($R_F$) from 0 to 6, morphological change from solid microspheres to hollow microspheres to nanoflakes then to tabular-shaped micro-crystals were observed with increased crystalline size from tens nanometers to hundred nanometers.[89] The crystallinity of the anatase increased with $R_F$ as well. The fluorine-induced particle size and morphology variation can be attributed to the strong etching effect and complexing ability of fluorine, leading to the dissolution and recrystallization of $TiO_2$. It was proposed that fluorine reacts with metastable $TiO_2$, forming soluble titanium fluorides species, which recrystallizes on the existing particles, thus leading to crystal growth.

### 2.2.2. Doping/substitution of oxygen by fluorine

When fluorine is added into the solution of alkoxide precursor, the precursor can be fluorinated through the reaction of fluorolysis (**Eq. 1.9**).[88,90] Fluorolysis reaction is partially similar with hydrolysis. Nucleophilic addition, proton transfer and departure of alcohol group are included in hydrolysis. However, fluorolysis involves firstly the protonation of the oxygen atom in alkoxy group (**Eq. 1.10**).[88] Then, metal atom undergoes fluorine attack, releasing alcohol molecule (**Eq. 1.11**). Bonded fluorine do not show reactivity as high as hydroxyl group which can condense to form metal oxo bridge. The formation of M-F-M bridge is based on the donor ability of $F^-$ toward another metal atom.[88] In fluorinated medium, hydrolysis and fluorolysis likely compete during the synthesis, possibly leading to the incorporation of fluorine within the final structure.

Fluorolysis: $M(OR)_n + xHF \rightarrow M(OR)_{n-x}F_x + xROH$ (**Eq. 1.9**)

$M - O - R + H^+ \rightarrow [M - O(H) - R]^+$ (**Eq. 1.10**)

$[M - O(H) - R]^+ + F^- \rightarrow M - F + ROH$ (**Eq. 1.11**)

As for fluorinated titania, it is possible that fluorine locates both at the external surface[20,81] (surface adsorption) and in the solid[83,86,91] (lattice doping) (**Figure 1.9**).

**Surface adsorption.** In some synthetic conditions, Ti-F-Ti bridge may not be formed. Fluorine plays a role of complexing agent and can be adsorbed on the surface of $TiO_2$ by

displacing $OH^-$ groups. In this case, fluorine can affect surface properties in terms of adsorption, interfacial charge separation and transfer, thus leading to modification of $TiO_2$ properties.[21,80,92]

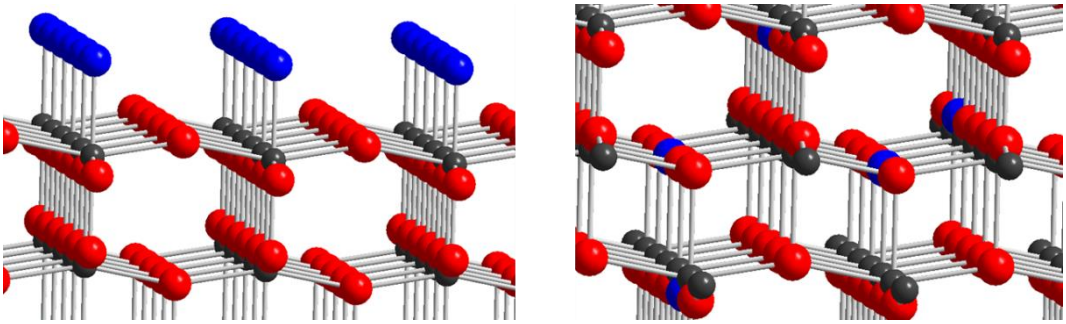

**Figure 1.9:** Ball and stick models for F-doped anatase $TiO_2$: (left) surface fluorination; (right) bulk doping. (dark gray: Ti; red: O; blue: F)

**Lattice fluorination.** Lattice fluorination involves substitution of divalent $O^{2-}$ ions by monovalent $F^-$ ions. The negative charge deficiency caused by $O^{2-}/F^-$ substitution can be counterbalanced by the reduction of $Ti^{4+}$ on $Ti^{3+}$ (**Eq. 1.12**).[83,91,93] Charge compensation induces the formation of bulk $Ti^{3+}$ species in the solid. The extra electron in $Ti^{3+}$ provides localized states below the conduction band and consequently modifies electronic structure of $TiO_2$.[91]

$$TiO_2 + xF^- \rightarrow Ti_x^{3+}Ti_{1-x}^{4+}O_{2-x}F_x + xO^- \qquad \textbf{(Eq. 1.12)}$$

Many researches aimed at crystal engineering of $TiO_2$ using fluorine, few of them studied the chemical states of fluorine within lattice.[86,91] Combining computational and experimental analysis, Czoska et al. showed that impurity of fluorine do not directly bonded with $Ti^{3+}$. As oxygen atom is coordinated with three titanium in $TiO_2$ anatase network, is that the fluorine shows the same coordination mode or different local environment? In addition, can charge deficiency induced by substitution of $O^{2-}/F^-$ be balanced by other mechanism while maintaining the valence of Ti? In chapter II.1, a new substitution mechanism is proposed and the fluorine environment is studied thoroughly.

### 2.2.3. Surface engineering

It is well-known that the interaction between molecules/ions and surfaces of material largely influences their physico-chemical properties. For $TiO_2$, it has been demonstrated that

different surfaces have different reactivity, thus affecting the photocatalytical and electrochemical properties by means of surface adsorption, charge transfer and ion transport.[19] Controlling exposed surfaces of $TiO_2$ is therefore highly desirable for various applications. Fluorine has been shown to be an effective structure directing agent for anisotropic growth of anatase crystals and widely used to synthesize faceted $TiO_2$ anatase.[19,20]

Mesoscopic properties and applications of {001} anatase facets were rarely reported before 2008 due to the synthetic difficulty of stabilizing anatase crystals with high proportion of {001} facets. Promising properties associated with the {001} facets have stimulated great efforts on synthesizing such crystals. Significant progress have been made by Yang et al. who experimentally synthesized anatase microcrystals with a large percentage {001} facets in a fluorinated medium (**Figure 1.10a,b**).[20] Surface engineering of $TiO_2$ anatase using fluorine has been extensively studied since then.

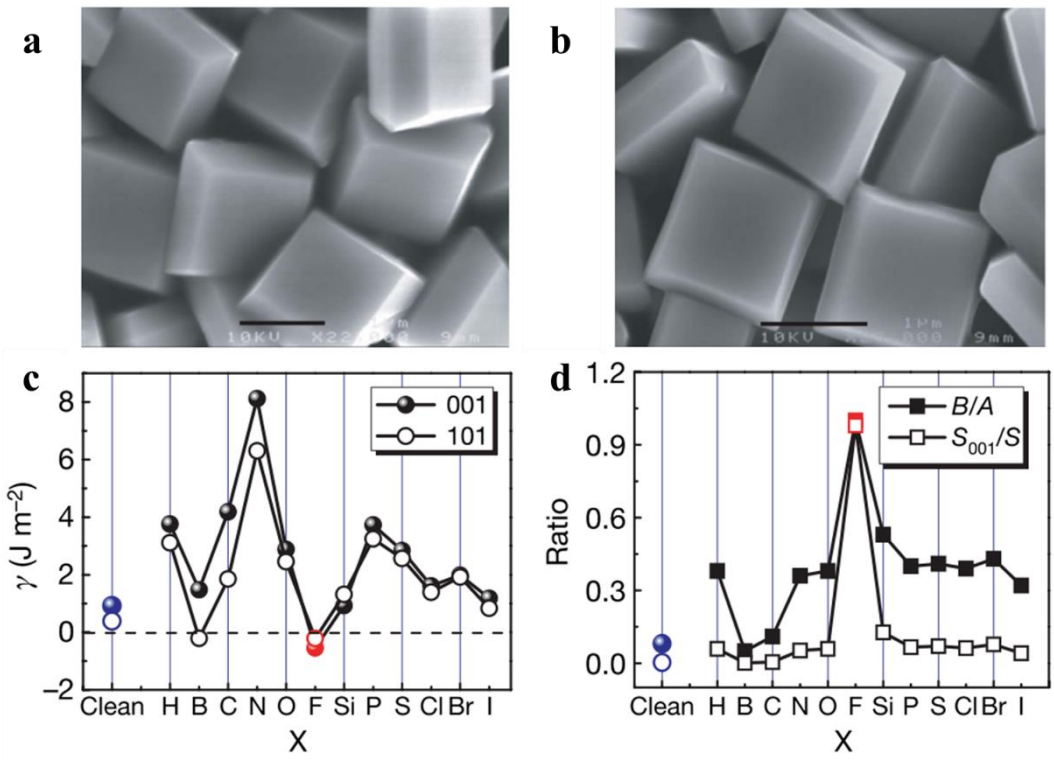


**Figure 1.10:** (a,b) SEM images of $TiO_2$ anatase microcrystals using different concentration of fluorine. (c) Calculated energies of the (001) and (101) surfaces surrounded by X atoms. (d) Plots of the optimized value of B/A and percentage of {001} facets for anatase single crystals with various adsorbate atoms X.[20] Reprinted with permission from Yang, H. G. et al. Nature 2008, 453, 638. Copyright 2014 Nature Publishing Group.

Yang et al. theoretically investigated the effects of 12 non-metallic adsorbate atoms on the surface energy of {101} and {001} facets.[20] They found that fluorine-adsorbed surfaces not only had the lowest energy for both {101} and {001} facets, but also led to (001) surfaces more stable than that of (101) (**Figure 1.10c**). Chemisorption of fluorine onto the (001) surfaces prevents crystal growth along [001] direction and favors anisotropic growth along horizontal plan. The results showed that highly truncated octahedron dominated by fluorine-terminated {001} facets is thermodynamically favorable morphology of $TiO_2$ anatase (**Figure 1.10d**). The reason why fluorine can lower the surface energy of {001} facets has been reported by Ma and co-workers by using DFT calculations.[94] They found that the adsorption of fluorine on (101) surfaces significantly weaken the Ti-O bonds, whereas they are strengthened in (001) surfaces. Therefore, {001} facets become more stable than {101} when fluorine is bonded on the surface. Again, DFT calculations performed by Zhang et al. confirmed the strong adsorption energy when HF is adsorbed on (001) surfaces. However, the interaction of NaF with (001) surfaces showed mush higher adsorption energy, indicating that the molecular form of HF is vital for stabilizing the {001} facets.

Yang et al. synthesized $TiO_2$ anatase particles with 35 % of {001} facets by using $TiF_4$ and HF as the source of titanium and fluorine, respectively (**Figure 1.10a**).[20] A higher percentage area of 47 % (**Figure 1.10b**) was obtained with reduced $TiF_4$ concentration and extended reaction time. The percentage was further improved to 64 % by using isopropanol as solvent.[95] Isopropanol not only provides reaction medium but also acts as protecting agent to strengthen adsorption of fluorine onto (001) surfaces, thus favoring anisotropic growth of crystals. The synergistic effects of alcohol are also effective for ethanol, tert-butanol and benzyl alcohol.[96] By hydrothermally treating tetrabutyl titanate, $(TiOBu)_4$, in 47 wt. % hydrofluoric acid solution at 180 °C, Han et al. obtained anatase nanosheets with average size of 130 nm and a thickness of ca. 8 nm.[97] The average percentage of {001} facets was as high as 89 %. Solvothermal synthesis using $TiF_4$, HF and 1-butanol mixture solution at 210 °C for 24 h produced anatase nanosheets with a thickness of 27.9 nm and a side length of 4140 nm, corresponding to 98.7 % of exposed {001} facets.[98]

Influence of reagent stoichiometry and reaction temperature on proportion of {001} facets was systematically studied by Menzel et al.[99] This study provides guidelines on controlling {001} facets in anatase crystals by adjusting synthesis parameters. **Figure 1.11** shows ternary diagram of the dependence of $TiO_2$ nanoparticle morphology on the molar ratio

of titanium source (titanium isopropoxide), fluoride-source (aqueous HF, 50 wt. %), and water. The syntheses were performed hydrothermally at 180 °C. They showed that water and fluorine concentrations are competitive on determining the morphology of anatase nanoparticles. At high water concentration, surface of anatase particles will be dominated by hydroxyl groups which promote isotropic crystal growth by oxolation reaction. Contrarily, high concentration of fluorine induces F-terminated {001} facets, thus favoring lateral growth. However, at very high fluorine concentration, etching effect of HF led to reduced particle sizes and the formation of $TiOF_2$ or soluble titanium fluoride. Reaction temperature is also an important parameter for synthesizing anatase crystals with high percentage {001} facets because it affects reaction process on thermodynamic way. High temperature favors nucleation and growth processes, leading to larger particles along with larger proportion of {001} facets. Nevertheless, particle growth *via* Ostwald ripening and oriented attachment mechanisms at high temperature competes with classic crystal growth, suggesting that the reaction temperature couldn't be too high.

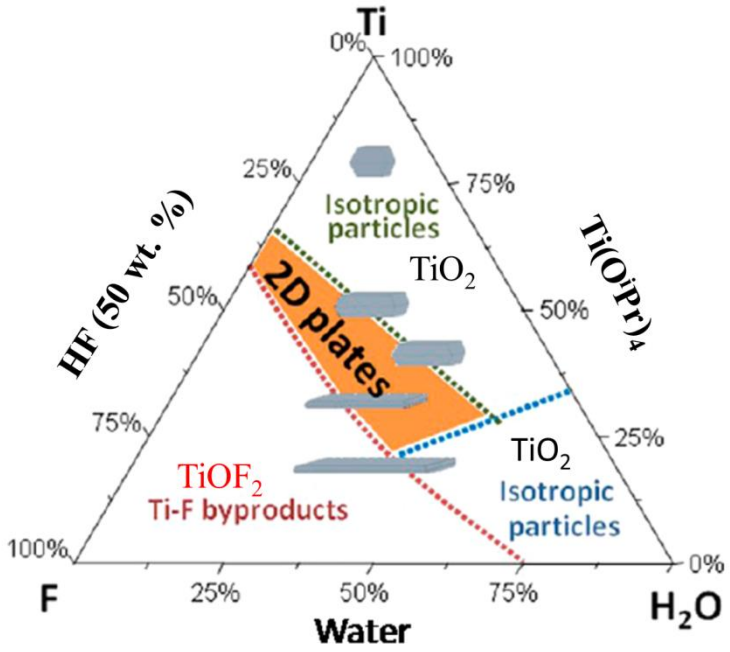


**Figure 1.11:** Ternary diagram illustrating the dependence of $TiO_2$ nanoparticle morphology on the molar ratio of titanium source (titanium isopropoxide), fluoride-source (aqueous HF, 50 wt. %), and water. Reaction temperature T = 180 °C.[99] Reprinted with permission from Menzel, R. et al. Chem. Mater. 2013, 25, 2137. Copyright 2013 American Chemical Society.

$TiO_2$ anatase facets can be effectively tailored using fluorine. However, catalytical and electrochemical properties can be influenced by both surface and particle size. It is important to downsize $TiO_2$ particles while maintaining high proportion of reactive facets. In chapter

II.3, controlling over size and facets of $TiO_2$ in fluorinated medium are achieved by varying synthetic parameters.

# 3. Conclusion

This chapter provides a bibliographic background of our research. Among the 11 allotropy of titanium dioxide, $TiO_2$ anatase shows promising properties in terms of photocatalysis and electrochemistry. $TiO_2$ anatase can be used as anode for lithium-ion batteries due to that it avoids safety problems caused by electrolyte decomposition and lithium plating as for carbonaceous-based compounds. Lithium can be inserted in $TiO_2$ anatase through a two-phase reaction driven by paring effect of $LiO_6$ octahedra. We also showed that particle size and exposed surface can strongly affect the electrochemical properties of $TiO_2$ anatase vs. $Li^+$. Further application of $TiO_2$ anatase in energy storage emerged recently is anode for sodium-ion batteries. It has a lower operating potential than in LIBs, thus providing higher power density. However, there isn't convincing and unified reports regarding the mechanism of sodium insertion into $TiO_2$.

We then presented an effective solution-based method for elaboration of $TiO_2$, the sol-gel. In the sol-gel processing, solution-phase small titanium alkoxide precursor undergoes hydrolysis and condensation reactions and grows into larger $TiO_2$ particles. The synthesis can be influenced by the nature of precursor, solvent and, particularly, anions. Anions play a decisive role during the precipitation of $TiO_2$, thus affecting particle size, morphology and chemical composition. We emphasized the role of fluorine which has been shown to be efficient in stabilizing $TiO_2$ anatase phase and guiding particle growth. Very recently, fluorine has been widely used as structure directing agent to prepare $TiO_2$ anatase with tailored facets.

# References

(1) Fujishima, A.; Honda, K. Electrochemical Photolysis of Water at a Semiconductor Electrode. *Nature* **1972**, *238*, 37.

(2) Grätzel, M. Photoelectrochemical cells. *Nature* **2001**, *414*, 338.

(3) Kavan, L.; Grätzel, M.; Gilbert, S. E.; Klemenz, C.; Scheel, H. J. Electrochemical and Photoelectrochemical Investigation of Single-Crystal Anatase. *J. Am. Chem. Soc.* **1996**, *118*, 6716.

(4) Chen, X.; Mao, S. S. Titanium dioxide nanomaterials: Synthesis, properties, modifications, and applications. *Chem. Rev.* **2007**, *107*, 2891.

(5) Schneider, J.; Matsuoka, M.; Takeuchi, M.; Zhang, J.; Horiuchi, Y.; Anpo, M.; Bahnemann, D. W. Understanding $TiO_2$ Photocatalysis: Mechanisms and Materials. *Chem. Rev.* **2014**, *114*, 9919.

(6) Bai, Y.; Mora-Seró, I.; De Angelis, F.; Bisquert, J.; Wang, P. Titanium Dioxide Nanomaterials for Photovoltaic Applications. *Chem. Rev.* **2014**, *114*, 10095.

(7) O'regan, B.; Grätzel, M. A low-cost, high-efficiency solar-cell based on dye-sensitized colloidal $TiO_2$ films. *Nature* **1991**, *353*, 737.

(8) Bai, J.; Zhou, B. Titanium Dioxide Nanomaterials for Sensor Applications. *Chem. Rev.* **2014**, *114*, 10131.

(9) Cava, R. J.; Murphy, D. W.; Zahurak, S.; Santoro, A.; Roth, R. S. The crystal structures of the lithium-inserted metal oxides $Li_{0.5}TiO_2$ anatase, $LiTi_2O_4$ spinel, and $Li_2Ti_2O_4$. *J. Solid State Chem.* **1984**, *53*, 64.

(10) Ohzuku, T.; Kodama, T.; Hirai, T. Electrochemistry of anatase titanium dioxide in lithium nonaqueous cells. *J. Power Sources* **1985**, *14*, 153.

(11) Sudant, G.; Baudrin, E.; Larcher, D.; Tarascon, J.-M. Electrochemical lithium reactivity with nanotextured anatase-type $TiO_2$. *J. Mater. Chem.* **2005**, *15*, 1263.

(12) Froeschl, T.; Hoermann, U.; Kubiak, P.; Kucerova, G.; Pfanzelt, M.; Weiss, C. K.; Behm, R. J.; Huesing, N.; Kaiser, U.; Landfester, K.; Wohlfahrt-Mehrens, M. High surface area crystalline titanium dioxide: potential and limits in electrochemical energy storage and catalysis. *Chem. Soc. Rev.* **2012**, *41*, 5313.

(13) Lu, X.; Wang, G.; Zhai, T.; Yu, M.; Gan, J.; Tong, Y.; Li, Y. Hydrogenated $TiO_2$ Nanotube Arrays for Supercapacitors. *Nano Lett.* **2012**, *12*, 1690.

(14) Zhang, H.; F. Banfield, J. Thermodynamic analysis of phase stability of nanocrystalline titania. *J. Mater. Chem.* **1998**, *8*, 2073.

(15) Asahi, R.; Taga, Y.; Mannstadt, W.; Freeman, A. J. Electronic and optical properties of anatase $TiO_2$. *Phys. Rev. B* **2000**, *61*, 7459.

(16) Lazzeri, M.; Vittadini, A.; Selloni, A. Structure and energetics of stoichiometric $TiO_2$ anatase surfaces. *Phys. Rev. B* **2001**, *63*, 155409.

(17) Lazzeri, M.; Vittadini, A.; Selloni, A. Erratum: Structure and energetics of stoichiometric $TiO_2$ anatase surfaces. *Phys. Rev. B* **2002**, *65*, 119901.

(18) Ye, L.; Mao, J.; Liu, J.; Jiang, Z.; Peng, T.; Zan, L. Synthesis of anatase $TiO_2$ nanocrystals with {101}, {001} or {010} single facets of 90% level exposure and liquid-phase photocatalytic reduction and oxidation activity orders. *J. Mater. Chem. A* **2013**, *1*, 10532.

(19) Liu, G.; Yang, H. G.; Pan, J.; Yang, Y. Q.; Lu, G. Q.; Cheng, H.-M. Titanium Dioxide Crystals with Tailored Facets. *Chem. Rev.* **2014**, *114*, 9559.

(20) Yang, H. G.; Sun, C. H.; Qiao, S. Z.; Zou, J.; Liu, G.; Smith, S. C.; Cheng, H. M.; Lu, G. Q. Anatase $TiO_2$ single crystals with a large percentage of reactive facets. *Nature* **2008**, *453*, 638.

(21) Kapilashrami, M.; Zhang, Y.; Liu, Y.-S.; Hagfeldt, A.; Guo, J. Probing the Optical Property and Electronic Structure of $TiO_2$ Nanomaterials for Renewable Energy Applications. *Chem. Rev.* **2014**, *114*, 9662.

(22) Tarascon, J. M.; Armand, M. Issues and challenges facing rechargeable lithium batteries. *Nature* **2001**, *414*, 359.

(23) Kötz, R.; Carlen, M. Principles and applications of electrochemical capacitors. *Electrochim. Acta* **2000**, *45*, 2483.

(24) Xu, Y.; Zhou, M.; Wang, X.; Wang, C.; Liang, L.; Grote, F.; Wu, M.; Mi, Y.; Lei, Y. Enhancement of Sodium Ion Battery Performance Enabled by Oxygen Vacancies. *Angew. Chem. Int. Ed.* **2015**, *54*, 8768.

(25) Xu, K. Nonaqueous Liquid Electrolytes for Lithium-Based Rechargeable Batteries. *Chem. Rev.* **2004**, *104*, 4303.

(26) Harry, K. J.; Hallinan, D. T.; Parkinson, D. Y.; MacDowell, A. A.; Balsara, N. P. Detection of subsurface structures underneath dendrites formed on cycled lithium metal electrodes. *Nat. Mater.* **2014**, *13*, 69.

(27) Chandrashekar, S.; Trease, N. M.; Chang, H. J.; Du, L.-S.; Grey, C. P.; Jerschow, A. $^7$Li MRI of Li batteries reveals location of microstructural lithium. *Nat. Mater.* **2012**, *11*, 311.

(28) Goodenough, J. B.; Kim, Y. Challenges for Rechargeable Li Batteries. *Chem. Mater.* **2010**, *22*, 587.

(29) Palacin, M. R. Recent advances in rechargeable battery materials: a chemist's perspective. *Chem. Soc. Rev.* **2009**, *38*, 2565.

(30) Wang, Q.; Zakeeruddin, S. M.; Exnar, I.; Grätzel, M. A new strategy of molecular overcharge protection shuttles for lithium ion batteries. *Electrochem. Commun.* **2008**, *10*, 651.

(31) Gentili, V.; Brutti, S.; Hardwick, L. J.; Armstrong, A. R.; Panero, S.; Bruce, P. G. Lithium Insertion into Anatase Nanotubes. *Chem. Mater.* **2012**, *24*, 4468.

(32) Shin, J.-Y.; Samuelis, D.; Maier, J. Sustained Lithium-Storage Performance of Hierarchical, Nanoporous Anatase $TiO_2$ at High Rates: Emphasis on Interfacial Storage Phenomena. *Adv. Funct. Mater.* **2011**, *21*, 3464.

(33) Sun, C. H.; Yang, X. H.; Chen, J. S.; Li, Z.; Lou, X. W.; Li, C.; Smith, S. C.; Lu, G. Q.; Yang, H. G. Higher charge/discharge rates of lithium-ions across engineered $TiO_2$ surfaces leads to enhanced battery performance. *Chem. Commun.* **2010**, *46*, 6129.

(34) Wagemaker, M.; Borghols, W. J. H.; Mulder, F. M. Large Impact of Particle Size on Insertion Reactions. A Case for Anatase $Li_xTiO_2$. *J. Am. Chem. Soc.* **2007**, *129*, 4323.

(35) Shen, K.; Chen, H.; Klaver, F.; Mulder, F. M.; Wagemaker, M. Impact of Particle Size on the Non-Equilibrium Phase Transition of Lithium-Inserted Anatase $TiO_2$. *Chem. Mater.* **2014**, *26*, 1608.

(36) Koudriachova, M. V.; de Leeuw, S. W.; Harrison, N. M. Orthorhombic distortion on Li intercalation in anatase. *Phys. Rev. B* **2004**, *69*, 054106.

(37) Morgan, B. J.; Watson, G. W. Role of Lithium Ordering in the $Li_xTiO_2$ Anatase → Titanate Phase Transition. *J. Phys. Chem. Lett.* **2011**, *2*, 1657.

(38) Macklin, W. J.; Neat, R. J. Performance of titanium dioxide-based cathodes in a lithium polymer electrolyte cell. *Solid State Ionics* **1992**, *53–56*, 694.

(39) Wagemaker, M.; Kearley, G. J.; van Well, A. A.; Mutka, H.; Mulder, F. M. Multiple Li Positions inside Oxygen Octahedra in Lithiated $TiO_2$ Anatase. *J. Am. Chem. Soc.* **2003**, *125*, 840.

(40) Arico, A. S.; Bruce, P.; Scrosati, B.; Tarascon, J.-M.; van Schalkwijk, W. Nanostructured materials for advanced energy conversion and storage devices. *Nat. Mater.* **2005**, *4*, 366.

(41) Bruce, P. G.; Scrosati, B.; Tarascon, J.-M. Nanomaterials for Rechargeable Lithium Batteries. *Angew. Chem. Int. Ed.* **2008**, *47*, 2930.

(42) Patra, S.; Davoisne, C.; Bruyère, S.; Bouyanfif, H.; Cassaignon, S.; Taberna, P.-L.; Sauvage, F. Room-Temperature Synthesis of High Surface Area Anatase $TiO_2$ Exhibiting a Complete Lithium Insertion Solid Solution. *Part. Part. Syst. Charact.* **2013**, *30*, 1093.

(43) Ganapathy, S.; Wagemaker, M. Nanosize Storage Properties in Spinel $Li_4Ti_5O_{12}$ Explained by Anisotropic Surface Lithium Insertion. *ACS Nano* **2012**, *6*, 8702.

(44) Bousa, M.; Laskova, B.; Zukalova, M.; Prochazka, J.; Chou, A.; Kavan, L. Polycrystalline $TiO_2$ Anatase with a Large Proportion of Crystal Facets (001): Lithium Insertion Electrochemistry. *J. Electrochem. Soc.* **2010**, *157*, A1108.

(45) Liu, G.; Yin, L.-C.; Pan, J.; Li, F.; Wen, L.; Zhen, C.; Cheng, H.-M. Greatly Enhanced Electronic Conduction and Lithium Storage of Faceted $TiO_2$ Crystals Supported on Metallic Substrates by Tuning Crystallographic Orientation of $TiO_2$. *Adv. Mater.* **2015**, *27*, 3507.

(46) Hahn, B. P.; Long, J. W.; Rolison, D. R. Something from Nothing: Enhancing Electrochemical Charge Storage with Cation Vacancies. *Acc. Chem. Res.* **2013**, *46*, 1181.

(47) Jung, W. I.; Sakamoto, K.; Pitteloud, C.; Sonoyama, N.; Yamada, A.; Kanno, R. Chemically oxidized manganese dioxides for lithium secondary batteries. *J. Power Sources* **2007**, *174*, 1137.

(48) Koo, B.; Xiong, H.; Slater, M. D.; Prakapenka, V. B.; Balasubramanian, M.; Podsiadlo, P.; Johnson, C. S.; Rajh, T.; Shevchenko, E. V. Hollow Iron Oxide Nanoparticles for Application in Lithium Ion Batteries. *Nano Lett.* **2012**, *12*, 2429.

(49) Yabuuchi, N.; Kubota, K.; Dahbi, M.; Komaba, S. Research Development on Sodium-Ion Batteries. *Chem. Rev.* **2014**, *114*, 11636.

(50) Kavan, L.; Kratochvilová, K.; Grätzel, M. Study of nanocrystalline $TiO_2$ (anatase) electrode in the accumulation regime. *J. Electroanal. Chem.* **1995**, *394*, 93.

(51) Xu, Y.; Memarzadeh Lotfabad, E.; Wang, H.; Farbod, B.; Xu, Z.; Kohandehghan, A.; Mitlin, D. Nanocrystalline anatase $TiO_2$: a new anode material for rechargeable sodium ion batteries. *Chem. Commun.* **2013**, *49*, 8973.

(52) Wu, L.; Bresser, D.; Buchholz, D.; Giffin, G. A.; Castro, C. R.; Ochel, A.; Passerini, S. Unfolding the Mechanism of Sodium Insertion in Anatase $TiO_2$ Nanoparticles. *Adv. Energy Mater.* **2015**, *5*, 1401142.

(53) Kim, K.-T.; Ali, G.; Chung, K. Y.; Yoon, C. S.; Yashiro, H.; Sun, Y.-K.; Lu, J.; Amine, K.; Myung, S.-T. Anatase Titania Nanorods as an Intercalation Anode Material for Rechargeable Sodium Batteries. *Nano Lett.* **2014**, *14*, 416.

(54) Gonzalez, J. R.; Alcantara, R.; Nacimiento, F.; Ortiz, G. F.; Tirado, J. L. Microstructure of the epitaxial film of anatase nanotubes obtained at high voltage and the mechanism of its electrochemical reaction with sodium. *CrystEngComm* **2014**, *16*, 4602.

(55) Shen, K. Thesis, *Lithium and Sodium Insertion in Nanostructured Titanates*, Delft University of Technology, 2014.

(56) Cargnello, M.; Gordon, T. R.; Murray, C. B. Solution-Phase Synthesis of Titanium Dioxide Nanoparticles and Nanocrystals. *Chem. Rev.* **2014**, *114*, 9319.

(57) Roy, R. Aids in hydrothermal experimentation .2. Methods of making mixtures for both dry and wet phase equilibrium studies. *J. Am. Ceram. Soc.* **1956**, *39*, 145.

(58) Roy, R. Gel Route to Homogeneous Glass Preparation. *J. Am. Ceram. Soc.* **1969**, *52*, 344.

(59) McCarthy, G. J.; Roy, R.; McKay, J. M. Preliminary study of low-temperature glass fabrication from noncrystalline silicas. *J. Am. Ceram. Soc.* **1971**, *54*, 637.

(60) Dislich, H. New Routes to Multicomponent Oxide Glasses. *Angew. Chem. Int. Ed.* **1971**, *10*, 363.

(61) Zelinski, B. J. J.; Uhlmann, D. R. Gel Technology in Ceramics. *J. Phys. Chem. Solids* **1984**, *45*, 1069.

(62) Mackenzie, J. D. Unusual non-crystalline solids from gels in 2004. *J. Non-Cryst. Solids* **1985**, *73*, 631.

(63) Sakka, S.; Kamiya, K. The sol-gel transition in the hydrolysis of metal alkoxides in relation to the formation of glass-fibers and films. *J. Non-Cryst. Solids* **1982**, *48*, 31.

(64) Dislich, H.; Hinz, P. History and principles of the sol-gel process, and some new multicomponent oxide coatings. *J. Non-Cryst. Solids* **1982**, *48*, 11.

(65) Livage, J.; Henry, M.; Sanchez, C. Sol-gel chemistry of transition metal oxides. *Prog. Solid State Chem.* **1988**, *18*, 259.

(66) Hench, L. L.; West, J. K. The sol-gel process. *Chem. Rev.* **1990**, *90*, 33.

(67) Bradley, D. C.; Mehrotra, R. C.; Gaur, D. P. *Metal Alkoxides*; Academic Press: London, 1978.

(68) Barringer, E. A.; Bowen, H. K. High-purity, monodisperse $TiO_2$ powders by hydrolysis of titanium tetraethoxide. 1. Synthesis and physical properties. *Langmuir* **1985**, *1*, 414.

(69) Boyd, T. Preparation and properties of esters of polyorthotitanic acid. *J. Polym. Sci.* **1951**, *7*, 591.

(70) Vallet-Regí, M.; Veiga Blanco, M. L.; Mata Arjona, A. Textura de Geles de $TiO_2$. *An. Quim.* **1980**, *76B*, 172.

(71) Sanchez, C.; Livage, J.; Henry, M.; Babonneau, F. Chemical modification of alkoxide precursors. *J. Non-Cryst. Solids* **1988**, *100*, 65.

(72) Nabavi, M.; Doeuff, S.; Sanchez, C.; Livage, J. Chemical modification of metal alkoxides by solvents: A way to control sol-gel chemistry. *J. Non-Cryst. Solids* **1990**, *121*, 31.

(73) Fornasieri, G.; Rozes, L.; Le Calvé, S.; Alonso, B.; Massiot, D.; Rager, M. N.; Evain, M.; Boubekeur, K.; Sanchez, C. Reactivity of Titanium Oxo Ethoxo Cluster $[Ti_{16}O_{16}(OEt)_{32}]$. Versatile Precursor of Nanobuilding Block-Based Hybrid Materials. *J. Am. Chem. Soc.* **2005**, *127*, 4869.

(74) Barringer, E. A.; Bowen, H. K. Formation, Packing, and Sintering of Monodisperse $TiO_2$ Powders. *J. Am. Ceram. Soc.* **1982**, *65*, 199.

(75) Rozes, L.; Sanchez, C. Titanium oxo-clusters: precursors for a Lego-like construction of nanostructured hybrid materials. *Chem. Soc. Rev.* **2011**, *40*, 1006.

(76) Doeuff, S.; Henry, M.; Sanchez, C.; Livage, J. Hydrolysis of titanium alkoxides: Modification of the molecular precursor by acetic acid. *J. Non-Cryst. Solids* **1987**, *89*, 206.

(77) Pottier, A.; Chaneac, C.; Tronc, E.; Mazerolles, L.; Jolivet, J.-P. Synthesis of brookite $TiO_2$ nanoparticles by thermolysis of $TiCl_4$ in strongly acidic aqueous media. *J. Mater. Chem.* **2001**, *11*, 1116.

(78) Shuang, Y.; Hou, Y.; Zhang, B.; Yang, H. G. Impurity-Free Synthesis of Cube-Like Single-Crystal Anatase $TiO_2$ for High Performance Dye-Sensitized Solar Cell. *Ind. Eng. Chem. Res.* **2013**, *52*, 4098.

(79) Liu, L.; Gu, X.; Ji, Z.; Zou, W.; Tang, C.; Gao, F.; Dong, L. Anion-Assisted Synthesis of $TiO_2$ Nanocrystals with Tunable Crystal Forms and Crystal Facets and Their Photocatalytic Redox Activities in Organic Reactions. *J. Phys. Chem. C* **2013**, *117*, 18578.

(80) Liu, S.; Yu, J.; Cheng, B.; Jaroniec, M. Fluorinated Semiconductor Photocatalysts: Tunable Synthesis And Unique Properties. *Adv. Colloid Interface Sci.* **2012**, *173*, 35.

(81) Luan, Y.; Jing, L.; Xie, Y.; Sun, X.; Feng, Y.; Fu, H. Exceptional Photocatalytic Activity of 001-Facet-Exposed $TiO_2$ Mainly Depending on Enhanced Adsorbed Oxygen by Residual Hydrogen Fluoride. *ACS Catal.* **2013**, *3*, 1378.

(82) Wang, Y.; Zhang, H.; Han, Y.; Liu, P.; Yao, X.; Zhao, H. A selective etching phenomenon on {001} faceted anatase titanium dioxide single crystal surfaces by hydrofluoric acid. *Chem. Commun.* **2011**, *47*, 2829.

(83) Yu, J. C.; Yu, J. G.; Ho, W. K.; Jiang, Z. T.; Zhang, L. Z. Effects of $F^-$ doping on the photocatalytic activity and microstructures of nanocrystalline $TiO_2$ powders. *Chem. Mater.* **2002**, *14*, 3808.

(84) Yu, J.; Wang, W.; Cheng, B.; Su, B.-L. Enhancement of Photocatalytic Activity of Mesporous $TiO_2$ Powders by Hydrothermal Surface Fluorination Treatment. *J. Phys. Chem. C* **2009**, *113*, 6743.

(85) Chen, J. S.; Tan, Y. L.; Li, C. M.; Cheah, Y. L.; Luan, D.; Madhavi, S.; Boey, F. Y. C.; Archer, L. A.; Lou, X. W. Constructing Hierarchical Spheres from Large Ultrathin Anatase $TiO_2$ Nanosheets with Nearly 100% Exposed (001) Facets for Fast Reversible Lithium Storage. *J. Am. Chem. Soc.* **2010**, *132*, 6124.

(86) Dong, Y.; Kapilashrami, M.; Zhang, Y.; Guo, J. Morphology change and band gap narrowing of hierarchical $TiO_2$ nanostructures induced by fluorine doping. *CrystEngComm* **2013**, *15*, 10657.

(87) Yan, M.; Chen, F.; Zhang, J.; Anpo, M. Preparation of Controllable Crystalline Titania and Study on the Photocatalytic Properties. *J. Phys. Chem. B* **2005**, *109*, 8673.

(88) Rudiger, S.; Kemnitz, E. The fluorolytic sol-gel route to metal fluorides-a versatile process opening a variety of application fields. *Dalton Trans.* **2008**, 1117.

(89) Yu, J.; Xiang, Q.; Ran, J.; Mann, S. One-step hydrothermal fabrication and photocatalytic activity of surface-fluorinated $TiO_2$ hollow microspheres and tabular anatase single micro-crystals with high-energy facets. *CrystEngComm* **2010**, *12*, 872.

(90) Kemnitz, E.; Groß, U.; Rüdiger, S.; Shekar, C. S. Amorphous Metal Fluorides with Extraordinary High Surface Areas. *Angew. Chem. Int. Ed.* **2003**, *42*, 4251.

(91) Czoska, A. M.; Livraghi, S.; Chiesa, M.; Giamello, E.; Agnoli, S.; Granozzi, G.; Finazzi, E.; Di Valentin, C.; Pacchioni, G. The nature of defects in fluorine-doped $TiO_2$. *J. Phys. Chem. C* **2008**, *112*, 8951.

(92) Liu, S.; Yu, J.; Jaroniec, M. Anatase $TiO_2$ with Dominant High-Energy {001} Facets: Synthesis, Properties, and Applications. *Chem. Mater.* **2011**, *23*, 4085.

(93) De Angelis, F.; Di Valentin, C.; Fantacci, S.; Vittadini, A.; Selloni, A. Theoretical Studies on Anatase and Less Common $TiO_2$ Phases: Bulk, Surfaces, and Nanomaterials. *Chem. Rev.* **2014**, *114*, 9708.

(94) Ma, X.; Dai, Y.; Wei, W.; Huang, B.; Whangbo, M.-H. Insights into How Fluorine-Adsorption and n-Type Doping Affect the Relative Stability of the (001) and (101) Surfaces of $TiO_2$: Enhancing the Exposure of More Active but Thermodynamically Less Stable (001). *J. Phys. Chem. Lett.* **2015**, *6*, 1876.

(95) Yang, H. G.; Liu, G.; Qiao, S. Z.; Sun, C. H.; Jin, Y. G.; Smith, S. C.; Zou, J.; Cheng, H. M.; Lu, G. Q. Solvothermal Synthesis and Photoreactivity of Anatase $TiO_2$ Nanosheets with Dominant {001} Facets. *J. Am. Chem. Soc.* **2009**, *131*, 4078.

(96) Zhu, J.; Wang, S.; Bian, Z.; Xie, S.; Cai, C.; Wang, J.; Yang, H.; Li, H. Solvothermally controllable synthesis of anatase $TiO_2$ nanocrystals with dominant {001} facets and enhanced photocatalytic activity. *CrystEngComm* **2010**, *12*, 2219.

(97) Han, X.; Kuang, Q.; Jin, M.; Xie, Z.; Zheng, L. Synthesis of Titania Nanosheets with a High Percentage of Exposed (001) Facets and Related Photocatalytic Properties. *J. Am. Chem. Soc.* **2009**, *131*, 3152.

(98) Wen, C. Z.; Zhou, J. Z.; Jiang, H. B.; Hu, Q. H.; Qiao, S. Z.; Yang, H. G. Synthesis of micro-sized titanium dioxide nanosheets wholly exposed with high-energy {001} and {100} facets. *Chem. Commun.* **2011**, *47*, 4400.

(99) Menzel, R.; Duerrbeck, A.; Liberti, E.; Yau, H. C.; McComb, D.; Shaffer, M. S. P. Determining the Morphology and Photocatalytic Activity of Two-Dimensional Anatase Nanoplatelets Using Reagent Stoichiometry. *Chem. Mater.* **2013**, *25*, 2137.

# Chapter II. Synthesis of $Ti_{0.78}\square_{0.22}O_{1.12}F_{0.40}(OH)_{0.48}$: Structural characterization and formation mechanism

As shown in bibliographic part, fluorine has been used to tune the physico-chemical properties of $TiO_2$ by means of modifying particle size, morphology and chemical composition. Based on this statement, this chapter is devoted to stabilize $TiO_2$ anatase nanoparticles by using a solution-based sol-gel method performed in fluorine medium. The crystalline structure, local environment and chemical composition of the resulting phase are studied. Thereafter, time-dependent study provides details regarding the formation mechanism of the resulting phase.

## 1. Elaboration and structural characterization

### 1.1. Introduction

Titanium dioxide ($TiO_2$) is a multifunctional material that can be used in a broad range of applications including photocatalytic hydrogen production by water splitting, rechargeable batteries/supercapacitors, dye-sensitized solar cells, sensors, and biomedical devices.[1-6] The abundance and low toxicity of titanium have stimulated the investigation of $TiO_2$ in the domain of material science and engineering. Over the years, several approaches have been used to enhance the physico-chemical properties of $TiO_2$. The strategy includes downsizing particles to nanoscale, surface engineering and doping with hetero elements.[6-8] A recent study reported that fluorine can act as structure directing agent that effectively controls the surface orientation of $TiO_2$.[9] This synthesis is based on the reaction of titanium precursor with aqueous hydrogen fluoride (HF) under hydrothermal conditions. A large percentage of high energy (001) surfaces can be stabilized in the fluorine medium. It was shown that fluorine can locate at the surface and in the bulk structure of $TiO_2$.[9,10] However, the concentration of

fluorine incorporated in $TiO_2$ remains at doping level. It is a great challenge to achieve high substitution rate in $TiO_2$.

In the structure of $TiO_2$, the replacement of divalent oxide anions $O^{2-}$ by monovalent fluoride anions $F^-$ creates one negative charge deficiency. The counterbalance of such deficiency can be achieved by reducing $Ti^{4+}$ to $Ti^{3+}$.[10-12] The general formula of this polyanionic compound can be written as $Ti^{4+}_{1-x}Ti^{3+}_xO_{2-x}F_x$. Here, we propose a new mechanism that charge compensation leads to the creation of cation vacancies. One titanium vacancy can be formed by substituting four oxygen by four fluorine anions, resulting in a chemical composition of $Ti_{1-x}\square_xO_{2-4x}F_{4x}$, where $\square$ represents a cation vacancy. It is of interest to understand how strongly $TiO_2$ can be modified while maintaining its original framework. Local insights into the fluorinated $TiO_2$ phase should also be gained.

Here, the solution-based synthesis was performed at low temperature in a fluorine medium. The use of low temperature can stabilize metastable compounds, thus achieving a high substitution rate. Our solution-based synthesis method allows generating Ti-based polyanionic anatase compound in which cationic and anionic sublattices are concomitantly modified. Experimental and computational approaches are applied to understand the structural and compositional modifications. A general chemical formula of the new family of material is proposed: $Ti_{1-x-y}\square_{x+y}O_{2-4(x+y)}F_{4x}(OH)_{4y}$.

## 1.2. Experimental method

### 1.2.1. Materials synthesis

The synthesis was performed using a mild solvothermal process. Typically, a solution containing 27 mmol of HF (40%) and 25 mL of isopropanol was added to 13.5 mmol of titanium isopropoxide (4 mL) in a 50 ml Teflon line container. After sealing, the solution was heated at 90 °C for 12 hours. After cooling down to room temperature, the white precipitate was separated from the solution using centrifugation (4400 rpm) and washed three times with ethanol. The solid was dried at 80 °C overnight and was further outgassed at 150 °C overnight under primary vacuum prior to structural and thermogravimetric analyses. For comparative study, $TiO_2$ anatase was synthesized using the same solvothermal process without HF. A post thermal treatment was applied at 400 °C under air for 2 hours to obtain a pure $TiO_2$ anatase.

### 1.2.2. Characterization methods

The structure and chemical composition of the as-prepared sample was characterized by X-ray powder diffraction, transmission electron microscopy, pair distribution function, X-ray photoelectron spectroscopy, $^{1}H$ and $^{19}F$ solid-state nuclear magnetic resonance and thermogravimetric analyses. The structure was modeled by DFT calculations. Details about these methods are available in the relevant publication paper.[13]

## 1.3. Results and Discussion

### 1.3.1. Structural characterization

Titanium isopropoxide as precursor, aqueous hydrofluoric acid as fluorinating and hydrolysis agent and isopropanol as solvent were used to stabilize fluoride anions within the anatase lattice. The synthesis was performed at 90 $^{o}$C under solvothermal conditions. The resulting sample was first characterized by powder X-ray diffraction analysis. **Figure 2.1a** shows the XRD pattern of the resulting phase. The diffraction peaks at $2\theta = 25.2^{o}$, $37.8^{o}$ and $48.0^{o}$ can be indexed to the (101), (004) and (200) planes of tetragonal structure of $TiO_2$ anatase with a space group: $I4_1/amd$ (ICSD # 44882), indicating the formation of single anatase phase. The average particle size calculated on the basis of (101) peak using Debye-Sherrer equation is 5.5(1) nm.

The stabilization of crystalline nanoparticles was confirmed by transmission electron micrographs (**Figure 2.1b&c**). Large aggregates of nanosized particles can be observed in the TEM image. High resolution micrograph of an isolated particle shows lattice spacing of 0.354 nm, characteristic of (101) plane of $TiO_2$ anatase (**Figure 2.1c**). The particle size is ca. 7 nm, larger than that obtained from the broadening of (101) peak in XRD pattern. This discrepancy might be due to the effect of lattice strain which has been commonly observed for anisotropic particles.[14]

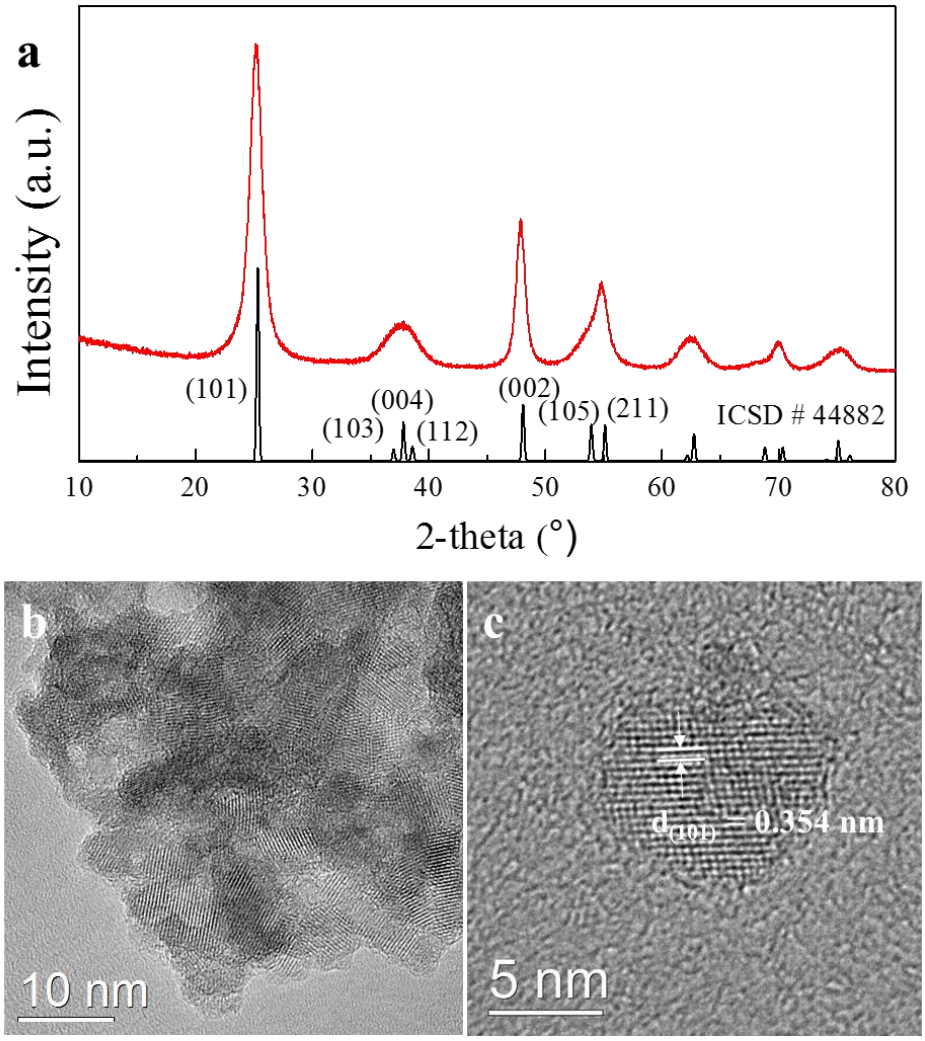


**Figure 2.1:** (a) Powder X-ray diffraction pattern obtained from the sample prepared by solvothermal method. (b) Transmission electron micrograph of the resulting anatase nanoparticles. (c) High resolution transmission electron micrograph of an isolated particle.

To investigate the atomic structure of the as-prepared anatase phase, total scattering data was collected at the beamline 11-ID-B at the Advanced Photon Source (Argonne National Laboratory). Pair Distribution Function (PDF) data was obtained by Fourier transformation of the high energy X-ray data. PDF analysis allows describing distance distribution of the pairs in short and long range order, thus being capable of probing amorphous and nanosized materials. This technique is widely used for the study of the structure of nanomaterials.[15,16] **Figure 2.2** shows comparison of the PDF data of the as-prepared anatase with pure $TiO_2$ anatase. The intensity of the PDF oscillations for the as-prepared sample is weaker than pure $TiO_2$, indicating that the atomic sites in the as-prepared sample may not be fully occupied, it exists defects in its structure. The 1$^{st}$ peak in PDF corresponds to the bond between cation and anion. The ratio between the intensity of the 1$^{st}$

peak for the as-prepared anatase and pure $TiO_2$ is 0.74. The ratio for the 2nd peak, corresponding to the distance Ti-Ti, is 0.54, which is the square of the ratio for the 1st peak. This result indicates that only Ti site is not fully occupied in the as-prepared anatase, generating cation vacancy of 26 %.

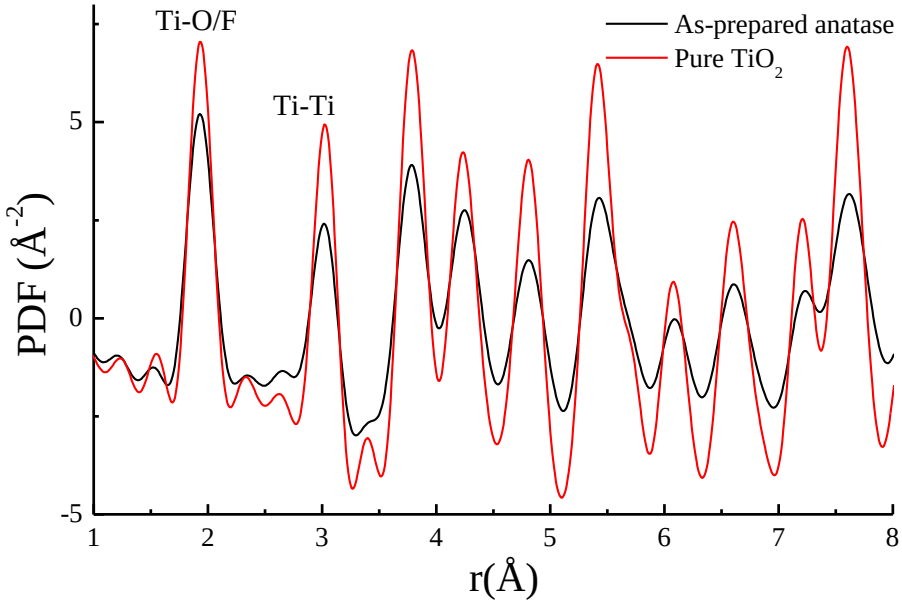


**Figure 2.2:** Comparison of the PDF data for the as-prepared anatase and pure $TiO_2$ anatase.

The fit of the PDF data was performed by using a Rietveld method in real space.[17] Anatase-type structure was used to fit the PDF data. It is shown in **Figure 2.3a** that the fit using single anatase structure yielded a good fit with the reliability factor Rw = 19.6 %, ruling out the presence of a second amorphous phase. PDF refinement of the reference pure $TiO_2$ is also shown for comparison (**Figure 2.3b**). **Table 2.1** shows structure parameters extracted from the PDF refinements. The crystal parameters of the as-prepared anatase phase are similar to those of pure $TiO_2$ anatase. The bond length between cation and anion in the as-prepared anatase is larger than that for pure $TiO_2$, which might be due to the incorporation of $F^-$ having larger ionic radii than $O^{2-}$. The refined Ti (4a) site occupancy for the as-prepared phase is ca. 74 (4) %, indicating the presence of cationic vacancies incorporated into the anatase lattice. Control of the concentration of cation vacancies will be detailed in Chapter III.2.6.2.

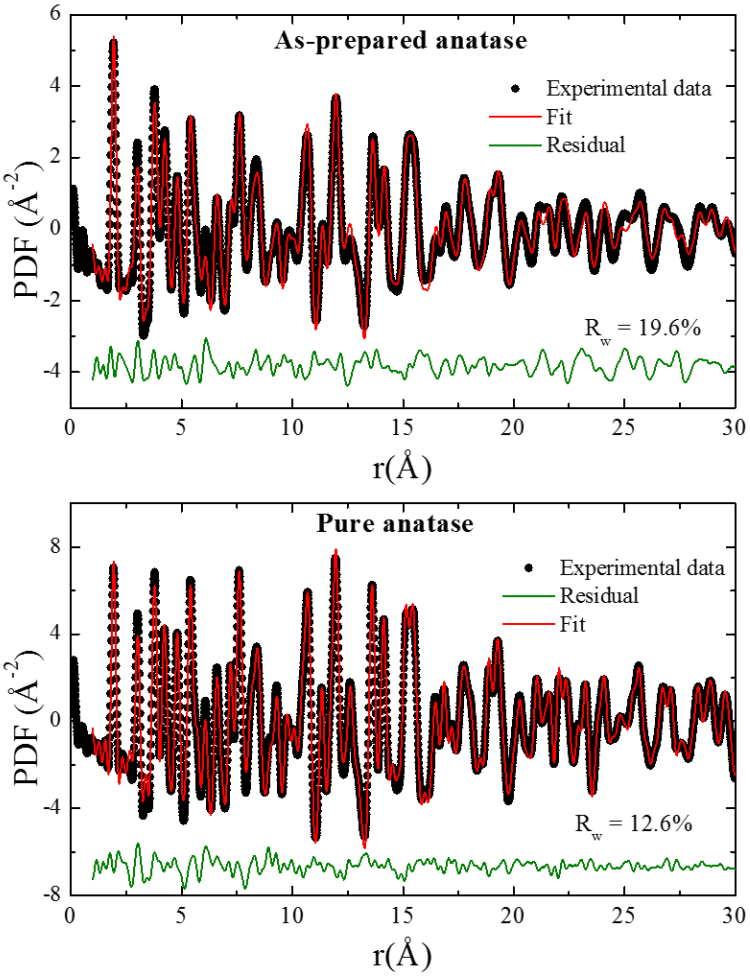


**Figure 2.3:** Pair Distribution Functions (solid black circle) of the as-prepared anatase (top) and pure $TiO_2$ (bottom). The tetragonal anatase-type $TiO_2$ models fitted to the data are shown in red and the residual in green. Fit range: 1 – 30 Å.

**Table 2.1: Structural parameters extracted from the refinement of the PDFs for pure $TiO_2$ anatase and the as-prepared anatase.**

| | **Pure $TiO_2$** | **As-prepared anatase** |
|---|---|---|
| **a (Å)** | 3.7695(5) | 3.784(1) |
| **c (Å)** | 9.454(2) | 9.448(6) |
| **V (Å$^3$)** | 134.33(4) | 135.28(10) |
| **$d_{Ti-O/F}$ (Å)** | 2*1.972(3) | 2*1.984(6) |
| | 4*1.925(1) | 4*1.929(1) |
| **Ti (4a) occupancy** | 1.00(1) | 0.74(4) |

## 1.3.2. Determination of the chemical composition

X-ray photo-electron spectroscopy (XPS) was performed to probe the valence states of elements in the as-prepared anatase. **Figure 2.4a & b** show the X-ray photo-electron spectrums of the elements $F_{1s}$ and $Ti_{2p}$ in the anatase phase, respectively. The presence of

fluorine within the anatase phase was confirmed by the peak at 684.5 eV characteristic of F-Ti bond. The Ti $2p_{3/2}$ peak was fitted using a single component centered at 458.9 eV which is characteristic of tetravalent titanium, ruling out the presence of trivalent Ti. XPS analysis indicates that fluorine is incorporated into the anatase lattice. The deficiency of negative charge caused by $O^{2-}/F^{-}$ substitution was not compensated by the reduction of $Ti^{4+}$.

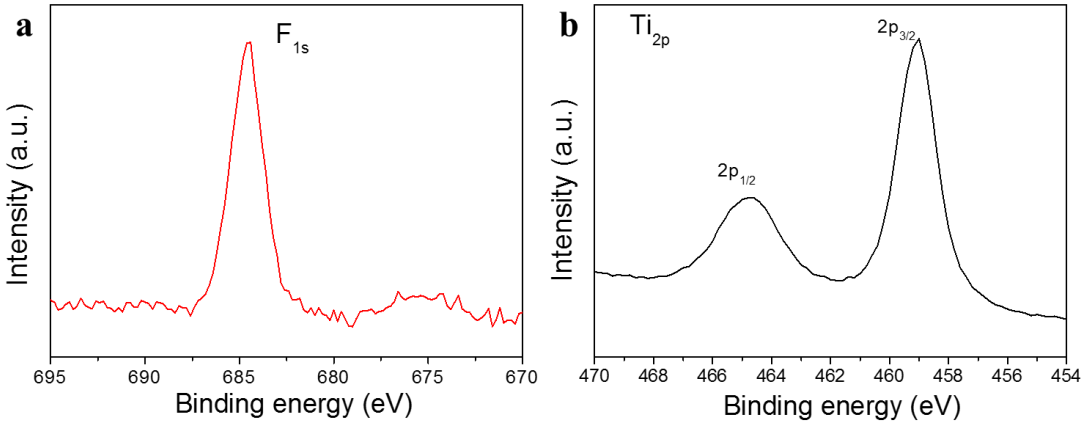


**Figure 2.4:** X-ray photo-electron spectra of $F_{1s}$ (a) and $Ti_{2p}$ (b) in the as-prepared anatase.

The presence of $OH^{-}$ groups in the as-prepared anatase phase was confirmed by $^{1}H$ solid state NMR spectroscopy. The spectrum displayed in **Figure 2.5** shows isotropic chemical shifts ranging from ~0 to ~12 ppm. The results of the reconstruction of the NMR lines are shown in **Table 2.2**. The five contributions indicate different distances of O-H bond, which can be ascribed to possible hydrogen bonds with polyanions ($F^{-}$ and $O^{2-}$) in the anatase phase.

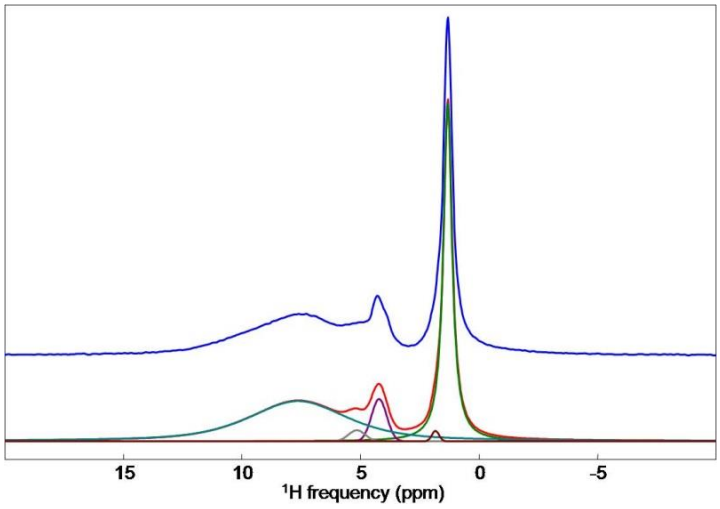


**Figure 2.5:** Experimental (in blue) $^{1}H$ solid state MAS (60 kHz) NMR spectrum of the as-prepared anatase. The fitted spectrum with five NMR lines is shown in red.

**Table 2.2:** Isotropic chemical shifts $\delta_{iso}$ (ppm), line widths LW (ppm), and relative intensities I (%) of the NMR lines obtained from the reconstruction of the $^{1}H$ solid state MAS (60 kHz) NMR spectrum shown in Figure 2.4.

| $\delta_{iso}$ (±0.05) | LW (±0.05) | I (±0.5) |
|---|---|---|
| 1.3 | 0.44 | 43.7 |
| 1.8 | 0.37 | 0.8 |
| 4.2 | 0.76 | 6.5 |
| 5.2 | 0.83 | 1.8 |
| 7.6 | 4.9 | 47.2 |

According to the above results, the defective mechanism of the substitution of $O^{2-}$ by $F^{-}/OH^{-}$ is proposed. Partial substitution of divalent oxygen by monovalent fluorine and hydroxyl groups induced the formation of cation vacancies. Each atomic replacement leads to a (-1) charge deficiency which can be counterbalanced by the formation of one titanium vacancy for every four substitutions. Thus, the general chemical formula of this new family of material can be written as $Ti_{1-x-y}\square_{x+y}O_{2-4(x+y)}F_{4x}(OH)_{4y}$, where $\square$ represents a cation vacancy.

In order to determine an accurate chemical composition of the as-prepared anatase, additional characterizations tools such as $^{19}F$ solid state NMR spectroscopy and thermo-gravimetric analysis (TGA) were performed. The fluorine content was quantified by $^{19}F$ solid state NMR spectroscopy by using reference samples, i.e. NaF, $LaF_3$ and $YF_3$. A molar ratio of F/Ti close to 0.5 was obtained. Method regarding fluorine quantification by $^{19}F$ NMR analysis is detailed in the Appendix 3 and the reference.[13] Thermogravimetric analysis (TGA) was then performed under He atmosphere to quantify the amount of $OH^{-}$ groups (**Figure 2.6**). The TGA curve shows three distinct weight losses below 600 °C. By coupling the TGA with a mass spectrometer analysis we were able to identify the released gaseous species. At temperature below 150 °C, a weight loss of 2.5 wt. % corresponds to the evaporation of water molecules physically adsorbed on anatase particles. Then, a weight loss of 5.5 wt. % can be observed between 150 and 350 °C. Mass fragments m/z = 17 and 18 indicate that this weight loss is caused by the occurrence of a dehydroxylation reaction. Finally, fluorine starts to be released at 250°C (m/z ($F^{+}$) = 19) with a major weight loss at 450°C.

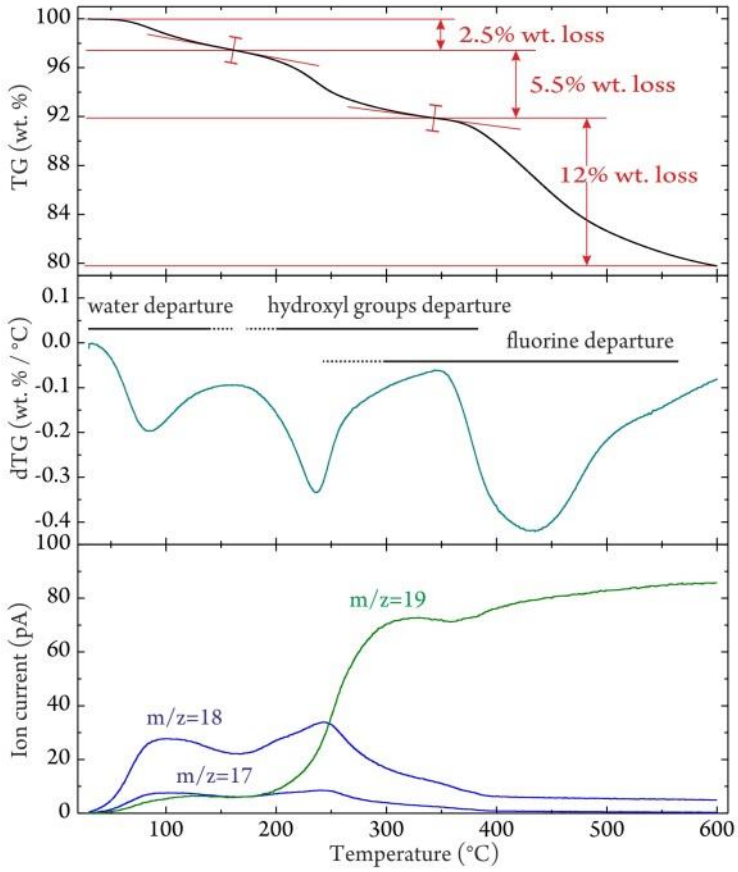


**Figure 2.6:** Thermogravimetric with mass spectrometer analyses performed under He of the as-prepared anatase.

The combination of chemical analyses with the PDF refinement allows the following chemical composition of the as-prepared anatase to be established: $Ti_{0.78}\square_{0.22}O_{1.12}F_{0.4}(OH)_{0.48}$. The incorporation of fluorine within anatase structure can be ascribed to fluorolysis of Ti precursor.[18] In this sample, 44% of the anionic sites are occupied by monovalent anions, i.e. $F^-$ and $OH^-$, leading to a high concentration of cation vacancies (22%). Both cationic and anionic sublattices modification indicates that anatase structure can be drastically modified while keeping its original crystalline framework. A possible atomic arrangement of the atoms for a simplified, hydroxide-free composition $Ti_{0.78}\square_{0.22}O_{1.12}F_{0.88}$ was simulated using DFT-based molecular dynamics performed by Dr. D. Corradini and Dr. M. Salanne. **Figure 2.6** shows snapshots of a $TiO_2$ anatase crystal and $Ti_{0.78}\square_{0.22}O_{1.12}F_{0.88}$ obtained from DFT at 0K and after 10 ps of DFT-based molecular dynamics at 300 K, respectively. The fluorinated defective structure of $Ti_{0.78}\square_{0.22}O_{1.12}F_{0.88}$ obtained at 300 K retains the features of the anatase network, highlighting the high compositional and structural versatility of the anatase phase.

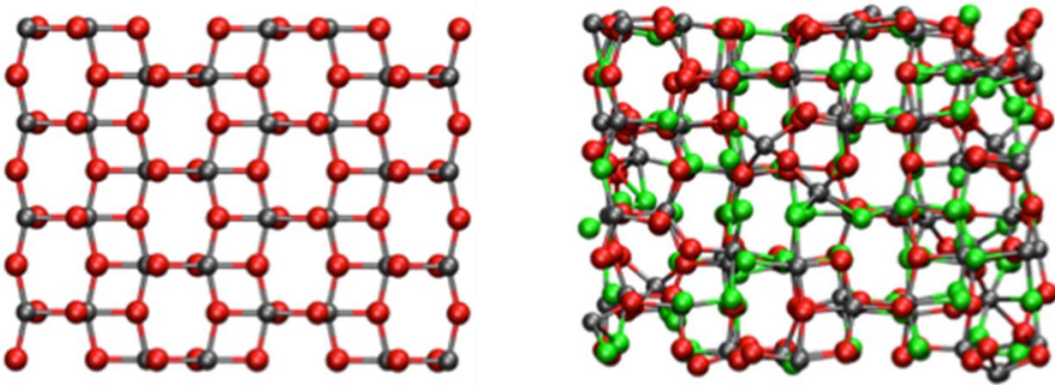

**Figure 2.7:** Snapshot of a $TiO_2$ anatase crystal obtained from DFT at 0K (left). Snapshot obtained after 10 ps of DFT-based molecular dynamics at 300 K of $Ti_{0.78}\square_{0.22}O_{1.12}F_{0.88}$ (right). (grey: Ti, green: F and red: O)

### 1.3.3. Local atomic structure

Significant deviation of chemical composition from stoichiometric $TiO_2$ to cation-defected $Ti_{0.78}\square_{0.22}O_{1.12}F_{0.4}(OH)_{0.48}$ indicates that the anatase framework can accommodate strong local substitutional disorder while keeping its long-range structural order. Absence of significant difference on the long range order in the experimental and calculated PDFs of $Ti_{0.78}\square_{0.22}O_{1.12}F_{0.4}(OH)_{0.48}$ suggests that cation vacancies are not locally ordered within the anatase lattice.

To probe the local atomic structure of $Ti_{0.78}\square_{0.22}O_{1.12}F_{0.4}(OH)_{0.48}$, and particularly the fluorine environment, $^{19}F$ magic angle spinning (MAS) solid-state NMR analysis was carried out by Dr. M. Body and Prof. C. Legein at Université du Maine. The $^{19}F$ MAS NMR spectrum shown in **Figure 2.8** was reconstructed using three lines located at $^{19}F$ $\delta_{iso}$ ~ -88, -4 and 98 ppm (**Table 2.3**), indicating three different environments for fluorine. Within the pure $TiO_2$ anatase, an oxygen atom is surrounded by three titanium atoms, i.e. $Ti_3$-O. However, the presence of cation vacancies in $Ti_{0.78}\square_{0.22}O_{1.12}F_{0.4}(OH)_{0.48}$ induces two additional coordination modes for the anions. Anion can be surrounded by two Ti and one vacancy ($Ti_2\square_1$-X) and/or one Ti and two vacancies ($Ti_1\square_2$-X) with X= $O^{2-}$, $F^-$ and $OH^-$.

The matching between the different fluorine environments and the three NMR lines is based on the relation between coordination number of $F^-$ and the chemical shift. The chemical shift of $F^-$ decreases when the number of cation bonded with $F^-$ increases. Thus, the three lines located at $^{19}F$ $\delta_{iso}$ ~ -88, -4 and 98 ppm can be assigned to $Ti_3$-F, $Ti_2\square_1$-F and $Ti_1\square_2$-F with the concentrations of 4 %, 64 % and 32 %, respectively. This trend has been observed for $^{19}F$

in $NbF_5$ and $TaF_5$ and for $^{17}O$ in $TiO_2$(B).[19,20] Typical atomic arrangements for the three fluorine coordination modes in $Ti_{0.78}\square_{0.22}O_{1.12}F_{0.88}$ obtained *via* DFT-based molecular dynamics are shown in **Figure 2.8**. It shows that 96 % of fluorine locates close to at least one cation vacancy. Nevertheless, assuming random distributions of vacancies and Ti on the (4a) cation and of O/F/OH on the (8e) anionic Wyckoff sites, the total concentration of the fluorine located close to vacancy is 51.5 %. The difference between experimental and calculated fluorine environment indicates a preferential localization of fluorine close to vacancy. The broadening of the NMR lines indicates widely distributed Ti-F distances, highlighting local disorder for fluorine environments. Note that this disorder increases with the number of cation vacancy close to fluorine.

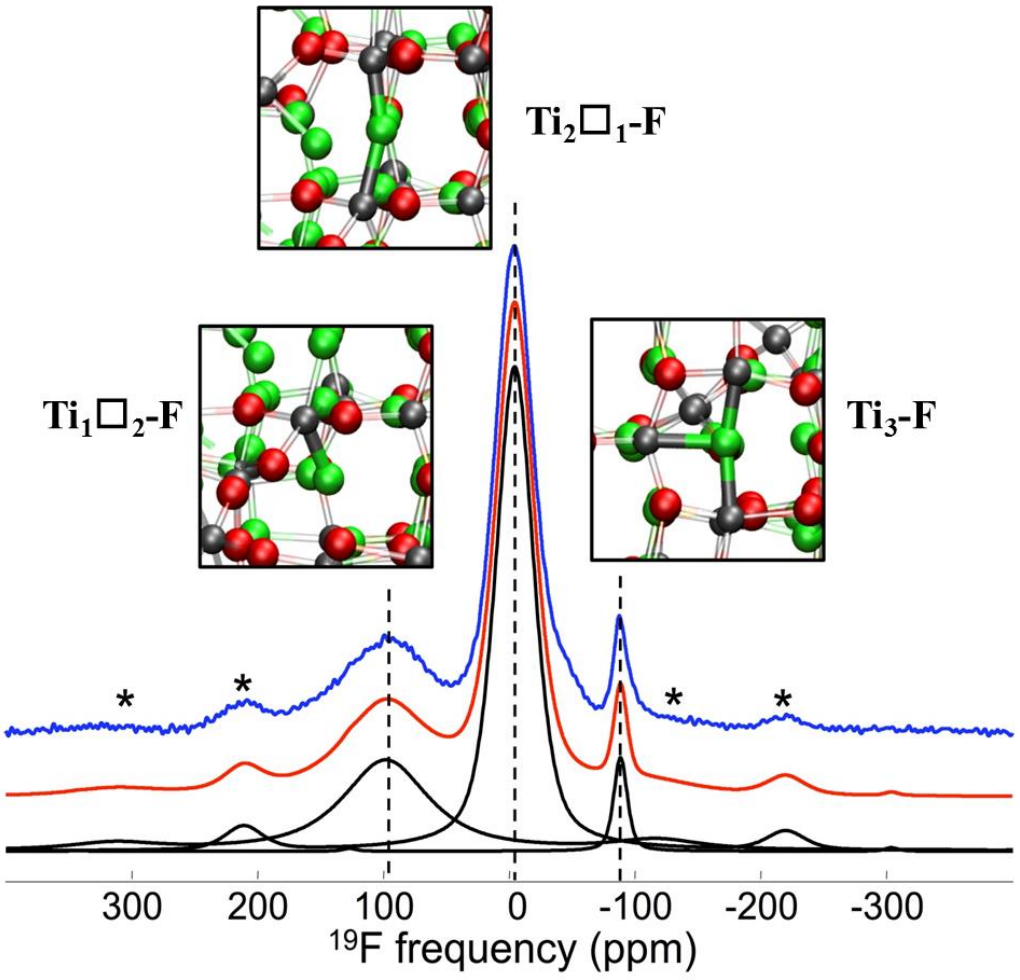


**Figure 2.8:** Experimental (in blue) $^{19}F$ solid state MAS (60 kHz) NMR spectrum of $Ti_{0.78}\square_{0.22}O_{1.12}F_{0.4}(OH)_{0.48}$ anatase, fitted (in red) with three NMR lines (in black, indicated by vertical dashed lines), which are assigned to $Ti_1\square_2$-F, $Ti_2\square_1$-F and $Ti_3$-F (from left to right) environments. The asterisks indicate the spinning sidebands. Corresponding structures are also shown (grey: Ti, green: F and red: O, on each snapshot the illustrated bonds are shown as thick solid cylinders, while the other bonds are shown as thin transparent cylinders).

**Table 2.3:** Isotropic chemical shifts $\delta_{iso}$ (ppm), line widths LW (ppm), and relative intensities I (%) of the NMR lines obtained from the reconstruction of the $^{19}F$ solid state MAS (60 kHz) NMR spectrum of $Ti_{0.78}\square_{0.22}O_{1.12}F_{0.4}(OH)_{0.48}$ (**Figure 2.7**) and assignment of these NMR lines.

| $\delta_{iso}$ (±0.5) | LW (±0.5) | I (±0.5) | Assignment |
|---|---|---|---|
| -88.5 | 12.7 | 4.4 | $Ti_3$-F |
| -4.5 | 35.6 | 63.7 | $Ti_2\square_1$-F |
| 98.0 | 80.8 | 31.9 | $Ti_1\square_2$-F |

Static DFT calculations were used to study the stabilization of such preferential location of fluorine. To do that, one cation vacancy was created in a $Ti_{127}\square_1F_4O_{252}$ supercell by replacing 4 $O^{2-}$ by 4 $F^-$. In this case, fluorine can locate close to or away from the vacancy, generating local environments of $Ti_2\square_1$-F and $Ti_3$-F, respectively. The configuration where the vacancy is surrounded by 6 $O^{2-}$ was used as an energy reference. We then progressively added fluorine close to the vacancy and monitored the variation of the energy of the systems. Four configurations were created based on the number of fluorine close to the vacancy. **Figure 2.9** shows the evolution of the energy of the systems as a function of the number of fluorine located close to the vacancy. The results indicate a continuous decrease in energy when the number of fluorine increases, indicating the stabilization of the vacancy by fluoride atoms. The most stable configuration corresponds to the four fluoride anions located within the equatorial plane of the vacancy. This is consistent with a simple electrostatic consideration. Two F/O atoms located in the vicinity of a vacancy will strongly repulse each other. As $F^-$ contains less negative charge than $O^{2-}$, the repulsion is thus much weaker between two $F^-$ than between two $O^{2-}$. The results confirm the preferential location of fluorine close to Ti vacancy, as indicated by solid state $^{19}F$ NMR analysis.

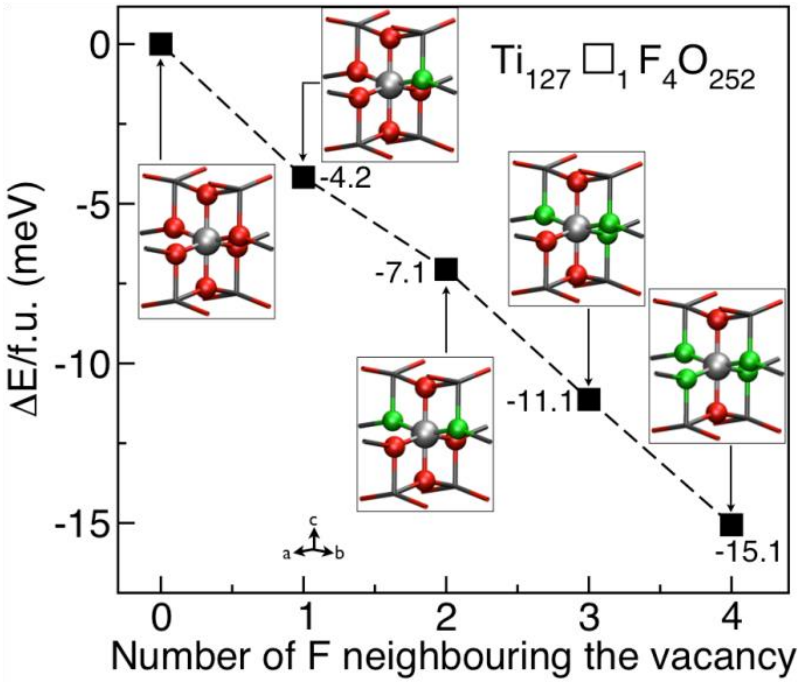


**Figure 2.9:** DFT calculations performed on a $Ti_{127}\square_1F_4O_{252}$ supercell containing one vacancy □ (light gray) was built by replacing 4 oxygen atoms (red) with 4 fluorine atoms (green). The anionic environment was tuned by adding fluorine in the vicinity of the vacancy. In all cases the F not placed around the vacancy substituted random O in the lattice and thus had the $Ti_3$-F environment. The sticks in the snapshots link the central vacancies to their neighboring atoms (only the 6 atoms around the vacancy are drawn).

# 2. Formation mechanism of $Ti_{0.78}\square_{0.22}O_{1.12}F_{0.4}(OH)_{0.48}$

## 2.1. Introduction

Hydrothermal/solvothermal methods are widely used in preparing metal oxides nanoparticles due to advantages of low cost, energy efficiency, environmental geniality, and versatility.[21] Changing certain experimental parameters (e.g. temperature, solvent and precursors)[14,22] enables tailoring structure, morphology and chemical compositions. The understanding of formation mechanisms is crucial for describing what occurs during the reaction and furthermore, for optimizing the synthesis parameters to get certain materials. In order to rationally design the synthesis for controlling the materials properties, a detailed knowledge of how transition metal precursor reacts and grows into solid nanoparticles is needed. Time-dependent studies on nanoparticles formation, taking place during the hydrothermal/solvothermal processes, enable identifying the possible presence of intermediate phases formed during the reaction and provide deeper understanding on the condensation of precursors into solid via nucleation and crystallization processes.

$TiO_2$ anatase, a polymorph of titanium dioxide, is a promising material that is widely used in the domain of catalysis, energy storage and conversion.[6,23,24] The expose of the high reactive facets {001} in $TiO_2$ anatase has been reported to be effectively controlled by fluorine.[8,9] Adsorption of fluorine at the (001) surface can guide anisotropic growth of anatase particles.[25] Moreover, strong complexing ability of fluorine drives dissolution and recrystallization of $TiO_2$, leading to the increase of particle size.[26] In these cases, fluorine finally adsorbed at the surface of $TiO_2$, as claimed by the authors according to the XPS analysis. However, the mechanistic role of fluorine may not be as simple as that. When fluorine source is added in precursor prior to the reaction, it can react with the precursor immediately through fluorolysis reaction (**Eq. 1.9**).[18] Donor ability of fluorine ions induces the formation of metal-fluorine bridges, resulting in the incorporation of fluorine within the lattice.[27,28] In the previous part, we reported that fluorine can incorporate in $TiO_2$ anatase framework, resulting in cation-defected polyanionic phase $Ti_{0.78}\square_{0.22}O_{1.12}F_{0.4}(OH)_{0.48}$. The study of the formation mechanism of such defective anatase could provide more insights into the role of fluorine during the sol-gel reaction. Here, we combine XRD, high-resolution TEM, pair distribution function and $^{19}F$ solid-state NMR analyses as well as chemical analysis to

gain structural and compositional insights into nanoparticles formation and to unravel the formation mechanism of the cation-defected fluorinated anatase.

## 2.2. Experimental methods

### 2.2.1. Synthesis method

Titanium tetra-isopropoxide (TTIP, ≥97%, Sigma Aldrich); isopropanol (PriOH, Reag.Ph.Eur. grade, VMR); aqueous hydrofluoric acid solution (HF, 40 wt%, Prolabo); and ethanol (EtOH, 96% vol, VWR) were used as received.

Syntheses via solvothermal process took place in stainless steel autoclave with a 50 mL Teflon liner cup inside. In a typical experiment, 1.2 mL aqueous hydrofluoric acid solution was mixed with 24.8 mL isopropanol. The mixture was then poured into Teflon liner cup containing 4 mL TTIP under stirring. After sealing the autoclave, the mixed solution was heated inside an oven at 90 °C for a certain time from 1 h to 12 h, and left to cool down to room temperature. The resulting precipitate was washed twice by 30 mL ethanol, centrifuged at 4400 rpm for 15 min and eventually, dried at 80 °C under air for 2 h. Further thermal purification was carried out using a tubular furnace under primary vacuum at 50 °C overnight. However, no precipitate was obtained for synthesis less than 4 h but gel phase. In this case, the gel was transferred directly into tubular furnace and desiccated under the same condition used as thermal purification mentioned above.

### 2.2.2. Characterization methods

Chemical elementary analysis was carried out at the central service of analysis (UMR 5280, Villeurbanne, France). Quantification of fluorine was performed by combining an oxidizing combustion system and chromatographic analysis. To do that, the sample was first introduced into a pyrolysis tube under argon. After the pyrolysis at 1000°C, the fluorinated compounds in the sample were burned and oxidized by a stream of oxygen, resulting in the formation of $F_2$ and/or HF which were collected in 5 ml of absorbent liquid. A constant volume of the absorbent liquid was analyzed by ion chromatography method to quantify the fluorine. The detection was realized by conductimetry. To quantify the titanium, the sample was first mineralized in acidic medium. The content of titanium was detected by inductively coupled plasma atomic emission spectroscopy (ICP-AES).

## 2.3. Results and Discussion

### 2.3.1. Time-dependent structural evolution

$Ti_{0.78}\square_{0.22}O_{1.12}F_{0.4}(OH)_{0.48}$ was solvothermally synthesized at 90 °C for 12 h by using titanium tetra-isopropoxide as precursor, aqueous hydrofluoric acid (40 wt.%) as fluorinating agent and isopropanol as solvent. Its formation mechanism was studied by varying the synthesis time from 1 h to 12 h. The syntheses were first monitored by using X-ray diffraction and transmission electron microscopy (TEM) methods. **Figure 2.10** shows the XRD patterns for the samples prepared from 1 to 5 hours. At the early stage of reaction (1 h), XRD shows a poor crystallized pattern. A peak located at 2θ = ca. 23.7° may be assigned to the (100) plane of cubic $TiOF_2$ (space group: Fm-3m). As the reaction proceeded, this peak progressively decreased and vanished after 5 h of reaction, indicating that this peak is associated to intermediate phase prior to the formation of anatase. The XRD pattern of the sample obtained after 5 h of reaction can be indexed to a tetragonal cell with space group $I4_1/amd$ characteristic of $TiO_2$ anatase, confirming the formation of the single phase of anatase.

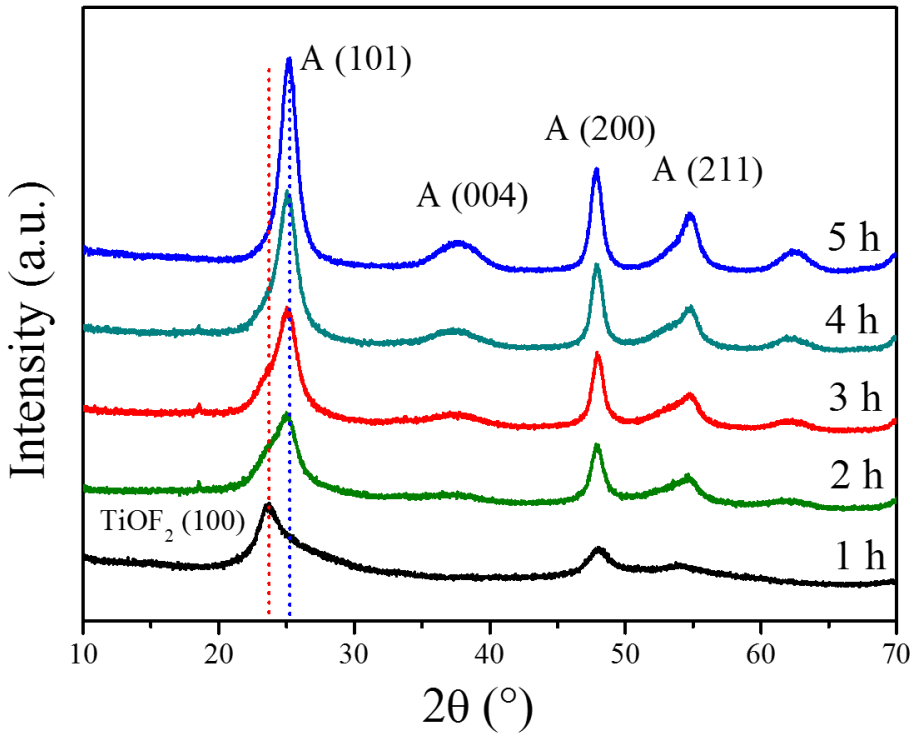


**Figure 2.10:** Evolution of the XRD patterns of the samples synthesized within the first 5 hours. Dot red and blue lines indicate the reflection of (100) and (101) planes of $TiOF_2$ and $TiO_2$ anatase, respectively. 'A' refers to $TiO_2$ anatase phase.

**Figure 2.11** shows transmission electron micrographs of the samples obtained after 1, 2 and 5 h of reaction. TEM images of the sample obtained after 1 h of reaction show that the solid is dominated by amorphous particles (yellow circles) whose size ranges from 3–4 nm. Additionally, larger particles of ca. 7 nm were observed featuring crystal lattice spacing of 0.19 nm corresponding to (200) plane in $TiO_2$ anatase. While the reaction time prolonged, the crystalline phase increased progressively and, concomitantly the amorphous one reduced. No amorphous particles can be observed for the sample obtained after 5 h of reaction. According to the XRD and TEM analyses, the amorphous phase can be attributed to $TiOF_2$ which might act as an intermediate phase during the formation of the anatase nanoparticles.

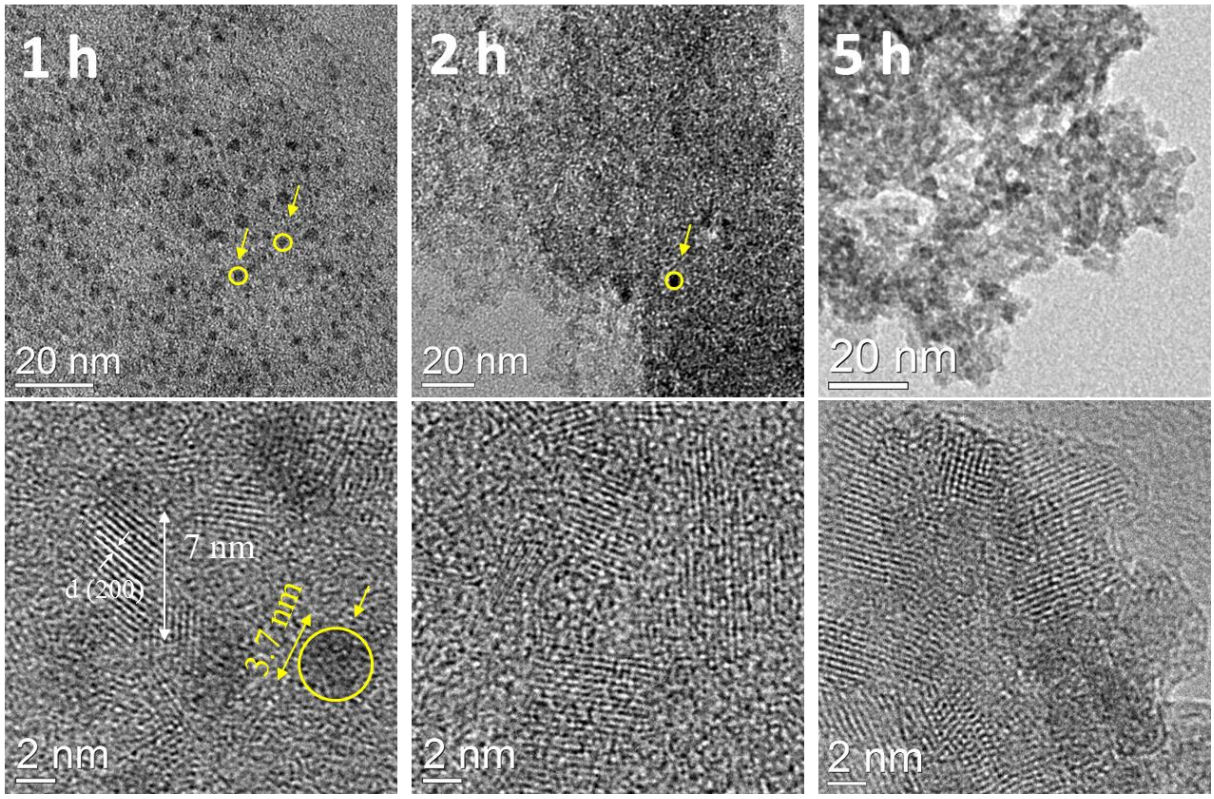


**Figure 2.11:** Transmission electron micrograph of the resulting samples obtained after different reaction time (top) and the corresponding high resolution micrographs (bottom). Yellow circles indicate amorphous particles.

Pair distribution function (PDF) analysis, which permits to probe both amorphous and nanostructured materials at atomic scale,[29] was carried out to further identify the nature of the intermediate phase observed by TEM and to gain insights into the crystallization processes of the anatase.

**Analysis of PDF peaks**

PDF data can be analyzed by direct comparison of the evolution of PDF peak features with the reference one.[30] The peak analysis provides direct observation about bond lengths, local ordering and coordination number from the positions, the width and the area of peaks, respectively.[16] **Figure 2.12** shows the evolution of time-dependent PDFs at short range order (1 – 6 Å) as well as their comparison with reference $TiO_2$ anatase and $TiOF_2$. The feature of the 1st peak, corresponding to the bond of Ti-O/F, did not vary significantly while reaction time increased. The results of fitting Gaussian function to the peak are displayed in **Figure 2.13**. It shows that the position of the peak increased progressively with respect to reaction time, indicating the elongation of Ti-O/F bond length. This is probably caused by structural rearrangement and/or modification of Ti coordination sphere. Larger peak width at shorter reaction time indicates a wide distance distribution of Ti-O/F. Note that the position of the PDF peaks locates between the average distances of Ti-O/F in $TiO_2$ and $TiOF_2$, indicating that the fluorine concentration in the obtained samples might be lower than $TiOF_2$. The area of the 1st peak remains constant along the reaction, indicating that titanium is octahedrally coordinated. In the titanium precursor $Ti(O^iPr)_4$, the coordination number of Ti equals to its oxidation state 4+. Coordination expansion of Ti at the early stage of reaction indicates that the precursor reacted with $H_2O$ and HF.

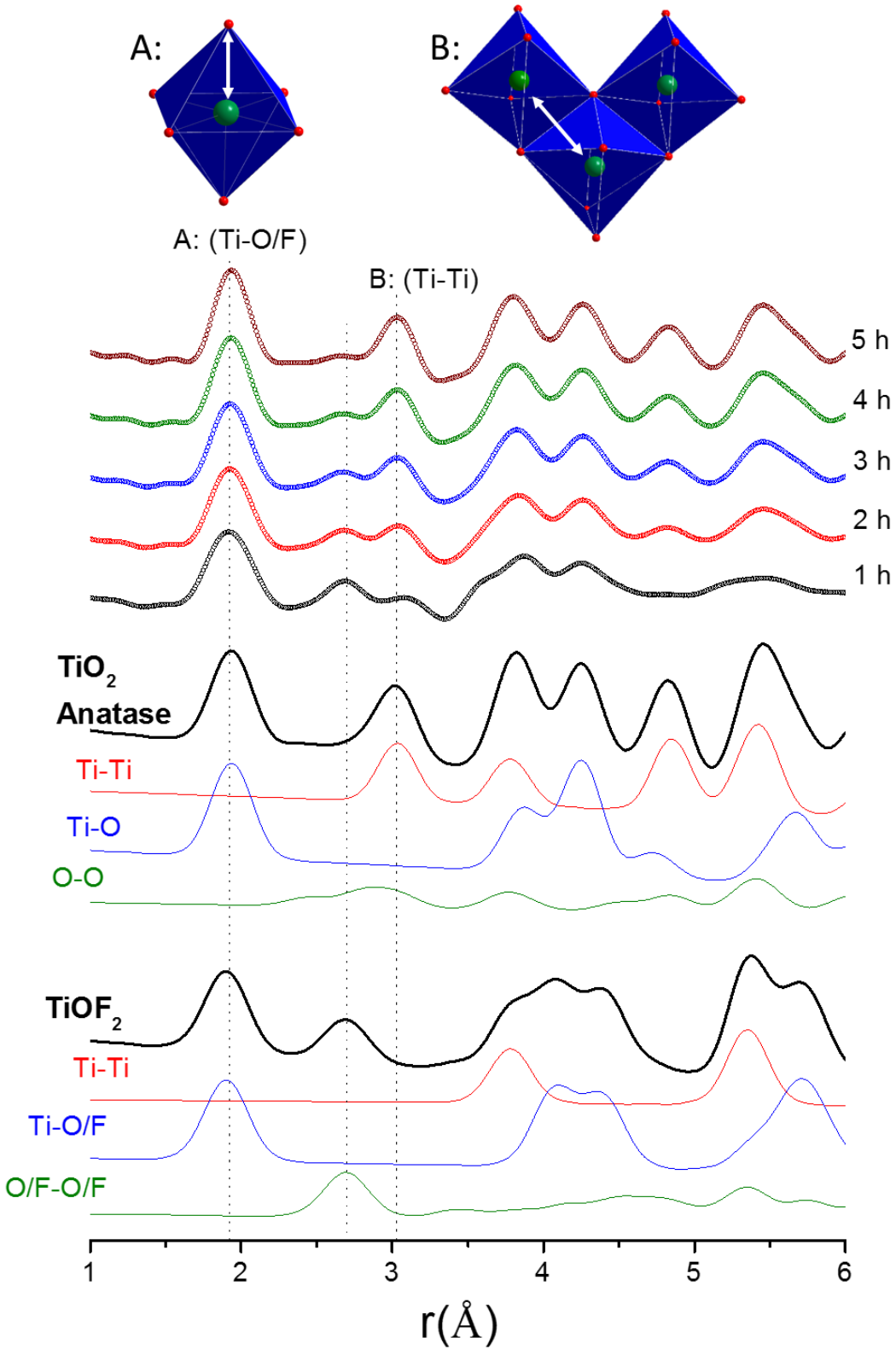


**Figure 2.12:** Comparison between time-dependent PDFs and the reference bulk $TiOF_2$ (ICSD # 38132) and $TiO_2$ (ICSD # 94566) as well as their calculated partial PDFs. 'A' and 'B' schematically show atomic distances corresponding to the position of the 1st and the 3rd peak in PDFs, respectively (green: Ti and red: O/F).

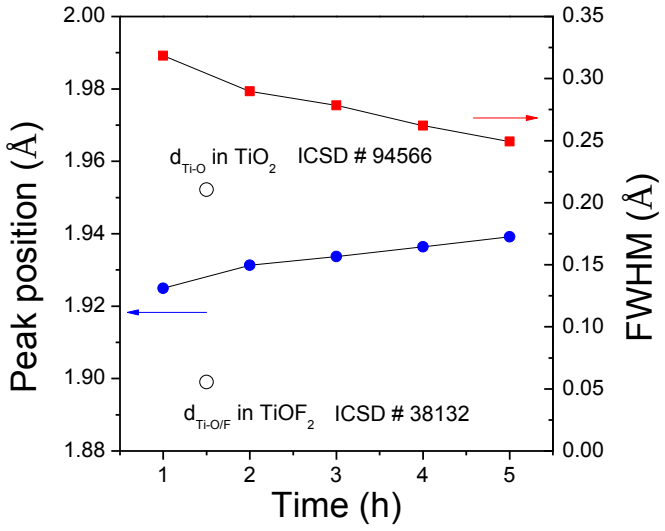


**Figure 2.13:** Results from fitting Gaussian function to the 1st peak of the time-dependent PDFs. The average Ti-O/F bond distances in bulk anatase ($d_{Ti-O}$ in $TiO_2$) and in bulk $TiOF_2$ ($d_{Ti-O/F}$ in $TiOF_2$) are pointed by black circles for comparison.

Pronounced variation regarding the intensity of PDF peaks was observed for the 2nd and 3rd peaks. The variation of the intensity of PDF peak reflects quantitative evolution of pairing atoms. The intensity of the 2nd peak at ca. 2.7 Å, characteristic of the first coordination sphere of anion-anion (X-X), decreased with reaction time. It can be observed, from the calculated partial PDFs of the reference sample, that O/F-O/F in $TiOF_2$ exhibits an intense peak at this region, whereas O-O in $TiO_2$ anatase shows wide distance distributions. This difference can be ascribed to distorted $TiO_6$ octahedra in $TiO_2$, generating three different O-O distances. Thus, the decrease in intensity of the 2nd peak indicates the decrease of $TiOF_2$ phase. In contrast, the intensity of the 3rd peak at ca. 3.1 Å, corresponding to Ti-Ti in edge-sharing octahedra (interatomic distance is schematically illustrated in **Figure 2.12**), increased with respect to reaction time. Since calculated partial PDF shows that this interatomic distance exists only in $TiO_2$ anatase, the variation of the 3rd peak in PDFs indicates the increase of anatase phase upon reaction. On the basis of the PDF peak analysis, phase transition from $TiOF_2$ to $TiO_2$ anatase has been visualized at atomic scale.

**PDF refinements**

In order to identify and get access to the structural parameters of phases presented in the solid, structural models were fit against the PDF data using a real-space refinement.[17] For the sample obtained after 1 h of the reaction, the presence of amorphous phase along with the limit of PDF correlations to about 20 Å prevent the extraction of reliable structure parameters.

Hence, both $TiOF_2$ and anatase models were used to fit the PDFs obtained after 2, 3 and 4 h of reaction (**Figure 2.14**). It is shown that the 2-phase refinement provides a good fit to the PDF data at both short and long range order. The contribution of $TiOF_2$ to the PDF is shown in **Figure 2.14** for the sample prepared for 2 h. The $TiOF_2$ shows local ordering, indicating an amorphous nature of this phase. This phase can be thus related to the amorphous particles observed by TEM.

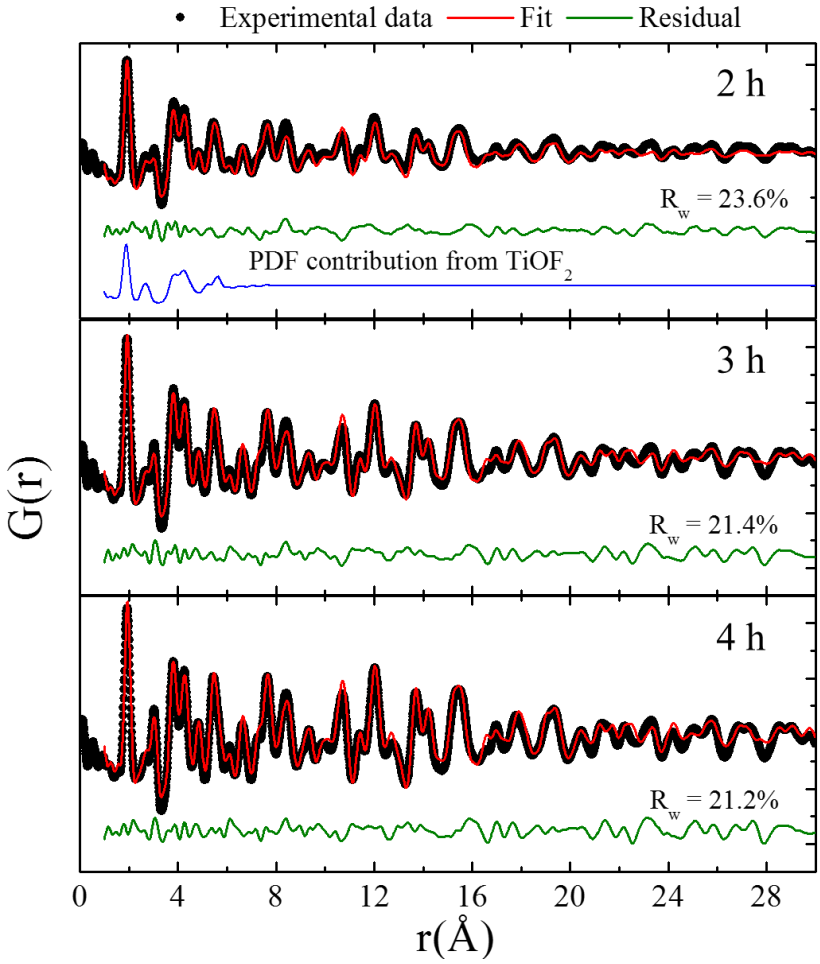


**Figure 2.14:** Fits of the time-dependent PDF data using a two-phase refinement including $TiOF_2$ and $TiO_2$ anatase phases.

The PDF fits enable quantifying phases in a multi-phase refinement by refining the scale factor of phases. The molar fraction of both anatase and $TiOF_2$ was extracted with respect to time of reaction and the results are shown in **Figure 2.15**. A molar ratio of 37 % of $TiOF_2$ was found in the solid after 2 h of reaction. It decreased gradually to 25 % and 14 % after 3 and 4 h of reaction, respectively. Contrarily, anatase phase increased at the expense of $TiOF_2$ and single anatase phase was obtained after 5 h of reaction.

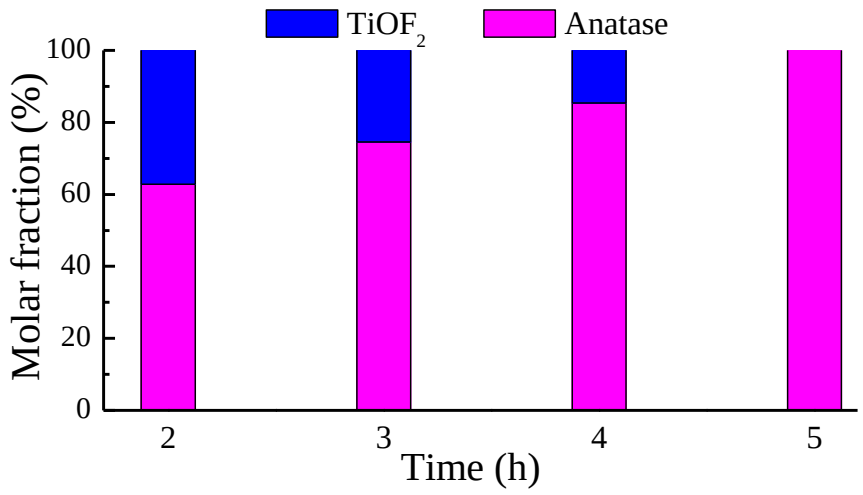


**Figure 2.15:** Evolution of molar faction of $TiO_2$ anatase and $TiOF_2$ obtained from PDF fits.

The coherence length of nanoparticles can be directly obtained from the r value where PDF oscillations damp to zero. As $TiOF_2$ shows local ordering, significant extension of the PDF oscillations from 1 h (ca. 20 Å) to 2 h (ca. 40 Å) of reaction indicates particle growth and/or structural ordering of the anatase phase. **Figure 2.16** shows the evolution of the optimized spherical particle sizes (sp-diameter) of $TiOF_2$ and anatase phases extracted from the fits to the time-dependent PDFs. $TiOF_2$ showing local ordering can be observed all along the reaction. The sp-diameter of the anatase phase increased slightly from 2 h to 5 h and maintained similar value thereafter, indicating that anatase particle sizes did not vary when pure anatase phase was formed after 5 h of reaction. This was confirmed by TEM analysis.

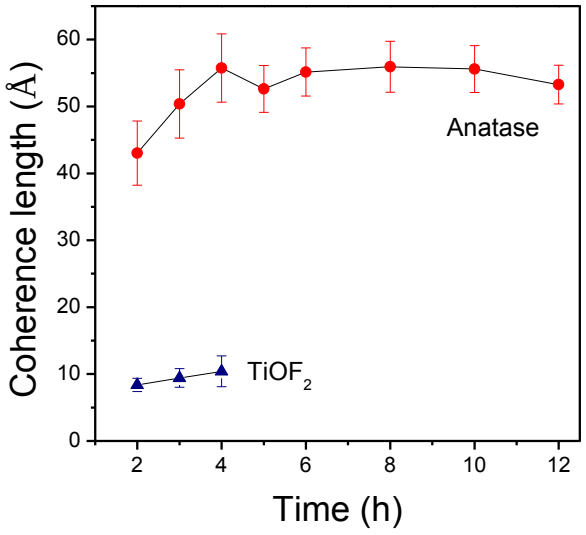


**Figure 2.16:** Evolution of the sp-diameter of $TiOF_2$ and anatase phases extracted from the fits to the time-dependent PDFs.

Cation vacancies in the fluorinated anatase, created by the substitution of $O^{2-}$ by monovalent anions, i.e. $F^-/OH^-$, were obtained by refining titanium occupancy in the anatase phase. **Figure 2.17** shows the evolution of the concentration of cation vacancies with respect to reaction time. It reached almost ~50 % for the anatase obtained after 2 h of reaction. Such a high value indicates a high concentration of monovalent anions in the anatase phase at the early stage of the reaction. While the reaction progressed, the concentration of Ti vacancy decreased gradually to ~37 % after 5 h of reaction, where single phase of anatase was obtained. The evolution of the concentration of cation vacancies in the anatase as a function of reaction time reveals structural rearrangement of the anatase phase. Such structural rearrangement can be related with the increase of sp-diameters of the anatase particles. Both can be ascribed to the condensation reaction of $OH^-$ groups, forming Ti oxo bonds which are the base of the anatase network.

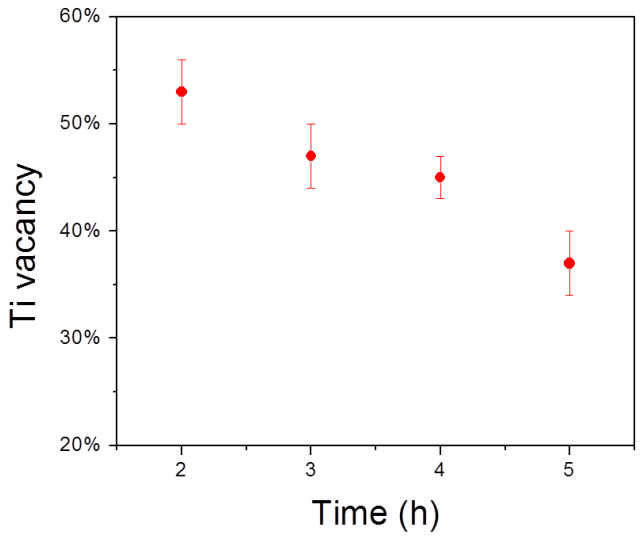


**Figure 2.17:** Evolution of the concentration of cation vacancies in anatase phases extracted from the time-dependent PDFs.

## 2.3.2. Compositional study

Chemical analysis, performed at the central service of analysis (SCA, Villeurbanne), was then applied to probe the evolution of the chemical composition of the solids. Evolution of the molar ratio between fluorine and titanium in the solid are gathered in **Table 2.4**. A high ratio of fluorine (F/Ti = 1.86) was obtained for the solid obtained after 1 h of reaction, indicating that titanium precursor is highly reactive towards fluorine. Thereafter, gradual decrease of fluorine in the solid reflects a continuous defluorination reaction caused mainly by the dissolution of $TiOF_2$.

**Table 2.4: Evolution of the experimental and calculated chemical composition of the solids and the anatase phases obtained at different stage of the reaction.**

| Time (h) | Experimental F/Ti in solid | Calculated F/Ti in anatase | Calculated OH/Ti in anatase | Proposed composition of anatase |
|---|---|---|---|---|
| 2 | 1.33 | 0.94 | 3.06 | $Ti_{0.50}\square_{0.50}F_{0.47}(OH)_{1.53}$ |
| 3 | 1.24 | 0.97 | 2.43 | $Ti_{0.54}\square_{0.46}O_{0.16}F_{0.53}(OH)_{1.31}$ |
| 4 | 1.04 | 0.88 | 2.14 | $Ti_{0.57}\square_{0.43}O_{0.28}F_{0.50}(OH)_{1.22}$ |
| 5 | 0.75 | 0.75 | 1.54 | $Ti_{0.63}\square_{0.37}O_{0.52}F_{0.51}(OH)_{0.97}$ |
| 12 | 0.51 | 0.51 | 0.62 | $Ti_{0.78}\square_{0.22}O_{1.12}F_{0.4}(OH)_{0.48}$ |

Combining PDF phase quantification and chemical analysis, we calculated the fluorine concentration in the anatase phase using the following equation:

$$\frac{F}{Ti}(anatase) = \frac{\frac{F}{Ti}(solid) - \frac{F}{Ti}(TiOF_2) * \%\ molar\ of\ TiOF_2}{\%\ molar\ of\ anatase} \qquad (\boldsymbol{Eq.2.1})$$

Where F/Ti (solid) and F/Ti ($TiOF_2$) are the F/Ti ratio in the solid and $TiOF_2$, respectively. % molar of $TiOF_2$ and % molar of anatase are the molar fraction of $TiOF_2$ and anatase obtained from the PDF quantification, respectively. The value of F/Ti ($TiOF_2$) is unknown because $TiOF_2$ is amorphous, its chemical composition might be nonstoichiometric. Thus, we assume two values of F/Ti in $TiOF_2$, i.e. 1.5 and 2.

The calculation results using F/Ti ($TiOF_2$) = 2 are gathered in **Table 2.4**. The F/Ti ratio in the anatase phase decreased slowly with reaction time, indicating that defluorination reaction occurred within the anatase phase. Quantification of $OH^-$ was realized by using the general formula of the cation-defected anatase, i.e. $Ti_{1-x-y}\square_{x+y}O_{2-4(x+y)}F_{4x}(OH)_{4y}$, where proportions of vacancy and fluorine are known. The evolution of OH/Ti is shown in **Table 2.4**. As time prolonged, the OH/Ti ratio decreased as expected, which was caused by condensation reactions (**Eq. 1.5 – 7**). The decreasing rate for OH/Ti is higher than that for F/Ti, indicating that dehydroxylation process is more favorable than defluorination process.

In the case of F/Ti ($TiOF_2$) = 1.5, the evolution of F/Ti in anatase showed same trend as that for F/Ti ($TiOF_2$) = 2. It decreased slightly as the reaction progressed. OH/Ti in anatase decreased as well and showed higher rate than defluorination.

On the basis of the rough calculation using F/Ti ($TiOF_2$) = 2, the chemical compositions of the anatase phases formed after different time of reaction were proposed and

shown in **Table 2.4**. The deviation of the chemical composition indicates structural rearrangement within anatase nanoparticles. Even if single anatase phase was obtained after 5 h of reaction, structural rearrangement occurred continuously until 12 h of reaction, highlighting the metastable feature of the cation-defected anatase framework.

### 2.3.3. Evolution of fluorine environment

$^{19}F$ solid-state NMR spectroscopy was carried out to follow the local environment of fluorine during the synthesis. It is known that $TiOF_2$ generally shows corner-sharing $Ti(O/F)_6$ octahedra, in which $F^-$ coordinated with two $Ti^{4+}$. For the fluorinated anatase, however, 3 coordination modes of fluorine were demonstrated in Chapter II.1. **Figure 2.18a** shows the evolution of $^{19}F$ spectrum with respect to time of reaction. Three fluorine environments can be clearly distinguished by three resonances at ca. -90, 0 and 100 ppm, characteristic to $Ti_3$-F, $Ti_2\square_1$-F and $Ti_1\square_2$-F, respectively. The most intense peak at $^{19}F$ $\delta_{iso}$ ~ 0 ppm indicates a preferential coordination mode of fluorine in the solid. The presence of fluorine environment of $Ti_3$-F indicates that the anatase phase was fluorinated at the very early stage of the reaction, which is in good agreement with chemical analysis.

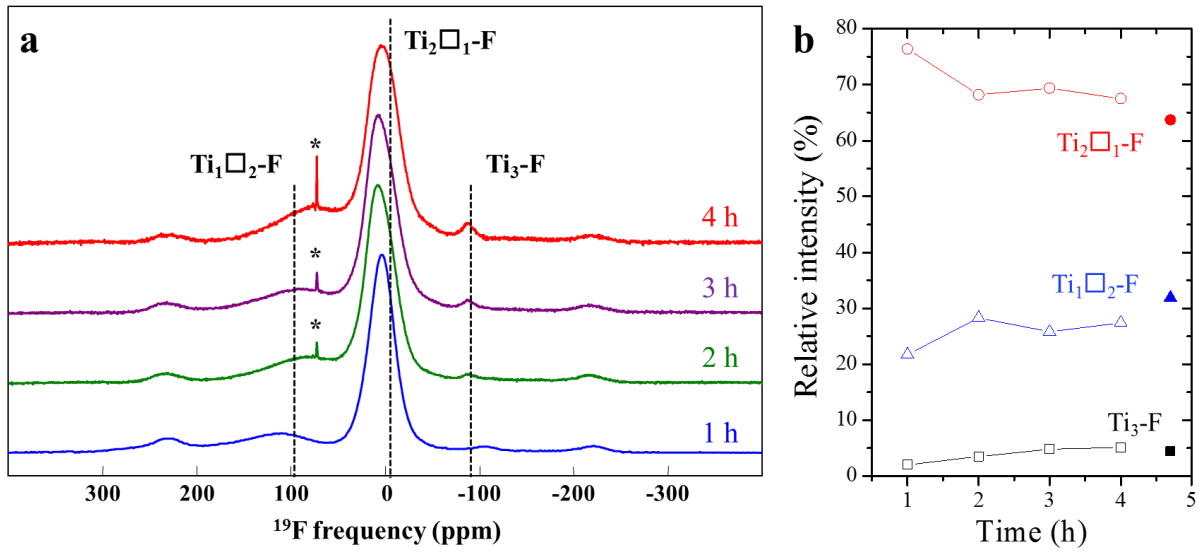


**Figure 2.18:** (a) $^{19}F$ solid-state NMR spectrum of the samples obtained after 1 h to 4 h of reaction (* marks impurity species; dot lines mark the $\delta_{iso}$ of fluorine for $Ti_{0.78}\square_{0.22}O_{1.12}F_{0.4}(OH)_{0.48}$). (b) Relative intensities of the three NMR lines. Solid symbols represent the relative intensities of the $^{19}F$ NMR lines for $Ti_{0.78}\square_{0.22}O_{1.12}F_{0.4}(OH)_{0.48}$.

**Figure 2.18b** shows evolution of the relative intensities of the three NMR lines obtained from the reconstruction of the $^{19}F$ NMR spectrum. The sample obtained after 1 h of

reaction contains 76.4 % of $Ti_2\square_1$-F, 21.7 % of $Ti_1\square_2$-F and 2 % $Ti_3$-F. The high concentration of $Ti_2\square_1$-F indicates that amorphous $TiOF_2$ phase is dominated by 2-fold fluorine. In such an amorphous phase, fluorine environment of $Ti_1\square_2$-F is possible, but remains at a low concentration. The intensity of $Ti_3$-F increased gradually with reaction time, which is likely due to the progressive appearance of the anatase phase.

Evolution of fluorine environment in the time-dependent anatase phase was studied. To do so, we attempt to calculate the proportion of fluorine of different coordination mode in the anatase phase. As amorphous $TiOF_2$ comprises bridging and/or terminal fluorine, we need to distinguish the contributions of bridging and terminal $F^-$ from the fluorine in the anatase phase. We assume two possibilities: (1) $TiOF_2$ comprises 100 % bridging fluorine; (2) 80 % bridging $F^-$ and 20 % terminal $F^-$.

For the case (1), the concentration of terminal and 3-fold $F^-$ in the anatase phase can be directly obtained by the relative intensities of the NMR lines. It should distinguish the contribution of bridging $F^-$ of $TiOF_2$ and anatase phase. By combining the PDF, $^{19}F$ NMR and chemical analyses, it can be obtained through the following equation:

$$F_b(TiO_2)\,\% = \frac{\left[\frac{F}{Ti}(solid) * F_b(solid)\,\% - \frac{F}{Ti}(TiOF_2) * F_b(TiOF_2)\,\% * \%\ molar\ of\ TiOF_2\right]}{\frac{F}{Ti}(TiO_2) * \%\ molar\ of\ TiO_2} \qquad (\boldsymbol{Eq.2.2})$$

Where $F_b$(X) % represents the proportion of bridging fluorine in phases, $F_b$(solid) % can be obtained from $^{19}F$ NMR analysis, $F_b(TiOF_2)$ % is 100 %. F/Ti (X) refers to the ratio between fluorine and titanium in different phases, where F/Ti (solid) and F/Ti (anatase) are shown in **Table 2.4**, F/Ti ($TiOF_2$) equals to 2. % molar of X is the molar proportion of phases. % molar of $TiO_2$ and % molar of $TiOF_2$ is shown in **Figure 2.16**.

The total proportion of fluorine in the anatase phase can be obtained:

$$F_{total}\,(TiO_2)\,\% = F_t\,(TiO_2)\,\% + F_3\,(TiO_2)\,\% + F_b(TiO_2)\,\% \qquad (\boldsymbol{Eq.2.3})$$

Where $F_t(TiO_2)$ % and $F_3(TiO_2)$ % refer to the proportion of the terminal fluorine ($Ti_1\square_2$-F) and 3-fold fluorine ($Ti_3$-F) in the anatase phase, respectively. They can be obtained from the relative intensity of the NMR lines.

For the case (2), in addition to $F_b(TiO_2)$ %, we need to calculate $F_t(TiO_2)$ %. It can be obtained using **Eq. 2.2** by replacing $F_b(X)$ % by $F_t(X)$ %. $F_3(TiO_2)$ % is directly obtained from the relative intensity of the NMR lines.

The evolution of fluorine proportion of different environment in the time-dependent anatase phase obtained for these two cases are showed in **Figure 2.19**. Similar trend can be observed for these two cases. Terminal $F^-$ ($Ti_1\square_2$-F) decreased from ~45 % after 2 h to ~32 % after 3 h and remained unchanged thereafter, whereas bridging $F^-$ ($Ti_2\square_1$-F) increased slightly from 2 h and remained unchanged after 3 h of reaction. $Ti_3$-F kept almost constant and remained at a low concentration during the reaction, indicating solubility limit for $Ti_3$-F in the anatase phase. The results confirm preferential location of fluorine close to vacancies in the defective anatase. The proportion of different $F^-$ environment remained unchanged after 3 h of reaction. However, the F/Ti in anatase significantly decreased from 0.97 (3 h) to 0.51 (12 h), indicating that defluorination reaction occurred simultaneously for the three fluorine environments.

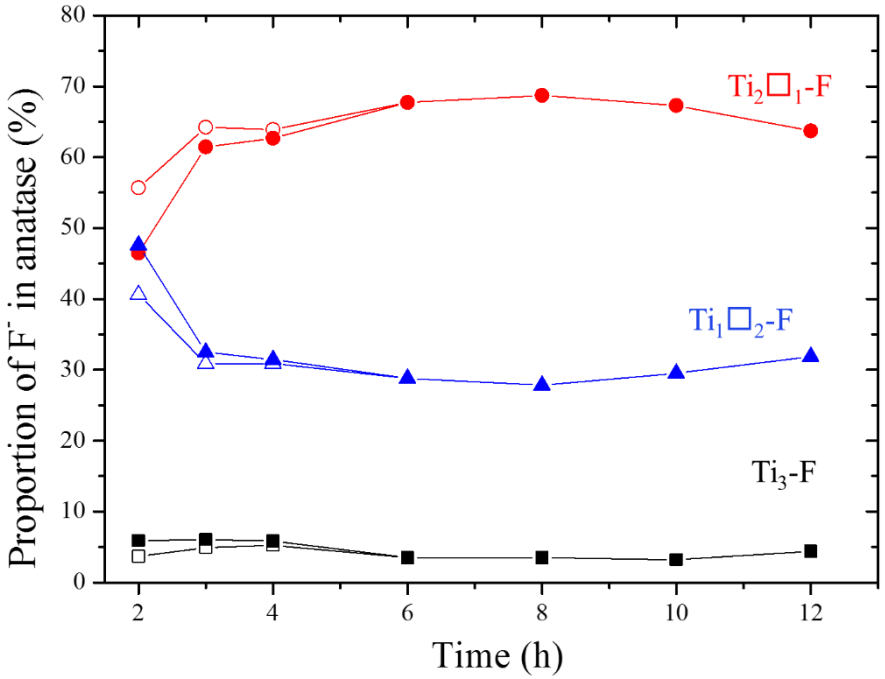


**Figure 2.19:** Evolution of relative concentration of fluorine in the time-dependent anatase phases. Solid and hollow symbols represent the results obtained from case (1) and (2), respectively.

## 2.3.4. Formation mechanism

According to the above results, the formation of $Ti_{0.78}\square_{0.22}O_{1.12}F_{0.4}(OH)_{0.48}$ can be divided into two steps: (1) dissolution/recrystallization of the intermediate phase $TiOF_2$; (2) structural rearrangement of fluorinated anatase nanoparticles.

The mechanism of the 1st step is illustrated in **Figure 2.20**. The sol-gel reaction was first initiated by adding aqueous HF in TTIP through hydrolysis and fluorolysis reactions. Further condensation led to the formation of amorphous $TiOF_2$. As the reaction progressed, $TiOF_2$ continuously dissolved into the solution and recrystallized to form crystalline fluorinated anatase nanoparticles. $TiOF_2$ has been commonly reported as intermediate[31,32] or precursor[33,34] for the elaboration of $TiO_2$ anatase. The formation of $TiOF_2$ at the beginning of the reaction indicates that titanium precursor is highly reactive towards fluorine. Fluorolysis very likely occurred simultaneously with hydrolysis. High reactivity of Ti precursor towards fluorine can be ascribed to that (i) fluorine has similar nucleophilicity with oxygen (partial charge: $\delta(F) = -0.42$ in HF, $\delta(O) = -0.4$ in $H_2O$), (ii) fluorolysis is favorable in acidic condition because this process involves protonation of the oxygen atom in alkoxy group (**Eq. 1.10**).[18]

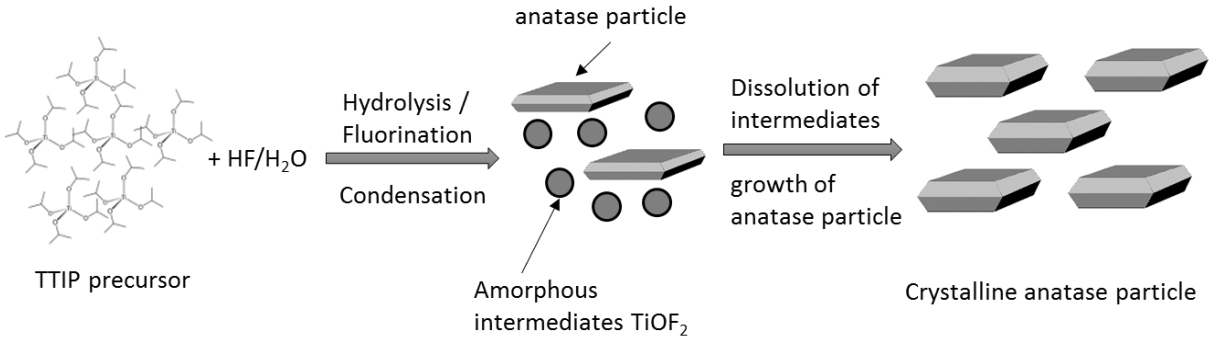


**Figure 2.20:** Formation mechanism of fluorinated anatase nanoparticles.

The 2nd step consists of structural rearrangement of the fluorinated anatase nanoparticles. Anatase nanoparticles remained at several nanometers during the reaction, indicating that the low temperature method is effective at inhibiting particle growth. The concentration of cation vacancies and monovalent anions in the anatase phase decreased with reaction time, indicating structural rearrangement of the anatase phase. Such rearrangement is dominated by the condensation reactions of $OH^-$ groups. Concomitantly, the anatase phase was defluorinated. The defluorination reaction occurred simultaneously for the three fluorine environments in anatase phase. It should be noted that structural rearrangement continued even after single anatase phase ($Ti_{0.63}\square_{0.37}O_{0.52}F_{0.51}(OH)_{0.97}$) was formed after 5 h of reaction,

leading to the formation of $Ti_{0.78}\square_{0.22}O_{1.12}F_{0.4}(OH)_{0.48}$ after 12 h of reaction. However, this phase is metastable, the concentration of vacancy and monovalent anions decreased continuously while the reaction time was prolonged to 120 h (results not shown).

### 2.3.5. Effect of temperature

The synthesis was performed at 150 °C to study the effect of reaction temperature on the formation mechanism of anatase phase. **Figure 2.21a** shows the evolution of the XRD patterns of the samples obtained after different reaction time at 150 °C. The XRD pattern of the sample obtained after 0.5 h of reaction can be indexed to $TiOF_2$ and $TiO_2$ anatase. $TiOF_2$ vanished after 1 h of reaction indicates that it acted as intermediate phase during the formation of anatase phase. The disappearance of $TiOF_2$ at 150 °C is faster than that at 90 °C, indicating that the dissolution/recrystallization processes of $TiOF_2$ is thermodynamically favored.

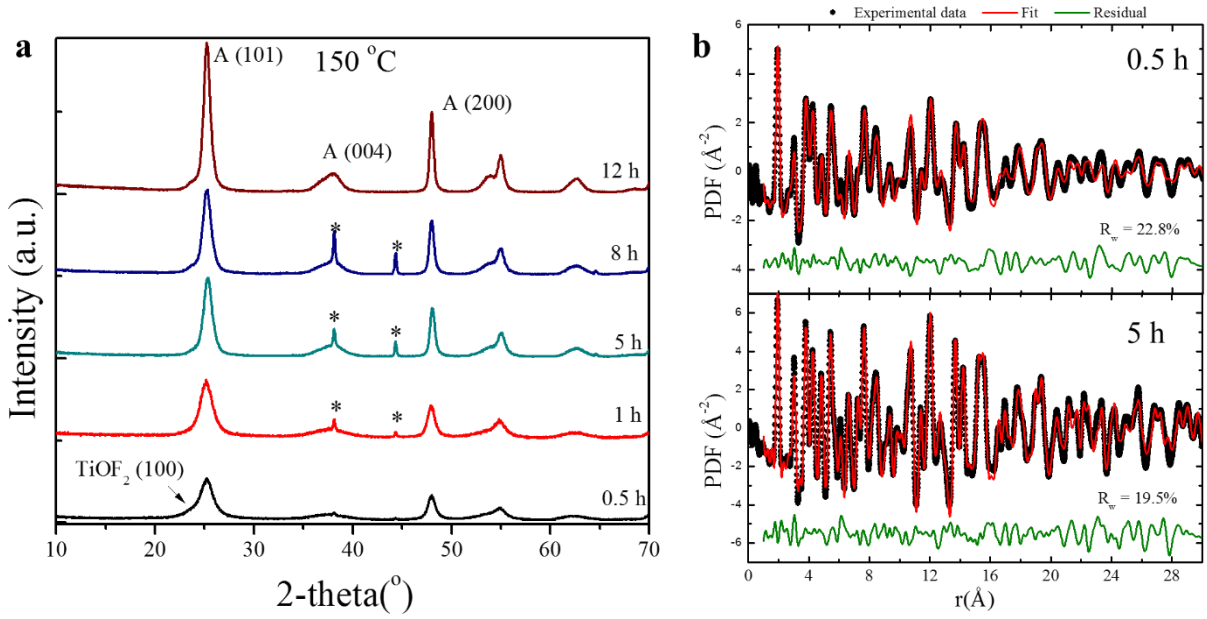


**Figure 2.21:** (a) Evolution of the XRD patterns of the time-dependent samples prepared at 150 °C. 'A' refers to anatase phase. Asterisk indicates reflections of sample holder. (b) PDF refinements of the samples obtained after 0.5 h and 5 h of reaction.

**Figure 2.21b** shows representative PDF refinements. The PDF of the sample obtained after 0.5 h of reaction was refined using a 2-phase refinement including $TiOF_2$ and $TiO_2$ anatase models. The refined sp-diameter of $TiOF_2$ is 9 (1) Å, confirming amorphous feature of $TiOF_2$. The PDF fit of the sample obtained after 5 h of reaction using $TiO_2$ anatase

structure yielded a good fit, indicating the formation of single phase crystalline anatase phase. The refined Ti occupancy is 82.6 %, indicating the presence of cation vacancies.

We then compare the evolution of cation vacancies and particle size of the time-dependent anatase phase prepared at 90 °C and 150 °C (**Figure 2.22**). For the anatase prepared at 90 °C, the concentration of cation vacancies decreased as a function of reaction time, which was caused by structural rearrangement. Similar trend can be observed for the anatase prepared at 150 °C, indicating that structural rearrangement of anatase phase can take place at higher temperature. Difference was observed regarding the particle size. The anatase particle size is independent with reaction time for the reaction at 90 °C, prolonging reaction time did not induce particle growth. However, for the reaction occurred at 150 °C, anatase particle grew from 4.3 nm after 0.5 h to 10.4 nm after 12 h of reaction. Such particle growth can be ascribed to Oswald ripening and/or oriented attachment occurring at high temperature.[14,35] The latter mechanism was confirmed by TEM analysis which will be detailed in Chapter III.2.6.

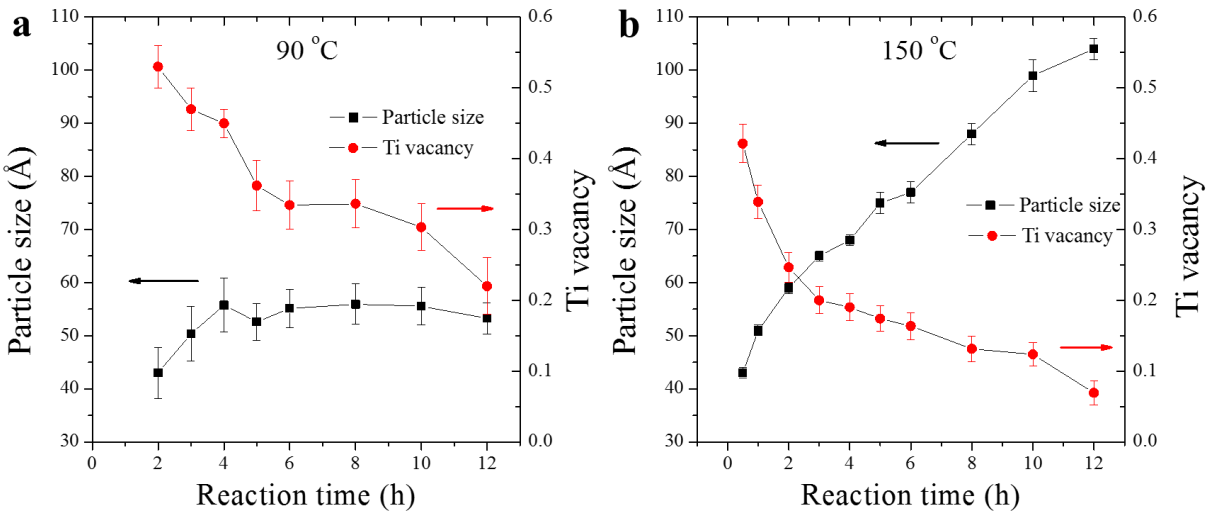


**Figure 2.22:** Evolution of particle size and cation vacancy in the time-dependent anatase phases prepared at 90 °C (a) and 150 °C (b).

It was shown that the formation mechanism of the anatase phase is similar at different reaction temperature. It involves two steps: dissolution and recrystallization of $TiOF_2$ and structural rearrangement of anatase phase with defluorination and dehydroxylation reactions. The former processes are favored at higher temperature. The high temperature can also favor particle growth of the anatase phase.

Some authors claimed that the anatase particles formed in the fluorine medium contain fluorine at the surface of particles.[9,14,36] Absence of the information of fluorine in the lattice might be due to the lack of high penetrating analytical techniques or the occurrence of complete defluorination reaction. The latter is promoted by higher reaction temperature and longer reaction time. Besides, it is worthy to point out that the chemical composition of the cation-defected fluorinated anatase can be controlled by adjusting reaction time. It is believed that increase of reaction time can reduce the concentration of cation vacancies and monovalent anions in anatase phase, thus providing the finest control over the chemical composition of the anatase phase.

# 3. Conclusion

In this chapter, sol-gel synthesis was performed in fluorine medium at 90 °C by using $Ti(OiPr)_4$ as precursor, $Pr^iOH$ as solvent and aqueous HF as fluoro/hydrolysis agent. The resulting phase show anatase framework with particle sizes of several nanometers. PDF analysis showed the presence of cation vacancies within the as-prepared anatase structure. Combining XPS, $^1H$ & $^{19}F$ NMR and thermogravimetric analyses, we determined its chemical composition: $Ti_{0.78}\square_{0.22}O_{1.12}F_{0.4}(OH)_{0.48}$. A large concentration of cation vacancies (22 %) was introduced into the anatase structure. The presence of vacancies is induced by the compensation of negative charge deficiency created by the replacement of divalent anion $O^{2-}$ by monovalent anions $F^-/OH^-$. Both cationic and anionic modifications indicate the compositional and structural versatility of the anatase framework.

Significant deviation of the chemical composition indicates high substitutional disorder within the cation-defected anatase. The structure disorder is highlighted by the three coordination modes of fluorine with Ti ($Ti_3$-F, $Ti_2\square_1$-F and $Ti_1\square_2$-F), with a preferential location of $F^-$ around cation vacancy. DFT calculations using $Ti_{127}\square_1F_4O_{252}$ supercell confirmed such vacancy/fluorine ordering, as the system energy decreased as a function of the number of fluorine surrounding vacancy. Our work shows that Ti-based compounds can be drastically modified, achieving metastable composition, while keeping the same crystallographic structure. The results provide a simple and effective method of synthesizing defective materials.

In the second part, the formation mechanism of $Ti_{0.78}\square_{0.22}O_{1.12}F_{0.4}(OH)_{0.48}$ was studied time-dependently. A two-step process was proposed. The titanium precursor is highly reactive towards fluorine, leading to the formation of amorphous $TiOF_2$ at the beginning of the reaction. Dissolution of $TiOF_2$ and the recrystallization on anatase framework was directly observed by PDF analysis. Combining chemical analysis and the PDF refinement, the chemical composition of the time-dependent anatase phase was calculated. The anatase phase obtained after 2 h of reaction ($Ti_{0.50}\square_{0.50}F_{0.47}(OH)_{1.53}$) contained high concentration of cation vacancies and monovalent anions, i.e. $OH^-$, $F^-$. They decreased progressively as a function of reaction time, indicating structural rearrangement of the anatase phase. Such process occurred even if single anatase phase was formed after 5 h of reaction, highlighting the metastable nature of the cation-defected anatase. The structural rearrangement accompanied with

variation of chemical composition of the anatase is dominated by dehydroxylation process through condensation reactions. More insights into fluorine local environments showed that anatase phase was fluorinated at the beginning of the reaction. The defluorination of the anatase phase occurred simultaneously for fluorine with different environment. The two-step formation mechanism of cation-defected anatase is also suitable for the reaction performed at higher temperature, e.g. 150 °C. The dissolution/recrystallization processes are thermodynamically favored. High temperature can also induce significant particle growth of anatase phase. Our study provides a comprehensive understanding of what happens in solution-based synthesis performed in fluorine medium. Control over chemical composition and particle size of cation-defected anatase can be achieved by changing reaction time.

# References

(1) Fujishima, A.; Honda, K. Electrochemical Photolysis of Water at a Semiconductor Electrode. *Nature* **1972**, *238*, 37.

(2) O'regan, B.; Grätzel, M. A low-cost, high-efficiency solar-cell based on dye-sensitized colloidal $TiO_2$ films. *Nature* **1991**, *353*, 737.

(3) Grätzel, M. Photoelectrochemical cells. *Nature* **2001**, *414*, 338.

(4) Kavan, L.; Grätzel, M.; Gilbert, S. E.; Klemenz, C.; Scheel, H. J. Electrochemical and Photoelectrochemical Investigation of Single-Crystal Anatase. *J. Am. Chem. Soc.* **1996**, *118*, 6716.

(5) Khan, S. U. M.; Al-Shahry, M.; Ingler, W. B. Efficient photochemical water splitting by a chemically modified n-$TiO_2$. *Science* **2002**, *297*, 2243.

(6) Chen, X.; Mao, S. S. Titanium dioxide nanomaterials: Synthesis, properties, modifications, and applications. *Chem. Rev.* **2007**, *107*, 2891.

(7) Fattakhova-Rohlfing, D.; Zaleska, A.; Bein, T. Three-Dimensional Titanium Dioxide Nanomaterials. *Chem. Rev.* **2014**, *114*, 9487.

(8) Liu, G.; Yang, H. G.; Pan, J.; Yang, Y. Q.; Lu, G. Q.; Cheng, H.-M. Titanium Dioxide Crystals with Tailored Facets. *Chem. Rev.* **2014**, *114*, 9559.

(9) Yang, H. G.; Sun, C. H.; Qiao, S. Z.; Zou, J.; Liu, G.; Smith, S. C.; Cheng, H. M.; Lu, G. Q. Anatase $TiO_2$ single crystals with a large percentage of reactive facets. *Nature* **2008**, *453*, 638.

(10) Yu, J. C.; Yu, J. G.; Ho, W. K.; Jiang, Z. T.; Zhang, L. Z. Effects of $F^-$ doping on the photocatalytic activity and microstructures of nanocrystalline $TiO_2$ powders. *Chem. Mater.* **2002**, *14*, 3808.

(11) Czoska, A. M.; Livraghi, S.; Chiesa, M.; Giamello, E.; Agnoli, S.; Granozzi, G.; Finazzi, E.; Di Valentin, C.; Pacchioni, G. The nature of defects in fluorine-doped $TiO_2$. *J. Phys. Chem. C* **2008**, *112*, 8951.

(12) De Angelis, F.; Di Valentin, C.; Fantacci, S.; Vittadini, A.; Selloni, A. Theoretical Studies on Anatase and Less Common $TiO_2$ Phases: Bulk, Surfaces, and Nanomaterials. *Chem. Rev.* **2014**, *114*, 9708.

(13) Li, W.; Corradini, D.; Body, M.; Legein, C.; Salanne, M.; Ma, J.; Chapman, K. W.; Chupas, P. J.; Rollet, A.-L.; Julien, C.; Zaghib, K.; Duttine, M.; Demourgues, A.; Groult, H.; Dambournet, D. High Substitution Rate in $TiO_2$ Anatase Nanoparticles with Cationic Vacancies for Fast Lithium Storage. *Chem. Mater.* **2015**, *27*, 5014.

(14) Menzel, R.; Duerrbeck, A.; Liberti, E.; Yau, H. C.; McComb, D.; Shaffer, M. S. P. Determining the Morphology and Photocatalytic Activity of Two-Dimensional Anatase Nanoplatelets Using Reagent Stoichiometry. *Chem. Mater.* **2013**, *25*, 2137.

(15) Billinge, S. J. L.; Levin, I. The problem with determining atomic structure at the nanoscale. *Science* **2007**, *316*, 561.

(16) Egami, T.; Billinge, S. J. L. *Underneath the Bragg Peaks: Structural Analysis of Complex Materials*; Pergamon Press: Oxford, 2004.

(17) Farrow, C. L.; Juhas, P.; Liu, J. W.; Bryndin, D.; Bozin, E. S.; Bloch, J.; Proffen, T.; Billinge, S. J. L. PDFfit2 and PDFgui: computer programs for studying nanostructure in crystals. *J. Phys.: Condens. Matter* **2007**, *19*, 335219.

(18) Rudiger, S.; Kemnitz, E. The fluorolytic sol-gel route to metal fluorides-a versatile process opening a variety of application fields. *Dalton Trans.* **2008**, 1117.

(19) Biswal, M.; Body, M.; Legein, C.; Sadoc, A.; Boucher, F. $NbF_5$ and $TaF_5$: Assignment of $^{19}F$ NMR resonances and chemical bond analysis from GIPAW calculations. *J. Solid State Chem.* **2013**, *207*, 208.

(20) Ren, Y.; Liu, Z.; Pourpoint, F.; Armstrong, A. R.; Grey, C. P.; Bruce, P. G. Nanoparticulate $TiO_2$(B): An Anode for Lithium-Ion Batteries. *Angew. Chem. Int. Ed.* **2012**, *51*, 2164.

(21) Walton, R. I. Subcritical solvothermal synthesis of condensed inorganic materials. *Chem. Soc. Rev.* **2002**, *31*, 230.

(22) Cargnello, M.; Gordon, T. R.; Murray, C. B. Solution-Phase Synthesis of Titanium Dioxide Nanoparticles and Nanocrystals. *Chem. Rev.* **2014**, *114*, 9319.

(23) Sang, L.; Zhao, Y.; Burda, C. TiO2 Nanoparticles as Functional Building Blocks. *Chem. Rev.* **2014**, *114*, 9283.

(24) Kapilashrami, M.; Zhang, Y.; Liu, Y.-S.; Hagfeldt, A.; Guo, J. Probing the Optical Property and Electronic Structure of $TiO_2$ Nanomaterials for Renewable Energy Applications. *Chem. Rev.* **2014**, *114*, 9662.

(25) Ong, W.-J.; Tan, L.-L.; Chai, S.-P.; Yong, S.-T.; Mohamed, A. R. Highly reactive {001} facets of $TiO_2$-based composites: synthesis, formation mechanism and characterization. *Nanoscale* **2014**, *6*, 1946.

(26) Yu, J.; Xiang, Q.; Ran, J.; Mann, S. One-step hydrothermal fabrication and photocatalytic activity of surface-fluorinated $TiO_2$ hollow microspheres and tabular anatase single micro-crystals with high-energy facets. *CrystEngComm* **2010**, *12*, 872.

(27) Kemnitz, E.; Groß, U.; Rüdiger, S.; Shekar, C. S. Amorphous Metal Fluorides with Extraordinary High Surface Areas. *Angew. Chem. Int. Ed.* **2003**, *42*, 4251.

(28) Ruediger, S. K.; Gro; Feist, M.; Prescott, H. A.; Shekar, S. C.; Troyanov, S. I.; Kemnitz, E. Non-aqueous synthesis of high surface area aluminium fluoride-a mechanistic investigation. *J. Mater. Chem.* **2005**, *15*, 588.

(29) Billinge, S. J. L.; Kanatzidis, M. G. Beyond crystallography: the study of disorder, nanocrystallinity and crystallographically challenged materials with pair distribution functions. *Chem. Commun.* **2004**, 749.

(30) Chaudhuri, S.; Chupas, P.; Morgan, B. J.; Madden, P. A.; Grey, C. P. An atomistic MD simulation and pair-distribution-function study of disorder and reactivity of [small alpha]-AlF3 nanoparticles. *Phys. Chem. Chem. Phys.* **2006**, *8*, 5045.

(31) Wen, C. Z.; Zhou, J. Z.; Jiang, H. B.; Hu, Q. H.; Qiao, S. Z.; Yang, H. G. Synthesis of micro-sized titanium dioxide nanosheets wholly exposed with high-energy {001} and {100} facets. *Chem. Commun.* **2011**, *47*, 4400.

(32) Ding, X.; Hong, Z.; Wang, Y.; Lai, R.; Wei, M. Synthesis of square-like anatase $TiO_2$ nanocrystals based on $TiOF_2$ quantum dots. *J. Alloys Compd.* **2013**, *550*, 475.

(33) Wen, C. Z.; Hu, Q. H.; Guo, Y. N.; Gong, X. Q.; Qiao, S. Z.; Yang, H. G. From titanium oxydifluoride (TiOF2) to titania (TiO2): phase transition and non-metal doping with enhanced photocatalytic hydrogen (H2) evolution properties. *Chem. Commun.* **2011**, *47*, 6138.

(34) Chen, L.; Shen, L.; Nie, P.; Zhang, X.; Li, H. Facile hydrothermal synthesis of single crystalline TiOF2 nanocubes and their phase transitions to TiO2 hollow nanocages as anode materials for lithium-ion battery. *Electrochim. Acta* **2012**, *62*, 408.

(35) Wang, F.; Richards, V. N.; Shields, S. P.; Buhro, W. E. Kinetics and Mechanisms of Aggregative Nanocrystal Growth. *Chem. Mater.* **2014**, *26*, 5.

(36) Gordon, T. R.; Cargnello, M.; Paik, T.; Mangolini, F.; Weber, R. T.; Fornasiero, P.; Murray, C. B. Nonaqueous Synthesis of $TiO_2$ Nanocrystals Using $TiF_4$ to Engineer Morphology, Oxygen Vacancy Concentration, and Photocatalytic Activity. *J. Am. Chem. Soc.* **2012**, *134*, 6751.

# Chapter III: Structural, compositional and morphological impacts of the sol-gel synthesis parameters for the preparation of $TiO_2$-based compounds in a fluorinating medium

In the previous chapter, a polyanionic titanium-based anatase framework was synthesized by a solvothermal method. The non-stoichiometric compound $Ti_{0.78}\square_{0.22}O_{1.12}F_{0.4}(OH)_{0.48}$ contains a high concentration of cation vacancies and polyanions. Here, we systematically investigate the influence of synthetic parameters on the structure, composition and morphology of the cation-defected anatase.

## 1. Experimental method

In this part, we systematically studied the effect of synthesis parameters on the products obtained from reaction between titanium alkoxides precursors and hydrofluoric acid under solvothermal condition. The following parameters which can influence the structure and chemical composition of the resulting phases were varied: the fluorine content (molar ratio between fluorine and titanium, denoted as 'R' thereafter), the nature of the titanium precursor and solvent, the hydrolysis rate (molar ratio between $H_2O$ and titanium, denoted as 'h'), the reactant concentration and the reaction temperature.

Three different titanium alkoxides (Sigma-Aldrich) were used as precursor: titanium ethoxide ($Ti(OCH_2CH_3\}_4$, $Ti(OEt)_4$, TTE); titanium isopropoxide ($Ti\{OCH(CH_3)_2\}_4$, $Ti(O^iPr)_4$, TTIP) and titanium butoxide ($Ti(OCH_2CH_2CH_2CH_3)_4$, $Ti(OBu)_4$, TTB). The solvents used are ethanol (EtOH), isopropanol ($Pr^iOH$) and 2-butanol (2-BuOH). F/Ti was varied from 1.0 to 4.0. Deionized water was used to tune the hydrolysis rate. The reactant concentration (referred as the concentration of precursor) was tuned from 0.11 to 0.90 $mol.L^-$

[1]. The reaction temperature was varied from 90 °C to 190 °C. Syntheses were typically performed at a reactant concentration of 0.45 mol.$L^{-1}$ at 90 °C without additional water added. In this case, 13.5 mmol titanium alkoxide precursor was poured inside a Teflon liner cup, then a solution containing aqueous hydrofluoric acid and alcohol was added under stirring. The volume of HF added in the synthesis depends on the molar ratio of (R = F/Ti). The volume of the alcohol was adjusted, so the total volume of the solution equals 30 ml. The mixed solution was placed inside an autoclave hermetically closed and then heated in an oven for 12 h at 90 °C. After the reaction, the autoclave was left to cool down at room temperature. The resulting white precipitate was washed twice by ethanol and subsequently centrifuged at 4400 rpm for 15 min. After drying in an oven at 80 °C for 2 h, the obtained white crystals were grinded to powder for further characterization.

# 2. Results and Discussion

## 2.1. Effect of the nature of the solvent

It is well-known that solvents can strongly influences the hydrolysis and condensation reactions of alkoxide precursors.[1-3] Different solvents were used to probe its impact on the structural features of the obtained precipitates. The molar ratio R was set to 2 and TTIP was used as precursor while the used solvents were EtOH, $Pr^{i}OH$ and 2-BuOH. **Figure 3.1** presents the evolution of the XRD patterns of the samples obtained using different solvents. The samples prepared with ethanol and isopropanol display a similar XRD pattern which was indexed with a tetragonal unit cell (space group: $I4_1/amd$) characteristic of $TiO_2$ anatase. The sample prepared using 2-butanol presents different diffraction peaks. The peaks located at 2θ = 13.8°, 23.5° and 27.8° can be respectively assigned to (101), (002) and (200) plans of a titanium oxyhydroxyfluoride with hexagonal tungsten bronze (HTB) framework (space group: ($P6_3/mmc$).[4] The chemical composition of the reported HTB-type phase is $Ti_{0.75}O_{0.25}(OH)_{1.3}F_{1.2}$. The peak at 2θ = 15.1° indicates the presence of another phase which can be attributed to the (200) plane of $TiO_2$-B (Space group: C2/m).

Fluorine elemental analysis using $^{19}F$ solid NMR permits fluorine quantification of the resulting anatase phases. The anatase phases prepared in ethanol and isopropanol contain 7.8

and 10.8 wt. % of fluorine, respectively. Fluorine concentration in the HTB-type phase can be calculated based on its chemical composition, that is, 26.9 wt. % of fluorine in the HTB-type phase. It is shown that the longer the alkyl chains of the solvent, the higher the fluorine concentration in the resulting phases.

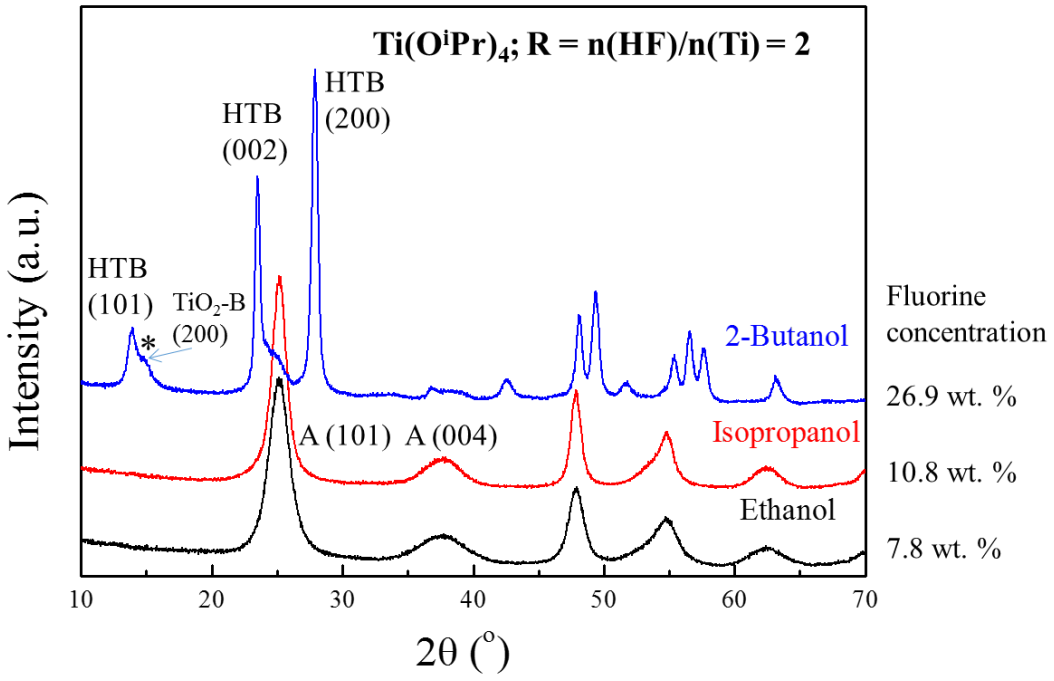


**Figure 3.1:** Evolution of the X-ray diffraction patterns of the samples prepared in different alcohol solvent using titanium isopropoxide as precursor and a molar ratio R = 2. 'A' refers to anatase phase; asterisk refers to (200) planes of $TiO_2$-B.

The results of the XRD analysis demonstrate that solvents play a key role on the reactivity of titanium precursor. Particularly, the alkoxide reactivity towards fluorine is strongly affected by the solvent since 2-butanol medium enabled the stabilization of a fluoride-rich phase, while ethanol and isopropanol stabilized oxide-rich phases. Such a different can be rationalized by ligand interchange between titanium alkoxide and the solvent.[2,5] This reaction, known as alcohol interchange reaction, can be expressed as:

$$Ti(OR)_n + xR'OH \rightarrow Ti(OR)_{n-x}(OR')_x + xROH \qquad \textbf{(Eq. 3.1)}$$

Due to the high electrophilic character of titanium, the alcohol interchange reaction takes place instantaneously.[1] This process modifies the structure of alkoxide precursor at a molecular level, consequently affecting its reactivity.

The formation of fluoride-rich compound in 2-butanol indicates a higher reactivity of $Ti(OBu)_4$ towards fluorine. It has been reported that the reactivity of alkoxides towards water increases while the length of the alkyl chains decreases: $Ti(OEt)_4 > Ti(O^iPr)_4 > Ti(OBu)_4$.[3,6] The difference in reactivity can be explained as follows: (i) shorter alkyl chains lead to the increase of the positive partial charge of Ti, thus becoming more reactive towards nucleophilic attack; (ii) long alkyl chains exert steric hindrance during the nucleophilic substitution. The rate of hydrolysis reaction decreases while the size of alkoxy group increases. The fluorolysis reaction (**Eq. 1.9-11**) shows similar mechanism with hydrolysis.[7] Thus, the increase of the size of alkoxy group can also decreases its rate. Experimentally, the reactivity of alkoxide precursor towards fluorine increased with the length of alkoxy chains, indicating that fluorolysis is relatively more favorable than hydrolysis for larger alkoxy chains. Moreover, changes of hydro/fluorolysis rate modify the functionality of precursor, affecting the condensation processes, and finally leading to the formation of the phases with different structure and chemical composition.

## 2.2. Nature of the alkoxide precursor

Similarly to solvent, the impact of the nature of the alkoxide precursor on the stabilized crystal structure was investigated. Two syntheses were conducted by fixing the fluorine content (R = 2) and using 2-butanol as solvent, while changing the nature of the alkoxide precursor. **Figure 3.2** displays the evolution of the XRD patterns of the samples prepared using $Ti(OBu)_4$ and $Ti(O^iPr)_4$ as precursor. The two samples show almost similar diffraction patterns which can be indexed with the HTB (majority contribution) and $TiO_2$-B (minority contribution) phases. Hence, the nature of the alkoxide precursor has little structural and compositional influences. This is in agreement with the above results showing that the solvent dictates the reactivity of alkoxide through alcohol interchange reaction.

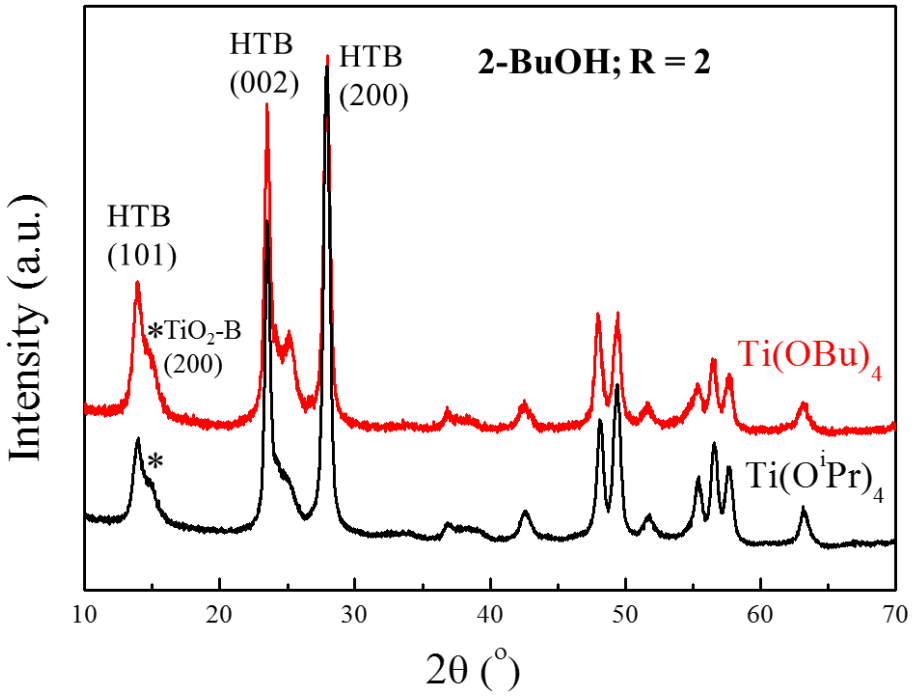


**Figure 3.2:** Evolution of X-ray diffraction patterns of the samples prepared using two different alkoxide precursor. The solvent and fluorine content are 2-butanol and R = 2, respectively. Asterisk refers to (200) planes of $TiO_2$-B.

## 2.3. The fluorine content (R)

In this section, we investigated the structural impact of the fluorine content. Since in parts 2.1 and 2.2, we have shown that the reactivity of titanium alkoxide was altered by the solvent molecule, we systematically investigated the impact of the fluorine content in different solvents.

### 2.3.1. In isopropanol

Syntheses using $Ti(O^iPr)_4$ as precursor and its parent alcohol, isopropanol, as solvent were first carried out to study the effect of the fluorine content. The molar ratio R = F/Ti was tuned from 1.0 to 3.7. **Figure 3.3** shows the evolution of the XRD patterns of the samples obtained by adjusting the fluorine content. Four domains can be distinguished: (i) $R < 2.2$, (ii) $2.2 \leq R \leq 2.4$, (iii) $2.6 \leq R \leq 3.5$, and (iv) $R = 3.7$. For $R < 2.2$, XRD patterns are indexed with a tetragonal cell (space group: $I4_1/amd$) characteristic of $TiO_2$ anatase. The increase of R to 2.2 led to the appearance of a peak located at $2\theta = 27.8°$. This peak became more pronounced at R = 2.4 and can be indexed with the HTB-type structure (space group: $P6_3/mmc$).[4] The

HTB phase continuously grew while R increased. The anatase phase disappeared at R = 2.6. Concomitantly, a peak located at 2θ = 15.1°, assigned to (200) plans of $TiO_2$-B, first appeared and tended to vanish while R increased. An almost pure HTB-type phase was obtained at R = 3.7. Thus, structural changes from anatase to a fluorinated framework related to the HTB phase was obtained by changing the fluorine content R. Further increasing R to 4.0 did not result in any precipitate, which is due to the formation of soluble titanium fluorides complexes.[8]

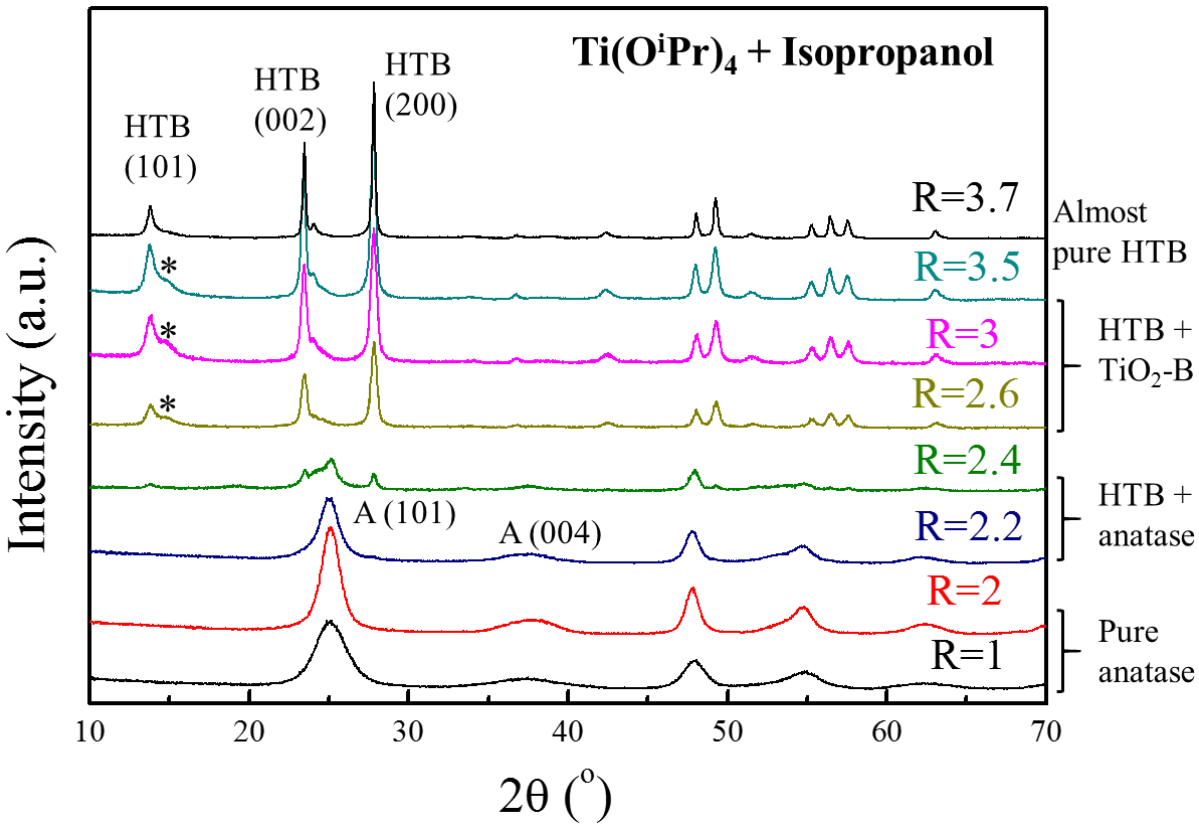


**Figure 3.3:** Evolution of the XRD patterns as a function of the molar ratio R = F/Ti. The precursor and solvent used were titanium isopropoxide and isopropanol, respectively. 'A' refers to anatase phase. Asterisk refers to (200) planes of $TiO_2$-B.

To gain further insights into fluorine local environment, magic-angle $^{19}F$ NMR spectroscopy was used on the samples prepared with different fluorine content. The evolution of the fluorine local environment while adjusting the fluorine content was monitored by the corresponding $^{19}F$ NMR spectrums which are gathered in **Figure 3.4**. We can distinguish two domains: R ≤ 2.4 and R ≥ 2.6. For R ≤ 2.4, NMR spectra show three fluorine environments characterized by three resonances located at ca. 90, 0 and -80 ppm, which can be assigned to the fluorine coordinated with 1 ($Ti_1\square_2$-F), 2 ($Ti_2\square_1$-F) and 3 ($Ti_3$-F) titanium atoms in the

structure of cation-defected anatase, respectively. The results confirm the presence of cation vacancies and fluorine in the anatase phase. For R = 2.4, it is clearly shown that the intensity of the resonances of $Ti_1\square_2$-F and $Ti_3$-F decreased, which is due to the decrease of anatase phase as shown by XRD analysis. For R ≥ 2.6, however, only the NMR line of $Ti_2\square_1$-F can be observed, indicating that, in the HTB phase, one fluorine atom coordinates with two titanium atoms. This is consistent with the structure of the HTB phase where $TiX_6$ ($X = O^{2-}$, $OH^-$, $F^-$) octahedra are corner-shared (**Figure 3.5**).[4]

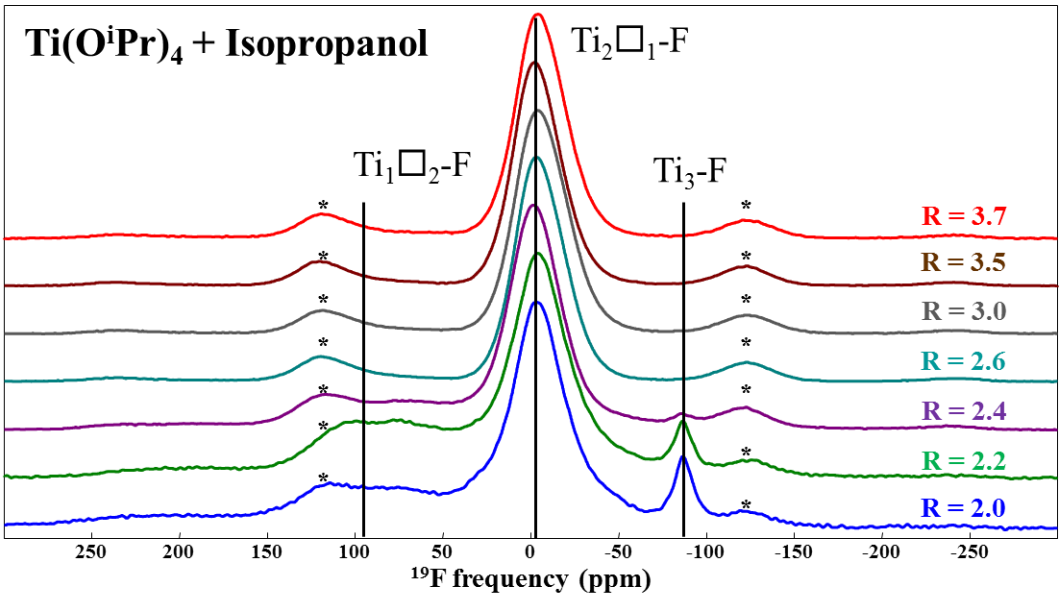


**Figure 3.4:** Evolution of $^{19}F$ solid state NMR spectrums as a function of R for the materials prepared using $Ti(O^iPr)_4$ and isopropanol (Asterisk refers to first spinning sidebands of the (main) isotropic line).

Fluorine-driven phase change from oxide-rich anatase to fluoride-rich HTB can be rationalized by the connection mode of $TiX_6$ octahedral subunits. The hydrolysis and fluorolysis reactions were initiated by adding aqueous HF in the TTIP solution, leading to the formation of $TiX_6$ octahedra. These octahedra connected with each other through condensation reactions and a macromolecular framework is thus formed. Its structure depends on the assembling pathway of the octahedral subunits. Due to the fact that fluorine atoms prefer a 2-fold coordination, increasing fluorine content favors fluorolysis, leading to much fluorinated octahedra subunits, thus increasing the probability of corner-sharing. Octahedra in the structure of anatase and HTB are shared by edge and corner, respectively (**Figure 3.5)**. $TiO_2$-B contains octahedra shared by both corner and edge. Therefore, when the fluorine content increased, $TiO_2$-B would mediate the phase transition from anatase to HTB.

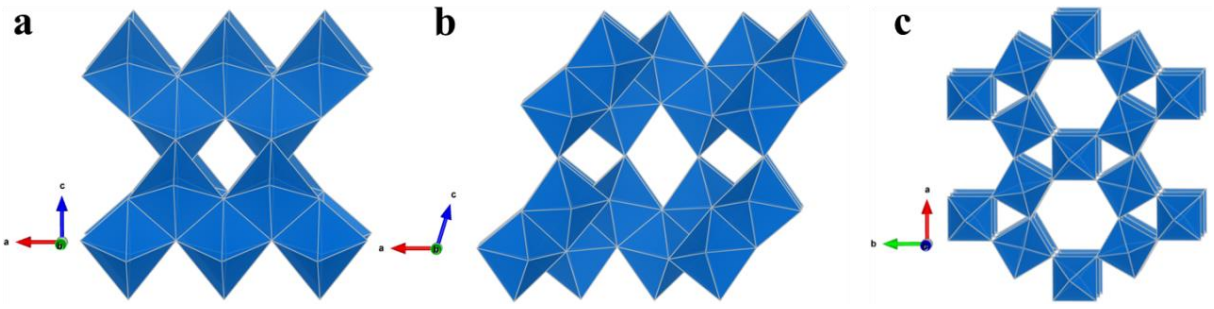


**Figure 3.5:** Structural representation of (a) $TiO_2$ anatase, (b) $TiO_2$-B and (c) hexagonal tungsten bronze (HTB) framework.

The above study showed that fluorine content dictates the structure of the Ti-based compounds. It has been reported that anions play a decisive role on the precipitation processes of metal oxides, strongly affecting the particle size and morphology.[6] The impact of fluorine anion on the size and morphology of $TiO_2$ particles has been widely demonstrated.[8-10] **Figure 3.6** shows transmission electron micrographs of the samples prepared at different fluorine content. For R = 1, aggregated anatase particles were observed with crystalline size of ca. 3.5 nm (**Figure 3.6a**). The HTB phase obtained at R = 3.7 shows crystals with crystalline size of ca. 50 nm (**Figure 3.6b**). The results indicate that the phase change from anatase to HTB was accompanied with a morphological evolution. High fluorine content promotes the crystallization process of HTB phase.

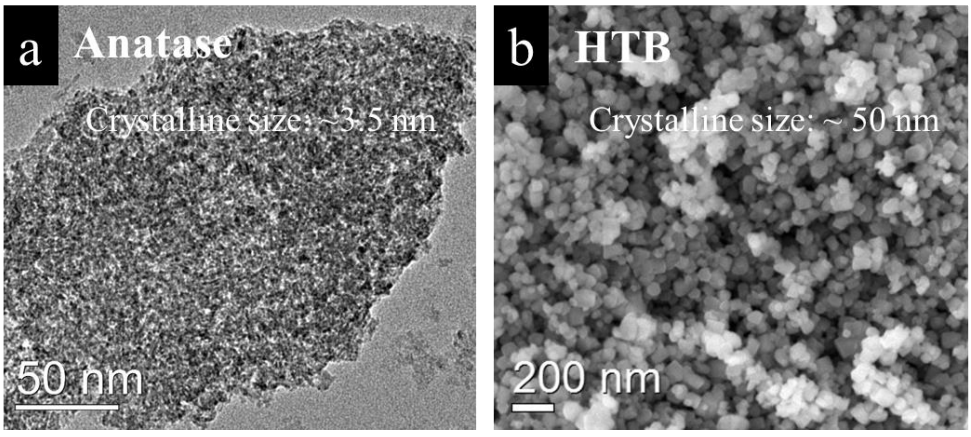


**Figure 3.6:** TEM (a) and SEM (b) images of the anatase and HTB phases, respectively.

### 2.3.2. In 2-butanol

The effect of fluorine content (R = F/Ti) was studied in the solvent of 2-butanol. Syntheses using $Ti(OBu)_4$ as precursor and its parent alcohol, 2-butanol, as solvent were

carried out with adjusting fluorine content from 1.0 to 3.7. **Figure 3.7** shows the evolution of the XRD patterns of the samples obtained at different R. Three domains can be distinguished: (i) R = 1; (ii) 2 ≤ R ≤ 3.5; (iii) R = 3.7. XRD pattern of the sample obtained at R = 1 was indexed with a tetragonal symmetry (space group: $I4_1/amd$) characteristic of $TiO_2$ anatase. When the R increased to 2.0, the anatase phase vanished and the XRD patterns of the newly formed phase can be indexed with HTB-type structure (space group: $P6_3/mmc$). Concomitantly, a peak located at 2θ = 15.1° appeared and can be assigned to $TiO_2$-B. It decreased progressively while R increased. The intensity of the XRD reflections of the HTB phase increased with R, indicating that higher crystallinity of the HTB phase was obtained. For R = 3.7, sharp XRD reflections indicate the stabilization of well crystallized HTB phase. No precipitate was obtained at R = 4.0, which is due to the formation of soluble complexes at high fluorine content.

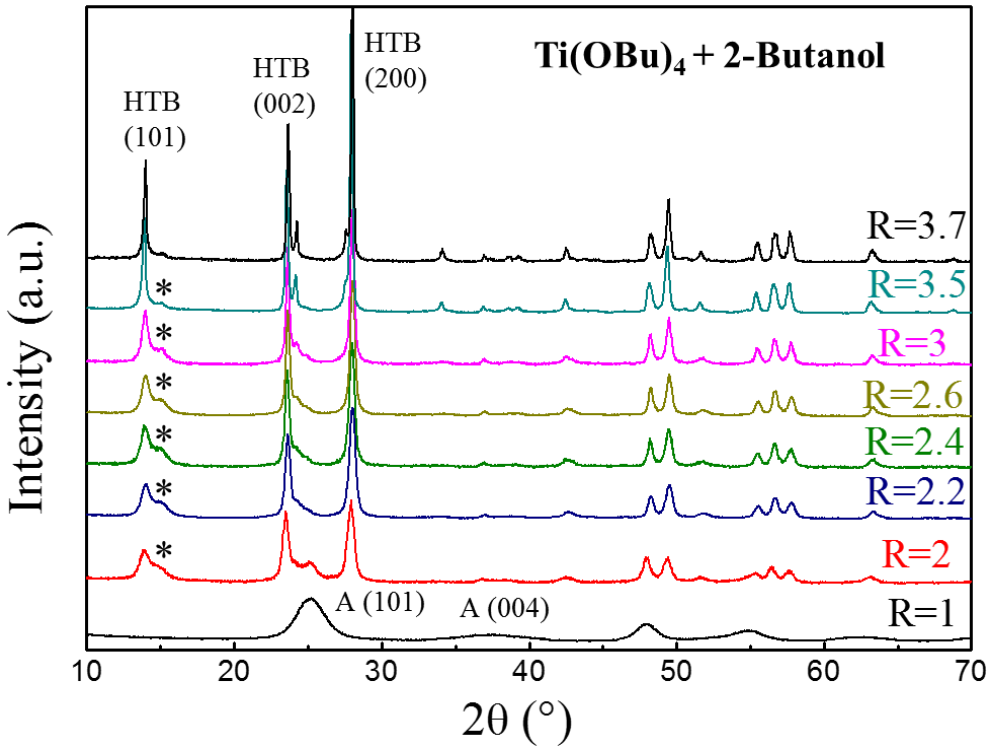


**Figure 3.7:** Evolution of the XRD patterns as a function of the molar ratio R = F/Ti. The precursor and solvent used were $Ti(OBu)_4$ and 2-butanol, respectively. 'A' refers to anatase phase. Asterisk refers to (200) planes of $TiO_2$-B.

XRD analysis indicates that $Ti(O^iPr)_4$ and $Ti(OBu)_4$ showed different reactivity towards fluorine in their parent alcohol solvent. While the fluorine content increased, phase transition from anatase to HTB can be observed. This phase change occurred at relatively lower fluorine content for $Ti(OBu)_4$, indicating that $Ti(OBu)_4$ is more reactive towards

fluorine. The reason is ascribed to that long alkyl chain in $Ti(OBu)_4$ lowered the rate of the hydrolysis reaction,[6] favoring the fluorolysis reaction, thus leading to the crystallization of HTB-type phase.

### 2.3.3. In ethanol

In this part, the effect of fluorine content was investigated by using $Ti(OEt)_4$ and ethanol as the precursor and solvent, respectively. The molar ratio R = F/Ti was varied from 1.0 to 3.0. **Figure 3.8** displays the evolution of the XRD patterns of the samples obtained at different R. All the samples show same diffraction patterns which were indexed with a tetragonal cell characteristic of $TiO_2$ anatase. Further increase of R to 3.5 led to the formation of soluble complexes. Thus, fluorine content has little impact on the structure of the phases formed in the solvent of ethanol.

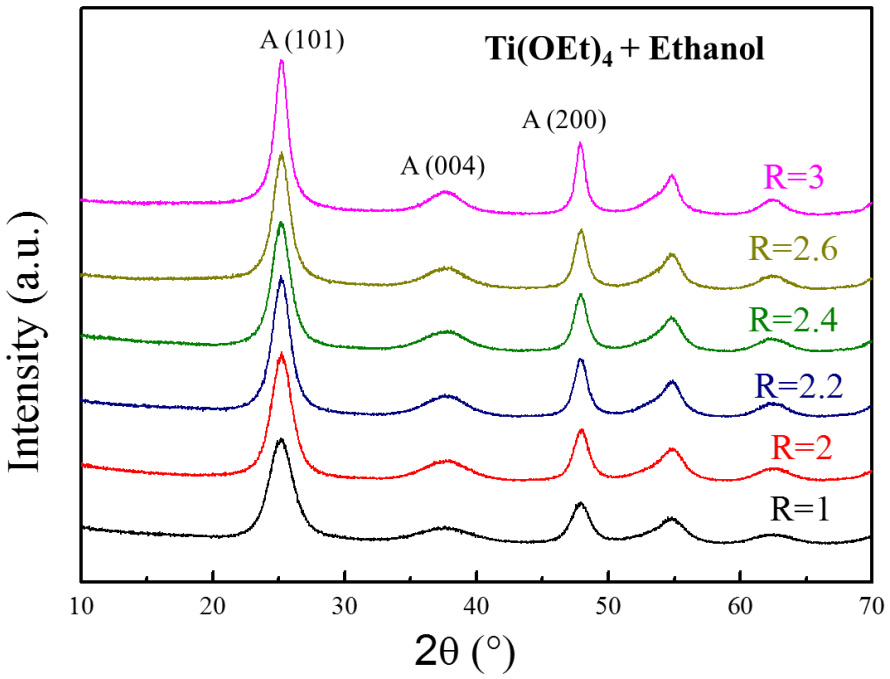


**Figure 3.8:** Evolution of the XRD patterns as a function of the molar ratio R = F/Ti. The precursor and solvent used were $Ti(OEt)_4$ and ethanol, respectively. 'A' refers to anatase phase.

The results are in contrast with that obtained for isopropanol and 2-butanol showing phase changes while increasing R. Again, this can be ascribed to the different reactivity of Ti precursor towards fluorine. $Ti(OEt)_4$ contains shorter alkyl groups, thus becoming much more reactive towards water molecules. Hydrolysis dominates over fluorolysis even at high fluorine content.

The chemical formula of cation-defected fluorinated anatase can be expressed as: $Ti_{1-x-y}\square_{x+y}O_{2-4(x+y)}F_{4x}(OH)_{4y}$. Fluorine concentration can be quantified using elementary analysis performed by $^{19}F$ NMR. It is shown in **Table 3.1** that the concentration of fluorine incorporated in the anatase phases increased from 7.1 wt. % for R = 1 to 9.7 wt. % for R = 3.

The average particle size of $Ti_{1-x-y}\square_{x+y}O_{2-4(x+y)}F_{4x}(OH)_{4y}$ anatase can be estimated by the width of the main peak at $2\theta = \sim 25^{o}$ which is related to the (101) plane. **Figure 3.8** shows that the width of the (101) peak decreased with R, indicating that the particle sizes increased. A rough calculation on the basis of Debye-Scherrer equation shows that the average particle size increased from 3.8 nm for R = 1 to 6.7 nm for R = 3 (**Table 3.1**), confirming that high fluorine content favors the crystallization processes of anatase phase.[9]

**Table 3.1: Influence of the fluorine content R on the crystalline size and fluorine concentration in the anatase phases prepared in ethanol.**

| R (F/Ti) | Average crystallite size (Å)[a] | wt. % of $F^-$ |
|---|---|---|
| 1 | 38 (1) | 7.1% |
| 2.2 | 48 (2) | 7.8% |
| 3 | 67 (3) | 9.7% |

[a]Average crystallite size was obtained from the (101) direction.

Magic-angle $^{19}F$ NMR spectroscopy was used to gain further insights into the fluorine local environment of the samples prepared with different fluorine content. The evolution of the fluorine local environment was monitored by the corresponding $^{19}F$ NMR spectrum which are gathered in **Figure 3.9a**. NMR spectra show three fluorine environments characterized by three resonances located at ca. 90, 0 and -80 ppm. These three resonances are assigned to $Ti_1\square_2$-F, $Ti_2\square_1$-F and $Ti_3$-F in the structure of the cation-defected anatase. The results confirmed the incorporation of cation defects in the anatase network through substitution of divalent anions by monovalent ones.

**Figure 3.9b** shows the evolution of the relative intensity of the three fluorine environments as a function of R. The intensity of the fluorine bonded with two Ti atoms increased with R, while the others decreased. The results are consistent with that fluorine favors a 2-fold coordination. Thus, the increase of fluorine content leads to the increase of the proportion of $Ti_2\square_1$-F.

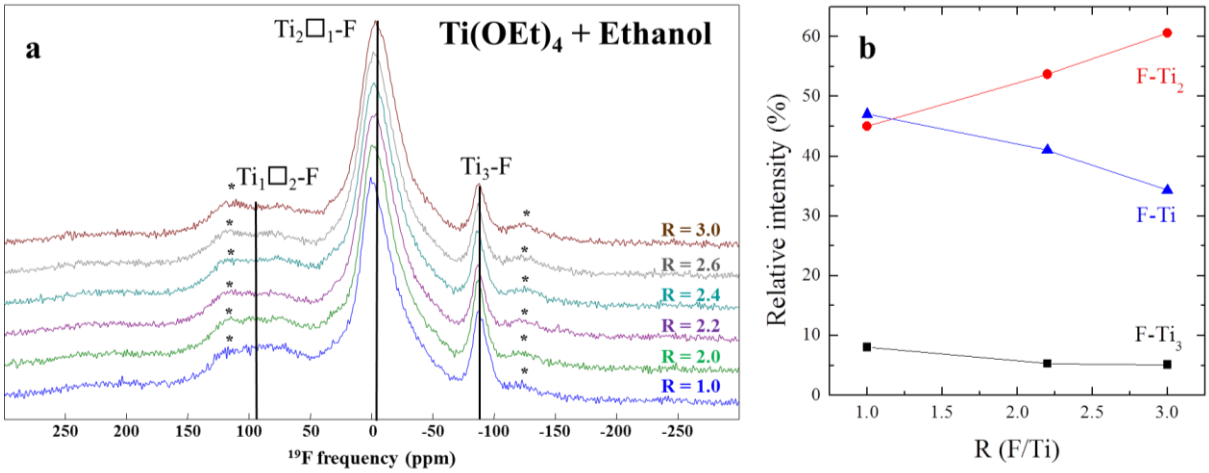


**Figure 3.9:** (a) Evolution of $^{19}F$ solid state NMR spectrums as a function of fluorine content (R) for the materials prepared using $Ti(OEt)_4$ as precursor and ethanol as solvent (Asterisk refers to first spinning sidebands of the (main) isotropic line). (b) Evolution of the relative intensity of three fluorine environments in (a).

The results show that a fine control of fluorine concentration in $Ti_{1-x-y}\square_{x+y}O_{2-4(x+y)}F_{4x}(OH)_{4y}$ can be achieved by tuning F/Ti in the ethanol solvent. Moreover, fluorine affects the crystallization process, thus providing control over particle sizes of the cation-defected anatase.

## 2.4. Hydrolysis rate (h)

The hydrolysis rate (molar ratio of water to titanium alkoxide, h) can strongly affect the functionality of titanium precursor. The study of the influence of hydrolysis rate was carried out by using $Ti(O^iPr)_4$ as precursor and isopropanol as solvent at a fluorine content of R = 3.0. Because aqueous HF solution contains 60 wt. % of water, the hydrolysis rate without additional water added is h = 5. h was then increased to 10 and 15. The evolution of XRD patterns as a function of h is shown in **Figure 3.10**. For h = 5, the diffraction peaks are indexed with HTB-type phase in majority as well as a minority phase of $TiO_2$-B. By increasing the hydrolysis rate to h = 10, the formation of anatase phase was observed and coexisted with HTB and $TiO_2$-B. While more water was added (h = 15), the resulting products were mainly composed of anatase phase with minor HTB and $TiO_2$-B.

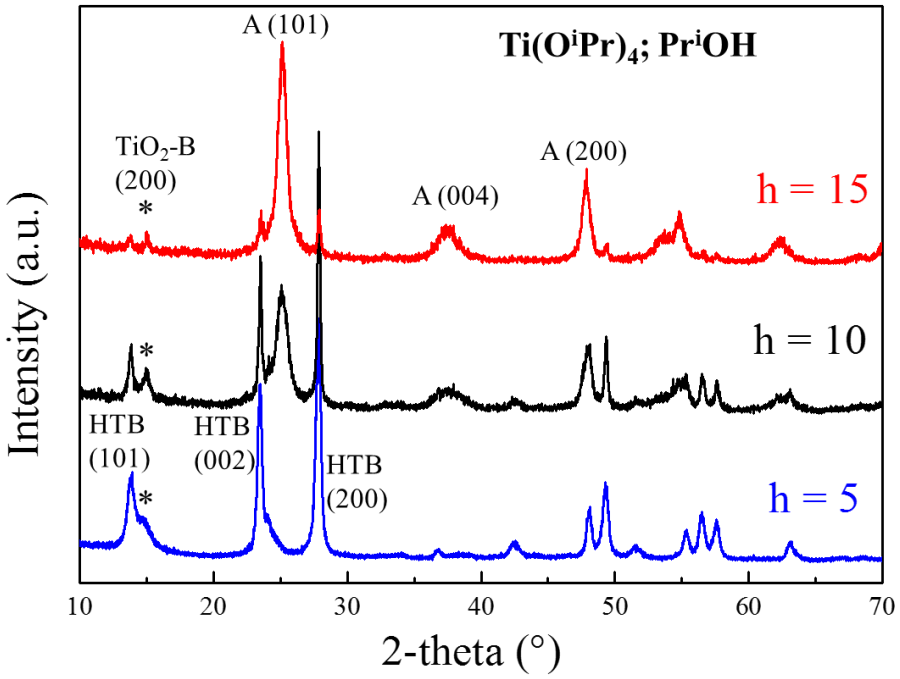


**Figure 3.10:** Influence of hydrolysis ratio (h) on the X-ray diffraction patterns of the materials synthesized by using titanium isopropoxide as precursor and isopropanol as solvent at fluorine ratio of F/Ti = 3. 'A' refers to anatase phase. Asterisk refers to (200) planes of $TiO_2$-B.

The phase change from HTB to anatase with the increase of hydrolysis rate highlights the role of water on modifying the hydro/fluorolysis and condensation reactions of alkoxide precursor. Reverse phase change observed in tuning fluorine ratio indicates competitive reaction between fluorolysis and hydrolysis. Increase of the amount of water in the synthesis favors hydrolysis reaction and leads to much hydroxylated titanium octahedra subunits, thus suppressing the fluoride-rich HTB phase and favoring the formation of an oxide-rich anatase phase. Pure anatase phase is expected at higher hydrolysis rate.

## 2.5. Precursor concentration

The influence of the precursor concentration was performed by tuning the concentration of titanium isopropoxide. The amount of HF was adjusted to keep a constant fluorine content R = 2. The syntheses were carried out in isopropanol. The concentration of $Ti(O^iPr)_4$ varied from 0.11 to 0.90 mol.$L^{-1}$. We are grateful to Dr. Jiwei Ma for performing the syntheses. **Figure 3.11** shows the evolution of the XRD patterns of the samples obtained at different concentration of precursor. For Ti concentration equal or below 0.45 mol.$L^{-1}$, XRD patterns can be indexed with a tetragonal cell characteristic of $TiO_2$ anatase. When the Ti

concentration increased to 0.90 mol.L$^{-1}$, the resulting phase is composed of HTB-type titanium oxyhydroxyfluoride in majority and $TiO_2$-B in minority. This study indicates that concentrated reactant can favor the formation of fluoride-rich phases.

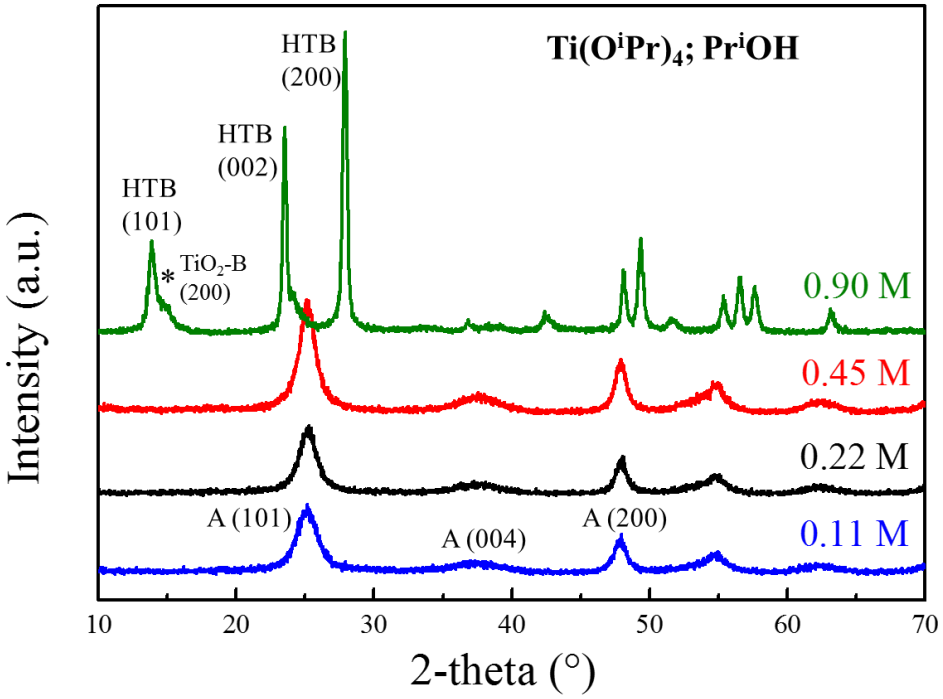


**Figure 3.11:** Evolution of the XRD patterns of the samples prepared at different Ti precursor concentration. TTIP and isopropanol were used as precursor and solvent, respectively. The amount of HF was adjusted to keep R = 2. 'A' refers to anatase phase. Asterisk refers to (200) planes of $TiO_2$-B.

## 2.6. Influence of the reaction temperature

### 2.6.1. Particle size and morphology

Temperature provides a thermodynamic control over the processes of nucleation and growth, thus affecting particle sizes and morphologies.[11,12] To investigate the effect of temperature on the sol-gel processes taking place in the fluorinated medium, syntheses were performed at temperatures ranging from 110 to 190 °C, using $Ti(O^iPr)_4$ and $Pr^iOH$ as the precursor and solvent, respectively. The fluorine content was set to R = 2.0. **Figure 3.12** displays the evolution of the X-ray diffraction patterns as a function of reaction temperature. The as-prepared samples show same diffraction patterns which can be indexed with tetragonal unit cell ($I4_1/amd$) characteristic of $TiO_2$ anatase. This result indicates that reaction temperature did not affect the structure of the resulting phases. However, significant

variations were observed for the diffraction reflections regarding the intensity and the width of the peaks, indicating changes in terms of size, morphology and crystallinity.

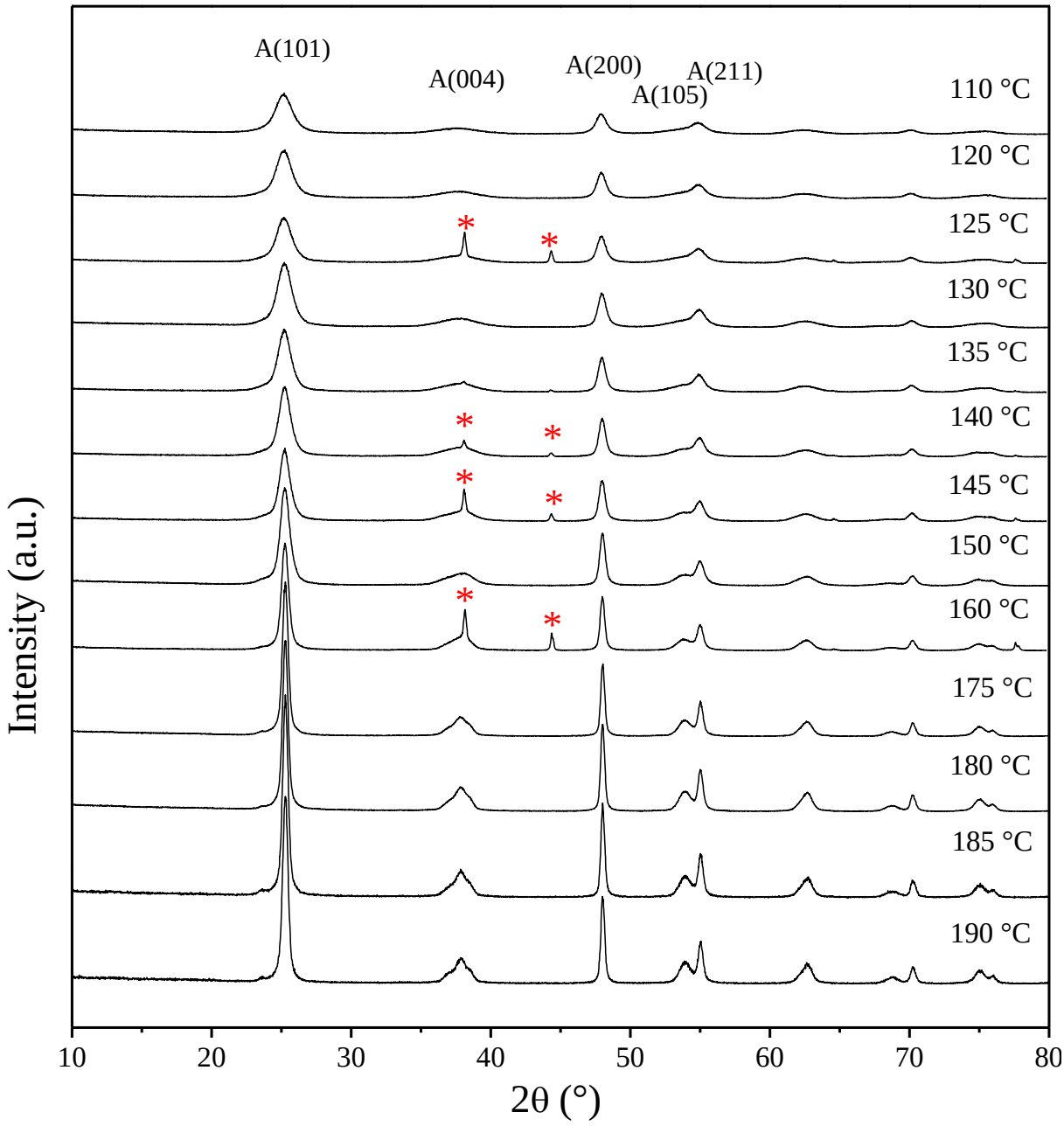


**Figure 3.12:** Evolution of the XRD patterns as a function of reaction temperature for the samples synthesized using $Ti(O^iPr)_4$ as precursor, isopropanol as solvent at a fluorine content of F/Ti = 2.0 (A refers to anatase phase; asterisk represents the reflections of sample holder).

With the increase of reaction temperature, the intensity of the diffraction peaks steadily increased indicating the enhanced crystallinity of the anatase particles. The diffraction peaks became narrower at higher temperature, indicating larger particle sizes. The average crystallite sizes can be evaluated by using the Debye-Scherrer equation based on the

Full Width at Half Maximum (FWHM) of the (101) reflection (assuming that the width of the peak originates from size effect only). **Figure 3.13** shows the average crystallite size of the temperature-dependent anatase particles. It increased from ca. 5 nm to ca. 19 nm when the temperature varied from 110 to 190 °C. The effect on particle size indicates that particle growth is thermodynamically favored at high temperature.

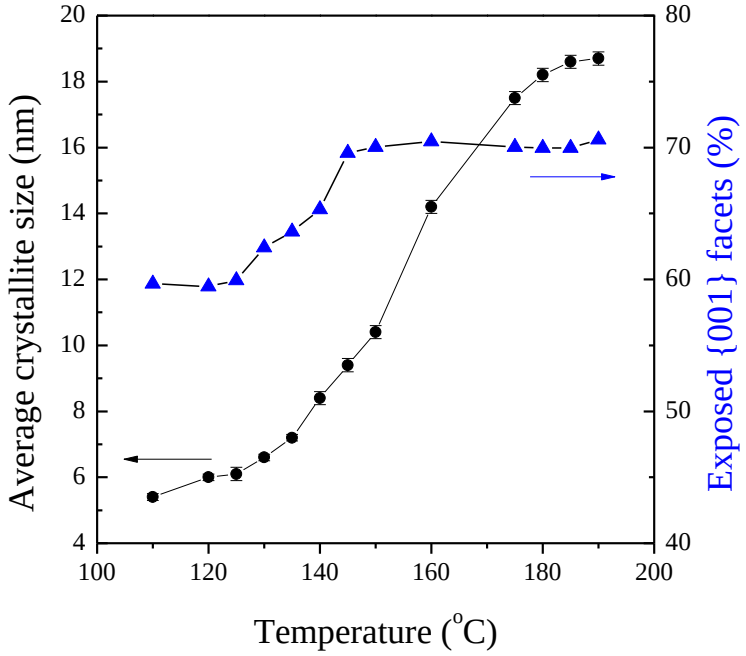


**Figure 3.13:** Evolution of average crystallite size of anatase and exposed {001} facets as a function of reaction temperature.

The morphological evolution of the anatase particles with temperature was studied by assuming that $TiO_2$ anatase shows shape of Wulff construction,[13] that is, truncated octahedron dominated by eight {101} and two {001} facets (**Figure 1.3**). The percentage of exposed {001} facets of the temperature-dependent anatase nanoparticles can be calculated based on this geometry and the results are shown in **Figure 3.13** (The calculation method is available in the Appendix 1). It is shown that the anatase prepared at 110 °C has ca. 60 % of exposed {001} facets. The percentage of exposed {001} facets increased progressively from 120 °C and reached ca. 70 % at 150 °C. Thereafter, the percentage kept almost constant whatever the reaction temperature. These results confirmed that fluorine can act as structure directing agent that stabilizes high energy {001} facets of $TiO_2$ anatase.[14-16] The exposed {001} facets increased with temperature. However, such increase ceased at 150 °C, indicating the occurrence of processes that inhibit anisotropic growth of anatase particles.

The size and morphology variation of the temperature-dependent anatase nanoparticles was further confirmed by TEM analysis (**Figure 3.14**). The anatase nanoparticles prepared at 110 °C showed highly aggregated sheet-like particles with the size of several nm. When the temperature was increased to 130 °C, the particles became larger and stacked anatase nanosheets can be clearly observed. While the reaction temperature steadily increased, the size of anatase nanosheets continuously grew. The shape of particles evolved into a truncated octahedron possessing a rectangular outline. The anatase nanosheets prepared at 190 °C have the largest size with an average side length of 30 nm and a thickness of 6 nm. The TEM results show good correlation with the evolution of the crystallite size and morphology obtained by XRD analysis. It should be noted that Moiré patterns were observed for the anatase prepared at high temperature, i.e. ≥ 160 °C, which is due to the interference between the lattices of stacked crystals. Similar phenomenon was also observed by Yang and co-workers for anatase nanosheets with high percentage of exposed {001} facets.[17] This observation confirmed the stacking of anatase particles along [001] direction.

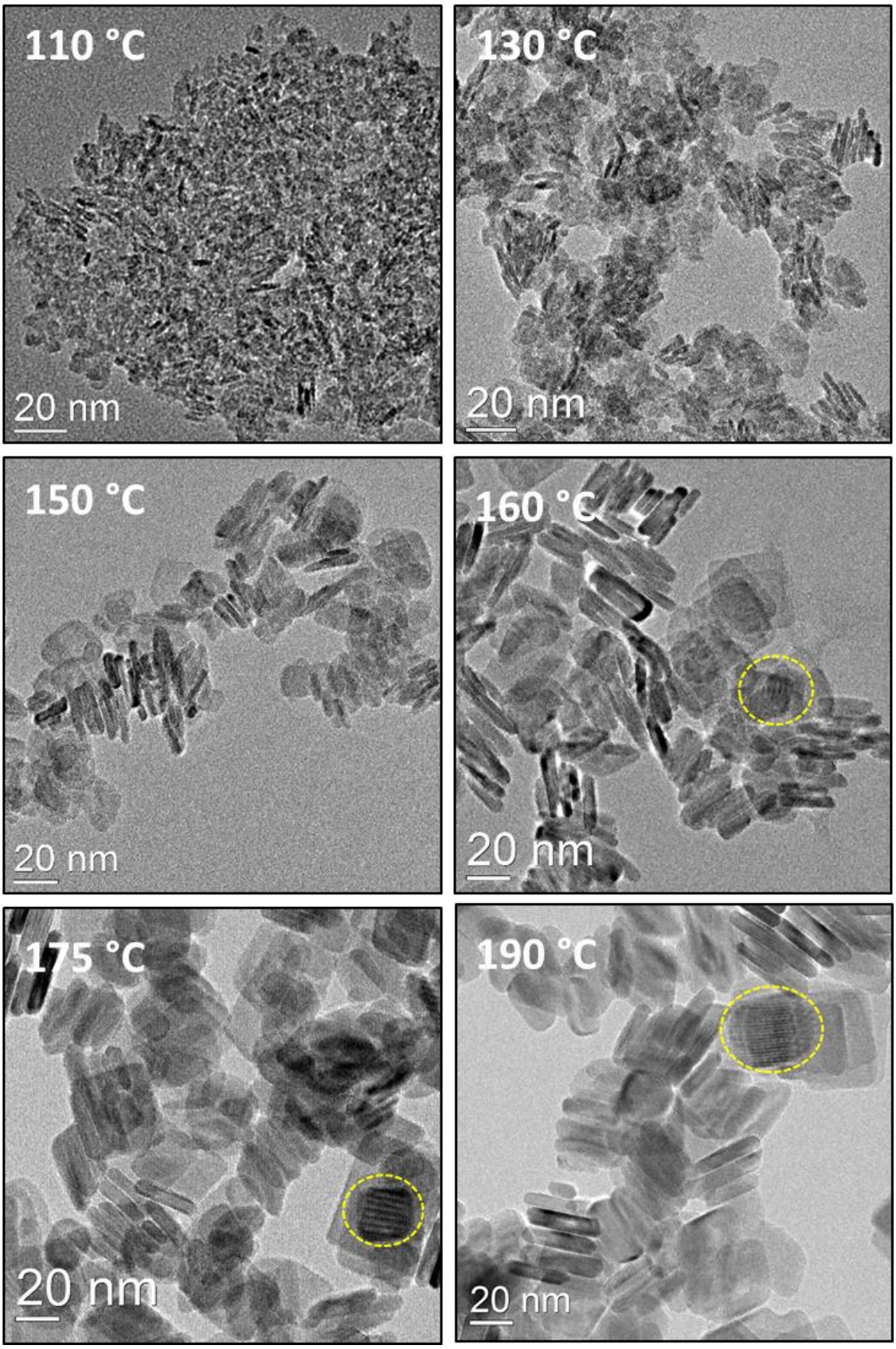


**Figure 3.14:** Transmission electron microscopy images of temperature-dependent anatase nanoparticles. Yellow dotted circles in panel mark Moiré patterns frequently observed in the TEM images.

High-resolution TEM analysis was performed to provide more details. HRTEM images of edge-on anatase nanosheets are shown in **Figure 3.15**. Crystal lattice spacing of 0.235 nm corresponds to the (004) planes of anatase $TiO_2$, indicating that the top and bottom faces of the nanosheets exposed (001) surfaces. It can be observed that the nanoparticles show similar side length but different thickness, indicating the occurrence of particle growth through oriented attachment (OA).[18] It has been reported that hydrothermal treatment of anatase nanosheets with exposed {001} facets usually led to particle coarsening via OA.[17] In that case, adjacent particles which show similar surface properties tend to assemble by eliminating {001} facets through condensation reaction of $OH^-$ groups at the surface.

The stacking of the anatase nanoparticles, as demonstrated by the presence of Moiré patterns in **Figure 3.14**, increases the probability of OA. Area marked by white rectangle in **Figure 3.15a** shows OA of two anatase nanosheets prepared at 150 °C, which results in particle two times thicker than original ones. At higher temperature, i.e. 190 °C, particle coarsening *via* OA was also observed (**Figure 3.15b**). Some tiny holes/gaps, as marked by dotted red rectangle, may originate from the OA of particles with (001) surfaces partially adsorbed by fluorine. In this case, fluorine atoms may prevent the condensation of surface hydroxyl groups, leading to the creation of tiny holes. It should be noted that OA hasn't been observed for the anatase nanosheets obtained below 150 °C, indicating particle growth via OA is thermodynamically hindered.

It is shown in **Figure 3.13** that the percentage of exposed {001} facets increased with temperature. Such anisotropic growth of anatase nanosheets stopped at temperatures higher than 150 °C. This phenomenon can be explained by the occurrence of OA at high temperature, eliminating {001} facets.

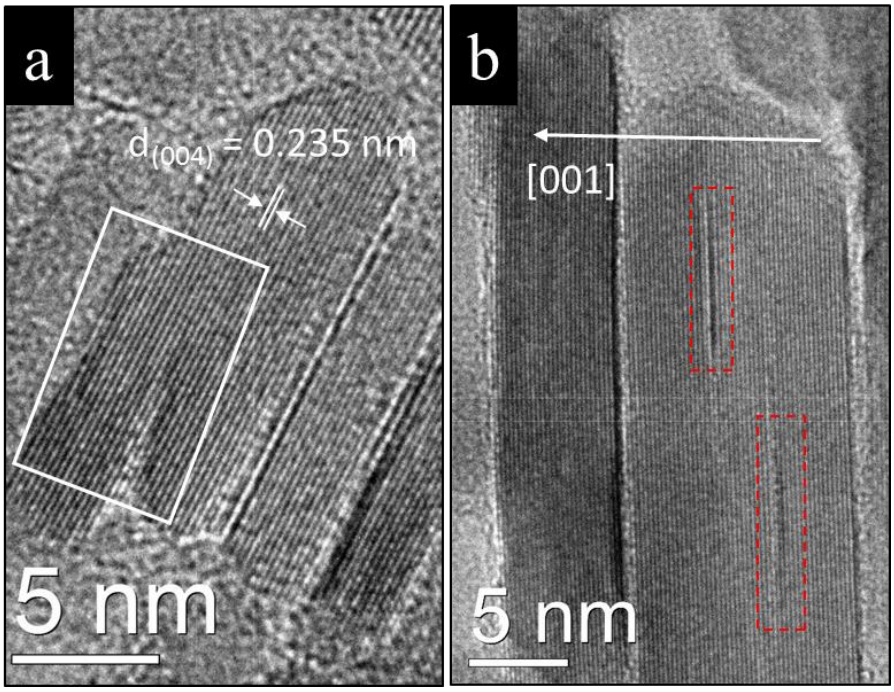


**Figure 3.15:** High-resolution TEM images of the samples obtained at 150 °C (a) and 190 °C (b). White rectangle in panel 'a' show particle growth via oriented attachment. Red dotted rectangles in panel b show the holes/gaps within particles.

### 2.6.2. Chemical composition and $F^-$ environment

In chapter II.1, we studied the structural features of the fluorinated anatase prepared at 90 °C. A high rate of $F^-$ and $OH^-$ was incorporated in anatase lattice, leading to charge deficiency which is compensated by the creation of cationic vacancies. Its chemical composition is $Ti_{0.78}\square_{0.22}O_{1.12}F_{0.4}(OH)_{0.48}$, where $\square$ represents cation vacancy. Here, pair distribution function and $^{19}F$ solid state NMR analyses were carried out to investigate the evolution of the chemical composition and fluorine local environments of the anatase phases prepared at different temperatures.

**Variation of the chemical composition in anatase**

The concentration of cation vacancies in the anatase phase was determined by refining the titanium occupancy in the PDF refinement. **Figure 3.16a** shows the correlation between the synthesis temperature and the vacancy rate of the anatase. The increase of reaction temperature led to a gradual decrease in vacancy concentration in anatase phase. Since cation vacancy in $Ti_{1-x-y}\square_{x+y}O_{2-4(x+y)}F_{4x}(OH)_{4y}$ is created by the substitution of $O^{2-}$ by $F^-$ and $OH^-$, the decrease in vacancy concentration indicates a decrease of the concentration of $F^-$ and $OH^-$.

It seems that, according to the PDF analysis, the concentration of Ti vacancy and reaction temperature show linear correlation. Stoichiometric $TiO_2$ is expected at 175 °C. $^{19}F$ NMR analysis was then carried out to quantify the fluorine concentration in temperature-dependent anatase phase. **Figure 3.16b** shows the evolution of fluorine concentration as a function of reaction temperature. For the anatase prepared at 110 °C, 10.1 wt. % of fluorine was incorporated in the anatase. When the temperature increased, the $F^-$ concentration decreased gradually and reached 5.1 wt. % at 160 °C. The decrease of the amount of fluorine well correlated the decrease of cationic vacancy. However, 4.5 wt. % of fluorine was incorporated in the anatase obtained at 175 °C. It varied slightly at higher temperature, indicating the presence of cation vacancies. The results are in contrast with that obtained by the PDF, indicating that the diffraction-based methods are not sensible enough of probing small trace of vacancy.

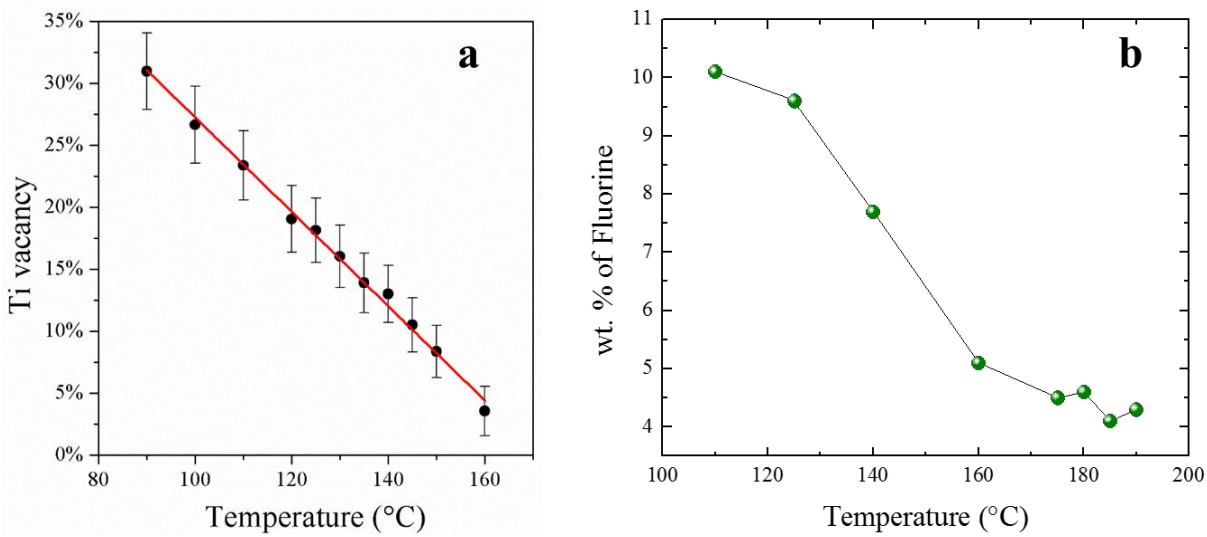


**Figure 3.16:** Correlation between the synthesis temperature and (a) the vacancy concentration, (b) fluorine concentration in anatase.

The study of the formation mechanism of cation-defected anatase (Chapter II.2.) showed that structure rearrangement of anatase phase occurred during the reaction. The study at 90 and 150 °C showed that high temperature can favor the processes of defluorination and dehydroxylation. Thus, anatase formed at higher temperature contained lower vacancy rate. Here, such effect of reaction temperature on the structural rearrangement of anatase phase was confirmed, as the concentration of Ti vacancy and fluorine decreased as a function of temperature.

Fluorine has been widely used as structure directing agent to tune the particle size and morphology of $TiO_2$ anatase prepared by solution-phase methods.[8,14,15,19,20] The enhanced photocatalytical and electrochemical properties are ascribed to the stabilization of large percentage of high energy (001) surfaces. However, the reaction temperature used in the literatures commonly ranged from 160 to 200 °C.[8,10,20-22] Incorporation of fluorine and the creation of cation vacancies in the anatase structure are still possible. Both defect chemistry and doping strategy can improve the properties of metal oxides.[23,24] Therefore, in addition to the effect of surface orientation, the effect of defect and fluorine should be considered to understand the enhanced properties of $TiO_2$ prepared in a fluorinating medium.

**Evolution of the local environment**

Local structure of the temperature-dependent anatase was studied by both PDF and $^{19}F$ NMR analyses. The PDF features at short range order provide insights into the local structure of the anatase phase. **Figure 3.17** shows the results of fitting Gaussian functions to the first peak in the PDFs. The position of the 1st peak in PDF, corresponding to the average bond length of Ti and anions, remains constant within the whole family of materials (**Figure 3.17a**). However, the width of the peak continually decreases with reaction temperature, indicating a narrower distribution of the interatomic distanced between Ti and anions (**Figure 3.17b)**. Thus, the anatase phase formed at higher temperature is locally more ordered.

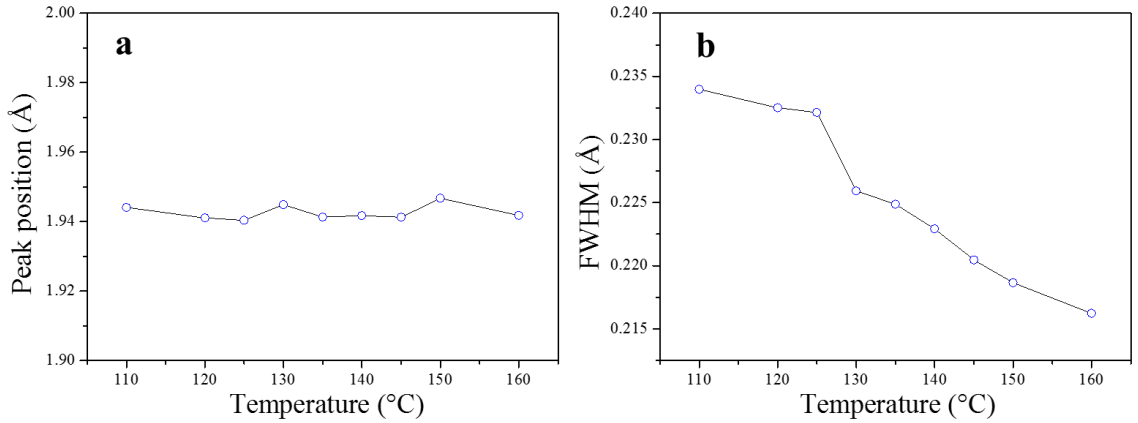


**Figure 3.17:** Gaussian fit of the first PDF peak for the whole series of materials: (a) evolution of the position of the first peak characteristic of the distance between titanium and its first neighbors; (b) evolution of the full width at half maximum (FWHM) of the first PDF peak.

The evolution of the fluorine environment in the temperature-dependent anatase phase is gathered in **Figure 3.18a**. All the samples displayed three NMR resonances located at ca. 90, 0 and -80 ppm which can be assigned to $Ti_1\square_2$-F, $Ti_2\square_1$-F and $Ti_3$-F, respectively. The

relative intensities of each NMR lines are shown in **Figure 3.18b**. The proportion of the three fluorine environments did not vary significantly while increasing the temperature. $Ti_3$-F remained at a low proportion, indicating the solubility limit of 3-fold fluorine in anatase structure. A large amount of fluorine (~95%) located close to cation vacancies confirms the preferential localization of fluorine close to vacancies, as shown in Chapter II.1. The results indicate that reaction temperature has little effect on local environment of fluorine.

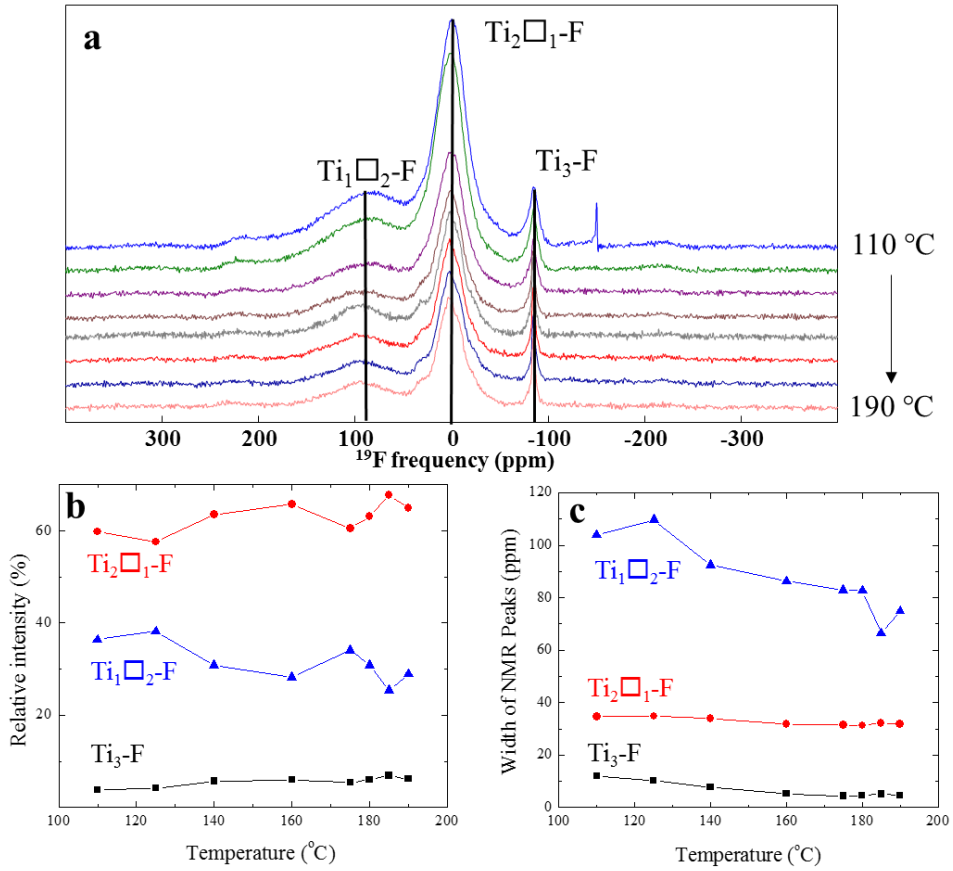


**Figure 3.18:** (a) $^{19}F$ NMR spectra as a function of reaction temperature. Evolution of relative intensity (b) and width (c) of NMR signals with temperature.

Pronounced variation of the NMR lines was observed regarding the width of the resonances. The NMR lines became narrower when the temperature increased. **Figure 3.18c** shows evolution of the width of NMR peaks as a function of temperature. The decrease in the width of the resonances of $Ti_1\square_2$-F and $Ti_3$-F indicates narrowed Ti-F distance distributions. The results indicate that the local structure of the anatase obtained at higher temperature is locally more ordered, which is in good agreement with the results of PDF peak fitting.

# 3. Conclusion

In this chapter, the structural, compositional and morphological effects of sol-gel synthesis parameters on the reaction of titanium alkoxides and HF were systematically studied. The nature of alcohol solvent plays a crucial role that affects the structure of the resulting phase. That can be ascribed to the alcohol interchange reaction which modifies the chemical composition of alkoxide precursor, thus giving rise to different reactivity. The reactivity towards fluorine increases relatively with the length of alkyl chains. The increase of fluorine content induced phase changes from edge-sharing (anatase) to edge- and corner-sharing ($TiO_2$-B) to corner-sharing (HTB). However, titanium ethoxide is far less reactive with fluorine, no phase change took place, only anatase phases were stabilized.

Our study provides control over the particle sizes, morphology and chemical composition of cation-defected $Ti_{1-x-y}\square_{x+y}O_{2-4(x+y)}F_{4x}(OH)_{4y}$ anatase by varying fluorine content and reaction temperature. Differently, particle size and fluorine concentration in anatase increased when the fluorine content increased. While increasing temperature, anatase particle size increased and, contrarily, the fluorine content decreased. Thus, fine control of anatase phase can be achieved by adjusting both fluorine content and temperature.

The study at high reaction temperature showed that fluorine and Ti vacancy are still incorporated within the anatase phase. This result indicates that the enhanced properties of $TiO_2$ anatase reported in literature cannot be solely ascribed to surface orientation, defect chemistry and doping effect should be considered.

# References

(1) Nabavi, M.; Doeuff, S.; Sanchez, C.; Livage, J. Chemical modification of metal alkoxides by solvents: A way to control sol-gel chemistry. *J. Non-Cryst. Solids* **1990**, *121*, 31.

(2) Sanchez, C.; Livage, J.; Henry, M.; Babonneau, F. Chemical modification of alkoxide precursors. *J. Non-Cryst. Solids* **1988**, *100*, 65.

(3) Simonsen, M.; Søgaard, E. Sol–gel reactions of titanium alkoxides and water: influence of pH and alkoxy group on cluster formation and properties of the resulting products. *J. Sol-Gel Sci. Technol.* **2010**, *53*, 485.

(4) Demourgues, A.; Penin, N.; Dambournet, D.; Clarenc, R.; Tressaud, A.; Durand, E. About $MX_3$ and $MX_2$ ($M^{n+}$ = $Mg^{2+}$, $Al^{3+}$, $Ti^{4+}$, $Fe^{3+}$; $X^{p-}$ = $F^-$, $O^{2-}$, $OH^-$) nanofluorides. *J. Fluorine Chem.* **2012**, *134*, 35.

(5) Fornasieri, G.; Rozes, L.; Le Calvé, S.; Alonso, B.; Massiot, D.; Rager, M. N.; Evain, M.; Boubekeur, K.; Sanchez, C. Reactivity of Titanium Oxo Ethoxo Cluster $[Ti_{16}O_{16}(OEt)_{32}]$. Versatile Precursor of Nanobuilding Block-Based Hybrid Materials. *J. Am. Chem. Soc.* **2005**, *127*, 4869.

(6) Livage, J.; Henry, M.; Sanchez, C. Sol-gel chemistry of transition metal oxides. *Prog. Solid State Chem.* **1988**, *18*, 259.

(7) Rudiger, S.; Kemnitz, E. The fluorolytic sol-gel route to metal fluorides-a versatile process opening a variety of application fields. *Dalton Trans.* **2008**, 1117.

(8) Menzel, R.; Duerrbeck, A.; Liberti, E.; Yau, H. C.; McComb, D.; Shaffer, M. S. P. Determining the Morphology and Photocatalytic Activity of Two-Dimensional Anatase Nanoplatelets Using Reagent Stoichiometry. *Chem. Mater.* **2013**, *25*, 2137.

(9) Yu, J.; Xiang, Q.; Ran, J.; Mann, S. One-step hydrothermal fabrication and photocatalytic activity of surface-fluorinated $TiO_2$ hollow microspheres and tabular anatase single micro-crystals with high-energy facets. *CrystEngComm* **2010**, *12*, 872.

(10) Luan, Y.; Jing, L.; Xie, Y.; Sun, X.; Feng, Y.; Fu, H. Exceptional Photocatalytic Activity of 001-Facet-Exposed $TiO_2$ Mainly Depending on Enhanced Adsorbed Oxygen by Residual Hydrogen Fluoride. *ACS Catal.* **2013**, *3*, 1378.

(11) Park, J.; Joo, J.; Kwon, S. G.; Jang, Y.; Hyeon, T. Synthesis of Monodisperse Spherical Nanocrystals. *Angew. Chem. Int. Ed.* **2007**, *46*, 4630.

(12) Wang, Y.; He, J.; Liu, C.; Chong, W. H.; Chen, H. Thermodynamics versus Kinetics in Nanosynthesis. *Angew. Chem. Int. Ed.* **2015**, *54*, 2022.

(13) Lazzeri, M.; Vittadini, A.; Selloni, A. Structure and energetics of stoichiometric $TiO_2$ anatase surfaces. *Phys. Rev. B* **2001**, *63*, 155409.

(14) Yang, H. G.; Sun, C. H.; Qiao, S. Z.; Zou, J.; Liu, G.; Smith, S. C.; Cheng, H. M.; Lu, G. Q. Anatase $TiO_2$ single crystals with a large percentage of reactive facets. *Nature* **2008**, *453*, 638.

(15) Liu, G.; Yang, H. G.; Pan, J.; Yang, Y. Q.; Lu, G. Q.; Cheng, H.-M. Titanium Dioxide Crystals with Tailored Facets. *Chem. Rev.* **2014**, *114*, 9559.

(16) Ong, W.-J.; Tan, L.-L.; Chai, S.-P.; Yong, S.-T.; Mohamed, A. R. Highly reactive {001} facets of $TiO_2$-based composites: synthesis, formation mechanism and characterization. *Nanoscale* **2014**, *6*, 1946.

(17) Yang, X. H.; Li, Z.; Sun, C.; Yang, H. G.; Li, C. Hydrothermal Stability of {001} Faceted Anatase $TiO_2$. *Chem. Mater.* **2011**, *23*, 3486.

(18) Zhang, H.; Penn, R. L.; Lin, Z.; Colfen, H. Nanocrystal growth via oriented attachment. *CrystEngComm* **2014**, *16*, 1407.

(19) Liu, S.; Yu, J.; Cheng, B.; Jaroniec, M. Fluorinated Semiconductor Photocatalysts: Tunable Synthesis And Unique Properties. *Adv. Colloid Interface Sci.* **2012**, *173*, 35.

(20) Pan, J.; Liu, G.; Lu, G. Q.; Cheng, H.-M. On the True Photoreactivity Order of {001}, {010}, and {101} Facets of Anatase $TiO_2$ Crystals. *Angew. Chem. Int. Ed.* **2011**, *50*, 2133.

(21) Han, X.; Kuang, Q.; Jin, M.; Xie, Z.; Zheng, L. Synthesis of Titania Nanosheets with a High Percentage of Exposed (001) Facets and Related Photocatalytic Properties. *J. Am. Chem. Soc.* **2009**, *131*, 3152.

(22) Chen, J. S.; Tan, Y. L.; Li, C. M.; Cheah, Y. L.; Luan, D.; Madhavi, S.; Boey, F. Y. C.; Archer, L. A.; Lou, X. W. Constructing Hierarchical Spheres from Large Ultrathin Anatase $TiO_2$ Nanosheets with Nearly 100% Exposed (001) Facets for Fast Reversible Lithium Storage. *J. Am. Chem. Soc.* **2010**, *132*, 6124.

(23) Hahn, B. P.; Long, J. W.; Rolison, D. R. Something from Nothing: Enhancing Electrochemical Charge Storage with Cation Vacancies. *Acc. Chem. Res.* **2013**, *46*, 1181.

(24) Yu, J. C.; Yu, J. G.; Ho, W. K.; Jiang, Z. T.; Zhang, L. Z. Effects of $F^-$ doping on the photocatalytic activity and microstructures of nanocrystalline $TiO_2$ powders. *Chem. Mater.* **2002**, *14*, 3808.

# Chapter IV. Electrochemical Properties of $TiO_2$ Anatase and $Ti_{0.78}\square_{0.22}O_{1.12}F_{0.40}(OH)_{0.48}$ vs. $Li^+$ and $Na^+$

Titanium-based oxides and fluorides compounds can be used as electrode material, particularly negative electrode for lithium and sodium-ion rechargeable batteries. $TiO_2$ anatase is a promising anode material due to the enhanced safety and high power abilities, as shown in chapter I.1.3.2. In this chapter, we investigate the electrochemical properties of $TiO_2$ anatase and $Ti_{0.78}\square_{0.22}O_{1.12}F_{0.40}(OH)_{0.48}$ vs. $Li^+$ and $Na^+$ ions.

## 1. Experimental method

### 1.1. Elaboration of lithium and sodium half-cell

**Lithium cell.** The electrodes were prepared by hand-milling of active material (80 wt. %), acetylene black (10 wt. %) as conductive agent and polyvinylidene difluoride (10 wt. %) dissolved in N-methyl-2-pyrrolidone (NMP) as binder. The slurry mixture was diluted with NMP solution to a viscosity of paste. The resulting paste was coated onto copper foil by using the doctor blade. The electrode was dried in an oven at 75 °C overnight to evaporate the NMP solvent and then cut into chips with a diameter of 1 cm and a typical mass of active material of 2 mg. The chips were outgassed in a vacuum furnace at 110 °C overnight and stored inside a glove box under argon atmosphere for battery assembly. The electrochemical characterization *vs.* lithium was carried out inside a lithium half-cell in which metallic lithium was used as negative electrode. Such a half-cell was prepared inside a glove box using a coin cell. A solution of $LiPF_6$ dissolved in ethylene carbonate and dimethyl carbonate (LP30, Merck) was used as the electrolyte. Trilayer polypropylene membrane was used as the separator.

**Sodium cell.** The test of the electrochemical reaction with $Na^+$ was performed in the department of applied chemistry at Tokyo University of Science, in collaboration with Professor Shinichi Komaba and Mika Fukunishi. Electrodes were prepared by hand-milling of 80 wt. % active material, 10 wt. % black acetylene as the conductive agent and 10 wt. % carboxymethyl cellulose (CMC) as the binder. The mixed powder was dispersed into $H_2O_2$ solution and coated on aluminum paper which serves as current collector. The electrodes were dried at 80 °C under air for 6 hours and under primary vacuum for 12 hours. Sodium half cells were assembled inside a glove box by using sodium foil as the negative electrode. A solution of 1 M $NaPF_6$ dissolved in ethylene carbonate and diethyl carbonate was used as electrolyte. A sandwich-like film composed of glass filter in the two sides and polyolefin in the middle was used as separator.

## 1.2. Electrochemical measurement

Galvanostatic method was applied to perform the electrochemical measurement for both lithium and sodium cells. To do that, a constant current was imposed at the working electrode during charge and discharge and the variation of potential with time was recorded. As capacity is a function of current and time, one can obtain the capacity of a cell for a given potential. The current density is expressed in mA/g. The nC-rate notation means that the theoretical capacity can be achieved in 1/n hours. For example, 10 hours is needed to achieve the theoretical capacity for a 0.1C-rate. The theoretical capacity of a material can be calculated based on the Faraday law (**Eq. 4.1**).

$$Q = it = \frac{m}{M}\Delta x \frac{F}{3600} \qquad \textbf{(Eq. 4.1)}$$

Where i is the current density, t is the total time. F is the Faraday constant (F = 96480 C/mol). M is the molar mass of the material, m is the weight of active material in electrode. Δx is the number of lithium theoretically inserted into one mole active material. $Li^+$ and $Na^+$ insertion into $TiO_2$ can be expressed as: $x(Li^+/Na^+) + TiO_2 + xe^- = (Li/Na)_xTiO_2$. The calculated theoretical capacity of $TiO_2$ on the basis of $Ti^{4+}/Ti^{3+}$ redox couple is 335 mAh/g.

The galvanostatic intermittent titration technique (GITT) was conducted to determine the equilibrium voltage profile. The cells were intermittently discharged at 0.1C for 20 min

followed by a relaxation time of 20 hours. Evolution of the equilibrium voltage was collected during the 2nd cycle to eliminate irreversible reactions occurring during the 1st cycle.

## 1.3. Structural characterization

Electrodes at different stage of charge and discharge were characterized by high energy X-ray diffraction (λ = 0.2114 Å) and pair distribution functions (PDF). Electrodes were recovered in a glove box and packed inside in a Kapton capillary which was then sealed to prevent exposure to air. X-ray scattering measurements were performed at the 11-ID-B beamline at the Advanced Photon Source at Argonne National Laboratory. Details regarding the experimental methods are shown in the Appendix 2.

For conveniency, the scattering vector Q ($Å^{-1}$) in high energy X-ray diffraction data was converted to the diffraction angle 2θ by using the wavelength of Cu Kα radiation (λ = 1.54056 Å) according to the following equation: $2\theta = 2\sin^{-1}\frac{Q*\lambda_{Cu}}{4\pi}$.

# 2. Lithium insertion into $Ti_{0.78}\square_{0.22}O_{1.12}F_{0.4}(OH)_{0.48}$

## 2.1. Introduction

$TiO_2$ anatase has been intensively studied as negative electrode material for lithium-ion batteries.[1-4] It has an operating potential located within the electrolyte stabilization region. Consequently, it is used at addressing the safety issues caused by the use of low-voltage carbonaceous-based materials. Furthermore, $TiO_2$ anatase can sustain high rate of charge/discharge, providing high power applications. Lithium insertion into $TiO_2$ anatase induces a phase transition from tetragonal structure to orthorhombic Li-titanate, which manifests as a plateau region in voltage profile.[1,5] This 2-phase reaction highly depends on the particle size[6,7] and surface orientation.[8,9] Anatase-type defective $Ti_{0.78}\square_{0.22}O_{1.12}F_{0.40}(OH)_{0.48}$ has particle size of ca. 7 nm and exposes 54 % of high reactive facets {001} which can be used as anode material for Li-ions batteries. In addition, the presence of cation defects might favor lithium insertion as defective γ-$MnO_2$[10] and γ-$Fe_2O_3$[11] have shown enhanced electrochemical performance. Therefore, it is of particular interest to study the electrochemical properties of $Ti_{0.78}\square_{0.22}O_{1.12}F_{0.40}(OH)_{0.48}$ and $Li^+$. Galvanostatic analysis was carried out to investigate the electrochemical lithiation of $Ti_{0.78}\square_{0.22}O_{1.12}F_{0.40}(OH)_{0.48}$. Rate capability and high rate cyclability were also tested and compared with pure $TiO_2$ anatase. Finally, galvanostatic intermittent titration technique (GITT) and pair distribution function (PDF) analyses were performed to reveal lithium insertion mechanism into the cation-defected anatase.

## 2.2. Results and Discussions

### 2.2.1. Electrochemical performance

**Voltage profile**

The electrochemical reaction of $Ti_{0.78}\square_{0.22}O_{1.12}F_{0.40}(OH)_{0.48}$ electrode and $Li^+$ on the basis of $Ti^{4+}/Ti^{3+}$ redox couple can be expressed as:

$$Ti_{0.78}\square_{0.22}O_{1.12}F_{0.40}(OH)_{0.48} + nLi^+ + ne^- = Li_nTi_{0.78}\square_{0.22}O_{1.12}F_{0.40}(OH)_{0.48}\ (n \leq 0.78)\ \textbf{(Eq. 4.2)}$$

The theoretical capacity is 290 mAh/g. The Li/$Ti_{0.78}\square_{0.22}O_{1.12}F_{0.40}(OH)_{0.48}$ half-cell was cycled in a voltage window 1 – 3 V under a current density of 20 mA/g. **Figure 4.1** displays the voltage profile of the first two cycles. Two regions can be observed regarding the voltage curve of the 1st discharge: (i) An irreversible plateau region at ~ 2.8 V might be ascribed to lithium insertion into carbon fluoride $CF_x$.[12] The formation of $CF_x$ resulted from the reaction of highly reactive F-surface of $Ti_{0.78}\square_{0.22}O_{1.12}F_{0.40}(OH)_{0.48}$ with the carbon additive during the electrode processing. This can be mitigated by pre-treating $Ti_{0.78}\square_{0.22}O_{1.12}F_{0.40}(OH)_{0.48}$ in a NaOH solution (0.01 M) prior to the electrode elaboration (Inset in **Figure 4.1**). (ii) Voltage profile shows a solid solution behavior below the plateau region at ~ 2.8 V. The results are in contrast with reported $TiO_2$ anatase that a well-established plateau locates at ~ 1.7 V,[1,5] indicating a modified lithium insertion mechanism for $Ti_{0.78}\square_{0.22}O_{1.12}F_{0.40}(OH)_{0.48}$. A capacity of 490 mAh/g was delivered during the 1st discharge, which largely exceeded the theoretical one. Such a phenomenon has been observed for amorphous $TiO_2$ and is ascribed to lithium reacting with surface species such as $H_2O$, OH groups and fluorine. This process was not reversible, leading to a poor coulombic efficiency (47 %) of the 1st cycle. The irreversible capacity loss for nanosized $TiO_2$ can be mitigated by pre-treating the electrode material with $C_2H_5OLi$ prior to the cell assembly.[13]

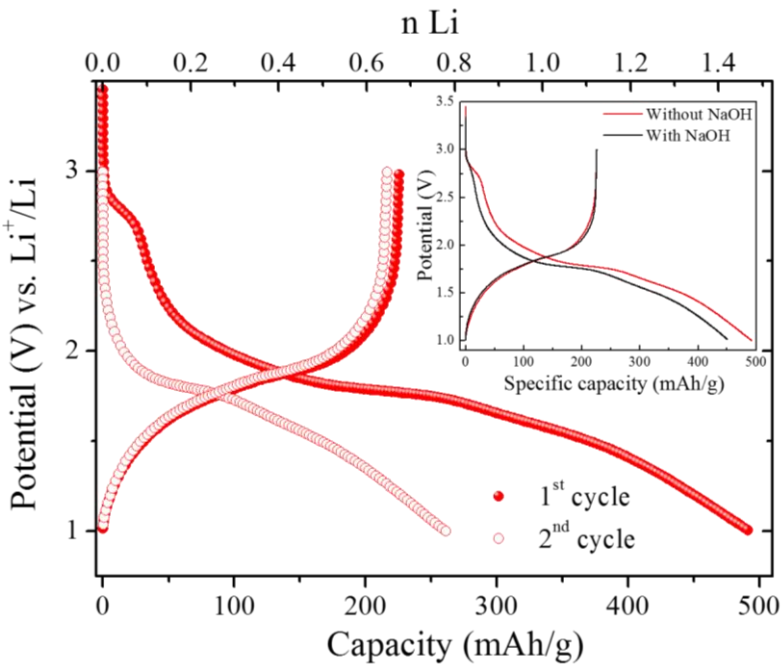


**Figure 4.1:** First and second discharge/charge curves of Li/$Ti_{0.78}\square_{0.22}O_{1.12}F_{0.4}(OH)_{0.48}$ cell cycled between 1 and 3V vs. Li, under 20 mA/g (inset: comparison of voltage profiles collected at the first cycle for as-prepared and NaOH treated $Ti_{0.78}\square_{0.22}O_{1.12}F_{0.4}(OH)_{0.48}$ electrodes).

### Rate capability

**Figure 4.2** displays the comparison of the rate capability between pure $TiO_2$ anatase and $Ti_{0.78}\square_{0.22}O_{1.12}F_{0.4}(OH)_{0.48}$ electrodes from 0.1 C to 10 C (note that for comparison purposes, 1 C = 335 mAh/g referring to the theoretical capacity of $TiO_2$). It is shown that $Ti_{0.78}\square_{0.22}O_{1.12}F_{0.4}(OH)_{0.48}$ delivered higher capacities at different current densities and a better rate capability compared to $TiO_2$ anatase, especially at high rate. At a current density of 1 C, $Ti_{0.78}\square_{0.22}O_{1.12}F_{0.4}(OH)_{0.48}$ electrode can deliver a capacity of 204 mAh/g, which is three times higher than that for $TiO_2$. When a 10-fold higher current density (10 C) was applied, only a modest drop in capacity to 134 mAh/g was observed for $Ti_{0.78}\square_{0.22}O_{1.12}F_{0.4}(OH)_{0.48}$, whereas $TiO_2$ anatase was almost inactive towards lithium insertion, suggesting a high efficient kinetics of lithium diffusion within $Ti_{0.78}\square_{0.22}O_{1.12}F_{0.4}(OH)_{0.48}$ at high rate of charge and discharge. A comparison with literature data revealed that $Ti_{0.78}\square_{0.22}O_{1.12}F_{0.4}(OH)_{0.48}$ shows an even better rate capability than nanoporous anatase.[2] At C-rate of 1C, 5C and 10 C, $Ti_{0.78}\square_{0.22}O_{1.12}F_{0.4}(OH)_{0.48}$ electrode can deliver capacity of 204, 185 and 134 mAh/g, respectively, as compared to 190, 142 and 118 mAh/g obtained for nanoporous anatase.

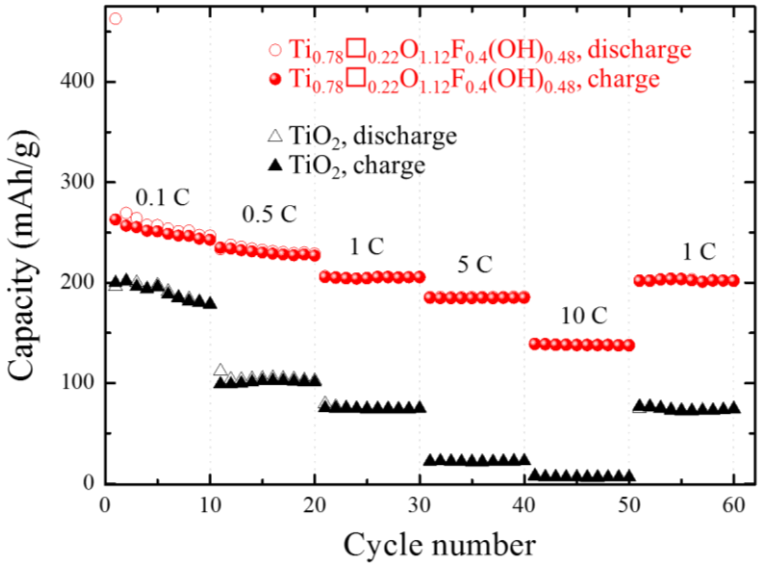


**Figure 4.2:** The rate capability of $Ti_{0.78}\square_{0.22}O_{1.12}F_{0.4}(OH)_{0.48}$ and stoichiometric pure $TiO_2$ anatase electrodes.

### Cyclability

To test the cyclability of lithium diffusion within $Ti_{0.78}\square_{0.22}O_{1.12}F_{0.4}(OH)_{0.48}$ at high current density, cells were cycled at C-rates of 1 C (335 mAh/g) and 50 C (16750 mA/g)

(**Figure 4.3**). Under 1 C, little capacity degradation was observed over 100 cycles. The 1st charge process delivered a capacity of 213 mAh/g and 90 % of them can be retained after 100 cycles of charge and discharge. The coulombic efficiency reached approximately to 100 % after the 2nd cycle. When the current density increased 50-fold to 50 C, the cell showed a good capacity retention. The capacity faded slowly as a function of the number of cycles. After 300 cycles, $Ti_{0.78}\square_{0.22}O_{1.12}F_{0.4}(OH)_{0.48}$ still delivered a specific capacity of 75 mAh/g. The coulombic efficiency improved rapidly to almost 100 % after few cycles, which is due to the progressive activation of the electrode. The cycling behavior at high rate demonstrated a good lithium storage ability.

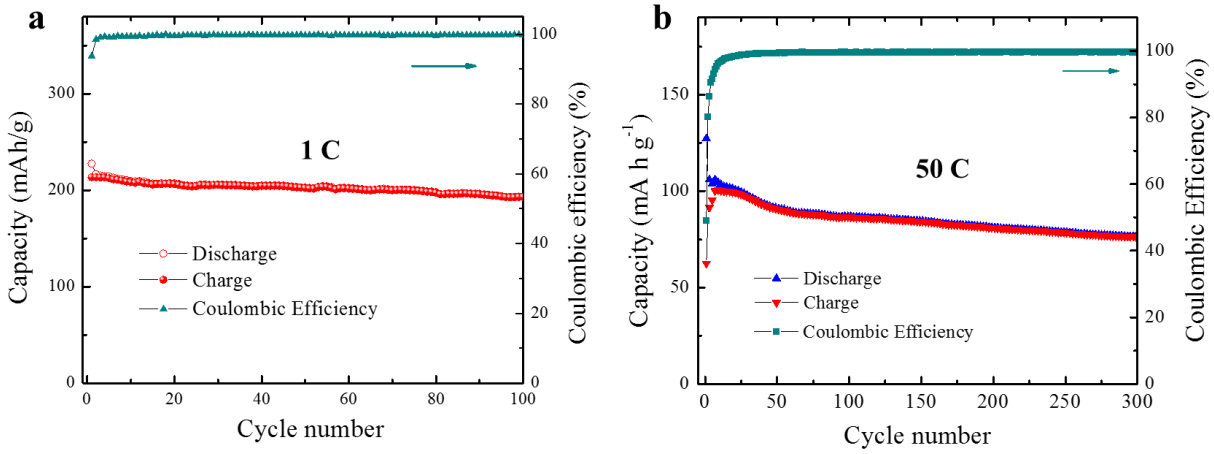


**Figure 4.3:** Cycling behavior of $Ti_{0.78}\square_{0.22}O_{1.12}F_{0.4}(OH)_{0.48}$ at current density of (a) 1C (335 mA/g) and (b) 50 C (16750 mA/g).

## 2.2.2. Lithium insertion mechanism

Solid solution behavior showed in the voltage profiles of $Li/Ti_{0.78}\square_{0.22}O_{1.12}F_{0.4}(OH)_{0.48}$ cells (**Figure 4.1**) indicates a modified $Li^+$ insertion mechanism as compared to $TiO_2$ anatase. The galvanostatic intermittent titration technique (GITT) and pair distribution function analyses were applied to gain more insights into lithium insertion in $Ti_{0.78}\square_{0.22}O_{1.12}F_{0.4}(OH)_{0.48}$.

### GITT measurements

GITT measurements were performed in the 2nd discharge to avoid the effect of irreversible reactions occurring during the 1st discharge. Cells were intermittently discharged at a current density of 0.1C for 20 min. Quasi-equilibrium voltage was recorded after 20 h of relaxation. **Figure 4.4** shows the results of GITT measurements of $TiO_2$ anatase and

$Ti_{0.78}\square_{0.22}O_{1.12}F_{0.4}(OH)_{0.48}$ electrodes. Quasi-equilibrium voltage of the cation-defected anatase decreased smoothly upon discharge, indicating monophasic lithium insertion mechanism. This is in contrast with pure $TiO_2$ anatase phase featuring a plateau region at ~ 1.8 V (**Figure 4.4b**). This plateau can be attributed to a well-known phase transition from anatase to lithium titanate, characterized by a symmetry change from tetragonal (space group: $I4_1/amd$) to orthorhombic (space group: Imma).[1,5]

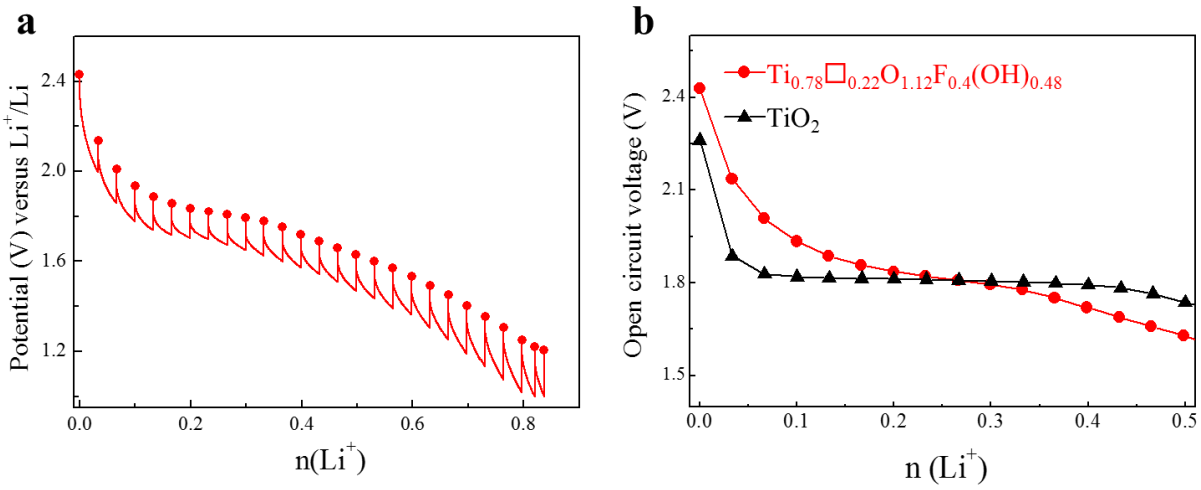


**Figure 3.4:** (a) Second discharge profiles obtained by GITT measurement for $Ti_{0.78}\square_{0.22}O_{1.12}F_{0.4}(OH)_{0.48}$. Circles represent the equilibrium voltage after 20 h of relaxation. (b) Open circuit voltage (OCV) obtained by GITT measurement for $TiO_2$ and $Ti_{0.78}\square_{0.22}O_{1.12}F_{0.4}(OH)_{0.48}$.

**Pair distribution function**

PDF refinement of the discharged electrode provided structural insights into the lithiated phase. Tetragonal anatase model was used to fit the PDF data. It is shown in **Figure 4.5a** that the refinement using one tetragonal phase yielded a poor fit (Rw = 33.3 %). A good fit was obtained by using two anatase tetragonal models (Rw = 23.9 %) (**Figure 4.5b**). The results of the 2-phase refinement are gathered in **Table 4.1**. These two anatase phases show different cell parameters and similar coherence length. Refining scale factor in the PDF fits allowed quantifying the proportion of each phases. However, due to the limitation of the instrument resolution, the lithium concentration incorporated into the anatase phase cannot be quantified by the PDF refinements.

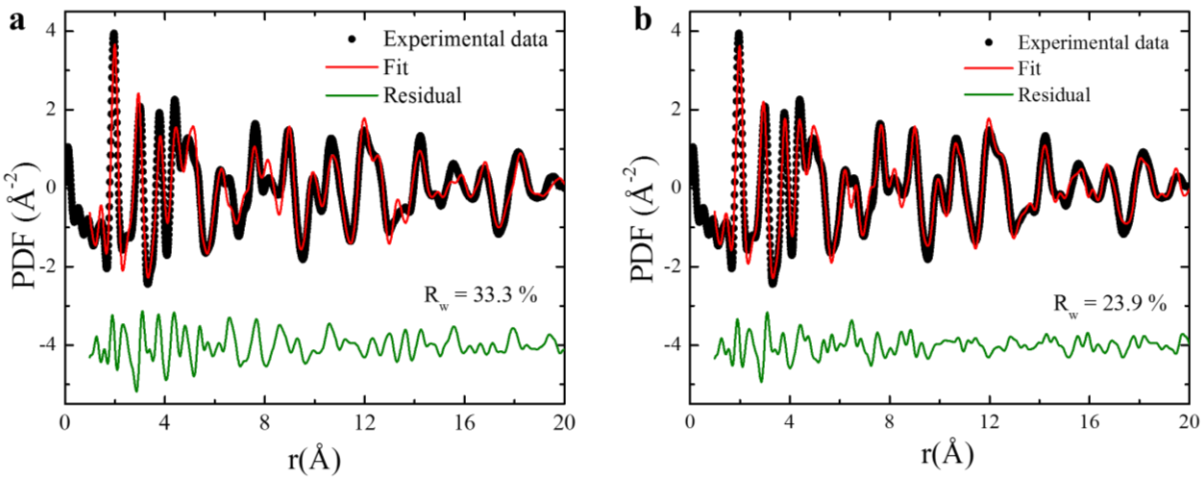


**Figure 4.5:** Refinement of the PDF of $Ti_{0.78}\square_{0.22}O_{1.12}F_{0.4}(OH)_{0.48}$ electrode discharged to 1.0 V using (a) one phase and (b) two phases of the anatase-type structure ($I4_1/amd$).

**Table 4.1: Results of the PDF refinement shown in Figure 3.5b.**

| Phase | a (Å) | c (Å) | Coherence length (Å) | quantification | Number of Li[a] |
|---|---|---|---|---|---|
| **I** | 3.982 (6) | 8.87 (2) | 65 (9) | 65 % | 0.77 |
| **II** | 3.876 (6) | 9.25 (2) | 50 (6) | 35 % | 0.36 |

[a]Number of Li in each anatase phase was determined by using Vegard's law.

The determination of lithium concentration in each anatase phase was based on the Vegard's law. The lattice parameters of $Li_xTiO_2$ anatase phase was shown to follow the Vegard's law.[14,15] Linear correlation of the cell parameter a as a function of the number of Li was obtained by using the literature data (**Figure 4.6**). The number of Li in the two anatase phases can thus be obtained and their chemical compositions were deduced: $Li_{0.77}Ti_{0.78}\square_{0.22}O_{1.12}F_{0.4}(OH)_{0.48}$ and $Li_{0.36}Ti_{0.78}\square_{0.22}O_{1.12}F_{0.4}(OH)_{0.48}$ (**Table 4.1**). The capacity calculated on the basis of the proportion of the Li-rich and Li-poor phases is in good agreement with the experimental one, indicating the reliability of the PDF analysis.

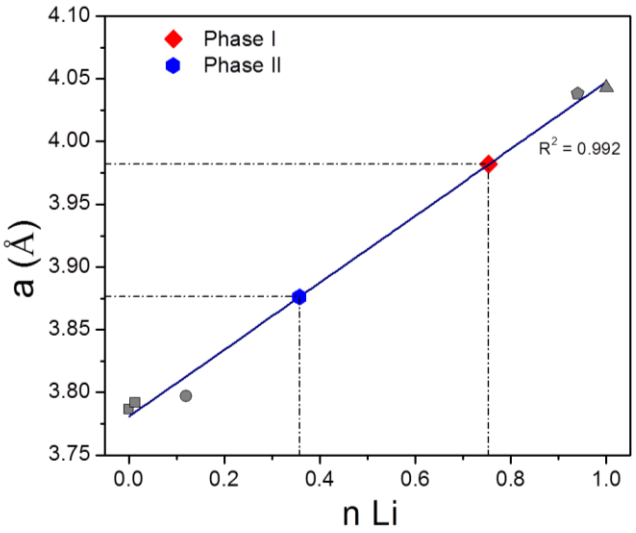


**Figure 4.6:** Prediction of the lithium content using Vegard's law. Grey points correspond to literature data.[3,4,14,16]

The coherence length for both lithiated anatase phases is similar with the pristine material, indicating that Li-rich and Li-poor phases do not coexist within one particle. Lithium would continuously react with anatase particles until $Ti^{4+}/Ti^{3+}$ redox couple is fully utilized, thereafter, lithiation takes place on the next particles. This process has been reported to be size-dependent.[6,15] For larger $TiO_2$ anatase particles, phase boundaries between Li-rich and Li-poor phases were observed within one particle, whereas phase boundary migration in smaller particles occurred instantaneously, leading to lithiation particle by particle.

**Lithium insertion mechanism**

Prior to the discussion of the lithium insertion mechanism into $Ti_{0.78}\square_{0.22}O_{1.12}F_{0.4}(OH)_{0.48}$, we first review the 2-phase reaction for $Li^+$ insertion in pure $TiO_2$ anatase. A recent DFT calculation revealed the mechanism of phase transition occurred during lithiation process.[17] The phase transition from tetragonal to orthorhombic structure was shown to be driven by pairing effect of edge-sharing $LiO_6$ octahedra occupying interstitial sites. This 2-phase reaction is strongly affected by particle sizes of $TiO_2$.[6,7,15] Reducing particle size favors monophasic lithium insertion. Solid solution mechanism was observed for $TiO_2$ anatase with particle sizes of ~4 nm.[18,19] However, $Ti_{0.78}\square_{0.22}O_{1.12}F_{0.4}(OH)_{0.48}$ displays particle size where phase transition is expected.[1,6] Therefore, cation defects might be at the origin of the modified lithium insertion mechanism.[20] The presence of Ti vacancies in $Ti_{0.78}\square_{0.22}O_{1.12}F_{0.4}(OH)_{0.48}$ can act as additional vacant sites for $Li^+$ accommodation, thus

alleviating the formation of edge-sharing $LiO_6$ octahedra and finally modifying the insertion mechanism.

The enhanced electrochemical performance vs. $Li^+$ for $Ti_{0.78}\square_{0.22}O_{1.12}F_{0.4}(OH)_{0.48}$ might be ascribed to the following factors:

1. Size effect: Li insertion is favored by reducing the diffusion path in nanosized particles.[7,15] The cation-defected fluorinated anatase showed particles sizes of ca. 7 nm, favoring lithium diffusion in the lattice.
2. Surface orientation: It was shown that Li diffusion at the surface of particles has higher energy barrier than in the lattice.[8] Among different surfaces of anatase particles, the reactive (001) surfaces have lower energy barrier for Li diffusion and higher electron migration rate.[8,9,21] Our anatase particles show 54 % of exposed (001) surfaces. Thus, $Li^+$ insertion/extraction kinetics are enhanced.
3. Defect chemistry: Cation vacancies might provide additional Li-diffusion paths, leading to enhanced Li ions mobility.[22]
4. Solid solution reaction: Modified mechanism from a two-phase transition to a solid solution behavior favors rapid lithium extraction and insertion, thus achieving high rate capability.[23]

# 3. Sodium insertion into $TiO_2$

## 3.1. Introduction

Lithium-ion batteries (LIBs) have been widely used as power source over the three decades since the first lithium-ion battery was commercialized in 1991.[24-27] Recently, the limits of the world's lithium resources and demand for large-scale energy storage have motivated the search for alternative charge carriers besides lithium. Therefore, researches have focused on sodium-ion batteries (SIBs) owning to cheap and abundant Na sources.[28-30] Nevertheless, compared with lithium ion, sodium ion has larger radius (1.02 Å vs. 0.76 Å for $Li^+$). Consequently, insertion of sodium ions into host materials would be different from those of their Li analogues. A lot of materials that can sustain lithium insertion are inactive towards sodium and many negative electrodes have different insertion mechanism during sodium uptake.[28,31] For example, lithium insertion into $Li_4Ti_5O_{12}$ exhibits a 2-phase reaction (spinel to rock salt $Li_7Ti_5O_{12}$),[32,33] whereas a three-phase separation mechanism (spinel to two rock salt phases of $Li_7Ti_5O_{12}$ and $Na_6LiTi_5O_{12}$) has been reported for sodium insertion.[34]

$TiO_2$ is a widely studied negative electrode for LIBs[1,7] and has been shown to be active during $Na^+$ uptake and release.[35,36] Nanosized $TiO_2$ has shown excellent lithium storage performance at high charge/discharge rate.[3,4] It is well-known that lithium insertion into $TiO_2$ anatase is based on a biphasic reaction characterized by a well-defined plateau at ~1.75 V *vs.* $Li^+/Li$ in voltage profile.[5] For the sodiation, however, the operating voltage is ~ 0.8 V *vs.* $Na^+/Na$. Considering the difference in standard potential (-2.71 V for $Na^+/Na$ vs. -3.05 V for $Li^+/Li$), the operating voltage for $Na/TiO_2$ cell is still lower than $Li/TiO_2$, indicating different insertion mechanism for $Li^+$ and $Na^+$. Cha et al. first investigated the sodiated $TiO_2$ by ex-situ XRD and claimed a solid solution sodium insertion mechanism.[37] However, the sodiated electrode showed almost amorphous diffraction features, indexation of the diffraction pattern is limited. The same mechanism was proposed by Kim et al. on the basis of ex-situ XAS and XRD analyses.[36] The authors showed that $Na^+$ insertion and extraction are based on $Ti^{4+}/Ti^{3+}$ redox couple accompanied with a volume variation of the anatase structure. Nevertheless, the lattice parameters were obtained by the diffraction data ranging from $2\theta = 35°$ to 70° only. The variation of the most intense peak at 25° for anatase was not considered. Subsequently, DFT calculations performed by Shen showed that sodium insertion into the anatase structure

is kinetically hindered.[38] According to XRD analysis, they claimed negligible change in cell parameters of $TiO_2$ upon sodiation, thus sodium did not insert into the anatase lattice but reacted with the surface. This conclusion seems debatable as the electrode showed amorphous features after sodiation. Latter, in-situ XRD analysis performed by Wu et al. confirmed that $TiO_2$ anatase structure undergoes an amorphization upon sodium insertion.[39] Reduction of some $Ti^{4+}$ to metallic $Ti^0$ was detected by XPS, releasing oxygen gas. Nevertheless, the $Ti^0$ signal might originate from the SEI layer formed during discharge. The contradiction reported by different researchers indicates that sodium insertion into $TiO_2$ anatase is complex and requires further investigation.

In the aforementioned sodiation mechanisms, most of researchers reported the amorphization of electrode. However, laboratory XRD analysis is not capable of probing the whole volume of electrode. For instance, an architecture consisting of amorphous shell and crystalline core exhibited amorphous features under Cu Kα radiation.[40] Thus, high penetrating methods are needed to probe the entire volume of sample. Furthermore, the characterization of amorphous phase needs more powerful techniques.

Here, we employ high energy X-ray diffraction in combination with the Pair Distribution Function (PDF) methods to investigate the sodium insertion mechanism in $TiO_2$ anatase nanoparticles. High energy X-ray diffraction is highly penetrating, thus being capable of probing the entire volume of sample. Furthermore, PDF is a well-established technique capable of probing materials with short and long range orders. This diffraction-based method is sensible towards the number of electron of the pairs. Sodium atom shows a stronger scattering ability than Li, thus making neutron diffraction unnecessary. The electrodes at different charge/discharge stages were analyzed and the mechanism of (de-)sodiation reaction in $TiO_2$ was proposed.

## 3.2. Results and Discussions

Pure $TiO_2$ anatase nanoparticles was obtained by heating $Ti_{0.78}\square_{0.22}O_{1.12}F_{0.40}(OH)_{0.48}$ at 450 °C under air for 4 hours. Laboratory X-ray diffraction pattern showed well crystallized nanoparticles with tetragonal symmetry of $I4_1/amd$ (**Figure 4.7**). The anatase network was further confirmed by PDF analysis, as shown in Chapter II.1. High-resolution transmission electron microscopy shows almost spherical nanoparticles with an average size of about 20

nm (Inset in **Figure 4.7**). The lattice fringe of 0.17 nm corresponds to the (202) plane of $TiO_2$ anatase.

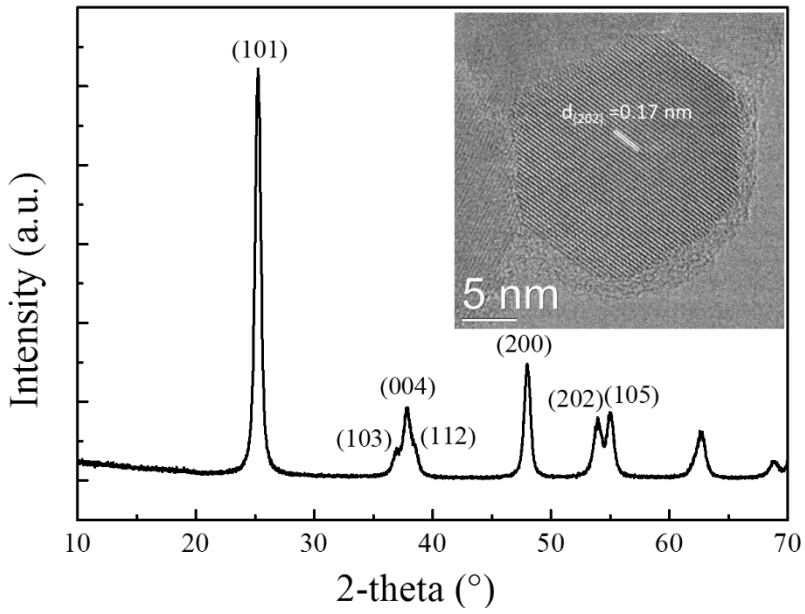


**Figure 4.7:** Laboratory X-ray diffraction pattern of $TiO_2$ (Inset: High-resolution TEM image of a $TiO_2$ particle).

### 3.2.1. Electrochemical characterization

The electrochemical reaction of sodium with $TiO_2$ can be written as follow:

$$xNa^+ + TiO_2 + xe^- \rightarrow Na_xTiO_2\ (0 \leq x \leq 1) \qquad \textbf{(Eq. 4.3)}$$

The theoretical capacity based on the $Ti^{4+}/Ti^{3+}$ redox couple is 335 mAh/g. The electrochemical characterization of $TiO_2$ anatase nanoparticles was performed inside a Na half-cell. **Figure 4.8a** displays the voltage profile of the Na half-cell cycled between 0 – 2 V at a current density of 10 mA/g. Upon the 1st discharge, the potential of the cell decreases rapidly from open circuit voltage to 0.3 V, delivering a capacity of ~100 mAh/g which corresponds to 0.3 $Na^+$ per formula unit of $TiO_2$. An irreversible plateau region, which can be attributed to a 2-phase reaction, was observed at ~0.2 V and delivered a capacity of ~280 mAh/g, corresponding to 0.84 $Na^+$ per $TiO_2$. The 1st discharging capacity is 380 mAh/g, exceeding the theoretical one.

During the 1st charge, the voltage steadily increased and no plateau region was observed. The delivery of a capacity of 200 mAh/g corresponds to 0.6 Na extracted from the lattice.

The voltage profile of the 2nd discharge shows a sloping curve, differing from that for the 1st discharge, indicating an irreversible structural change upon the plateau region. A capacity of 206 mAh/g can be delivered during the 2nd discharge and 89 % of them were maintained during the following charge process. The operating voltage of the cell is ca. 0.8 V which is in good agreement with literature data.[35,39]

Upon cycling, the Na-cell shows a stable cycling behavior with a reversible insertion/de-insertion of ca. 0.5 $Na^+$ per $TiO_2$ (**Figure 4.8b**). A capacity of 165 mAh/g was obtained after 50 cycles of charge and discharge, corresponding to 82.5 % of the capacity of the 1st charge. The coulombic efficiency increased upon the first few cycles and reached almost 100 % in the subsequent cycles, suggesting a progressive activation of the electrode.

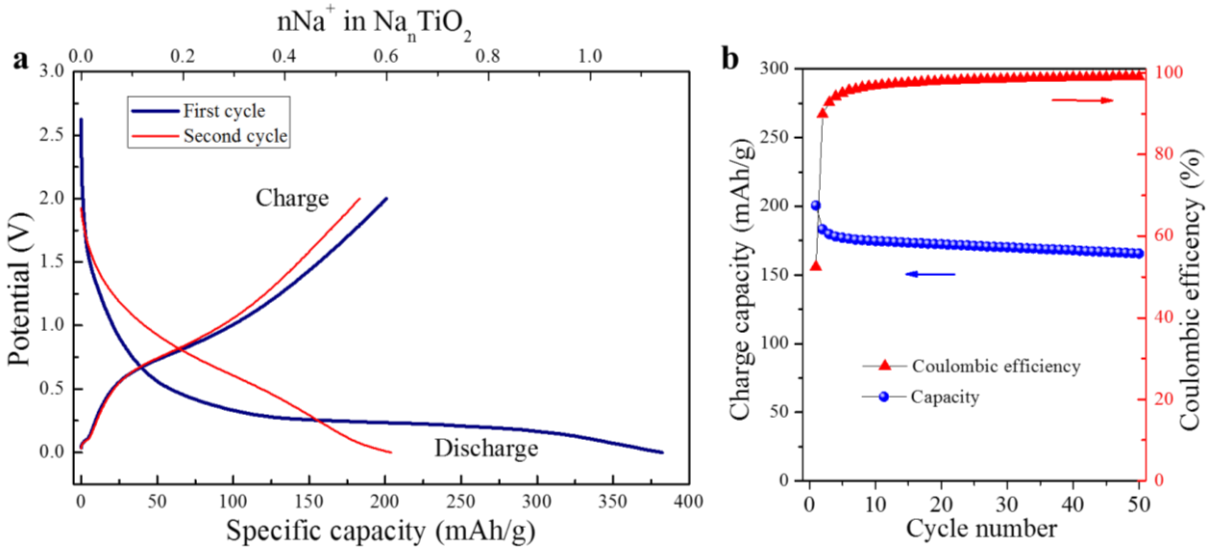


**Figure 4.8:** (a) Voltage profiles of $Na/TiO_2$ half-cell operated between 0 – 2 V at a current density of 10 mA/g. (b) The corresponding cycling performance.

The voltage profile of the $Na/TiO_2$ cell shows similar behavior with the literature data.[35,39] It has been reported that the capacity delivered between the OCV and 0.3 V for the 1st discharge originated from side reactions, i.e. decomposition of electrolyte and formation of SEI.[41] Different mechanisms have been reported regarding the plateau region, involving the contribution of pseudocapacitance,[38,42] solid-solution reaction[36,43] and phase transition.[39,41] Difference in voltage profile for the 1st discharge and subsequent cycles indicates that the

reaction occurred during the 1st discharge is irreversible. The reversibility of the cell is ascribed to the sodiated phase formed after the 1st discharge.

## 3.2.2. Structural characterization

### 3.2.2.1.High energy X-ray diffraction

High energy X-ray diffraction (λ = 0.2114 Å) was carried out to follow the structure variation upon charge and discharge. The diffraction data were collected at 11-ID-B at the Advanced Photon Source. The electrodes at three different stages of (de-)sodiation were analyzed: 1st discharge to 0.3 V (100 mAh/g) and to 0 V and 1st charge to 2 V. For conveniency, the scattering vector Q ($Å^{-1}$) in high energy X-ray diffraction data was converted to the diffraction angle 2θ by using the wavelength of Cu Kα radiation (λ = 1.54056 Å).

**Figure 4.9a** displays high energy X-ray data of the (de-)sodiated $TiO_2$ electrodes. The pristine material showed Bragg reflections which can be indexed with tetragonal unit cell of $TiO_2$ anatase. Prior to the onset of the plateau at 0.2V, the intensity of the diffraction reflections decreases, indicating loss of crystallinity of the electrode material. Neither the shift of reflections nor the presence of additional peak was observed, ruling out the insertion of $Na^+$ into the anatase network at this stage. Thus, we can conclude that the capacity delivered is mainly due to side reactions, in good agreement with the literature.[36,41]

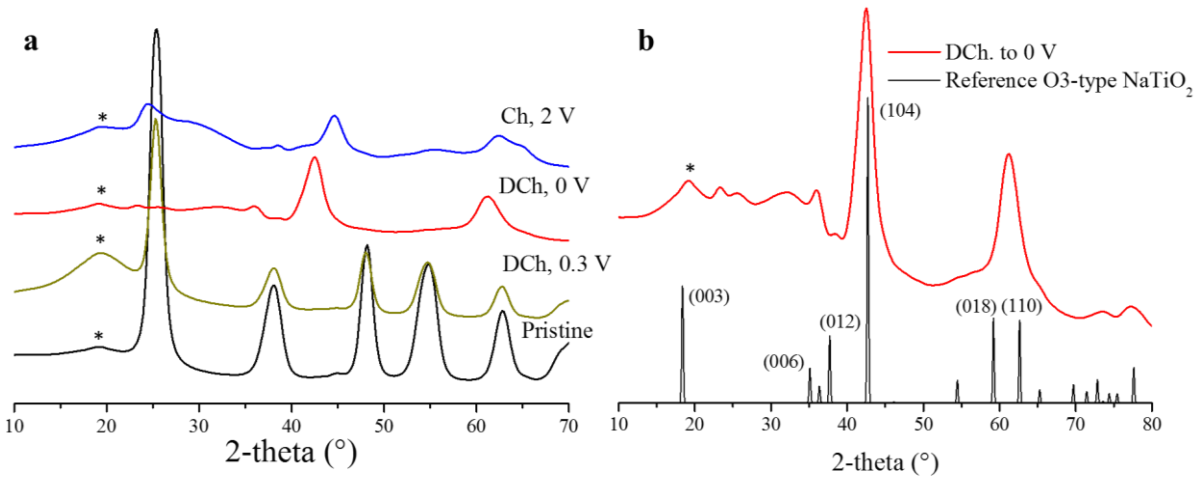


**Figure 4.9:** (a) High energy X-ray diffraction data collected at different stages of sodiation. (b) Comparison of high energy X-ray diffraction data of fully discharged electrode and reference O3-type $NaTiO_2$ with space group R-3m. Asterisk indicates the signal of sample holder.

After fully discharged to 0 V, the structure undergoes major changes as shown in X-ray data. The X-ray lines of anatase vanish and new Bragg peaks appear, indicating a phase transition upon sodiation, which is in good agreement with the presence of a plateau region. An O3-type $NaTiO_2$ rhombohedral structure (space group: R-3m) captures the major features of the experimental data (**Figure 4.9b**).[44] This phase can be synthesized by thermal treating the mixture of $TiO_2$ and metallic sodium at elevate temperature.[45,46]

After sodium extraction (charging process), the main lines shift to higher 2θ value, indicating the contraction of the cell. Additionally, a broad peak appears at 2θ = ~25°, which might be attributed to the recovery of the anatase-type structure upon charging.

### 3.2.2.2.Pair distribution function

Pair distribution function (PDF), obtained from Fourier transformation of the high energy X-ray scattering data, is a histogram that describes distance distribution of pairing atoms. It can provide atomic insights from short to long range order. The PDF profiles in the range of $1 \leq r \leq 6$ Å for the electrodes collected at different stage of charge/discharge are displayed in **Figure 4.10**. Peaks at short range were labeled for specific interatomic distances. The evolution of peak positions was followed by fitting Gaussian functions and the results are shown in **Table 4.2**.

The first peak in the PDF of the pristine electrode is related to Ti-O bond. The peak position at 1.941 Å is characteristic of the bond length of $Ti^{4+}$-O in $TiO_2$ anatase. When the electrode was discharged to 0.3 V, the position of the peak remains unchanged, indicating that there is no change in valence states of Ti at this stage of sodiation.

Further discharging to 0 V led to a broadening of peaks, indicating the presence of strong disorder in the sodiated material. Upon sodiation, the coherence length decreased from ~20 nm to ~3 nm, indicating the amorphization of the electrode after the potential plateau region. Fitting of the 1$^{st}$ peak shows distinction of three contributions located at 1.937, 2.083 and 2.366 Å, which can be assigned to the bond length of $Ti^{4+}$-O, $Ti^{3+}$-O and $Na^+$-O, respectively. These results indicate that sodium ions were inserted into $TiO_2$ on the basis of $Ti^{4+}/Ti^{3+}$ redox couple. The presence of the residual of $Ti^{4+}$ in the fully discharged electrode might be due to incomplete sodiation reaction.

When the electrode was charged to 2 V, the intensity of the peak of Na-O decreased significantly, indicating that $Na^+$ was successfully extracted from the structure. Shift of the Ti-O peak to lower r is in good agreement with the expected oxidation of $Ti^{3+}$ to $Ti^{4+}$. It should be noted that the residual of Na-O contribution at the end of the 1st charge indicates that a part of $Na^+$ was irreversibly trapped in the host material.

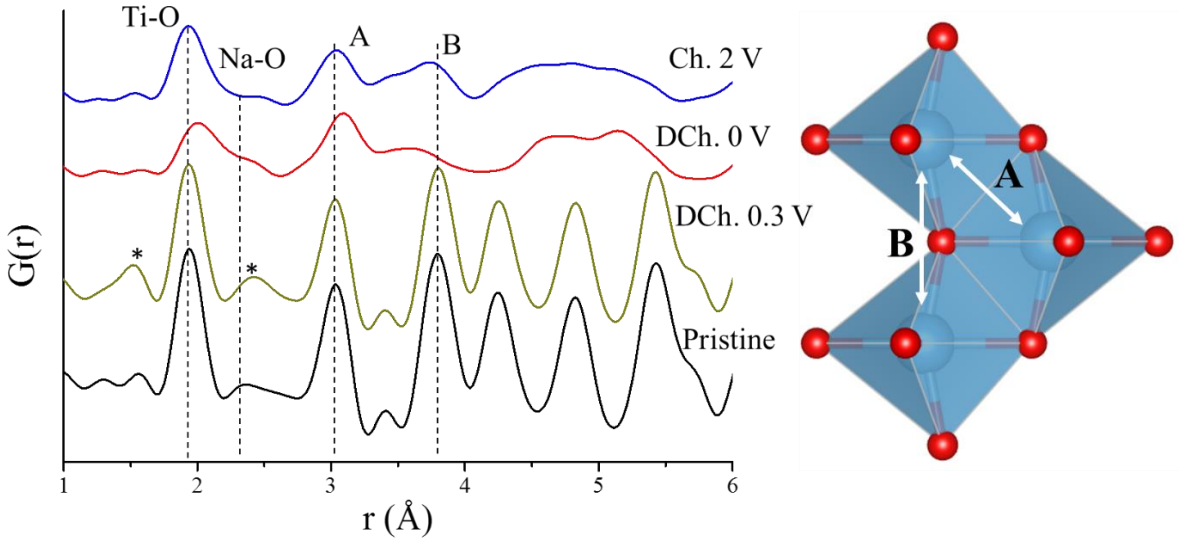


**Figure 4.10:** PDF profiles of the electrodes obtained at different stage of (de-)sodiation (left). A and B refer to the interatomic distances of Ti-Na/Ti in edge-sharing and corner-sharing $(Ti/Na)O_6$ octahedra, respectively. Asterisk indicates the signal of sample holder. A trimer of $MO_6$ octahedra (blue) illustrating the interatomic distances is shown in the right.

**Table 4.2: Results of fitting Gaussian function to the 1st peak in PDFs.**

| | Pristine | DCh, 0.3 V | DCh, 0 V | | | Ch, 2 V | | |
|---|---|---|---|---|---|---|---|---|
| **Position (Å)** | 1.941 | 1.939 | 1.937 | 2.083 | 2.366 | 1.895 | 2.014 | 2.396 |
| **Percentage of area** | | | 28.8% | 53.4% | 17.8% | 43.9% | 46.1% | 10.0% |

The peak A mainly corresponds to the distance between Ti-Ti/Na in edge-sharing $MO_6$ octahedra. It shifted to higher r for fully discharged $TiO_2$. It is expected that increase of Ti-O bond length and presence of the long Na-O bond can extend the distance between cations. The position of the peak A shifted to the left upon charge, which was caused by the reduction of Ti and the extraction of sodium-ions. Nevertheless, the peak B, corresponding to Ti-Ti/Na in corner-sharing octahedra, disappeared upon sodiation, indicating that the sodiated electrode material did not contain corner-sharing octahedral, and therefore structure transition occurred.

Nevertheless, the recovery of the peak B upon charge clearly indicates the re-formation of $TiO_2$ anatase.

**PDF refinements**

The PDF refinement using a Rietveld refinement method provides direct information on the real-space structure.[47] The fits to the PDFs of the (de-)sodiated electrodes were performed by using $TiO_2$ anatase and/or O3-type $NaTiO_2$ models.

Refinement of $TiO_2$ anatase model against the PDF of the electrode discharged to 0.3 V provided an excellent fit (**Figure 4.11**), indicating that the anatase crystalline structure was retained upon sodiation and no additional phase was formed. The refined lattice parameters were consistent with those of pristine material, indicating that no Na-ions were inserted into the anatase structure.

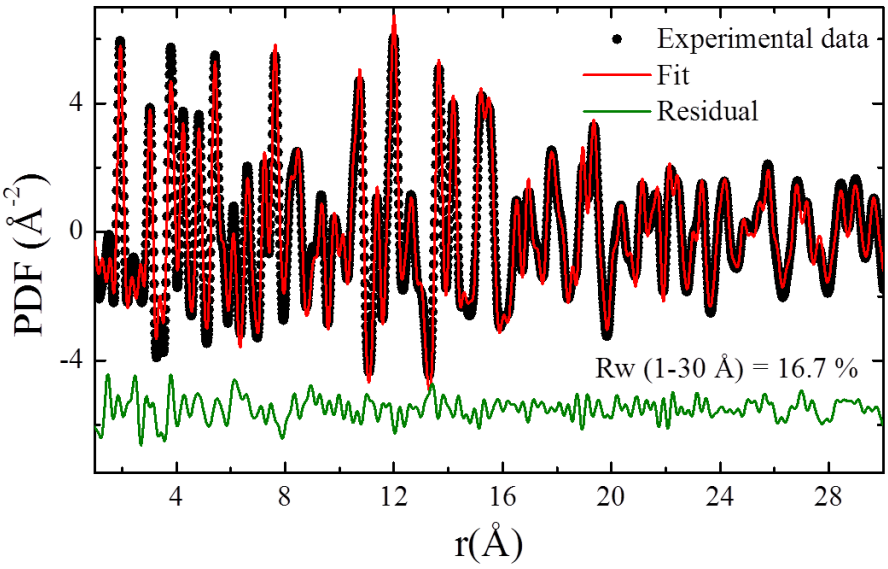


**Figure 4.11:** PDF refinement of the electrode discharged to 0.3 V using TiO2 anatase (space group: $I4_1/amd$) model.

The PDF of the fully discharged electrode was fitted using O3-type $NaTiO_2$ (space group: R-3m) phase. The lamellar structure of $NaTiO_2$ consists of an alternation of Na and Ti layers occupying 3a and 3b sites, respectively (**Figure 4.14**), where $(Ti/Na)O_6$ octahedra are edge-sharing. The PDF refinement procedure using O3-type $NaTiO_2$ phase was performed in three steps: first step, $Na_xTiO_2$ with Na defect; second step, $(Na_xTi_y)_{3a}(Na_zTi_{1-y})_{3b}O_2$, we consider a possible intermixing of Na and Ti atoms as this phenomenon has been commonly

observed for layered polycationic materials;[48,49] third step: $(Na_xTi_y)_{3a}(Na_zTi_\alpha)_{3b}O_2$, that is, with both Na and Ti defects.

For the first step, the refinement using $Na_xTiO_2$ shows that $x < 1$, indicating cation-defect in the fully discharged material. The PDF refinement in the second step shows that x, y and z are not close to 0, indicating strong intermixing of cations. For the third step, both occupancy of Na and Ti in the 3a and 3b sites were refined. The refinement is shown in **Figure 4.12**. A good fit for r region beyond 4 Å was obtained with a reliability factor of Rw = 26.5 % (4 – 30 Å). Nevertheless, the PDF features in local region (1 – 4 Å) cannot be well captured by the O3-type structure, yielding a high value of Rw = 41.4 % (1 – 30 Å). The difficulty of reproducing the local range of the PDF indicates strong disorder in the local structure.

The results of the refined parameters are shown in **Table 4.3**. The 3a sites in the rhombohedral structure are fully occupied with 43 % Na and 57 % Ti. The 3b sites are occupied by 39 % Na and 39 % Ti, indicating that cation defect in the 3b sites. The chemical formula of the resulting phase is $(Na_{0.43}Ti_{0.57})_{3a}(\square_{0.22}Na_{0.39}Ti_{0.39})_{3b}O_2$. The number of Na agrees well with the capacity obtained from the plateau region in **Figure 4.8a**.

The refined parameters are compared with the literature data (**Table 4.3**). The decrease in parameter c of $Na_{0.82}Ti_{0.96}O_2$ compared to $NaTiO_2$ can be explained by both the effects of defects and intermixing of cations. As the structure of O3-type $NaTiO_2$ shows an alternation of Na and Ti layers along c-direction, partially occupied cation sites would lead to the contraction of the lattice mainly along c-axis. However, parameter c in $Na_{0.54}TiO_2$ is larger than $Na_{0.82}Ti_{0.96}O_2$, indicating that the intermixing of Ti and Na mainly ascribes to the lattice contraction of $Na_{0.82}Ti_{0.96}O_2$. The presence of high valence Ti ions in the Na layer can lead to a strong contraction of the lattice, particularly along the c-axis.[46]

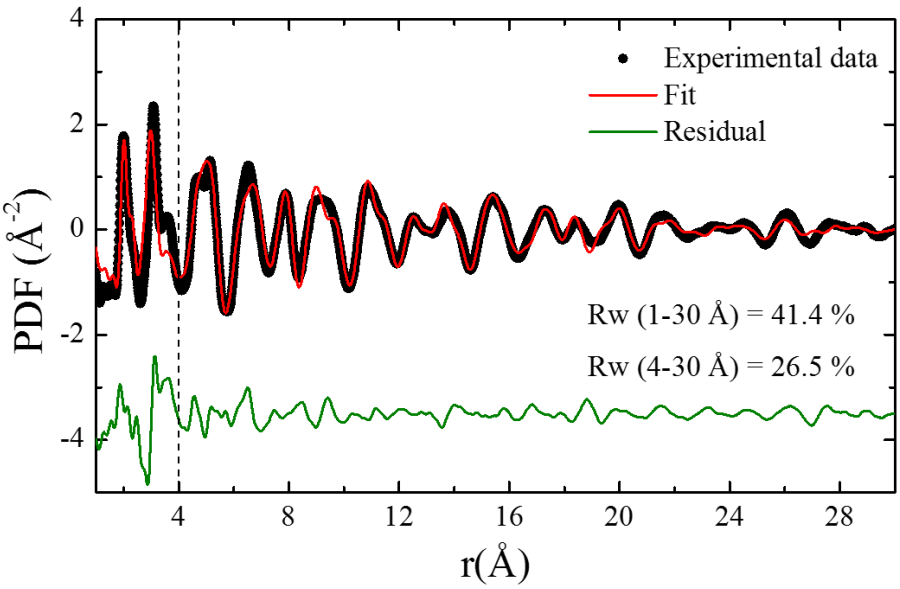


**Figure 4.12:** PDF refinement of the fully discharged electrode using O3-type $NaTiO_2$ (space group: R-3m) model.

**Table 4.3: Comparison of structure parameters of fitted $Na_{0.82}Ti_{0.96}O_2$ and reference $NaTiO_2$ and $Na_{0.54}TiO_2$.**

| | | Fitted $Na_{0.82}Ti_{0.96}O_2$ | $NaTiO_2$ (ICSD # 85657 ) | $Na_{0.54}TiO_2$ (ICSD # 68872) |
|---|---|---|---|---|
| **a (Å)** | | 2.989 (8) | 3.05414 (4) | 2.9791(6) |
| **c (Å)** | | 15.07 (9) | 16.2412 (2) | 16.9280(30) |
| **V (Å$^3$)** | | 116.60 | 131.20 | 130.11 |
| **Site occupancy** | Na (3a) | 0.43(25) | 0.984(7) | 0.54(1) |
| | Ti (3a) | 0.57(25) | 0.016(7) | 0.0 |
| | Na (3b) | 0.39(14) | 0.016(7) | 0.0 |
| | Ti (3b) | 0.39(1) | 0.984(7) | 1.0 |
| **$d_{Ti/Na-O\ average}$ (Å)** | | 2.022 | 2.075 | 2.021 |
| | | 2.305 | 2.390 | 2.460 |

According to the high energy X-ray analysis, anatase phase was partially recovered when the electrode was charged to 2 V. Thus, a two-phase refinement using $TiO_2$ anatase and O3-type $NaTiO_2$ models was performed to fit the PDF data of the charged electrode (**Figure 4.13**). A poor fit was obtained (Rw = 40.5 %), which might be caused by high disorder in the charged electrode material. The $TiO_2$ anatase shows local ordering only, indicating the amorphization of the electrode. The high disorder prevents extraction of accurate structural information, particularly for $TiO_2$. Proportion of each phase can be obtained by refining the scale factor. The results show that the de-sodiated electrode is composed by 20 % O3-type

$Na_{0.6}TiO_2$ and 80 % $TiO_2$. The retention of sodium titanate indicates that de-sodiation reaction was not complete.

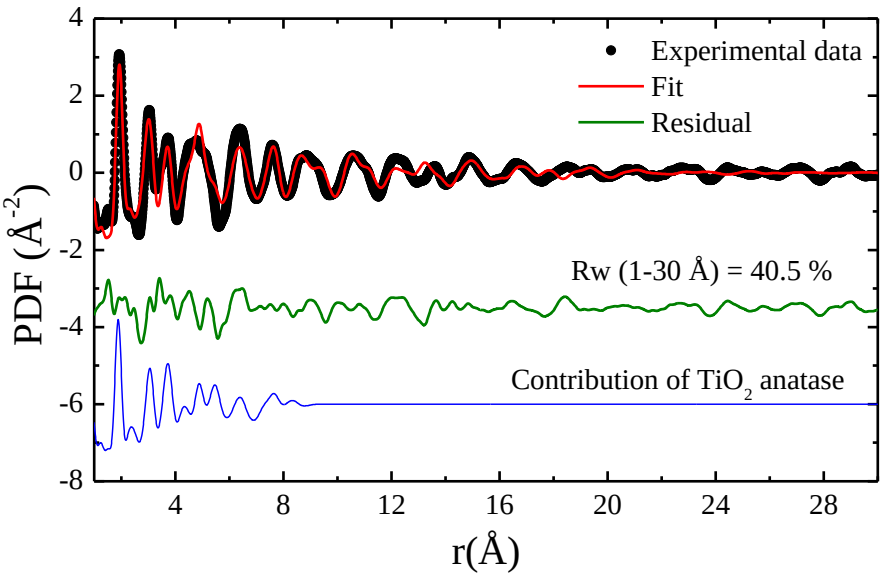


**Figure 4.13:** PDF refinement of the electrode charged to 2 V using O3-type $NaTiO_2$ (space group: R-3m) and $TiO_2$ (space group: $I4_1/amd$) models.

### 3.2.3. Sodium insertion mechanism in $TiO_2$

Electrochemical reaction between sodium and $TiO_2$ anatase was proposed on the basis of high energy X-ray diffraction and PDF analyses. When the cell was discharged to 0.3 V, no structural variation was observed and only side reactions occurred, consuming 0.3 $Na^+$ per $TiO_2$. Further discharging the electrode to 0 V led to sodium insertion in lattice accompanied with reduction of $Ti^{4+}$ to $Ti^{3+}$. The sodiation led to severe amorphization of the electrode material. An irreversible structural rearrangement from $TiO_2$ anatase to amorphous-like defective O3-type sodium titanate $(Na_{0.43}Ti_{0.57})_{3a}(\square_{0.22}Na_{0.39}Ti_{0.39})_{3b}O_2$ phase (space group: R-3m) occurred. The resulting sodium titanate is highly disordered. The structural rearrangement occurring upon sodiation ruled out the reported solid-solution and pseudocapacitance mechanisms.[36,38,42,43] Structure representation of $TiO_2$ anatase and O3-type $NaTiO_2$ is shown in **Figure 4.14**. Upon the extraction of Na-ions, amorphous-like $(Na_{0.43}Ti_{0.57})_{3a}(\square_{0.22}Na_{0.39}Ti_{0.39})_{3b}O_2$ can partially convert to amorphous $TiO_2$, resulting in the reversibility of the Na/$TiO_2$ cell.

The mechanism of structural rearrangement was proposed in the follow. For sodium insertion into anatase network, Shen showed that intercalation of 0.5 $Na^+$ per formula unit $TiO_2$ would cause significant volume expansion (10.08 %).[38] In fact, the maximum volume expansion ever reported was 2.24 %,[44] indicating that high concentration of sodium in anatase structure cannot be achieved through electrochemical sodiation. Furthermore, DFT simulations showed high energy barrier for $Na^+$ diffusion than $Li^+$, preventing $Na^+$ insertion into $TiO_2$ anatase.[38,50] As a result, the anatase framework cannot be retained upon sodiation and a structural rearrangement is necessary. In-situ gas chromatography performed by Wu et al. demonstrated that such a rearrangement induced a release of $O_2$.[39]

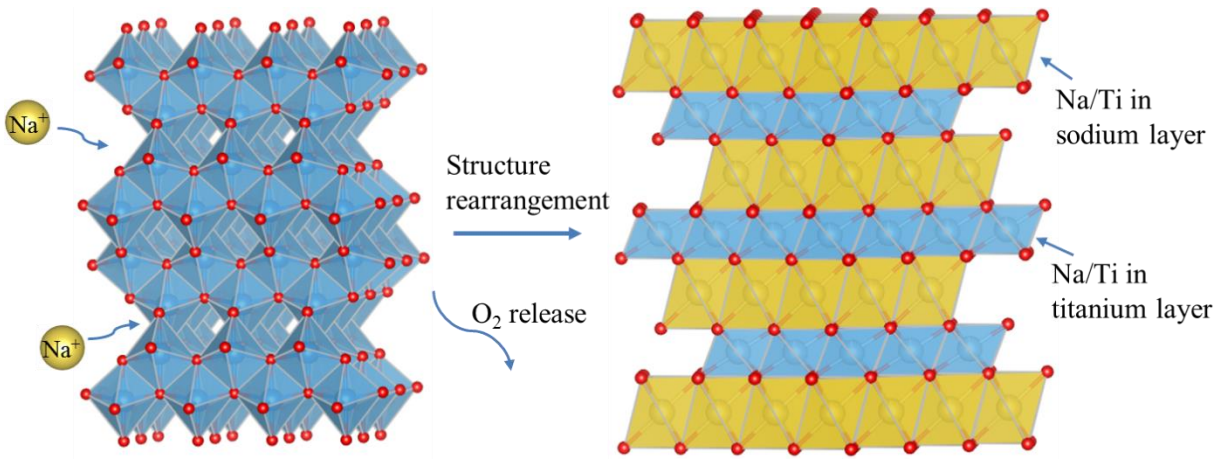


**Figure 4.14:** Sodiation-induced structural rearrangement of $TiO_2$ anatase with space group $I4_1/amd$ (left) to O3-type $NaTiO_2$ with space group R-3m (right). Blue: Ti/Na atom, red: O atom. Yellow octahedral: reported Na layer in $NaTiO_2$.

$TiO_2$ anatase network is composed of zig-zag chains, whereas the O3-type $NaTiO_2$ rhombohedral structure consists of an alternation of Na and Ti layers. During the structural rearrangement, some of Ti atoms in anatase need to migrate to Ti layers in the rhombohedral structure. However, this process should be sluggish upon sodiation. Consequently, some Ti atoms are trapped in the Na layers, and Na atoms are finally inserted to the Ti layers. The intermixing of cations led to strong local cation disorder within $(Na_{0.43}Ti_{0.57})_{3a}(\square_{0.22}Na_{0.39}Ti_{0.39})_{3b}O_2$.

The voltage profile showed solid solution-like potential curve for the 1st charge although phase transition occurred. This phenomenon can be explained by the amorphization and strong disorder in the structure. After the 1st discharge, the coherence length of the electrode material is small (~3 nm). In this case, the voltage profiles of de-sodiation reaction

are strongly affected by surface free energies, leading to a spectrum of voltage profiles of phase transition that produces a sloping curve similar to solid solution mechanism.[7,51] Structural ordering can influence the electrochemical behavior as well.[20,52] Solid solution-like voltage curve has been observed for phase transition of highly disordered $Na_3Fe_3(SO_4)_2(OH)_6$ upon sodium extraction.[52]

Good cyclability of the Na-cell might originate from the amorphization of the electrode. DFT calculations showed that amorphous $TiO_2$ involves insertion sites with largely distributed energy.[50] The lowest $Na^+$ insertion energy is -2.54 eV, smaller than that for crystalline anatase. Therefore, amorphous $TiO_2$ is thermodynamically more favorable for $Na^+$ insertion than crystalline phases.

# 4. Sodium insertion into $Ti_{0.78}\square_{0.22}O_{1.12}F_{0.4}(OH)_{0.48}$

## 4.1. Introduction

Polyanionic cation-defected $Ti_{0.78}\square_{0.22}O_{1.12}F_{0.4}(OH)_{0.48}$ with anatase framework showed modified lithium insertion mechanism: a solid solution reaction *vs.* a 2-phase transition. High content of cation vacancy (22 %) is likely the key point accounting for this modification. When it is used as anode for sodium-ion batteries, cation vacancy might provide additional diffusion path for Na-ion, favoring $Na^+$ insertion into the anatase lattice. Therefore, it is of interest to investigate sodiation process of $Ti_{0.78}\square_{0.22}O_{1.12}F_{0.4}(OH)_{0.48}$. Mechanism of sodium insertion into $TiO_2$ anatase was proposed in the previous part. High diffusion barrier for $Na^+$ induced structural rearrangement of $TiO_2$. The presence of cation vacancy in $Ti_{0.78}\square_{0.22}O_{1.12}F_{0.4}(OH)_{0.48}$ may reduce this energy barrier, thus accommodating $Na^+$ in the interstitial sites in the anatase structure. High energy X-ray diffraction and pair distribution function analyses were used here to reveal sodium insertion mechanism in $Ti_{0.78}\square_{0.22}O_{1.12}F_{0.4}(OH)_{0.48}$.

## 4.2. Results and Discussions

### 4.2.1. Electrochemical characterization

The reaction of sodium insertion into $Ti_{0.78}\square_{0.22}O_{1.12}F_{0.4}(OH)_{0.48}$ can be expressed as:

$$xNa^+ + xe^- + Ti_{0.78}\square_{0.22}O_{1.12}F_{0.4}(OH)_{0.48} = Na_xTi_{0.78}\square_{0.22}O_{1.12}F_{0.4}(OH)_{0.48}\ (x\leq 0.78) \quad \textbf{(Eq. 4.4)}$$

The theoretical capacity based on $Ti^{4+}/Ti^{3+}$ redox couple is 290 mAh/g. The electrochemical tests of $Ti_{0.78}\square_{0.22}O_{1.12}F_{0.4}(OH)_{0.48}$ *vs.* $Na^+$ was performed inside a Na half-cell in a potential window 0 – 2 V under a current density of 10 mA/g. Voltage profile was compared with that for $TiO_2$ anatase. Upon sodiation, voltage of the cell decreased steadily from open circuit voltage to 0 V (**Figure 4.15a**), delivering a capacity of 538 mAh/g. The smooth voltage curve observed during the 1st discharge is in contrast with that for $TiO_2$ anatase that a plateau region locates at ~0.2 V. The contradiction in voltage profile might indicate different insertion mechanism. Similar voltage behavior has been reported for small $TiO_2$ anatase nanoparticles

(7 nm).[38] The sodiation mechanism was proposed to be the surface reaction and there was no $Na^+$ lattice intercalation.

During the 1st charge, the potential of the cell continuously increased from 0 to 2 V, delivering a capacity of 222 mAh/g. High irreversible capacities led to a low coulombic efficiency (41.3 %) for the 1st cycle. A capacity of 237 mAh/g was obtained for the 2nd discharge and 84 % of them were retained upon charging. The operating potential is ca. 0.85 V which is slightly higher than that for $TiO_2$ anatase (0.8 V). This increased potential for $Ti_{0.78}\square_{0.22}O_{1.12}F_{0.4}(OH)_{0.48}$ is originated from the presence of fluorine which has a high ionicity and has been commonly used to increase the operating potential of cathode materials.[53]

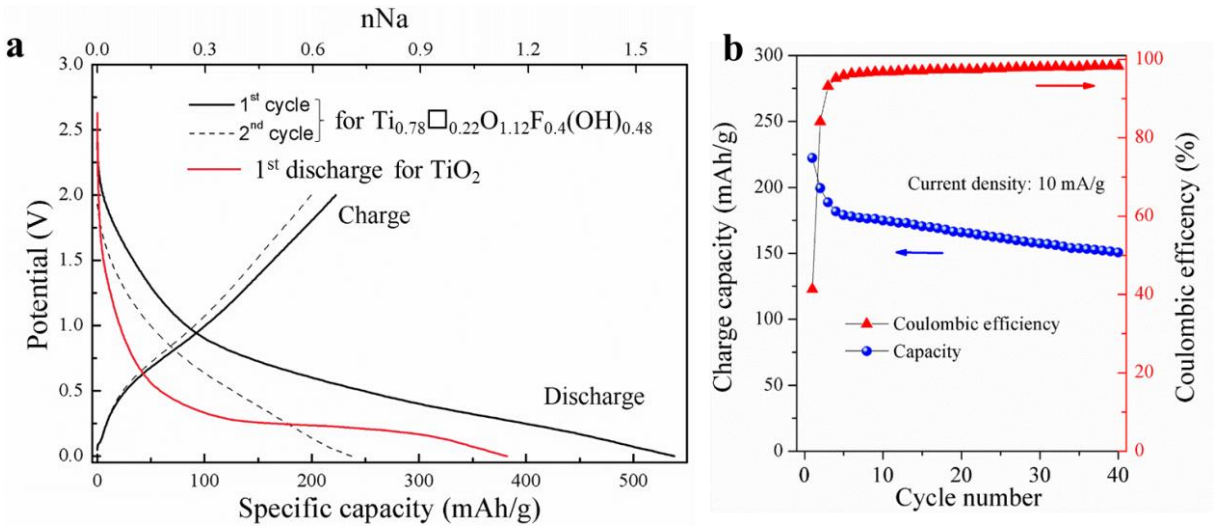


**Figure 4.15:** Electrochemical characterization of $Ti_{0.78}\square_{0.22}O_{1.12}F_{0.4}(OH)_{0.48}$ vs. $Na^+$: (a) voltage profiles, (b) cyclability. The cell was cycled between 0 – 2 V at a current density of 10 mA/g.

The cyclability of the cell is shown in **Figure 4.15b**. The coulombic efficiency increased significantly after a few cycles activation. However, capacity fading took place upon cycling and a capacity of 150 mAh/g, corresponding to 67.5 % of the capacity in the 1st charge, was delivered after 40 cycles of charge and discharge.

## 4.2.2. Structural characterization of sodiated electrodes

### 4.2.2.1.High energy X-ray diffraction

Sodiation of $Ti_{0.78}\square_{0.22}O_{1.12}F_{0.4}(OH)_{0.48}$ was analyzed by high energy X-ray diffraction. The electrodes at three different stages of (de-)sodiation were analyzed: 1st

discharge to 100 mAh/g and to 0 V and 1st charge to 2 V. The high energy X-ray diffraction data are shown in **Figure 4.16a**.

Diffraction reflections for pristine electrode can be indexed to a tetragonal anatase structure with space group $I4_1/amd$. When the electrode was discharged to 100 mAh/g, the decrease of the Bragg peaks indicates decrease in crystallinity of the electrode. The peaks at 2θ = ~ 48 and 55 ° slightly shift to left, indicating expansion of the anatase lattice.

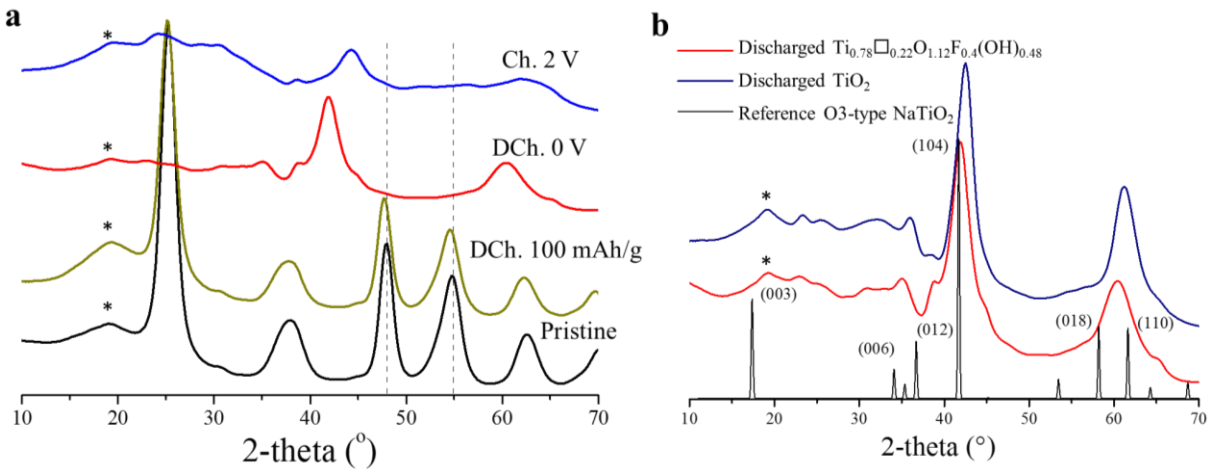


**Figure 4.16:** (a) High energy X-ray diffraction data collected at different stages of sodiation. (b) Comparison with fully discharged $TiO_2$. For seeking clarity, the unit was converted to 2θ by using the wavelength of Cu Kα radiation. Asterisk indicates the signal of sample holder. Dashed lines emphasize the shift of Bragg peaks.

When the electrode was discharged to 0 V, two main peaks emerged at 2θ = ~ 42 and 60 ° indicates phase separation upon sodiation. The newly formed phase displays similar diffraction features with that for fully discharged $TiO_2$ (**Figure 4.16b**), suggesting identical sodium insertion mechanism, that is, phase transition from anatase to O3-type $NaTiO_2$ rhombohedral structure. Note that the main diffraction peaks for the fully discharged $Ti_{0.78}\square_{0.22}O_{1.12}F_{0.4}(OH)_{0.48}$ locate at lower 2θ, indicating larger lattice parameters.

When the cell was charged to 2 V, the main peaks shift to higher 2θ value, indicating the contraction of lattice parameters. Additionally, the occurrence of a broad peak at 2θ = ~ 25° can be attributed to the recovery of the anatase-type structure upon charging.

The high energy X-ray diffraction analysis shows that $Ti_{0.78}\square_{0.22}O_{1.12}F_{0.4}(OH)_{0.48}$ exhibits similar mechanism with $TiO_2$ anatase during the uptake and release of Na-ions. It includes phase transition to rhombohedral structure upon sodiation and partial recovery of

anatase phase upon de-sodiation. However, $Ti_{0.78}\square_{0.22}O_{1.12}F_{0.4}(OH)_{0.48}$ shows a sloping voltage curve during the 1st discharge. Absence of a 2-phase plateau might be a result of continuous electrolyte decomposition.

#### 4.2.2.2.Pair distribution function

**Figure 4.17** shows PDF profiles in r range of $1 \leq r \leq 6$ Å of the electrodes obtained at different stage of (de-)sodiation. The position of the 1st peak was obtained by fitting Gaussian functions and the results are shown in **Table 4.4**.

The 1st peak in PDF, corresponding to the bond length between cation and anion, remains unchanged upon discharging to 100 mAh/g. The peak locates at 1.937 Å is characteristic to $Ti^{4+}$-O/F.

When the electrode was discharged to 0 V, the broadening of PDF peaks indicates structure disorder. The coherence length is ~3 nm, lower than that for the pristine material (7 nm). Such value is similar with that for the fully discharged $TiO_2$ anatase, indicating that the decrease in coherence length upon sodiation is independent with the particle size and chemical composition of the anatase phase. Peak fitting revealed three contributions located at 1.953 , 2.121 and 2.393 Å, characteristic to the bond length of $Ti^{4+}$-O/F, $Ti^{3+}$-O/F and $Na^+$-O/F, respectively. The results indicate that $Na^+$ was inserted into $Ti_{0.78}\square_{0.22}O_{1.12}F_{0.4}(OH)_{0.48}$ causing reduction of $Ti^{4+}$ to $Ti^{3+}$.

Upon sodium extraction (charging), the decrease of $Ti^{3+}$-O/F and $Na^+$-O/F indicates the extraction of $Na^+$ from the electrode material. Residual of these two contributions at the end of charge indicates that the de-sodiation reaction is not complete, a part of $Na^+$ was trapped in the host material.

The intensity of the peak B, corresponding to Ti-Ti/Na in corner-sharing (Ti/Na) octahedra, decreased significantly when the electrode was discharged to 0 V, indicating structural rearrangement upon sodiation. The recovery of this peak at the end of charge indicates that anatase-type structure might be recovered upon de-sodiation.

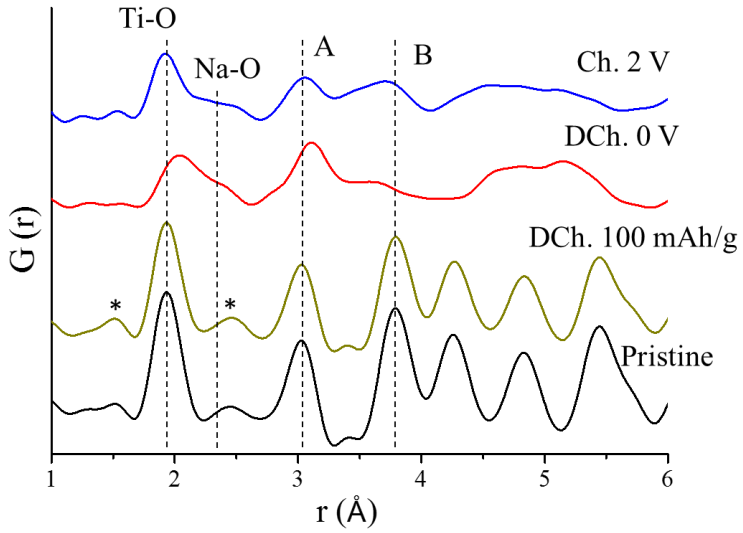


**Figure 4.17:** PDF profiles of the electrodes obtained at different stage of (de-)sodiation. A and B refer to the interatomic distances of Ti-Na/Ti in edge-sharing and corner-sharing $(Ti/Na)O_6$ octahedra, respectively. Asterisk indicates the signal of sample holder.

**Table 4.4: Results of fitting Gaussian function to the 1st peak in PDFs.**

| | **Pristine** | **DCh, 100 mAh/g** | **DCh, 0 V** | | | **Ch, 2 V** | | |
|---|---|---|---|---|---|---|---|---|
| **Position (Å)** | 1.938 | 1.937 | 1.953 | 2.121 | 2.393 | 1.916 | 2.178 | 2.477 |
| **Percentage of area** | | | 26.8% | 56.5% | 16.7% | 58.5% | 32.6% | 8.9% |

**PDF refinement**

The PDF refinement of the electrode discharged to 100 mAh/g was performed using cation-defected $TiO_2$ anatase model $Ti_xO_2$. A good fit was obtained with a reliability factor Rw = 25.9 %. It can be improved to Rw = 25.2 % by adding Na in the interstitial (8e) and Ti (4a) sites, that is $(Na_y)_{8e}(Na_zTi_x)_{4a}O_2$.

The refined structural parameters are compared with that for the pristine electrode (**Table 4.5**). It is shown that the lattice parameters of the anatase phase increased slightly upon sodium insertion, leading to a volume expansion of 0.8 %. The refined occupancy for Na (4a) and Na (8e) is 0.06 and 0.08, respectively. The results indicate that sodium can insert into the cation vacancies and interstitial sites in the cation-defected fluorinated anatase through a solid solution reaction. The number of inserted Na-ions corresponds to a capacity of 52 mAh/g.

The ability of $Na^+$ accommodation by $Ti_{0.78}\square_{0.22}O_{1.12}F_{0.4}(OH)_{0.48}$ might be attributed to both size effect and incorporation of cation vacancies. Cation vacancies can serve as vacant sites for $Na^+$ insertion. It has been shown that $Li^+$ can insert in nanosized $TiO_2$ anatase through a solid solution reaction prior to the well-known 2-phase reaction.[1,14] The number of $Li^+$ in the monophasic reaction increases with reducing particle size of $TiO_2$.[6,15] Similarly, $Ti_{0.78}\square_{0.22}O_{1.12}F_{0.4}(OH)_{0.48}$ with particle sizes of ca. 7 nm might be capable of accommodating $Na^+$ in its interstitial sites.

**Table 4.5: Structure parameters of fitting anatase model to the PDFs of the electrodes of pristine and discharged to 100 mAh/g.**

| | **Pristine** | **Discharged to 100 mAh/g** |
|---|---|---|
| **Symmetry** | $I4_1/amd$[a] | $I4_1/amd$[a] |
| **a (Å)** | 3.792 (1) | 3.805 (1) |
| **c (Å)** | 9.481 (5) | 9.490 (6) |
| **V (Å$^3$)** | 136.3 | 137.4 |
| **Ti(4a) (x,y,z)** | 0,0.75,0.125 | 0,0.75,0.125 |
| **O (8e) (x,y,z)** | 0,0.75,0.3367 (7) | 0,0.75,0.3356 (6) |
| **Na (8e) (x,y,z)** | | 0,0.75,0.537 (6) |
| **Na (4a) occupancy** | | 0.06 (7) |
| **Na (8e) occupancy** | | 0.08 (3) |

[a] Origin choice 2.

PDF refinement of the fully discharged $Ti_{0.78}\square_{0.22}O_{1.12}F_{0.4}(OH)_{0.48}$ followed the same procedure with that for the fully discharged $TiO_2$, as shown previously. O3-type $NaTiO_2$ (space group: R-3m) structure was fitted against the PDF (**Figure 4.18**). A good fit was obtained for the r range 4 – 30 Å (Rw = 28.4 %). However, the local range cannot be well fitted by the model, resulting in a high value of reliability factor (Rw = 39.1 % for 1 – 30 Å). The 2$^{nd}$ peak at ~3 Å in the PDF, corresponding to the distance of cation-cation in edge-sharing $(Ti/Na)X_6$ octahedra, was hardly reproduced, indicating cation disorder in the rhombohedral structure.

The results of the PDF refinement of the fully discharged $Ti_{0.78}\square_{0.22}O_{1.12}F_{0.4}(OH)_{0.48}$ are gathered in **Table 4.6**. The 3a sites in the rhombohedral structure are almost fully occupied with 60 % Na and 38 % Ti. The 3b sites are defective with 16 % Na and 54 % Ti. The chemical formula of the refined phase is $Na_{0.76}Ti_{0.92}O_2$. The fully occupied 3a sites was also observed for fully discharged $TiO_2$. Fully discharged $Ti_{0.78}\square_{0.22}O_{1.12}F_{0.4}(OH)_{0.48}$ shows

larger lattice parameters, which might be due to that, for fully discharged $TiO_2$, more Ti atoms occupy 3a sites, leading to strong contraction of the lattice.

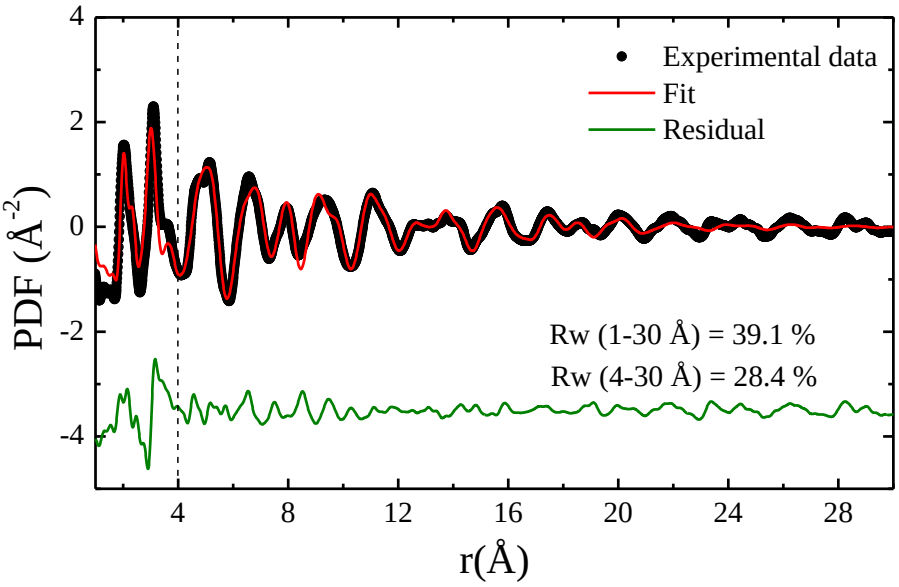


**Figure 4.18:** PDF refinement of the fully discharged electrode using O3-type $NaTiO_2$ (space group: R-3m) model.

**Table 4.6: Comparison of the results obtained from the PDF refinement the fully discharged $Ti_{0.78}\square_{0.22}O_{1.12}F_{0.4}(OH)_{0.48}$ and $TiO_2$ anatase by using O3-type $NaTiO_2$ model.**

| | | **Fully discharged $Ti_{0.78}\square_{0.22}O_{1.12}F_{0.4}(OH)_{0.48}$** | **Fully discharged $TiO_2$ anatase** |
|---|---|---|---|
| **a (Å)** | | 3.010(9) | 2.989(8) |
| **c (Å)** | | 15.36(9) | 15.07(9) |
| **V (Å$^3$)** | | 120.53 | 116.60 |
| **O (0,0,z)** | | 0, 0, 0.234(3) | 0, 0, 0.235(2) |
| **Site occupancy** | Na (3a) | 0.60(20) | 0.43(25) |
| | Ti (3a) | 0.38(12) | 0.57(25) |
| | Na (3b) | 0.16(18) | 0.39(14) |
| | Ti (3b) | 0.54(13) | 0.39(1) |
| **Thermal displacement parameters** | | U (Na/Ti in 3a site) = 0.035(6)<br>U (Na/Ti in 3b site) = 0.036(7)<br>U (O) = 0.029(6) | U (Na/Ti in 3a site) = 0.034(4)<br>U (Na/Ti in 3b site) = 0.035(6)<br>U (O) = 0.023(4) |

PDF fit of the fully charged electrode was performed using a 2-phase refinement involving $TiO_2$ anatase and O3-type $NaTiO_2$ models (**Figure 4.19**). The low quality of the refinement (Rw = 38.7 %) is due to strong disorder in the de-sodiated material. The refined spherical particle size of $TiO_2$ anatase is 9(1) Å, indicating the amorphization of the electrode upon charge. Refining scale factors of these two phases shows that the de-sodiated electrode

was composed by 75 % $TiO_2$ and 25 % $Na_{0.19}TiO_2$. The de-sodiation reaction was not complete as part of sodium titanate retained.

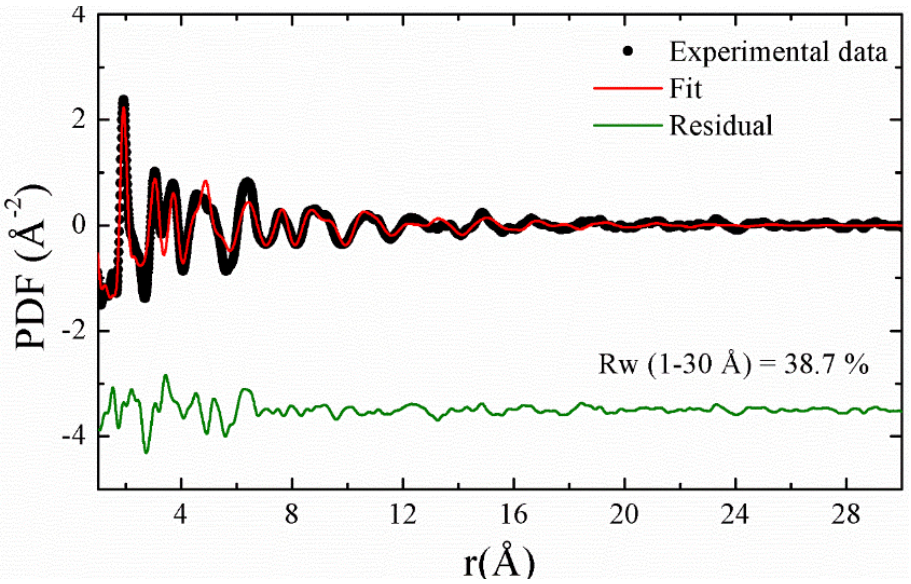


**Figure 4.19:** PDF refinement of the electrode charged to 2 V using O3-type $NaTiO_2$ (space group: R-3m) and $TiO_2$ (space group: $I4_1/amd$) models.

# 5. Conclusion

In this chapter, the electrochemical properties of $Ti_{0.78}\square_{0.22}O_{1.12}F_{0.4}(OH)_{0.48}$ and $TiO_2$ anatase vs. $Li^+/Na^+$ were studied. Lithium and sodium insertion mechanisms were investigated by GITT, high energy X-ray diffraction and pair distribution function analyses.

Electrochemical reaction between lithium and $Ti_{0.78}\square_{0.22}O_{1.12}F_{0.4}(OH)_{0.48}$ was first studied. $Ti_{0.78}\square_{0.22}O_{1.12}F_{0.4}(OH)_{0.48}$ exhibited good rate capability than pure $TiO_2$ anatase, particularly at high current density. The test of cyclability at extremely high rate showed excellent long-cycle capacity retention. Lithium insertion mechanism was investigated. $Ti_{0.78}\square_{0.22}O_{1.12}F_{0.4}(OH)_{0.48}$ showed a solid solution reaction instead of a well-established 2-phase reaction for pure $TiO_2$. Modification in $Li^+$ insertion mechanism might be ascribed to the incorporation of cation vacancies which prevent orthorhombic distortion driven by pairing effect of edge-sharing $LiO_6$ octahedra. The superior lithium storage performance can be attributed to size effect, surface orientation, defect chemistry and the modification of insertion mechanism. This study highlights the benefits of structure modification for enhanced lithium storage performance.

In the second part, high energy X-ray diffraction and PDF analyses provided new insights into sodium insertion in $TiO_2$ anatase. Based on these studies, the electrochemical reaction mechanism between Na and $TiO_2$ was proposed. $Na^+$ can insert into the host material on the basis of $Ti^{4+}/Ti^{3+}$ redox couple, leading to an irreversible phase transition to rhombohedral O3-type $(Na_{0.43}Ti_{0.57})_{3a}(\square_{0.22}Na_{0.39}Ti_{0.39})_{3b}O_2$ structure, which manifests as a plateau region in the voltage profile. The $Na^+$ insertion led to amorphization and strong disorder in the rhombohedral phase, thus modifying the subsequent electrochemical behavior. Intermixing of Ti and Na atoms was also observed in this defective structure, resulting in cation disorder and the contraction of lattice. Upon charge, part of defective sodium titanate can reversibly convert to amorphous $TiO_2$, giving rise to the cyclability of the $Na/TiO_2$ cell. The newly formed active $(Na_{0.43}Ti_{0.57})_{3a}(\square_{0.22}Na_{0.39}Ti_{0.39})_{3b}O_2$ appears as promising anode materials for sodium-ion batteries. This study provided structural information of the sodiated phase that has never been reported in the literature.

The third part was dedicated to investigate the electrochemical reaction of sodium and $Ti_{0.78}\square_{0.22}O_{1.12}F_{0.4}(OH)_{0.48}$. It exhibited similar $Na^+$ insertion mechanism with that for $TiO_2$ anatase. On the basis of $Ti^{4+}/Ti^{3+}$ redox couple, sodium can insert in the anatase lattice,

causing phase transition from anatase to rhombohedral structure. However, prior to phase transition, $Ti_{0.78}\square_{0.22}O_{1.12}F_{0.4}(OH)_{0.48}$ can accommodate 0.14 $Na^+$ in its Ti vacancy and interstitial sites through solid solution reaction. This behavior might be due to size effect and/or the presence of cation vacancy. This study indicates that, differing from $Li^+$ insertion, the presence of cation vacancy in the anatase structure cannot modify the $Na^+$ insertion mechanism.

# References

(1) Sudant, G.; Baudrin, E.; Larcher, D.; Tarascon, J.-M. Electrochemical lithium reactivity with nanotextured anatase-type $TiO_2$. *J. Mater. Chem.* **2005**, *15*, 1263.

(2) Shin, J.-Y.; Samuelis, D.; Maier, J. Sustained Lithium-Storage Performance of Hierarchical, Nanoporous Anatase $TiO_2$ at High Rates: Emphasis on Interfacial Storage Phenomena. *Adv. Funct. Mater.* **2011**, *21*, 3464.

(3) Gentili, V.; Brutti, S.; Hardwick, L. J.; Armstrong, A. R.; Panero, S.; Bruce, P. G. Lithium Insertion into Anatase Nanotubes. *Chem. Mater.* **2012**, *24*, 4468.

(4) Ren, Y.; Hardwick, L. J.; Bruce, P. G. Lithium Intercalation into Mesoporous Anatase with an Ordered 3D Pore Structure. *Angew. Chem. Int. Ed.* **2010**, *49*, 2570.

(5) Cava, R. J.; Murphy, D. W.; Zahurak, S.; Santoro, A.; Roth, R. S. The crystal structures of the lithium-inserted metal oxides $Li_{0.5}TiO_2$ anatase, $LiTi_2O_4$ spinel, and $Li_2Ti_2O_4$. *J. Solid State Chem.* **1984**, *53*, 64.

(6) Wagemaker, M.; Borghols, W. J. H.; Mulder, F. M. Large Impact of Particle Size on Insertion Reactions. A Case for Anatase $Li_xTiO_2$. *J. Am. Chem. Soc.* **2007**, *129*, 4323.

(7) Wagemaker, M.; Mulder, F. M. Properties and Promises of Nanosized Insertion Materials for Li-Ion Batteries. *Acc. Chem. Res.* **2013**, *46*, 1206.

(8) Sun, C. H.; Yang, X. H.; Chen, J. S.; Li, Z.; Lou, X. W.; Li, C.; Smith, S. C.; Lu, G. Q.; Yang, H. G. Higher charge/discharge rates of lithium-ions across engineered $TiO_2$ surfaces leads to enhanced battery performance. *Chem. Commun.* **2010**, *46*, 6129.

(9) Liu, G.; Yin, L.-C.; Pan, J.; Li, F.; Wen, L.; Zhen, C.; Cheng, H.-M. Greatly Enhanced Electronic Conduction and Lithium Storage of Faceted $TiO_2$ Crystals Supported on Metallic Substrates by Tuning Crystallographic Orientation of $TiO_2$. *Adv. Mater.* **2015**, *27*, 3507.

(10) Jung, W. I.; Sakamoto, K.; Pitteloud, C.; Sonoyama, N.; Yamada, A.; Kanno, R. Chemically oxidized manganese dioxides for lithium secondary batteries. *J. Power Sources* **2007**, *174*, 1137.

(11) Koo, B.; Xiong, H.; Slater, M. D.; Prakapenka, V. B.; Balasubramanian, M.; Podsiadlo, P.; Johnson, C. S.; Rajh, T.; Shevchenko, E. V. Hollow Iron Oxide Nanoparticles for Application in Lithium Ion Batteries. *Nano Lett.* **2012**, *12*, 2429.

(12) Li, Y.; Feng, Y.; Feng, W. Deeply fluorinated multi-wall carbon nanotubes for high energy and power densities lithium/carbon fluorides battery. *Electrochim. Acta* **2013**, *107*, 343.

(13) Brutti, S.; Gentili, V.; Menard, H.; Scrosati, B.; Bruce, P. G. $TiO_2$-(B) Nanotubes as Anodes for Lithium Batteries: Origin and Mitigation of Irreversible Capacity. *Adv. Energy Mater.* **2012**, *2*, 322.

(14) Wagemaker, M.; Kearley, G. J.; van Well, A. A.; Mutka, H.; Mulder, F. M. Multiple Li Positions inside Oxygen Octahedra in Lithiated $TiO_2$ Anatase. *J. Am. Chem. Soc.* **2003**, *125*, 840.

(15) Shen, K.; Chen, H.; Klaver, F.; Mulder, F. M.; Wagemaker, M. Impact of Particle Size on the Non-Equilibrium Phase Transition of Lithium-Inserted Anatase $TiO_2$. *Chem. Mater.* **2014**, *26*, 1608.

(16) Borghols, W. J. H.; Lutzenkirchen-Hecht, D.; Haake, U.; van Eck, E. R. H.; Mulder, F. M.; Wagemaker, M. The electronic structure and ionic diffusion of nanoscale $LiTiO_2$ anatase. *Phys. Chem. Chem. Phys.* **2009**, *11*, 5742.

(17) Morgan, B. J.; Watson, G. W. Role of Lithium Ordering in the $Li_xTiO_2$ Anatase → Titanate Phase Transition. *J. Phys. Chem. Lett.* **2011**, *2*, 1657.

(18) Patra, S.; Davoisne, C.; Bruyère, S.; Bouyanfif, H.; Cassaignon, S.; Taberna, P.-L.; Sauvage, F. Room-Temperature Synthesis of High Surface Area Anatase $TiO_2$ Exhibiting a Complete Lithium Insertion Solid Solution. *Part. Part. Syst. Charact.* **2013**, *30*, 1093.

(19) Patra, S.; Davoisne, C.; Bouyanfif, H.; Foix, D.; Sauvage, F. Phase stability frustration on ultra-nanosized anatase $TiO_2$. *Sci. Rep.* **2015**, *5*, 10928.

(20) Gibot, P.; Casas-Cabanas, M.; Laffont, L.; Levasseur, S.; Carlach, P.; Hamelet, S.; Tarascon, J. M.; Masquelier, C. Room-temperature single-phase Li insertion/extraction in nanoscale $Li_xFePO_4$. *Nat. Mater.* **2008**, *7*, 741.

(21) Bousa, M.; Laskova, B.; Zukalova, M.; Prochazka, J.; Chou, A.; Kavan, L. Polycrystalline $TiO_2$ Anatase with a Large Proportion of Crystal Facets (001): Lithium Insertion Electrochemistry. *J. Electrochem. Soc.* **2010**, *157*, A1108.

(22) Hahn, B. P.; Long, J. W.; Rolison, D. R. Something from Nothing: Enhancing Electrochemical Charge Storage with Cation Vacancies. *Acc. Chem. Res.* **2013**, *46*, 1181.

(23) Liu, H.; Strobridge, F. C.; Borkiewicz, O. J.; Wiaderek, K. M.; Chapman, K. W.; Chupas, P. J.; Grey, C. P. Capturing metastable structures during high-rate cycling of $LiFePO_4$ nanoparticle electrodes. *Science* **2014**, *344*, 1252817.

(24) Goodenough, J. B.; Kim, Y. Challenges for Rechargeable Li Batteries. *Chem. Mater.* **2010**, *22*, 587.

(25) Tarascon, J. M.; Armand, M. Issues and challenges facing rechargeable lithium batteries. *Nature* **2001**, *414*, 359.

(26) Whittingham, M. S. Lithium Batteries and Cathode Materials. *Chem. Rev.* **2004**, *104*, 4271.

(27) Dunn, B.; Kamath, H.; Tarascon, J.-M. Electrical Energy Storage for the Grid: A Battery of Choices. *Science* **2011**, *334*, 928.

(28) Yabuuchi, N.; Kubota, K.; Dahbi, M.; Komaba, S. Research Development on Sodium-Ion Batteries. *Chem. Rev.* **2014**, *114*, 11636.

(29) Pan, H.; Hu, Y.-S.; Chen, L. Room-temperature stationary sodium-ion batteries for large-scale electric energy storage. *Energy Environ. Sci.* **2013**, *6*, 2338.

(30) Kundu, D.; Talaie, E.; Duffort, V.; Nazar, L. F. The Emerging Chemistry of Sodium Ion Batteries for Electrochemical Energy Storage. *Angew. Chem. Int. Ed.* **2015**, *54*, 3431.

(31) Dahbi, M.; Yabuuchi, N.; Kubota, K.; Tokiwa, K.; Komaba, S. Negative electrodes for Na-ion batteries. *Phys. Chem. Chem. Phys.* **2014**, *16*, 15007.

(32) Colbow, K. M.; Dahn, J. R.; Haering, R. R. Structure and electrochemistry of the spinel oxides $LiTi_2O_4$ and $Li_{4/3}Ti_{5/3}O_4$. *J. Power Sources* **1989**, *26*, 397.

(33) Scharner, S.; Weppner, W.; Schmid‐Beurmann, P. Evidence of Two‐Phase Formation upon Lithium Insertion into the $Li_{1.33}Ti_{1.67}O_4$ Spinel. *J. Electrochem. Soc.* **1999**, *146*, 857.

(34) Sun, Y.; Zhao, L.; Pan, H.; Lu, X.; Gu, L.; Hu, Y.-S.; Li, H.; Armand, M.; Ikuhara, Y.; Chen, L.; Huang, X. Direct atomic-scale confirmation of three-phase storage mechanism in $Li_4Ti_5O_{12}$ anodes for room-temperature sodium-ion batteries. *Nat. Comm.* **2013**, *4*, 1870.

(35) Xu, Y.; Memarzadeh Lotfabad, E.; Wang, H.; Farbod, B.; Xu, Z.; Kohandehghan, A.; Mitlin, D. Nanocrystalline anatase $TiO_2$: a new anode material for rechargeable sodium ion batteries. *Chem. Commun.* **2013**, *49*, 8973.

(36) Kim, K.-T.; Ali, G.; Chung, K. Y.; Yoon, C. S.; Yashiro, H.; Sun, Y.-K.; Lu, J.; Amine, K.; Myung, S.-T. Anatase Titania Nanorods as an Intercalation Anode Material for Rechargeable Sodium Batteries. *Nano Lett.* **2014**, *14*, 416.

(37) Cha, H. A.; Jeong, H. M.; Kang, J. K. Nitrogen-doped open pore channeled graphene facilitating electrochemical performance of $TiO_2$ nanoparticles as an anode material for sodium ion batteries. *J. Mater. Chem. A* **2014**, *2*, 5182.

(38) Shen, K. Thesis, *Lithium and Sodium Insertion in Nanostructured Titanates*, Delft University of Technology, 2014.

(39) Wu, L.; Bresser, D.; Buchholz, D.; Giffin, G. A.; Castro, C. R.; Ochel, A.; Passerini, S. Unfolding the Mechanism of Sodium Insertion in Anatase $TiO_2$ Nanoparticles. *Adv. Energy Mater.* **2015**, *5*, 1401142.

(40) Dambournet, D.; Chapman, K. W.; Chupas, P. J.; Gerald, R. E.; Penin, N.; Labrugere, C.; Demourgues, A.; Tressaud, A.; Amine, K. Dual lithium insertion and conversion mechanisms in a titanium-based mixed-anion nanocomposite. *J. Am. Chem. Soc.* **2011**, *133*, 13240.

(41) Wu, L.; Buchholz, D.; Bresser, D.; Gomes Chagas, L.; Passerini, S. Anatase $TiO_2$ nanoparticles for high power sodium-ion anodes. *J. Power Sources* **2014**, *251*, 379.

(42) Gonzalez, J. R.; Alcantara, R.; Nacimiento, F.; Ortiz, G. F.; Tirado, J. L. Microstructure of the epitaxial film of anatase nanotubes obtained at high voltage and the mechanism of its electrochemical reaction with sodium. *CrystEngComm* **2014**, *16*, 4602.

(43) Yan, D.; Yu, C.; Bai, Y.; Zhang, W.; Chen, T.; Hu, B.; Sun, Z.; Pan, L. Sn-doped $TiO_2$ nanotubes as superior anode materials for sodium ion batteries. *Chem. Commun.* **2015**, *51*, 8261.

(44) Clarke, S. J.; Fowkes, A. J.; Harrison, A.; Ibberson, R. M.; Rosseinsky, M. J. Synthesis, Structure, and Magnetic Properties of $NaTiO_2$. *Chem. Mater.* **1998**, *10*, 372.

(45) Maazaz, A.; Delmas, C.; Hagenmuller, P. A study of the $Na_xTiO_2$ system by electrochemical deintercalation. *J. Inclusion Phenom.* **1983**, *1*, 45.

(46) Akimoto, J.; Takei, H. Growth and structure analysis of nonstoichiometric single crystal $NaxTiO_2$ ($x \sim 0.5$)with the α-$NaFeO_2$-type structure. *J. Solid State Chem.* **1990**, *85*, 31.

(47) Billinge, S. J. L.; Levin, I. The problem with determining atomic structure at the nanoscale. *Science* **2007**, *316*, 561.

(48) Yabuuchi, N.; Yoshii, K.; Myung, S.-T.; Nakai, I.; Komaba, S. Detailed Studies of a High-Capacity Electrode Material for Rechargeable Batteries, $Li_2MnO_3$−$LiCo_{1/3}Ni_{1/3}Mn_{1/3}O_2$. *J. Am. Chem. Soc.* **2011**, *133*, 4404.

(49) Tran, N.; Croguennec, L.; Ménétrier, M.; Weill, F.; Biensan, P.; Jordy, C.; Delmas, C. Mechanisms Associated with the "Plateau" Observed at High Voltage for the Overlithiated $Li_{1.12}(Ni_{0.425}Mn_{0.425}Co_{0.15})_{0.88}O_2$ System. *Chem. Mater.* **2008**, *20*, 4815.

(50) Legrain, F.; Malyi, O.; Manzhos, S. Insertion energetics of lithium, sodium, and magnesium in crystalline and amorphous titanium dioxide: A comparative first-principles study. *J. Power Sources* **2015**, *278*, 197.

(51) Van der Ven, A.; Wagemaker, M. Effect of surface energies and nano-particle size distribution on open circuit voltage of Li-electrodes. *Electrochem. Commun.* **2009**, *11*, 881.

(52) Gnanavel, M.; Lebedev, O. I.; Bazin, P.; Raveau, B.; Pralong, V. Reversible transformation from amorphouse $Na_3Fe_3(SO_4)_2(OH)_6$ to crystallized $NaFe_3(SO_4)_2(OH)_6$ Jarosite-type hydroxysulfate. *Solid State Ionics* **2015**, *278*, 38.

(53) Barpanda, P.; Tarascon, J. M. In *Lithium Batteries*; John Wiley & Sons, Inc.: 2013, p 127.

# General Conclusion and Perspectives

## General conclusion

$TiO_2$ is a multi-functional material that is widely used for applications in the domain of energy conversion and storage. It is a good candidate as anode material for lithium-ion batteries due to the reliability, safety and high power density. The increase of the demand of sustainable energy resources by portable devices, hybrid and electrical vehicles has stimulated the study of $TiO_2$ in the community of material science and engineering. Directly related to this topic, this thesis aims at tuning the physical-chemical properties of $TiO_2$ through structural, compositional and morphological modifications. To do that, we employed a low temperature solution-based synthesis method performed in fluorine medium. This method allows the finest control over size, morphology and composition of $TiO_2$ particles. Focused on $TiO_2$ modification and applications in energy storage, this thesis can be divided into three part:

1. Synthesis of cation-defected fluorinated anatase $Ti_{0.78}\square_{0.22}O_{1.12}F_{0.40}(OH)_{0.48}$ and the study of its formation mechanism;
2. Study the effect of synthesis parameters for better control of the structure, morphology and composition of $TiO_2$ anatase;
3. Electrochemical properties of $TiO_2/Ti_{0.78}\square_{0.22}O_{1.12}F_{0.40}(OH)_{0.48}$ vs. $Li^+$ and $Na^+$ ions.

In the first part, cation-defected fluorinated $Ti_{0.78}\square_{0.22}O_{1.12}F_{0.40}(OH)_{0.48}$ nanoparticles showing anatase network were synthesized solvothermally at a temperature of 90 °C by using $Ti(O^iPr)_4$ as precursor, $Pr^iOH$ as solvent and aqueous HF as fluorolysis and hydrolysis agent. The creation of cation vacancy was achieved by the compensation of negative charge induced by the substitution of divalent anions $O^{2-}$ by monovalent anions $F^-/OH^-$. Both cationic and anionic sublattice modifications highlight the versatility of the anatase structure. Three fluorine coordination modes ($Ti_3$-F, $Ti_2\square_1$-F and $Ti_1\square_2$-F) were found within $Ti_{0.78}\square_{0.22}O_{1.12}F_{0.40}(OH)_{0.48}$. A preferential localization of fluorine close to cation vacancy was shown experimentally. Such fluorine/vacancy ordering was confirmed by DFT modelling

that the system energy decreases as a function of the number of fluorine located close to vacancy.

The formation mechanism of $Ti_{0.78}\square_{0.22}O_{1.12}F_{0.40}(OH)_{0.48}$ was subsequently studied by analyzing samples collected at different reaction time. A two steps mechanism involving firstly the dissolution/recrystallization of amorphous intermediate $TiOF_2$ and secondly structural rearrangement of anatase phase was reported on the basis of structural and compositional analyses. The structural rearrangement accompanied with chemical composition modification of the anatase phase provides path of controlling the substitution rate in cation-defected $Ti_{1-x-y}\square_{x+y}O_{2-4(x+y)}F_{4x}(OH)_{4y}$ by tuning the reaction time.

In the second part, we were curious about the effect of the reaction parameters on the resulting phase formed in fluorine medium. Thus, a systematical study was carried out to investigate structural, compositional and morphological effects of the synthesis parameters including the nature of precursor, solvent and the concentration of reactants as well as the reaction temperature. The nature of alcohol solvent played important role on determining the structure of the resulting phase and little influence of the nature of precursor was observed. The fluorine content can influence the geometry and linking mode of the Ti building blocks, thus inducing phase change when varying the fluorine content. However, only anatase phase with different substitution rate can be stabilized in ethanol, allowing controlling the chemical composition of the anatase phase.

Great efforts were subsequently conducted on studying the effect of reaction temperature. We showed that temperature affects particle size, morphology and chemical compositions of the resulting anatase phase. The chemical composition in terms of the concentration of fluorine and cation vacancies of the anatase phase can be tuned by varying reaction temperature. Combining with the study of the formation mechanism, we are now able to control the structure, morphology and chemical composition of the cation-defected fluorinated anatase phase.

Titanium-based compounds have been widely used as electrode for rechargeable $Li^+/Na^+$ batteries. Hence, we studied, in the third part, the electrochemical properties of strongly defective $Ti_{0.78}\square_{0.22}O_{1.12}F_{0.40}(OH)_{0.48}$ and $TiO_2$ anatase. The lithium insertion in $Ti_{0.78}\square_{0.22}O_{1.12}F_{0.40}(OH)_{0.48}$ behaved a solid solution mechanism versus a well-known phase transition. Such a modified lithium insertion mechanism can be ascribed to the defect

chemistry. The origin of fast charge/discharge ability of $Ti_{0.78}\square_{0.22}O_{1.12}F_{0.40}(OH)_{0.48}$ was ascribed to size effect, surface orientation, defect chemistry and modified $Li^+$ insertion mechanism. This study highlights the importance of composition-structure-properties correlation and the benefit of the defect chemistry on electrochemical response of materials.

The electrochemical properties of $TiO_2$ anatase vs. $Na^+$ was then investigated. A 1st charging capacity of 200 mAh/g can be delivered by the $Na/TiO_2$ cell on the basis of $Ti^{4+}/Ti^{3+}$ redox couple. A good capacity retention was then observed for the subsequent 50 cycles. The operating potential is 0.8 V, lower than Li-cell. Mechanistic study regrading $Na^+$ insertion explained the change in voltage curve for the 1st discharge and subsequent cycles. An irreversible phase transition (structural rearrangement) from anatase to disordered rhombohedral O3-type $(Na_{0.43}Ti_{0.57})_{3a}(\square_{0.22}Na_{0.39}Ti_{0.39})_{3b}O_2$ layered structure was demonstrated accompanied by the amorphization of electrode. Intermixing of Ti and Na was observed in this defective structure, leading to strong local cation disorder. The sodium insertion mechanism is different with that for $Li^+$, which is attributed to larger $Na^+$ radius that structure rearrangement of anatase phase is needed upon sodiation. The resulting defective sodium titanate can reversibly convert to amorphous $TiO_2$ during $Na^+$ release, giving rise to the cyclability of the Na-cell.

Sodium insertion into $Ti_{0.78}\square_{0.22}O_{1.12}F_{0.40}(OH)_{0.48}$ was also studied. The cation-defected anatase phase showed similar $Na^+$ insertion mechanism with the stoichiometric $TiO_2$, Interestingly, $Ti_{0.78}\square_{0.22}O_{1.12}F_{0.40}(OH)_{0.48}$ can accommodate 0.14 $Na^+$ within the lattice through solid solution reaction prior to the phase transition.

This thesis provides a new method to introduce defects into titanium dioxide and to control its chemical composition. In the study of the formation mechanism of cation-defected anatase, we gained more insights into what happens in solution-based synthesis in fluorine medium. The study of the effects of synthesis parameters provides the ability of tuning the structure, morphology and chemical composition of the anatase phase. When the cation-defected anatase is used as electrode material for Li-ions batteries, the enhanced electrochemical performances highlight the benefits of structural modification on the lithium storage. The investigation of $Na^+$ insertion properties into $TiO_2$ and defective anatase phases provides unprecedented structural insights into the amorphization of $TiO_2$ anatase upon sodiation. The identification of disordered amorphous-like phase demonstrates the value of high energy X-ray diffraction and PDF analyses for the characterization of electrode material.

**Perspectives**

This thesis is the first step of introducing high concentration of cation vacancies by high substitutional rate in titanium dioxide. The solution-based low temperature method can be further applicable to tune the chemical composition and to create defects for other relevant metal oxides materials. Optimization of the chemical composition of $Ti_{1-x-y}\square_{x+y}O_{2-4(x+y)}F_{4x}(OH)_{4y}$ is necessary for better electrochemical performance vs. $Li^+$. The presence of vacancies in the cation-defected anatase led to enhanced lithium insertion properties. The effect of the concentration of vacancies should be studied in the future. The chemical states of Li in the lithiated $Ti_{0.78}\square_{0.22}O_{1.12}F_{0.40}(OH)_{0.48}$ and the possibility of $Li^+$ accommodation by vacancies would be of particular interest. Finally, the $Na^+$ insertion mechanism in $TiO_2$ anatase phase should be confirmed by in operando techniques.

# Appendix 1. X-ray diffraction characterization

The powder X-ray diffraction data were collected using a Rikaku diffractometer, equipped with Cu Kα radiation, in a Bragg-Brentano geometry.

**Calculation of average particle size of $TiO_2$ anatase**

X-ray diffraction patterns were used to estimate the particle sizes. They can be calculated on the basis of the reflection of (101) plane at 2θ (Cu Kα) = ~ 25 ° by using the Debye-Scherrer equation:

$$t_{(hkl)}(nm) = \frac{0.09\lambda}{2\Delta(\theta)\cos\theta}$$

Where $\lambda$ is the X-ray wavelength from Cu Kα radiation source with $\lambda$ = 1.5418 Å; $\theta$ is half of the angle where the peak locate at; full width at half-maximum (fwhm) of the peak at $2\theta$ is represented as $\Delta(\theta)$ which is obtained by fitting the Gaussian function within Fityk,[1] the width of the diffraction peak is considered to be effected by particle size only.

**Calculation of the proportion of exposed {001} facets**

According to Wulff construction, $TiO_2$ anatase particles show geometry of truncated octahedron with two {001} facets at the top and bottom and eight {101} facets at the side.[2] The {001} facets behave higher reactivity than thermodynamically the most stable {101} facets. TiO2 anatase particles with high percentage of the exposed {001} facets have been synthesized. The proportion of {001} facets can be estimated by direct observation from microscopic images or calculated from XRD patterns or Raman spectroscopy.[3,4] In this thesis, the calculation method using XRD patterns was employed. Particle thickness and length are related to the coherence domain along [001] and [100] direction, respectively. Coherence domain $t_{(hkl)}$ along [hkl] direction can be calculated using the Debye-Scherrer equation. Calculation of (001) facets proportion in $TiO_2$ anatase was achieved using particle thickness ($d$), particle length ($l$) and the angle ($\theta$) between (001) and (101) facets (**Figure A1**).

Surfaces of (001) and (101) facets can be written as:

$$S_{001} = 2 * \left(l - {}^{d}/_{\tan\theta}\right)^2;\ S_{101} = \frac{2d}{\sin\theta} * (2l - {}^{d}/_{\tan\theta})$$

and (001) facets proportion as :

$$P_{001} = \frac{S_{001}}{S_{001} + S_{101}}$$

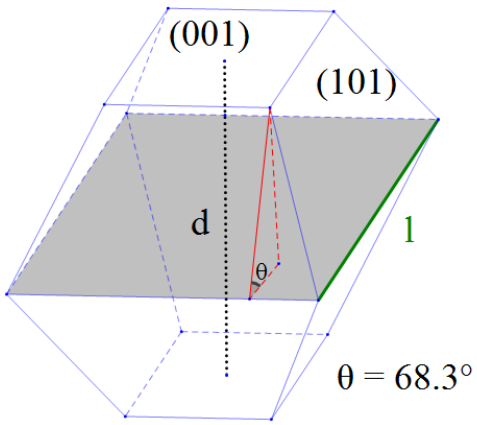


**Figure A1:** Schematic representation of (001) facet exposed $TiO_2$ anatase showing truncated octahedral geometry.

**References:**

(1) Wojdyr, M. Fityk: a general-purpose peak fitting program. *J. Appl. Crystallogr.* **2010**, *43*, 1126.

(2) Lazzeri, M.; Vittadini, A.; Selloni, A. Structure and energetics of stoichiometric $TiO_2$ anatase surfaces. *Phys. Rev. B* **2001**, *63*, 155409.

(3) Ong, W.-J.; Tan, L.-L.; Chai, S.-P.; Yong, S.-T.; Mohamed, A. R. Highly reactive {001} facets of $TiO_2$-based composites: synthesis, formation mechanism and characterization. *Nanoscale* **2014**, *6*, 1946.

(4) Tian, F.; Zhang, Y.; Zhang, J.; Pan, C. Raman Spectroscopy: A New Approach to Measure the Percentage of Anatase $TiO_2$ Exposed (001) Facets. *J. Phys. Chem. C* **2012**, *116*, 7515.

# Appendix 2. Pair distribution function

For pair distribution function (PDF) analysis, samples were loaded inside in a Kapton capillary and sealed prior to measurements. X-ray scattering measurements were performed at the 11-ID-B beamline at the Advanced Photon Source at Argonne National Laboratory. High energy X-rays ($\lambda = 0.2114$ Å) were used in combination with a large amorphous-silicon-based area detector to collect data to high values of momentum transfer $Q \sim 22$ Å$^{-1}$.[1,2] One-dimensional diffraction data were obtained by integrating the diffraction images within fit2D.[3] After correcting for background and Compton scattering, PDF profiles of the samples were extracted from the diffraction data within pdfget X2.[4] The information of PDF peaks was extracted from fitting Gaussian functions within Fityk.[5] Structure models were fitted to the PDF data using the PDFgui software.[6] Refined parameters were the lattice parameters, instrument parameters, atomic positions and occupancy as well as atomic displacement parameters.

**References:**


(1) Chupas, P. J.; Qiu, X. Y.; Hanson, J. C.; Lee, P. L.; Grey, C. P.; Billinge, S. J. L. Rapid-acquisition pair distribution function (RA-PDF) analysis. *J. Appl. Crystallogr.* **2003**, *36*, 1342.

(2) Chupas, P. J.; Chapman, K. W.; Lee, P. L. Applications of an amorphous silicon-based area detector for high-resolution, high-sensitivity and fast time-resolved pair distribution function measurements. *J. Appl. Crystallogr.* **2007**, *40*, 463.

(3) Hammersley, A. P.; Svensson, S. O.; Hanfland, M.; Fitch, A. N.; Hausermann, D. Two-dimensional detector software: From real detector to idealised image or two-theta scan. *High Pressure Res.* **1996**, *14*, 235.

(4) Qiu, X.; Thompson, J. W.; Billinge, S. J. L. PDFgetX2: a GUI-driven program to obtain the pair distribution function from X-ray powder diffraction data. *J. Appl. Crystallogr.* **2004**, *37*, 678.

(5) Wojdyr, M. Fityk: a general-purpose peak fitting program. *J. Appl. Crystallogr.* **2010**, *43*, 1126.

(6) Farrow, C. L.; Juhas, P.; Liu, J. W.; Bryndin, D.; Bozin, E. S.; Bloch, J.; Proffen, T.; Billinge, S. J. L. PDFfit2 and PDFgui: computer programs for studying nanostructure in crystals. *J. Phys.: Condens. Matter* **2007**, *19*, 335219.

# Appendix 3. Nuclear magnetic resonance

$^{19}F$ solid-state MAS NMR experiments were performed on an Avance 300 Bruker spectrometer operating at 7.0 T ($^{19}F$ Larmor frequencies of 282.2 MHz), using a 1.3 mm CP-MAS probehead. The room temperature 19F MAS spectra of $Ti_{1-x-y}\square_{x+y}O_{2-4(x+y)}F_{4x}(OH)_{4y}$ were recorded using a Hahn echo sequence with an inter-pulse delay equal to one rotor period. The $^{19}F$ MAS spectra were recorded at various spinning frequencies up to 64 kHz in order to discriminate between isotropic peaks and spinning sidebands. The 90° pulse length was set to 1.55 μs and the recycle delay was set to 20 sec. $^{19}F$ spectra are referenced to $CFCl_3$, and were fitted by using the DMFit software.[1] In order to quantify the fluorine content on the $Ti_{1-x-y}\square_{x+y}O_{2-4(x+y)}F_{4x}(OH)_{4y}$ sample, $^{19}F$ solid-state MAS NMR (Hahn echo) spectra were also recorded for $YF_3$ and $LaF_3$ and the masses of each sample in the rotor were measured. The fits of the spectra allow to determine the integrated intensities (I) for each sample. Since, for each sample, the recycle delays were chosen to ensure that the amount of signal detected is maximum (420 s for $YF_3$ and 120 s for $LaF_3$), we assume that the integrated intensities are proportional to the number of scans (256 for $Ti_{1-x-y}\square_{x+y}O_{2-4(x+y)}F_{4x}(OH)_{4y}$ and 16 for $YF_3$ and $LaF_3$) and to the molar quantity of fluorine atoms (n) in the rotor. This assumption is verified since the calculated I/n ratio for $YF_3$ and $LaF_3$ are equal. The intensities of the NMR signals of $Ti_{1-x-y}\square_{x+y}O_{2-4(x+y)}F_{4x}(OH)_{4y}$ (x + y = 0.22), $I_1$, and $YF_3$ (or $LaF_3$), $I_2$, allow to calculate x using the following formula where m and M are the mass and the molar mass, respectively:

$$\frac{I_1}{I_2} = \frac{\frac{4x.m_{Ti_{1-x-y}\square_{x+y}O_{2-4(x+y)}F_{4x}OH_{4y}}}{M_{Ti_{1-x-y}\square_{x+y}O_{2-4(x+y)}F_{4x}OH_{4y}}}}{\frac{3m_{YF_3}}{M_{YF_3}}}$$

$$x = \frac{\frac{I_1}{I_2}\frac{3m_{YF_3}}{M_{YF_3}}[0.78M_{Ti} + 2M_o + 0.88M_H]}{4m_{Ti_{1-x-y}\square_{x+y}O_{2-4(x+y)}F_{4x}OH_{4y}} + \frac{I_1}{I_2}\frac{3m_{YF_3}}{M_{YF_3}}4.(M_o + M_H - M_F)}$$

**References:**

(1) Massiot, D.; Fayon, F.; Capron, M.; King, I.; Le Calve, S.; Alonso, B.; Durand, J. O.; Bujoli, B.; Gan, Z. H.; Hoatson, G. Modelling one- and two-dimensional solid-state NMR spectra. *Magn. Reson. Chem.* **2002**, *40*, 70.

# Appendix 4. List of publications

1. "High Substitution Rate in Anatase $TiO_2$ Anatase Nanoparticles with Cationic Vacancies for Modified and Fast Lithium Storage" **Li W.**, Corradini D., Body M., Legein C., Salanne M., Ma J., Chapman K.W., Chupas P.J., Rollet A.-L., Julien C., Zhagib K., Duttine M., Demourgues A., Groult H., Dambournet D., *Chem. Mater.* **2015**, *27*, 5014-5019. (**Journal cover**)

2. "Atomic Insights into Nanoparticles Formation of Defective Fluorinated Anatase" **Li W.**, Legein C., Body M., Borkiewicz O.J., Groult H., Dambournet D., In preparation.

3. "Solvothermal Reaction of Titanium Alkoxides and Fluorine: Structural influence of synthesis parameters" **Li W.**, Legein C., Body M., Dambournet D., In preparation.

4. "Sodium Intercalation Mechanism into $TiO_2$ anatase Probed by PDF analysis" **Li W.,** Fukunishi M., Borkiewicz O.J., Groult H., Komaba S., Dambournet D., In preparation.

5. "Impact of Cationic Vacancies on the Na-ion Storage Properties of Fluorinated Anatase" **Li W.,** Fukunishi M., Borkiewicz O.J., Groult H., Komaba S., Dambournet D., In preparation.

6. "Oxide/Fluoride Ordering in Cubic $TiOF_2$ Probed by the Pair Distribution Function, $^{19}F$ NMR Spectroscopy and DFT-Calculations" **Li W.**, Burbano M., Legein C., Body M., Chennabasappa M., Demourgues A., Borkiewicz O.J., Salanne M., Dambournet D., In preparation.

7. "First Co-existence of Two Metallic Polymorphs Stabilized by Li-Induced Conversion Reaction in $CoF_2$" **Li W.**, Borkiewicz O.J., Doublet M.-L., Groult H., Chupas P.J., Chapman K.W., Dambournet D., In preparation.

# Résumé français

# Synthèse de $TiO_2$ anatase par voie sol-gel dans le milieu fluoré et ses applications comme électrode négative pour batteries aux $Li^+$ et $Na^+$

## 1. Introduction et état des arts

L'énergie est le fondement de toute l'activité des humains. Avec la croissance de la population mondiale et le développement économique, la consommation d'énergie augmente rapidement, en particulier dans ces dernières années. Actuellement, 87 % de la consommation totale d'énergie provient de la combustion de combustibles fossiles, générant une grande quantité des polluants atmosphériques et gaz à effet de serre. Cette émission non seulement provoque l'effet environnemental mais aussi conduit au réchauffement climatique. Par conséquent, l'exploitation des énergies durables est nécessaire pour réduire l'utilisation de combustibles fossiles.

Les accumulateurs au lithium ont reçu un gros intérêt récemment grâce à leur forte densité d'énergie gravimétrique et volumique. Ils sont été largement utilisés comme des sources d'énergie dans les appareils électriques portables et les véhicules électriques. Cependant, le coût, la sécurité et la densité de puissance entravent le développement des accumulateurs ions lithium. Notre recherche vise à résoudre ces problèmes par l'ingénierie de matériaux d'électrodes. Dans cette thèse, nous partons du dioxyde de titane ($TiO_2$), un matériau non toxique et abondant sur Terre. Des stratégies telles que la nanotechnologie, le dopage/substitution et le contrôle de la morphologie ont été utilisées pour modifier ses propriétés physicochimiques et électrochimiques.

Depuis Fujishima et Honda ont découvert l'activité photocatalytique de $TiO_2$ pour la photoélectrolyse de l'eau dans 1972,[1] applications de $TiO_2$ ont été étendues à de nombreux domaines, par exemple cellule photoélectrochimique,[1-3] photocatalyse,[4,5] cellule photovoltaïque,[6,7] capteur,[8] accumulateurs au lithium,[9-12] supercondensateurs.[13] Actuellement, $TiO_2$ a onze variétés. Parmi eux, anatase, rutile et brookite ont les plus stables polymorphes. Les autres variétés n'existent pas naturellement et leurs synthèses exiger de haute température ou pression.

## Structure de $TiO_2$

Les paramètres cristallins de $TiO_2$ anatase sont rassemblés dans le **Tableau 1**. $TiO_2$ anatase se cristallise dans une maille tétragonale avec un groupe d'espace de $I4_1/amd$. Une maille contient 4 unités de la formule $TiO_2$, c-t-d 12 atomes (**Figure 1a**). Un atome de Ti est lié avec six atomes de O, formant $TiO_6$ octaèdre. Un octaèdre $TiO_6$ partage 4 arêtes avec les voisins. Le réseau anatase 3D est formée par des chaînes zig-zag le long de l'axe c (**Figure 1b**). La densité atomique est de 3,9 $g/cm^3$, ce qui est plus faible que le rutile et brookite. Cela signifie que, anatase montre plus grande surface pour même masse de matériau, indiquant un degré d'ouverture structurelle plus élevé. En outre, cette structure crée des sites vacants qui peuvent accueillir hétéroatomes, menant aux propriétés d'intercalation.

Selon la construction Wulff, anatase $TiO_2$ montre la forme d'équilibre d'un octaèdre légèrement tronqué qui est dominé par huit {101} facettes sur les côtés (plus de 94%) et deux {001} facettes sur le haut et le bas (moins de 6%). La facette {001} est plus réactive car elle contient plus de Ti insaturé à la surface.

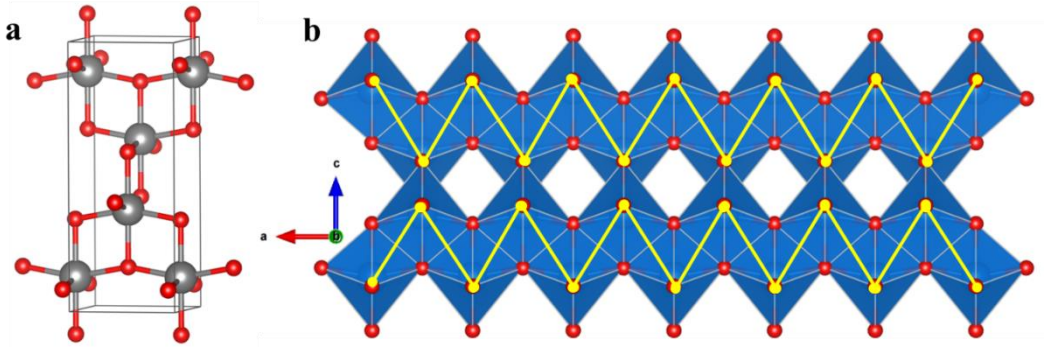


**Figure 1:** Structure de l'anatase: (a) un maille, (b) chaine en zig-zag (Gris: Ti, rouge: O).

**Tableau 1: Information structurelle de $TiO_2$ anatase (Référence: ICSD #44882).**

| Système cristallin | Group d'espace | Paramètres de maille (Å) | Volume ($Å^3$) | $d_{Ti-O}$ (Å) | Densité ($g/cm^3$) | Positions atomiques | | | | |
|---|---|---|---|---|---|---|---|---|---|---|
| | | | | | | Atomes | Site | x | y | z |
| Tétragonal | $I4_1/amd$ | a = b = 3.785<br>c = 9.514 | 136.3 | 2*1.964<br>4*1.937 | 3.88 | Ti | 4a | 0 | 0 | 0 |
| | | | | | | O | 8e | 0 | 0 | 0.2064 |

## Applications électrochimiques de $TiO_2$

Une des applications importantes pour $TiO_2$ est comme anode dans les accumulateurs au lithium. Les batteries ont trois composants : une cathode (électrode positive), une anode

(électrode négative) et un électrolyte. Un séparateur peut séparer les deux électrodes pour éviter un court-circuit interne. Quand un dispositif externe connecte les deux électrodes, la différence de potentiel entre deux électrodes va spontanément conduire l'électron de circuler du côté négatif vers positif. L'équilibre de la charge sera maintenu par le transport simultané des ions par l'électrolyte. La **Figure 2** montre schématiquement le principe de fonctionnement des accumulateurs au lithium,[14] Ce système utilise graphite comme anode et $LiMO_2$ en tant que cathode. Au cours du processus de la charge, le lithium est extrait de la cathode et induit l'oxydation du métal de transition qui libère des électrons vers le circuit externe par le collecteur de courant. Le lithium va ensuite migrer vers l'électrode négative où il s'est réduit à l'état métallique. Lors de la décharge, les processus opposés ont lieu, conduisant par conséquent au retour de lithium à la cathode. Le système est donc rechargeable.

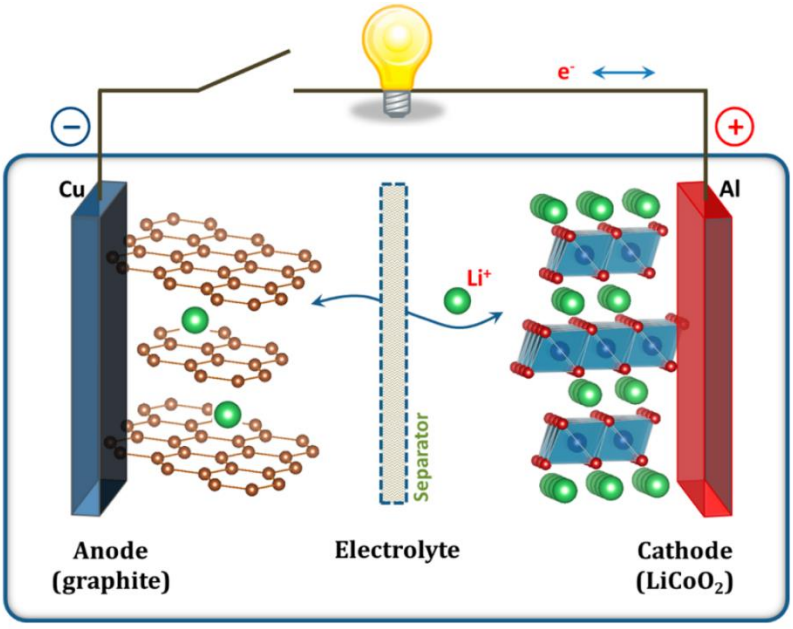


**Figure 2:** Le principe d'opération des accumulateurs lithium ions. M représente métaux de transition.[15]

Les accumulateurs au lithium peuvent être classés, à base des matériaux de l'électrode négative, en lithium métal et lithium ion. Le lithium métallique a un potentiel de travail le plus base et la capacité spécifique la plus élevée. Cependant, certains inconvénients ont limité leurs utilisations. La dendrite de lithium peut être formée par le dépôt de lithium métallique à la surface de l'électrode, conduisant à des problèmes majeurs de sécurité. De plus, une réduction de l'électrolyte a lieu au faible potentiel, générant une couche à la surface entre le graphite et l'électrolyte. Cette couche, appelée SEI (Solid Electrolyte interface), est

composée de sels de lithium (LiF, $Li_2CO_3$…) et est thermiquement instable, posant de sérieux problèmes de sécurité. Pour palier à ces problèmes, une des solutions est d'utiliser un matériau dont le potentiel se situe dans la zone de stabilité de l'électrolyte, à savoir supérieure à 1 V vs $Li^+/Li$. Le $TiO_2$ a un potentiel de travail dans cette zone de stabilité de l'électrolyte, améliorant ainsi la sécurité de la batterie. En outre, $TiO_2$ peut soutenir une densité de décharge/charge élevée et est prometteur pour les applications de haute puissance comme les véhicules électriques.[16-18] On note que $TiO_2$ est électrochimiquement active vers l'insertion de $Na^+$.[19] Il peut donc être utiliser comme anode dans les accumulateurs au sodium.

Les propriétés de l'insertion du lithium dans $TiO_2$ est influencée par la taille de particule[11,20,21] et l'orientation de surface.[18,22] La réduction de la taille des particules peut raccourcir le chemin de diffusion du lithium. Certaines surfaces peuvent diminuer la barrière d'énergie de la réaction de $Li^+$ avec la surface. La structure de bulk peut aussi affecter l'insertion du lithium, ex. la présence de défaut.[23] Ainsi, l'optimisation des propriétés électrochimiques de $TiO_2$ présentée dans cette thèse est réalisée en modifiant la taille, la surface et la structure de bulk des particules.

**Méthode Sol-gel**

Pour ce faire, une méthode de synthèse sol-gel est utilisée. Le procédé sol-gel est un outil polyvalent et largement utilisé pour préparer $TiO_2$ grâce à sa flexibilité dans l'introduction de dopant et le contrôle effectif de la taille, morphologie et la composition chimique de $TiO_2$. Il consiste en premier lieu à la formation de sols par hydrolyse et condensation de précurseurs inorganiques ou organo-métalliques. Deuxièmement, liquide de sols subit une série de réactions chimiques et se transforment vers un système diphasique contenant des phases liquides piégés en solide, appelé le gel. Oxydes de métal sont obtenues quand la phase liquide est retirée.

Nous utilisons d'alcoolates de titane $Ti(OR)_n$ comme précurseur où R représente un groupement alkyle ($C_nH_{2n+1}$). Une fois eau est ajouté dans la solution de précurseur, la réaction hydrolyse a lieu (**Eq. 1**), conduisant à la formation de Ti-OH hydroxo group. Le titane va ensuite se lier spontanément par la réaction de condensation (**Eq. 2-4**).

Hydrolyse: $Ti(OR)_n + xH_2O \rightarrow Ti(OR)_{n-x}(OH)_x + xROH$ **(Eq. 1)**

Olation: $-M-OH+H_2O-M- \rightarrow -M-OH-M-+H_2O$ (**Eq. 2**)

Oxolation: $-M-OH+HO-M- \rightarrow -M-O-M-+H_2O$ (**Eq. 3**)

Alcoxolation : $-M-OR+HO-M- \rightarrow -M-O-M-+ROH$ (**Eq. 4**)

Plusieurs paramètres chimiques de synthèse peuvent influencer le procédé sol-gel. Par exemple, la nature de précurseur et solvant, le taux d'hydrolyse et l'anion. Parmi eux, l'anion peut modifier la composition chimique de précurseur et affecter la précipitation de l'oxyde.[24] Le fluor est un anion complexant et a été trouvé de pouvoir efficacement contrôler la taille, la forme, la structure et la composition chimique des particules de $TiO_2$ synthétisés par voie sol-gel.[22,25-31] Le fluor favorise la formation de $TiO_2$ anatase en affectant l'assemblage de l'octaèdre $TiO_6$. En outre, l'incorporation de fluor dans la structure de $TiO_2$ est réalisée par la réaction de fluoration (**Eq. 5**).[32] En ce cas-là, la substitution de l'anion divalent $O^{2-}$ par l'anion monovalent $F^-$dans $TiO_2$engendre un déficit de charge négative. La compensation de la charge entraine la réduction de $Ti^{4+}$ en $Ti^{3+}$,[29,33,34] modifiant la structure électronique de $TiO_2$.

Fluorolysis: $Ti(OR)_n + xHF \rightarrow Ti(OR)_{n-x}F_x + xROH$ (**Eq. 5**)

Plus récemment, le fluor a été montré comme un agent dirigeant la structure pour la croissance anisotrope de cristaux d'anatase et largement utilisé pour stabiliser la surface réactive {001} de $TiO_2$ anatase.[22,30] L'adsorption du fluor en surface non seulement fait diminuer l'énergie de surface pour (101) et (001), mais aussi conduit à l'énergie de la surface (001) plus faible que (101) qui est généralement thermodynamiquement la plus stable. Dans cette thèse, fluor est utilisé pour modifier les propriétés physicochimiques de $TiO_2$ pour avoir de meilleures performances électrochimiques vis-à-vis du $Li^+$ et $Na^+$.

## 2. Synthèse de $Ti_{0.78}\square_{0.22}O_{1.12}F_{0.40}(OH)_{0.48}$

### Caractérisation structurale

Dans un première temps, une synthèse en utilisant $Ti(O^iPr)_4$ en tant que précurseur, $Pr^iOH$ comme solvant et HF aqueux comme agent fluorant a été effectuée à une température de 90 °C activée dans la condition solvothermale. La phase obtenue est caractéristique de la structure anatase (**Figure 3a**). Des aggrégats de particules sont observés par MET et la taille de particule est de l'ordre de ~7 nm (**Figure 3b,c**).

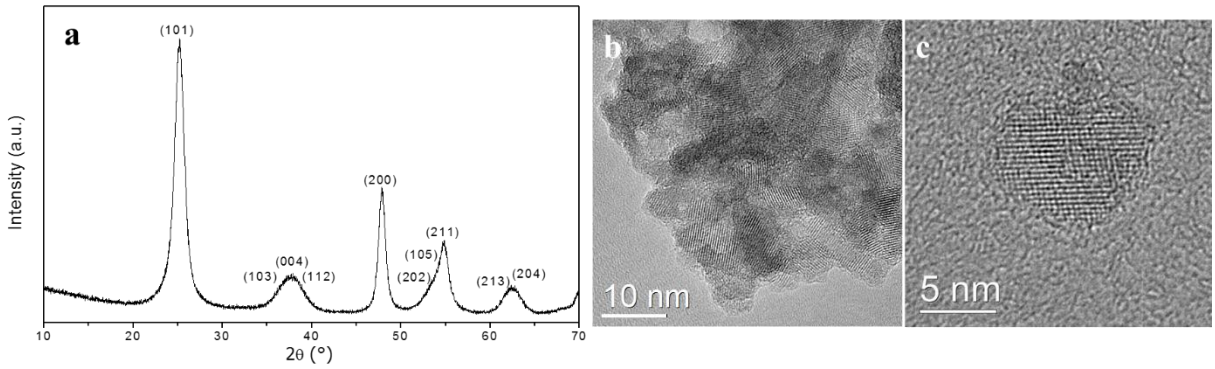


**Figure 3:** (a) Diffraction des rayons X ; (b,c) Images de MET.

L'analyse de la fonction de distribution des pairs (PDF) confirme la formation de l'anatase cristalline. Le taux d'occupation de titane est de 0,78. Cela signifie que 22 % de lacune cationique se trouve dans le réseau. L'analyse XPS montre la présence de fluor et $Ti^{4+}$, le signal de $Ti^{3+}$ n'a pas été observé. La réaction de déshydrolysation observée dans le diagramme thermogravimétrique montre la présence de groupement $OH^-$. En combinant les analyses chimiques et physiques, la composition chimique de cet anatase phase est déduite comme $Ti_{0.78}\square_{0.22}O_{1.12}F_{0.40}(OH)_{0.48}$. La création de lacune cationique compense la charge négative qui est entrainé par la substitution de l'anion divalent par de l'anion monovalent. Dans cet échantillon, 44 % de sites anioniques sont occupés par anions monovalent. Sa structure simulée par le calcul DFT est montrée dans la **Figure 4**. Pour simplifier la simulation, $OH^-$ est remplacé par $F^-$. La déviation de la composition chimique indique que le réseau de l'anatase peut accommoder un désordre fort en conservant sa structure originale.

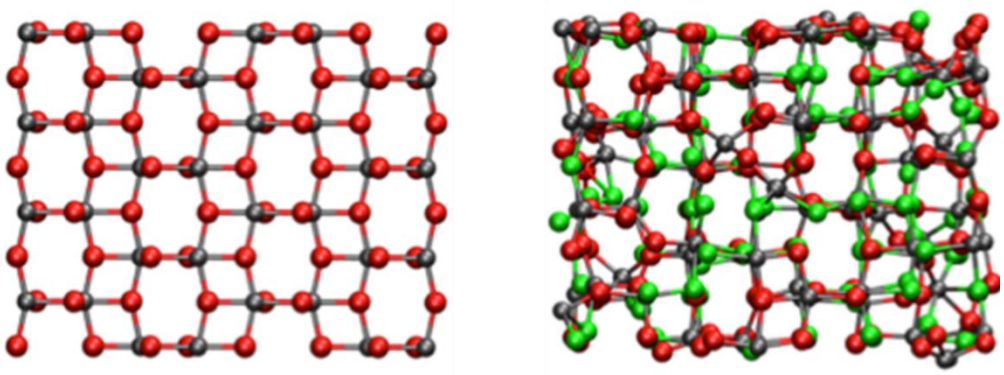

**Figure 4:** Structure de $TiO_2$ (gauche) et $Ti_{0.78}\square_{0.22}O_{1.12}F_{0.88}$ (droite) simulée par le calcul DFT (Gris: Ti, rouge: O, vert: F).

La structure locale de $Ti_{0.78}\square_{0.22}O_{1.12}F_{0.40}(OH)_{0.48}$ est étudiée par la $^{19}F$ RMN spectroscopie et le calcul de DFT. Trois pics observés dans le spectre de RMN montrent

différent environnement de fluor (**Figure 5a**). Les pics à -88, -4 et 98 ppm sont attribués à $Ti_3$-F, $Ti_2\square_1$-F et $Ti_1\square_2$-F avec les concentrations de 4 %, 64 % et 32 %, respectivement. Les concentrations de chaque environnement de fluor montrent une localisation préférentielle de fluor à côté de lacune. Les pics de RMN sont larges. Cela signifie que les distances de Ti-F sont largement distribuées, indiquant le désordre de la structure.

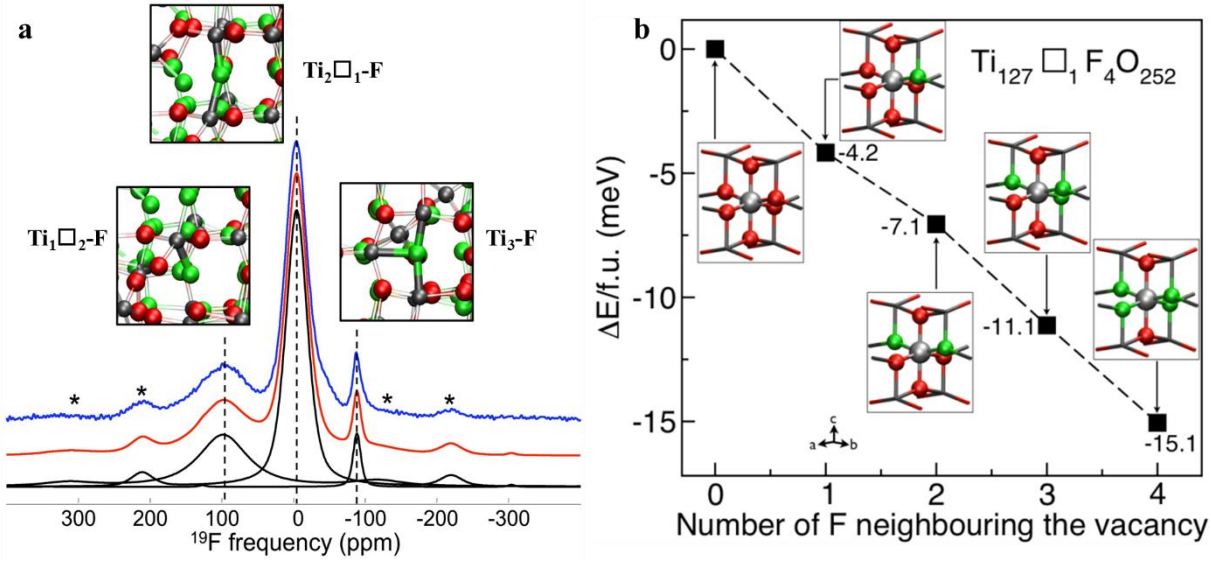


**Figure 5:** (a) Le spectre expérimental (bleu) et calculé (rouge) de $^{19}F$ RMN de $Ti_{0.78}\square_{0.22}O_{1.12}F_{0.40}(OH)_{0.48}$. Les lignes en noir montrent les trois environnements de fluor. Ses structures simulées sont aussi montrées. (b) Evolution de l'énergie de la structure on fonction du nombre de fluor effectué par DFT modélisation sur une surpercellule de $Ti_{127}\square_1F_4O_{252}$. Les structures de chaque configuration sont montrées. (Gris: Ti, rouge: O, vert: F)

Pour obtenir plus de détail sur la stabilisation de lacune cationique, modélisation DFT est effectuée sur une supercellule de $Ti_{127}\square_1F_4O_{252}$, où une lacune est créée par la substitution de 4 $O^{2-}$ par 4 $F^-$ (**Figure 5b**). Le seul environnement de fluor est $Ti_2\square_1$-F. On trouve que l'énergie de la structure diminue en fonction du nombre de fluor situé à côté de lacune. La configuration la plus stable correspond aux quatre anions fluorure situées dans le plan équatorial de la lacune. Ces résultats expliquent la localisation préférentielle de fluor à coté de lacune.

**Mécanisme de formation**

Le mécanisme de formation de $Ti_{0.78}\square_{0.22}O_{1.12}F_{0.40}(OH)_{0.48}$ est ensuite étudié en analysant les échantillons collectés en différent temps de réaction. L'analyse DRX montre la présence de l'intermédiaire de $TiOF_2$ avant la formation de la phase d'anatase (**Figure 6a**).

L'échantillon obtenu après 1 h de réaction est constitué majoritairement de particules amorphes dont la taille est ~3 nm (**Figure 6b**). Des particules cristallines de l'anatase sont aussi observées. La diminution de la phase amorphe en fonction du temps de réaction indique que $TiOF_2$ amorphe est l'intermédiaire pendant la formation de l'anatase. Ceci est confirmé par l'analyse de PDF. Donc, la phase anatase se forme par le processus de dissolution et recristallisation de $TiOF_2$.

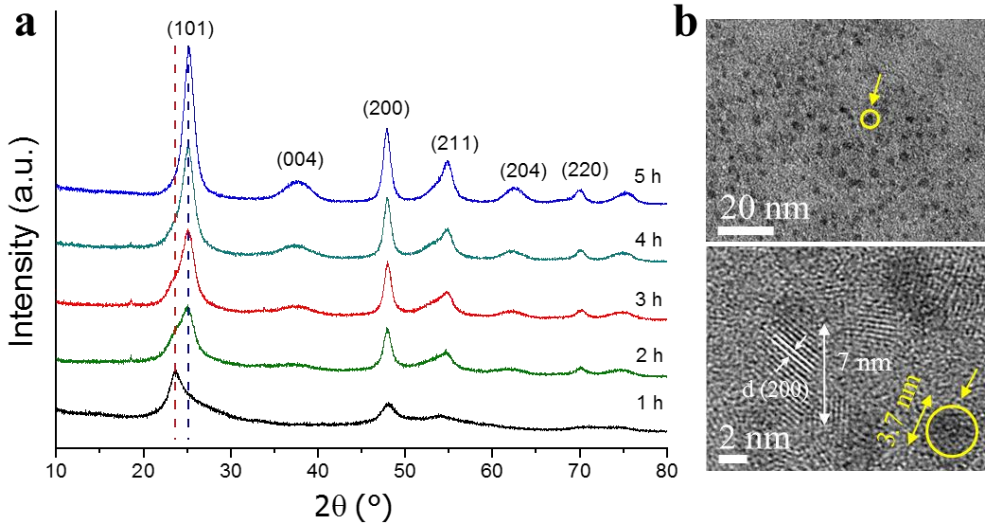


**Figure 6:** (a) Evolution de diagramme de DRX en fonction du temps de réaction. (b) Images de TEM de l'échantillon formé après 1 h de réaction.

Selon l'analyse chimique et la PDF, la composition chimique de l'anatase à différent temps de réaction est déduite (**Tableau 2**). En augmentant le temps de réaction, la concentration de lacune cationique diminue simultanément avec ceux de fluor et $OH^-$, indiquant l'occurrence du réarrangement structural de l'anatase. Ce processus continue jusqu'à la formation de $Ti_{0.78}\square_{0.22}O_{1.12}F_{0.40}(OH)_{0.48}$ après 12 h de réaction. L'occurrence d'oxolation peut faire diminuer la concentration du groupement $OH^-$. Le mécanisme de défluoration est étudié par la RMN du noyau $^{19}F$. La proportion des trois environnements de fluor dans l'anatase reste quasiment constante à partir de 3 h de réaction, indiquant que le processus de défluoration a lieu simultanément pour le fluor de différent environnement.

**Tableau 2: Evolution de la composition chimique de l'anatase en fonction du temps de réaction.**

| Time (h) | Calculated F/Ti in anatase | Calculated OH/Ti in anatase | Proposed composition of anatase |
|---|---|---|---|
| 2 | 0.94 | 3.06 | $Ti_{0.50}\square_{0.50}F_{0.47}(OH)_{1.53}$ |
| 3 | 0.97 | 2.43 | $Ti_{0.54}\square_{0.46}O_{0.16}F_{0.53}(OH)_{1.31}$ |
| 4 | 0.88 | 2.14 | $Ti_{0.57}\square_{0.43}O_{0.28}F_{0.50}(OH)_{1.22}$ |
| 5 | 0.75 | 1.54 | $Ti_{0.63}\square_{0.37}O_{0.52}F_{0.51}(OH)_{0.97}$ |
| 12 | 0.51 | 0.62 | $Ti_{0.78}\square_{0.22}O_{1.12}F_{0.4}(OH)_{0.48}$ |

Le mécanisme de la formation de $Ti_{0.78}\square_{0.22}O_{1.12}F_{0.40}(OH)_{0.48}$ est schématiquement montré dans la **Figure 7**. La réaction d'hydro/fluorolyse de $Ti(O^iPr)_4$ est initialisée par l'ajout de l'HF. La réaction de condensation conduit à la formation de l'intermédiaire de $TiOF_2$ amorphe. Cette phase continue à dissoudre dans la solution et recristallise pour former les nanoparticules cristallines d'anatase. Ensuite, le réarrangement structural de la phase d'anatase a lieu, conduisant à la diminution de la concentration de lacune cationique et les anions monovalents ($OH^-$ et $F^-$). Le mécanisme de dissolution/recristallisation de $TiOF_2$ et réarrangement structural de l'anatase a été confirmé par l'étude effectué à plus haute température, 150 °C. Cette étude nous permet de contrôler la composition chimique de l'anatase fluorée en ajustant le temps de réaction.

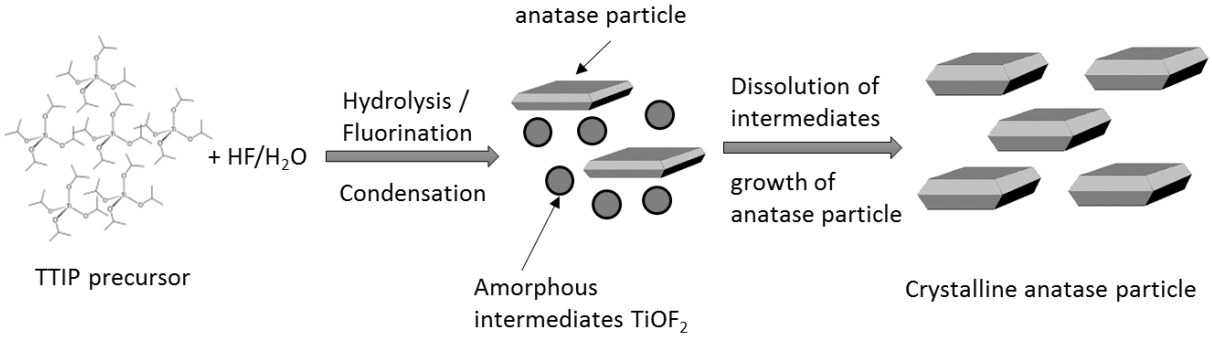


**Figure 7:** Schéma illustré le mécanisme de la formation de $Ti_{0.78}\square_{0.22}O_{1.12}F_{0.40}(OH)_{0.48}$ anatase.

# 3. Impact des paramètres de synthèse

On s'est intéressé ensuite à étudier l'effet des paramètres de la réaction en milieu fluoré. Ainsi, une étude systématique a été effectuée pour examiner les effets structuraux, compositionnels et morphologiques des paramètres de synthèse, y compris la nature du précurseur, le solvant et la concentration des réactants, ainsi que la température de réaction.

La nature du solvant à l'alcool a joué un rôle important dans la détermination de la structure de la phase résultante. La phase anatase est obtenue dans le solvant de l'éthanol et l'isopropanol, alors qu'un oxyhydroxyfluorure de titane présentant une structure de type bronze hexagonal de tungstène (HTB) est obtenu dans 2-butanol (**Figure 8**). Cet effet provient de la réaction de l'alcool d'échange,[35] modifiant ainsi la réactivité des précurseurs de titane. La formation de la phase riche en fluor, HTB, indique que $Ti(OBu)_4$ est plus réactive vers fluor. Cela peut être attribué aux différentes longueurs de la chaîne alkyle. Puisqu'il y a la compétition entre hydrolyse et fluorolyse, plus la chaîne est longue, moins il est réactive vers l'eau,[24] et donc, plus il est réactive vers fluor. La même phase obtenue pour les synthèses utilisant différent précurseur avec le même solvant a confirmé le rôle de solvant.

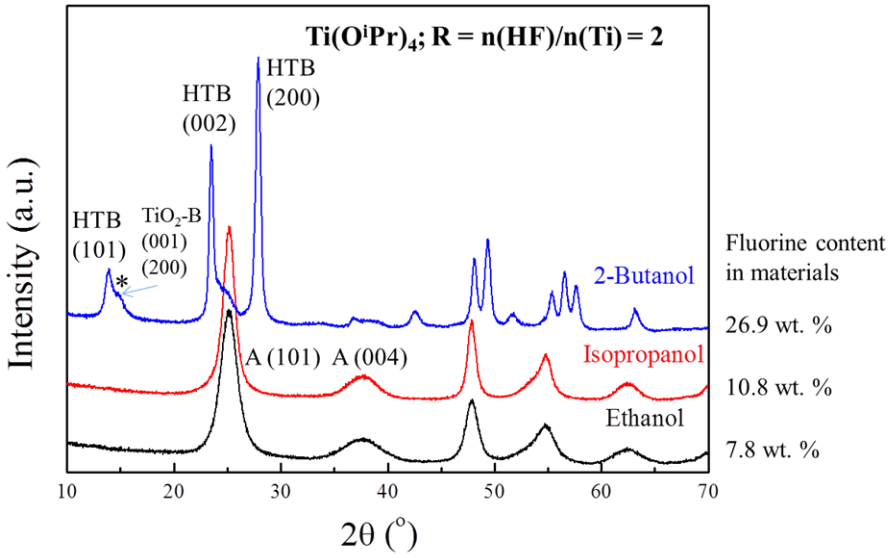


**Figure 8:** Diagrammes de DRX à différent solvant.

Comme solvant fortement influence la réactivité de précurseur. L'étude de l'effet du taux de fluor (fraction molaire entre F et Ti, R = F/Ti) est donc effectuée dans différent solvant. En augmentant le taux de fluor, l'analyse de DRX a montré différent résultats:

- Isopropanol: changement de phase de l'anatase vers HTB à partir de R = 2,2 (**Figure 9**).
- 2-Butanol : changement de phase de l'anatase vers HTB à partir de R = 2.
- Ethanol : toujours anatase, pas de changement de phase.

Le changement de phase de l'anatase riche en oxygène vers HTB riche en fluor peut être expliqué par le type de la connexion de $TiX_6$ octaèdres. A haut taux de fluor, $TiX_6$ est riche en fluor grâce à la réaction de fluorolyse. Le fluor préfère une coordinance 2. Par conséquent,

$TiX_6$ riche en fluor est probablement lié par sommet, conduisant à la formation de la phase HTB (**Figure 9**). Cette transition de phase a lieu à plus faible R pour 2-butanol par rapport à isopropanol, confirmant l'influence de la nature de solvant. Par contre, Il n'y a que l'anatase obtenue pour les synthèses dans l'éthanol. Cela peut être attribué à la faible réactivité de $Ti(OEt)_4$ vers fluor. Par ailleurs, on trouve que la composition chimique de l'anatase peut être contrôlée en variant R dans le solvant de l'éthanol.

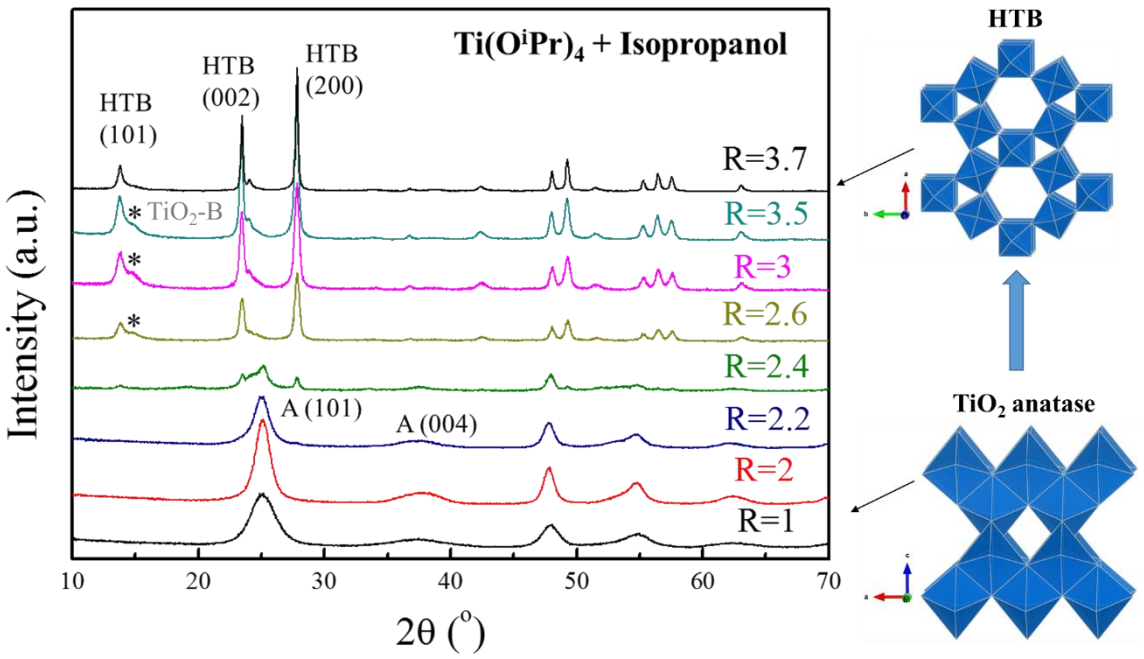


**Figure 9:** DRX en fonction du taux de fluor (R) pour les synthèses effectuées dans isopropanol. Structures de l'anatase et bronze hexagonal de tungstène (HTB) sont montrées à gauche. L'astérisque indique la phase $TiO_2$-B. 'A' représente anatase.

Le taux d'hydrolyse (fraction molaire de $H_2O$/Ti, h) peut affecter la réaction d'hydrolyse. A faible h, HTB riche en fluor est stabilisé. En augmentant le taux d'hydrolyse, la réaction de fluorolyse est inhibée, on favorise la formation de la phase riche en oxygène, l'anatase. L'étude de l'effet de la concentration de réactant a montré un changement de l'anatase vers l'HTB en augmentant la concentration.

L'effet de la température de réaction a été étudié en détail par la suite. Augmentation de la température de réaction de 110 à 190 ° C induit à la formation de la phase anatase pure. La taille des particules augmente avec la température de réaction (**Figure 10**). En outre, le pourcentage de la surface (001) de particules augmente en fonction de la température jusqu'à 160 °C. Par la suite, la morphologie des particules ne varie pas de manière significative à

cause de l'élimination de la surface (001) par la réaction de l'attachement orienté. La température de réaction fourni un contrôle effectif sur la composition chimique de l'anatase. La concentration de fluor et de lacune cationique dans$Ti_{1-x-y}\square_{x+y}O_{2-4(x+y)}F_{4x}(OH)_{4y}$diminuent en fonction de la température (**Figure 10**). La structure locale de fluor est devenue de plus ordonné quand la température augmente. Toutefois, le fluor ne peut pas être complètement éliminé, même à la température de 190 °C, une température couramment utilisée pour préparer des nanoparticules anisotropes de $TiO_2$ anatase. Ces résultats indiquent que, en plus de l'effet de surface, la chimie de défaut et l'effet de dopage devraient être aussi considérés pour les propriétés améliorées de $TiO_2$ anatase présentés dans la littérature. Cette étude nous permet de contrôler la structure, composition chimique et la morphologie de l'anatase fluorée en variant la température de synthèse.

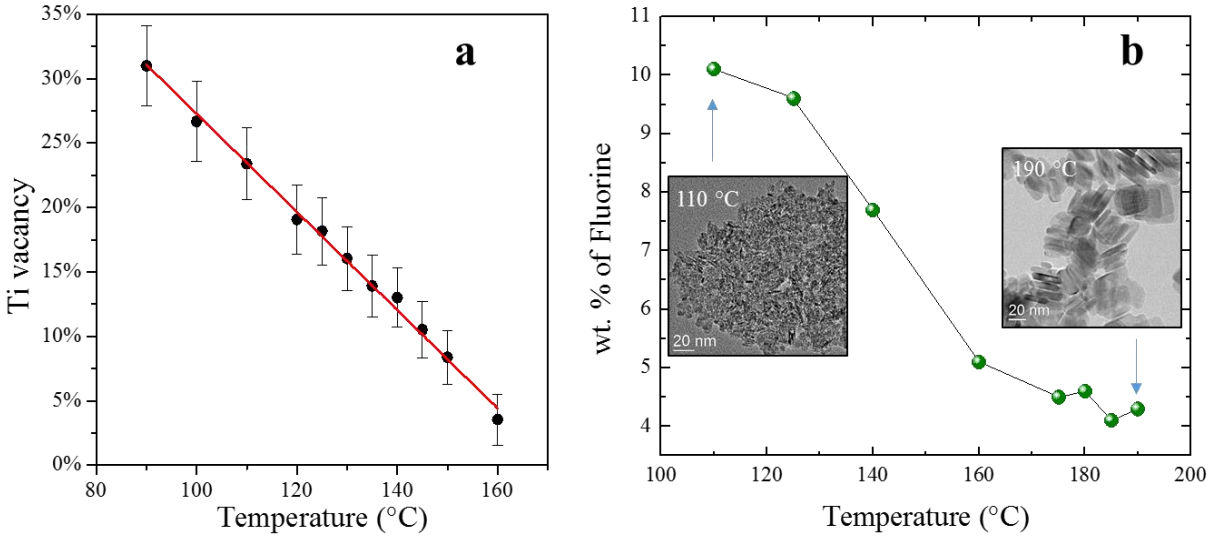


**Figure 10:** Evolution de la concentration de lacune cationique (Gauche) et fluor (Droite) en fonction de la température. Images de TEM sont aussi montrées.

# 4. Propriétés électrochimiques vis-à-vis du $Li^+$ et $Na^+$

### Propriétés électrochimiques de $Ti_{0.78}\square_{0.22}O_{1.12}F_{0.40}(OH)_{0.48}$ vs. $Li^+$

Matériaux à base de titane sont largement utilisés comme électrode négative pour les accumulateurs au $Li^+$.[36] On s'est intéressé ensuite à étudier l'insertion du $Li^+$ dans $Ti_{0.78}\square_{0.22}O_{1.12}F_{0.40}(OH)_{0.48}$, le résultat est comparé avec $TiO_2$ anatase. Il est démontré que, par rapport à $TiO_2$, $Ti_{0.78}\square_{0.22}O_{1.12}F_{0.40}(OH)_{0.48}$ a une meilleur densité de puissance (**Figure 10a**) à différent régime, surtout à haut densité de courant. A une densité de courant de 1 C

(335 mA/g), électrode de $Ti_{0.78}\square_{0.22}O_{1.12}F_{0.40}(OH)_{0.48}$ peut délivrer une capacité de 204 mAh/g, 3 fois plus élevé que $TiO_2$. A 10 C, une capacité de 134 mAh/g a été observée pour $Ti_{0.78}\square_{0.22}O_{1.12}F_{0.40}(OH)_{0.48}$, alors que $TiO_2$ anatase est presque inactive vers insertion du lithium, ce qui suggère une cinétique très efficaces pour la diffusion de lithium au sein de $Ti_{0.78}\square_{0.22}O_{1.12}F_{0.40}(OH)_{0.48}$ à haut régime. A 50 C, on observe une bonne tenue au cyclage après 300 cycles de charge/décharge pour $Ti_{0.78}\square_{0.22}O_{1.12}F_{0.40}(OH)_{0.48}$ (**Figure 11b**). L'efficacité coulombic a augmenté rapidement à 100 % au bout de quelques cycles.

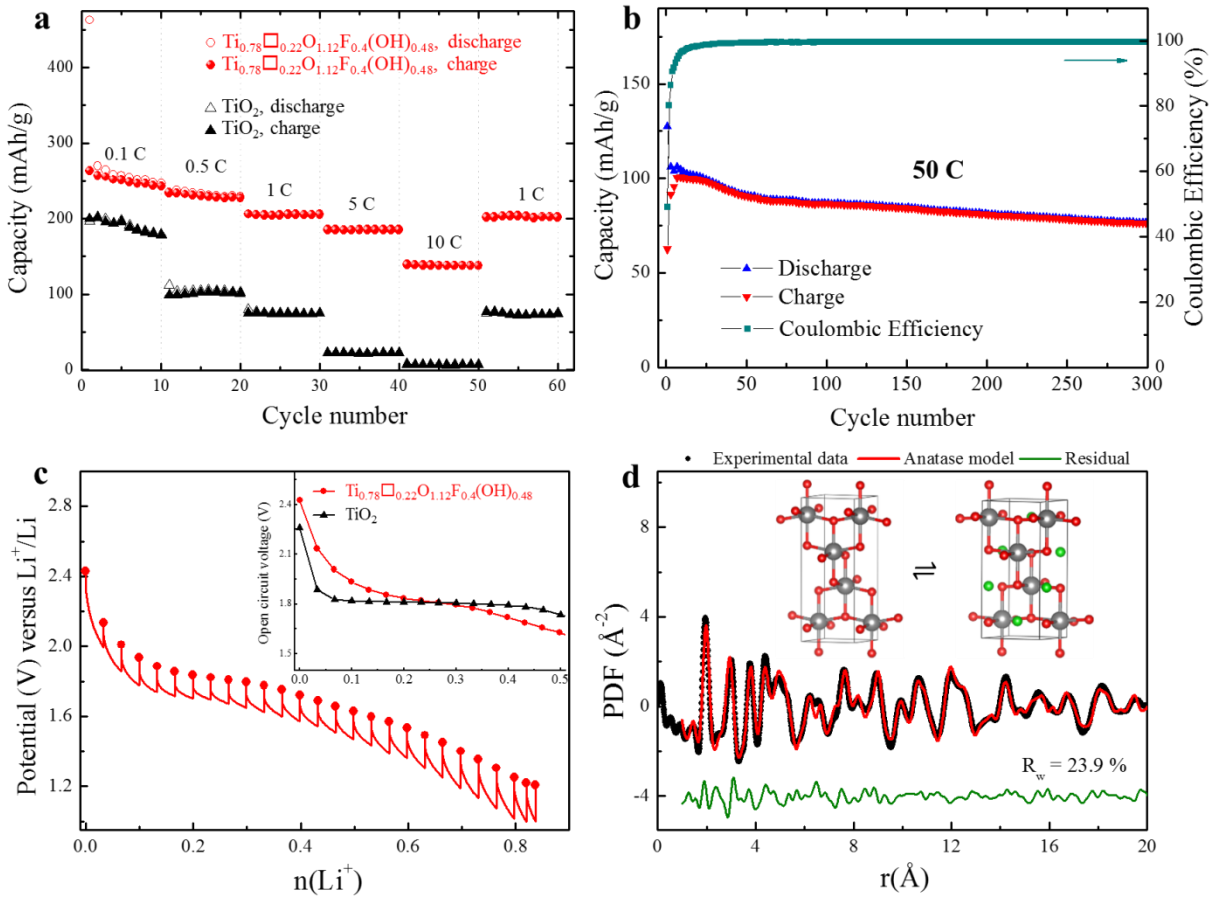


**Figure 11:** (a) Test de la densité de puissance de$Ti_{0.78}\square_{0.22}O_{1.12}F_{0.40}(OH)_{0.48}$ et $TiO_2$ anatase. (b) Cyclabilité à haut régime de 50 C. (c) Mesure de GITT réalisée dans la 2ème de décharge. (d) Raffinement de PDF de l'électrode de $Ti_{0.78}\square_{0.22}O_{1.12}F_{0.40}(OH)_{0.48}$ déchargé en utilisant la structure d'anatase. Les structures de $TiO_2$ anatase et $LiTiO_2$ sont montrées dedans.

Le mécanisme d'insertion du $Li^+$ dans $Ti_{0.78}\square_{0.22}O_{1.12}F_{0.40}(OH)_{0.48}$ a étudié afin de mieux comprendre sa meilleur performance électrochimique. A l'aide de la mesure de GITT, on observe une décroissance progressive du potentiel pendant la 2ème décharge (**Figure 11c**). Ce comportement est caractéristique d'une solution solide. Ceci est au contraire avec $TiO_2$ anatase qui présente un plateau de potentiel correspondant à la transition de phase de tétragonal à orthorhombique.[9,37] Le comportement solution solide de

$Ti_{0.78}\square_{0.22}O_{1.12}F_{0.40}(OH)_{0.48}$ a été confirmé par l'analyse de PDF de l'électrode complètement déchargé (**Figure 11d**). Le meilleur raffinement a été obtenu en utilisant que le modèle d'anatase. La modification de l'insertion du $Li^+$ pourrait être attribuée à la présence de lacunes qui empêchent la distorsion orthorhombique entraînée par 'pairing effect' de $LiO_6$ octaèdres.[38] Par conséquent, l'origine de la meilleur densité de puissance pour $Ti_{0.78}\square_{0.22}O_{1.12}F_{0.40}(OH)_{0.48}$ a été attribuée à : (i) réduction de taille de particule (7 nm);[16,20] (ii) expose de la surface réactive (54 % de la facette {001}); (iii) présence de lacune cationique;[23] (iv) modification du mécanisme d'insertion.[39]

**Propriétés électrochimiques de $TiO_2$ et $Ti_{0.78}\square_{0.22}O_{1.12}F_{0.40}(OH)_{0.48}$ vs. $Na^+$**

$TiO_2$ a été montré d'être actif sur l'insertion et désinsertion de sodium.[19] Mais, le mécanisme de sodiation est toujours en débat.[40-42] A l'aide de l'analyse de PDF, on a étudié le mécanisme d'insertion de $Na^+$ dans $TiO_2$ et $Ti_{0.78}\square_{0.22}O_{1.12}F_{0.40}(OH)_{0.48}$ anatase.

**Figure 12a** montre la courbe de charge/décharge de $TiO_2$. Pendant la 1ère décharge, le potentiel diminue progressivement jusqu'à 0.3 V. La courbe de potentiel présente un plateau à 0.2 V, délivrant une capacité de 280 mAh/g. La forme de la courbe est différente de celle en charge, indiquant le processus irréversible pendant la 1ère décharge. Le potentiel de travail est de 0.8 V, qui est inférieur de celui pour batterie au $Li^+$. L'électrode de $TiO_2$ a montré une bonne tenue au cyclage (**Figure 12b**). Après 50 cycles, le matériau a délivré une capacité de 165 mAh/g, ce qui correspond au 82.5 % de la capacité en 1ère charge.

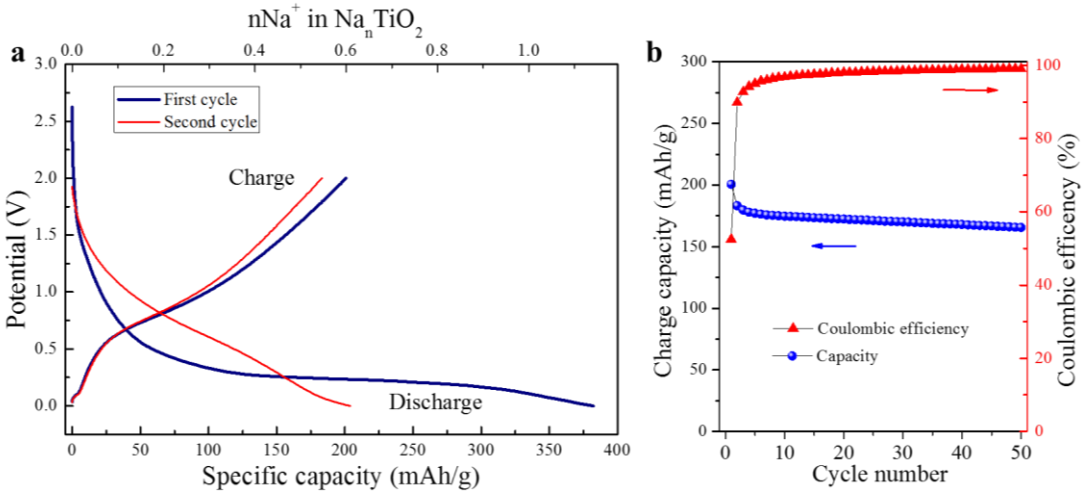


**Figure 12:** (a) Courbe de charge/décharge de pile $Na/TiO_2$. (b) Cyclabilité de $Na/TiO_2$.

Les diagrammes de rayon X à haut énergie des électrodes collectés à différent états de charge/décharge sont montrés dans **Figure 13a**. Le diagramme de la pristine est caractéristique de la structure de $TiO_2$ anatase. Quand l'électrode est déchargée à 0.3 V, il n'y a pas de changement du diagramme de rayon X. Pour l'électrode complètement déchargé, on observe la disparition des réflexions de l'anatase et la présence de nouveaux pics. Ces pics peuvent être indexés à la structure rhomboédrique de $NaTiO_2$ avec un groupe d'espace R-3m (**Figure 13b**). La présence de pic à ~25° en charge indique la récupération de $TiO_2$ anatase.

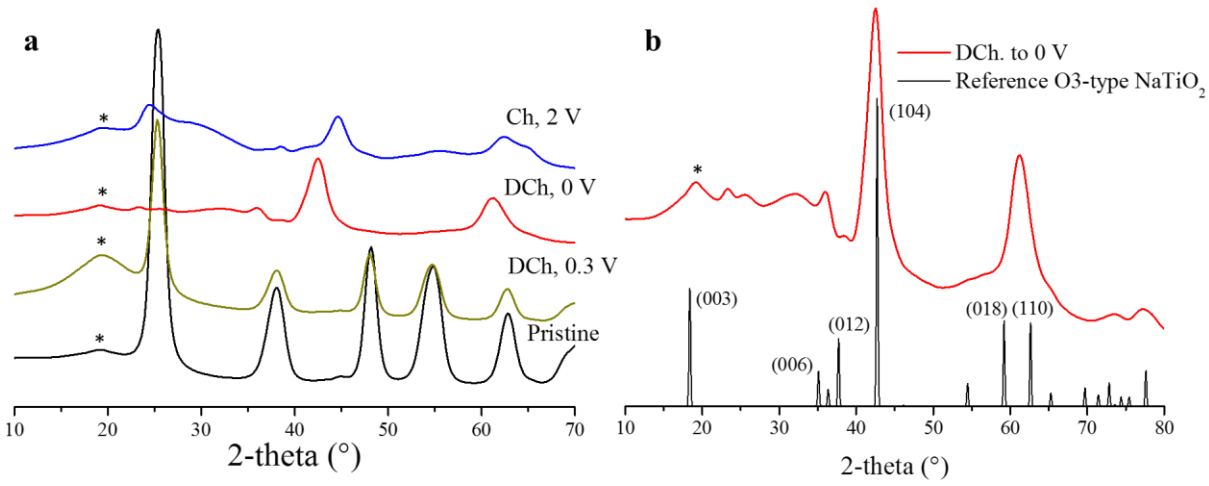


**Figure 13:** (a) Diagrammes de rayon X à haut énergie des électrodes collectés à différent états de charge et décharge. (b) Comparaison de l'électrode complètement déchargé avec $NaTiO_2$ référence.

Les informations structurales de l'électrode complètement déchargé ont été obtenues par le raffinement de PDF (**Figure 14**; **Tableau 3**). La région locale de la PDF ne peut pas être bien affinée, indiquant la présence de désordre local. Le domaine de cohérence est de ~3 nm qui est plus petit que le matériau pristine. La composition chimique est $Na_{0.82}Ti_{0.96}O_2$. La contraction volumique a été observée par rapport à la référence de $NaTiO_2$.[43] Cela est attribué à l'échange de cation dans les sites de Na et Ti. Cet échange de cation est l'origine du désordre local observé par le raffinement de PDF. En charge, le raffinement de PDF montre que 80 % de $TiO_2$ amorphe a été récupéré. Une partie de $Na^+$ est piégée dans l'électrode.

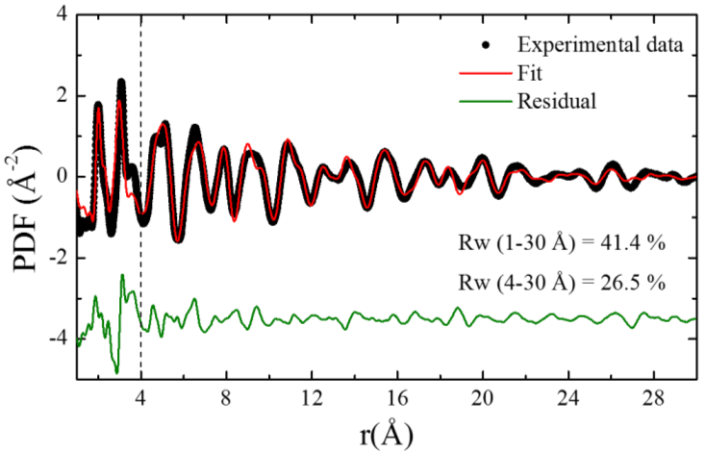


**Figure 14:** Raffinement de PDF de l'électrode complètement déchargé en utilisant la structure de $NaTiO_2$ (groupe d'espace: R-3m).

**Tableau 3: Comparaison de paramètres structuraux de $NaTiO_2$ obtenue de l'affinement de PDF et les données de référence.[43]**

| | | **Fitted $NaTiO_2$** | **$NaTiO_2$ (ICSD # 85657 )** |
|---|---|---|---|
| **a (Å)** | | 2.989 (8) | 3.05414 (4) |
| **c (Å)** | | 15.07 (9) | 16.2412 (2) |
| **V (Å$^3$)** | | 116.60 | 131.20 |
| **O (0,0,z)** | | 0, 0, 0.235 (2) | 0, 0, 0.2340 (2) |
| **Site occupancy** | Na (3a) | 0.43 (25) | 0.984(7) |
| | Ti (3a) | 0.57 (25) | 0.016(7) |
| | Na (3b) | 0.39 (14) | 0.016(7) |
| | Ti (3b) | 0.39 (1) | 0.984(7) |
| **$d_{Ti/Na-O average}$ (Å)** | | 2.022<br>2.305 | 2.075<br>2.390 |

Selon l'analyse d'électrochimie et de la PDF, le mécanisme d'insertion de $Na^+$ dans $TiO_2$ anatase a été proposé. Insertion de sodium est basé sur le couple redox de $Ti^{4+}/Ti^{3+}$. Ce processus manifeste comme une région de plateau dans le profil de voltage. La transition de phase de l'anatase à la structure laminaire de $Na_{0.82}Ti_{0.96}O_2$ a lieu dans le plateau de potentiel (**Figure 15**). Ce processus n'est pas réversible. Lors de la décharge, $Na_{0.82}Ti_{0.96}O_2$ convertie partiellement en $TiO_2$ amorphe. Ce processus est réversible, menant à la cyclabilité de la pile.

L'insertion du $Li^+$ dans $TiO_2$ anatase induit une distorsion orthorhombique de la structure tétragonale. Différent mécanisme pour l'insertion du $Na^+$ est attribué à ce que $Na^+$ a un rayon atomique plus grand que $Li^+$. $Na^+$ ne peut pas insérer dans des sites vacants dans la structure de l'anatase, un réarrangement structural est donc nécessaire.

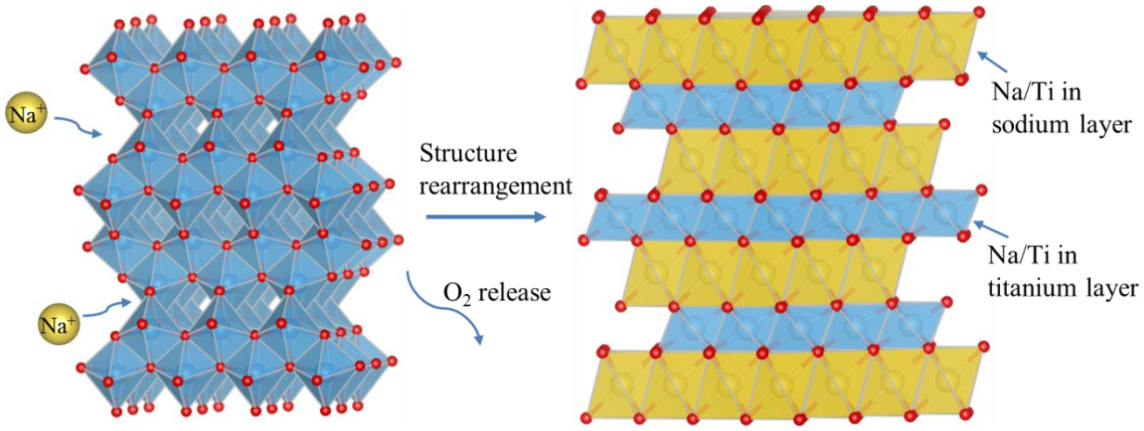


**Figure 15:** Mécanisme de l'insertion de $Na^+$ dans $TiO_2$ anatase (rouge : O, bleu : Ti, jaune : Na).

L'étude de l'insertion de sodium dans $Ti_{0.78}\square_{0.22}O_{1.12}F_{0.40}(OH)_{0.48}$ anatase a montré le mécanisme similaire avec $TiO_2$: transition de phase de la structure tétragonale au rhomboédrique pendant la décharge et la récupération de $TiO_2$ en charge. On note que la structure de l'anatase fluorée peut accommoder 0.14 $Na^+$ dans ses sites vacants et lacunes cationiques par la réaction de solution solide. Ce comportement pourrait être attribué à la présence de lacune et la réduction de taille de particules. Ce dernier est montré d'être efficace pour stocker le $Li^+$ par la réaction solution solide.

## 5. Conclusions et perspectives

Dans le cadre de cette thèse, on a développé une nouvelle méthode de synthèse à base de sol-gel dans le milieu fluoré pour synthétiser un oxyhydroxyfluorure de titane $Ti_{0.78}\square_{0.22}O_{1.12}F_{0.40}(OH)_{0.48}$ présentant la structure lacunaire d'anatase. La caractérisation structurale et la composition chimique ont été démontrées. Le mécanisme de formation de cette phase a été étudié à l'échelle atomique. Nous nous sommes intéressés ensuite à étudier l'effet des paramètres de synthèse sur la structure, composition et morphologie de la phase obtenue. Par conséquent, on est capable de contrôler la composition et la morphologie de l'anatase lacunaire en variant les paramètres de réaction. Des propriétés électrochimiques vis-à-vis au $Li^+$ ont été étudiés. $Ti_{0.78}\square_{0.22}O_{1.12}F_{0.40}(OH)_{0.48}$ a une meilleur performance électrochimique que $TiO_2$, surtout à haut régime de charge et décharge. Ce matériau lacunaire a présenté différent mécanisme pour l'insertion du $Li^+$: solution solide au lieu de transition de phase. Finalement, le diphasique mécanisme pour l'insertion du $Na^+$ dans l'anatase $TiO_2$ et $Ti_{0.78}\square_{0.22}O_{1.12}F_{0.40}(OH)_{0.48}$ a été également présenté.

En perspectives, notre méthode de synthèse peut être utilisée pour d'autres métaux. La composition chimique de l'anatase lacunaire devrait être optimisée pour une meilleure performance électrochimique. Il est nécessaire d'utiliser d'autres méthodes d'analyse à confirmer le mécanisme d'insertion du $Na^+$ dans la structure d'anatase.

## Références bibliographiques


(1) Fujishima, A.; Honda, K. Electrochemical Photolysis of Water at a Semiconductor Electrode. *Nature* **1972**, *238*, 37.

(2) Grätzel, M. Photoelectrochemical cells. *Nature* **2001**, *414*, 338.

(3) Kavan, L.; Grätzel, M.; Gilbert, S. E.; Klemenz, C.; Scheel, H. J. Electrochemical and Photoelectrochemical Investigation of Single-Crystal Anatase. *J. Am. Chem. Soc.* **1996**, *118*, 6716.

(4) Chen, X.; Mao, S. S. Titanium dioxide nanomaterials: Synthesis, properties, modifications, and applications. *Chem. Rev.* **2007**, *107*, 2891.

(5) Schneider, J.; Matsuoka, M.; Takeuchi, M.; Zhang, J.; Horiuchi, Y.; Anpo, M.; Bahnemann, D. W. Understanding $TiO_2$ Photocatalysis: Mechanisms and Materials. *Chem. Rev.* **2014**, *114*, 9919.

(6) Bai, Y.; Mora-Seró, I.; De Angelis, F.; Bisquert, J.; Wang, P. Titanium Dioxide Nanomaterials for Photovoltaic Applications. *Chem. Rev.* **2014**, *114*, 10095.

(7) O'regan, B.; Grätzel, M. A low-cost, high-efficiency solar-cell based on dye-sensitized colloidal $TiO_2$ films. *Nature* **1991**, *353*, 737.

(8) Bai, J.; Zhou, B. Titanium Dioxide Nanomaterials for Sensor Applications. *Chem. Rev.* **2014**, *114*, 10131.

(9) Cava, R. J.; Murphy, D. W.; Zahurak, S.; Santoro, A.; Roth, R. S. The crystal structures of the lithium-inserted metal oxides $Li_{0.5}TiO_2$ anatase, $LiTi_2O_4$ spinel, and $Li_2Ti_2O_4$. *J. Solid State Chem.* **1984**, *53*, 64.

(10) Ohzuku, T.; Kodama, T.; Hirai, T. Electrochemistry of anatase titanium dioxide in lithium nonaqueous cells. *J. Power Sources* **1985**, *14*, 153.

(11) Sudant, G.; Baudrin, E.; Larcher, D.; Tarascon, J.-M. Electrochemical lithium reactivity with nanotextured anatase-type $TiO_2$. *J. Mater. Chem.* **2005**, *15*, 1263.

(12) Froeschl, T.; Hoermann, U.; Kubiak, P.; Kucerova, G.; Pfanzelt, M.; Weiss, C. K.; Behm, R. J.; Huesing, N.; Kaiser, U.; Landfester, K.; Wohlfahrt-Mehrens, M. High surface area crystalline titanium dioxide: potential and limits in electrochemical energy storage and catalysis. *Chem. Soc. Rev.* **2012**, *41*, 5313.

(13) Lu, X.; Wang, G.; Zhai, T.; Yu, M.; Gan, J.; Tong, Y.; Li, Y. Hydrogenated $TiO_2$ Nanotube Arrays for Supercapacitors. *Nano Lett.* **2012**, *12*, 1690.

(14) Dunn, B.; Kamath, H.; Tarascon, J.-M. Electrical Energy Storage for the Grid: A Battery of Choices. *Science* **2011**, *334*, 928.

(15) Goodenough, J. B.; Park, K.-S. The Li-Ion Rechargeable Battery: A Perspective. *J. Am. Chem. Soc.* **2013**, *135*, 1167.

(16) Gentili, V.; Brutti, S.; Hardwick, L. J.; Armstrong, A. R.; Panero, S.; Bruce, P. G. Lithium Insertion into Anatase Nanotubes. *Chem. Mater.* **2012**, *24*, 4468.

(17) Shin, J.-Y.; Samuelis, D.; Maier, J. Sustained Lithium-Storage Performance of Hierarchical, Nanoporous Anatase $TiO_2$ at High Rates: Emphasis on Interfacial Storage Phenomena. *Adv. Funct. Mater.* **2011**, *21*, 3464.

(18) Sun, C. H.; Yang, X. H.; Chen, J. S.; Li, Z.; Lou, X. W.; Li, C.; Smith, S. C.; Lu, G. Q.; Yang, H. G. Higher charge/discharge rates of lithium-ions across engineered $TiO_2$ surfaces leads to enhanced battery performance. *Chem. Commun.* **2010**, *46*, 6129.

(19) Xu, Y.; Memarzadeh Lotfabad, E.; Wang, H.; Farbod, B.; Xu, Z.; Kohandehghan, A.; Mitlin, D. Nanocrystalline anatase $TiO_2$: a new anode material for rechargeable sodium ion batteries. *Chem. Commun.* **2013**, *49*, 8973.

(20) Wagemaker, M.; Borghols, W. J. H.; Mulder, F. M. Large Impact of Particle Size on Insertion Reactions. A Case for Anatase $Li_xTiO_2$. *J. Am. Chem. Soc.* **2007**, *129*, 4323.

(21) Shen, K.; Chen, H.; Klaver, F.; Mulder, F. M.; Wagemaker, M. Impact of Particle Size on the Non-Equilibrium Phase Transition of Lithium-Inserted Anatase $TiO_2$. *Chem. Mater.* **2014**, *26*, 1608.

(22) Liu, G.; Yang, H. G.; Pan, J.; Yang, Y. Q.; Lu, G. Q.; Cheng, H.-M. Titanium Dioxide Crystals with Tailored Facets. *Chem. Rev.* **2014**, *114*, 9559.

(23) Hahn, B. P.; Long, J. W.; Rolison, D. R. Something from Nothing: Enhancing Electrochemical Charge Storage with Cation Vacancies. *Acc. Chem. Res.* **2013**, *46*, 1181.

(24) Livage, J.; Henry, M.; Sanchez, C. Sol-gel chemistry of transition metal oxides. *Prog. Solid State Chem.* **1988**, *18*, 259.

(25) Liu, S.; Yu, J.; Cheng, B.; Jaroniec, M. Fluorinated Semiconductor Photocatalysts: Tunable Synthesis And Unique Properties. *Adv. Colloid Interface Sci.* **2012**, *173*, 35.

(26) Cargnello, M.; Gordon, T. R.; Murray, C. B. Solution-Phase Synthesis of Titanium Dioxide Nanoparticles and Nanocrystals. *Chem. Rev.* **2014**, *114*, 9319.

(27) Luan, Y.; Jing, L.; Xie, Y.; Sun, X.; Feng, Y.; Fu, H. Exceptional Photocatalytic Activity of 001-Facet-Exposed $TiO_2$ Mainly Depending on Enhanced Adsorbed Oxygen by Residual Hydrogen Fluoride. *ACS Catal.* **2013**, *3*, 1378.

(28) Wang, Y.; Zhang, H.; Han, Y.; Liu, P.; Yao, X.; Zhao, H. A selective etching phenomenon on {001} faceted anatase titanium dioxide single crystal surfaces by hydrofluoric acid. *Chem. Commun.* **2011**, *47*, 2829.

(29) Yu, J. C.; Yu, J. G.; Ho, W. K.; Jiang, Z. T.; Zhang, L. Z. Effects of $F^-$ doping on the photocatalytic activity and microstructures of nanocrystalline $TiO_2$ powders. *Chem. Mater.* **2002**, *14*, 3808.

(30) Yang, H. G.; Sun, C. H.; Qiao, S. Z.; Zou, J.; Liu, G.; Smith, S. C.; Cheng, H. M.; Lu, G. Q. Anatase $TiO_2$ single crystals with a large percentage of reactive facets. *Nature* **2008**, *453*, 638.

(31) Yu, J.; Wang, W.; Cheng, B.; Su, B.-L. Enhancement of Photocatalytic Activity of Mesporous $TiO_2$ Powders by Hydrothermal Surface Fluorination Treatment. *J. Phys. Chem. C* **2009**, *113*, 6743.

(32) Rudiger, S.; Kemnitz, E. The fluorolytic sol-gel route to metal fluorides-a versatile process opening a variety of application fields. *Dalton Trans.* **2008**, 1117.

(33) Czoska, A. M.; Livraghi, S.; Chiesa, M.; Giamello, E.; Agnoli, S.; Granozzi, G.; Finazzi, E.; Di Valentin, C.; Pacchioni, G. The nature of defects in fluorine-doped $TiO_2$. *J. Phys. Chem. C* **2008**, *112*, 8951.

(34) De Angelis, F.; Di Valentin, C.; Fantacci, S.; Vittadini, A.; Selloni, A. Theoretical Studies on Anatase and Less Common $TiO_2$ Phases: Bulk, Surfaces, and Nanomaterials. *Chem. Rev.* **2014**, *114*, 9708.

(35) Nabavi, M.; Doeuff, S.; Sanchez, C.; Livage, J. Chemical modification of metal alkoxides by solvents: A way to control sol-gel chemistry. *J. Non-Cryst. Solids* **1990**, *121*, 31.

(36) Wagemaker, M.; Mulder, F. M. Properties and Promises of Nanosized Insertion Materials for Li-Ion Batteries. *Acc. Chem. Res.* **2013**, *46*, 1206.

(37) Wagemaker, M.; Kearley, G. J.; van Well, A. A.; Mutka, H.; Mulder, F. M. Multiple Li Positions inside Oxygen Octahedra in Lithiated $TiO_2$ Anatase. *J. Am. Chem. Soc.* **2003**, *125*, 840.

(38) Morgan, B. J.; Watson, G. W. Role of Lithium Ordering in the $Li_xTiO_2$ Anatase → Titanate Phase Transition. *J. Phys. Chem. Lett.* **2011**, *2*, 1657.

(39) Liu, H.; Strobridge, F. C.; Borkiewicz, O. J.; Wiaderek, K. M.; Chapman, K. W.; Chupas, P. J.; Grey, C. P. Capturing metastable structures during high-rate cycling of $LiFePO_4$ nanoparticle electrodes. *Science* **2014**, *344*, 1252817.

(40) Kim, K.-T.; Ali, G.; Chung, K. Y.; Yoon, C. S.; Yashiro, H.; Sun, Y.-K.; Lu, J.; Amine, K.; Myung, S.-T. Anatase Titania Nanorods as an Intercalation Anode Material for Rechargeable Sodium Batteries. *Nano Lett.* **2014**, *14*, 416.

(41) Wu, L.; Bresser, D.; Buchholz, D.; Giffin, G. A.; Castro, C. R.; Ochel, A.; Passerini, S. Unfolding the Mechanism of Sodium Insertion in Anatase $TiO_2$ Nanoparticles. *Adv. Energy Mater.* **2015**, *5*, 1401142.

(42) Gonzalez, J. R.; Alcantara, R.; Nacimiento, F.; Ortiz, G. F.; Tirado, J. L. Microstructure of the epitaxial film of anatase nanotubes obtained at high voltage and the mechanism of its electrochemical reaction with sodium. *CrystEngComm* **2014**, *16*, 4602.

(43) Clarke, S. J.; Fowkes, A. J.; Harrison, A.; Ibberson, R. M.; Rosseinsky, M. J. Synthesis, Structure, and Magnetic Properties of $NaTiO_2$. *Chem. Mater.* **1998**, *10*, 372.

## Sol-gel synthesis of $TiO_2$ anatase in a fluorinated medium and its applications as negative electrode for $Li^+$ and $Na^+$ batteries

Titanium dioxide ($TiO_2$) is a multifunctional material and presents promising properties ranging from catalysis to energy storage and conversion. In order to obtain enhanced physico-chemical properties, several approaches were applied such as, reducing particle sizes, modifying morphology, doping with other elements. In this thesis, a new synthesis method based on sol-gel chemistry is developed in fluorinated medium. The divalent $O^{2-}$ in $TiO_2$ anatase is substituted by monovalent $F^-$ and $OH^-$ anions, the deficiency of negative charge is counterbalanced by the simultaneous formation of cationic $Ti^{4+}$ vacancies (□) which can be tuned by the reaction temperature. The new family of polyanionic materials has the general composition of $Ti_{1-x-y}\square_{x+y}O_{2-4(x+y)}F_{4x}(OH)_{4y}$ with up to 22 % of cationic vacancies. The drastically doped material keeps its original crystalline network and shows unique local structure. Its formation mechanism is investigated at atomic scale. The effects of synthesis parameters on structure, morphology and chemical composition of the resulting phase are studied in details. When used as anode for lithium-ion batteries, the cation-defected fluorinated anatase shows superior lithium storage performance, especially at high charge/discharge rate. The presence of vacancy modifies lithium insertion mechanism compared to stoichiometric $TiO_2$ anatase: a solid solution reaction was found instead a well-known two-phase reaction, highlighting the impact of structure modification on the electrochemical properties *vs.* $Li^+$. Sodium insertion mechanism into stoichiometric and defective anatase are studied at the last. Unprecedented insights into $Na^+$ insertion reaction are gained.

**Keywords:** Sol-gel, nonstoichiometric compounds, fluoride, titanate, lithium and sodium battery

## Synthèse de $TiO_2$ anatase par voie sol-gel dans le milieu fluoré et ses applications comme électrode négative pour batteries aux $Li^+$ et $Na^+$

Le dioxyde de titane ($TiO_2$) est un matériau polyvalent qui présente des propriétés intéressantes allant de la catalyse au stockage et conversion d'énergie. Afin d'améliorer ses propriétés physico-chimiques, plusieurs approches ont été appliquées telles que, la réduction de la taille des particules, modification de la morphologie, le dopage par d'autres éléments. Dans cette thèse, une nouvelle méthode de synthèse basée sur la chimie de sol-gel est développée en milieu fluoré. Les anions divalents de $O^{2-}$ dans $TiO_2$ anatase sont substitués par anions monovalents de $F^-$ et $OH^-$, le déficit de charge négative est compensée par la création simultanée de lacunes cationiques dont la concentration peut être réglés par la température de réaction. La nouvelle famille de matériaux polyanioniques a la composition générale de $Ti_{1-x-y}\square_{x+y}O_{2-4(x+y)}F_{4x}(OH)_{4y}$ avec de lacune cationique jusqu'à 22 %. Le matériau considérablement dopé maintient son réseau cristallin original et montre une structure locale unique. Son mécanisme de formation est étudié à l'échelle atomique. Les effets des paramètres de synthèse sur la structure, la morphologie et la composition chimique de la phase obtenue sont étudiés en détail. Lorsqu'il est utilisé comme anode pour batteries aux ions lithium, l'anatase fluorée lacunaire montre des performances supérieures pour le stockage de lithium, surtout à haute régime de charge/décharge. La présence de lacune modifie le mécanisme d'insertion du lithium par rapport à $TiO_2$ anatase stœchiométrique: une réaction de solution solide a été trouvé à la place une réaction diphasique, soulignant l'impact de la modification de la structure sur les propriétés électrochimiques vis-à-vis au $Li^+$. Enfin, le mécanisme d'insertion de sodium dans anatase stœchiométrique et lacunaire est étudié. Des aperçus sans précédent sont acquise pour la réaction d'insertion de $Na^+$.

**Mots clés:** Sol-gel, composés nonstoechiométriques, fluorure, titanate, batterie au lithium et sodium